Late-universe signals in the microwave sky: extragalactic dust, electrons, and other baryonic effects

by

Fiona McCarthy

A thesis
presented to the University of Waterloo
in fulfillment of the
thesis requirement for the degree of
Doctor of Philosophy
in
Physics and Astronomy

Waterloo, Ontario, Canada, 2021

Examining Committee Membership

The following served on the Examining Committee for this thesis. The decision of the Examining Committee is by majority vote.

External Examiner: Olivier Doré
Principal Scientist, Jet Propulsion Laboratory
California Institute of Technology

Supervisor(s): David Kubiznak
Adjunct Associate Professor, Physics and Astronomy,
University of Waterloo
Perimeter Institute for Theoretical Physics

Robert Mann
Professor, Physics and Astronomy, University of Waterloo

Internal Member: Matthew Johnson
Associate Professor, Physics and Astronomy,York University
Associate Faculty, Perimeter Institute for Theoretical Physics

Internal Member: Avery Broderick
Associate Professor, Physics and Astronomy, University of Waterloo,
Associate Faculty Member, Perimeter Institute of Theoretical Physics

Internal-External Member: Ghazal Geshnizjani
Research Associate Professor, Applied Mathematics,
University of Waterloo

Author's Declaration

This thesis consists of material all of which I authored or co-authored: see Statement of Contributions included in the thesis. This is a true copy of the thesis, including any required final revisions, as accepted by my examiners.

I understand that my thesis may be made electronically available to the public.

Statement of contributions

This thesis was largely written by myself and contains some Chapters which are edited versions of papers that were co-written and published. Chapters 2, 4, 5, and 6 serve as introductory Chapters which all follow standard textbook material, but which I have collected and written myself. Chapter 3 was co-written with David Kubizňák and Robert Mann and was published in [1]. Chapter 7 was co-written with Mathew Madhavacheril and was published at [2]. Chapter 8 was co-written with Matthew Johnson and was published in [3]. Chapter 9 was co-written with Simon Foreman and Alexander van Engelen and was published at [4]. Chapter 10 was co-written with Colin Hill and Mathew Madhavacheril and can be found at [5]. In all of Chapters 3, 7, 8, 9, and 10, I performed all technical calculations and created all the plots and figures as well as contributing significantly to the writing of the text.

During my PhD I also contributed extensively to a halo model python code (currently not public) which in particular is used to calculate power spectra in the plots in Chapter 5 as well as in other Chapters.

Abstract

This thesis collects much of the work I have done over the last four years as a PhD student. It has two focuses. Part I discusses gravitational radiation emitted from two maximally charged black holes in Einstein–Maxwell–dilaton theory, while Part II focuses on cosmological probes of late-universe physics.

Black holes are some of the most interesting solutions to Einstein's equations, the equations that govern the curvature of the spacetime we inhabit. The gravitational field around them is stronger than around any other astrophysical object, and the interaction of two black holes can cause strong disturbances in the spacetime, leading to the radiation of gravitational waves. Gravitational radiation is usually a complex problem that must be studied numerically, and analytic solutions are rare. However, in Einstein–Maxwell (EM) theory, where the Einstein equations are supplemented with the Maxwell equations governing the behaviour of electromagnetic fields, there exists a configuration of black holes which have electric charge which causes a repulsive force that counteracts their gravitational attraction. These black holes can be evolved quasi-statically leading to gravitational radiation that can be analytically approximated. In Chapter 3 of this thesis we analytically approximate the radiation when the EM equations are further supplemented with a dilaton (scalar) field.

The second part of this thesis relates to work I have done in relation to late-universe probes and secondary cosmic microwave background (CMB) effects, in particular motivated by the upcoming Simons Observatory and CMB-S4 CMB surveys. The CMB has been detected and mapped with exquisite detail by the *Planck* satellite on arcminute scales, and these experiments will extend to even smaller angular scales. In this regime "secondary" effects sourced in the late universe will dominate, in particular CMB lensing due to large masses and the interaction of the CMB with electrons (the Sunyaev–Zel'dovich effect). We also get closer to the regime in which the cosmic infrared background (CIB), sourced by thermal radiation from dust in star-forming galaxies, starts to dominate over the CMB. Robust and consistent modelling is required to understand how the different signals relate to and correlate with each other.

In this thesis we consider how various combinations of these phenomena correlate in different ways. Chapter 7 discusses how the correlation between CMB lensing and the CIB can be used to improve models of the latter. Chapter 8 discusses how CIB maps can be combined with Sunyaev–Zel'dovich probes to reconstruct the velocity field of the universe on the largest scales. In Chapters 9 and 10 we discuss how complex late-universe interactions can bias the inference of fundamental physics from the CMB lensing and lensed CMB maps, and develop several mitigation methods to ensure unbiased inference.

Acknowledgements

I have been very fortunate to have supervisors during my PhD who gave me the freedom to pursue my own interests when they diverged from theirs, and I am grateful for this. I thank David Kubizňák and Robb Mann for the time they put in to working with me, and the support they gave me even when I was no longer working directly with them. Additionally I thank Robb for the help with my scholarship application in my first year which helped a lot to give me independence. I also thank David for our weekly squash games (pre-pandemic), even if you usually beat me at the last minute!

Huge thanks go to Matt Johnson, who took me on as a student and brought me into his research group as I drifted towards cosmology. He has been incredibly kind and generous with his time and has introduced me to so much interesting science. Thank you Matt for being so wonderful to work with!

I thank as well the other members of my supervisory committee, Avery Broderick and Ghazal Geshnizjani, for their time and encouragement throughout my PhD, and the corrections they suggested to my thesis, and also I thank the external examiner Olivier Doré.

I thank all the people who I have worked with directly on the research in this thesis: Simon Foreman, Colin Hill, Matthew Johnson, David Kubizňák, Mathew Madhavacheril, Robert Mann, and Alexander van Engelen. Additionally I thank my collaborators on various other projects throughout my PhD; in particular Avery Broderick, Dagoberto Contreras, Moritz Munchmeyer, and Kendrick Smith. I have learnt so much from all of you. Lots of people I met and collaborated with during my time at PI have been so encouraging to me and I thank them for this, and for the advice many of them have given me, in particular Mat, Moritz, Simon, and Alex. I thank especially Kendrick and Matt for giving me their time when I knew so little about cosmology!

I thank all the people who make Perimeter a community, including the administrative, facilities, and research staff. I also particularly thank the person who decided to put a squash court in the building, whoever that might be!

As a beginning graduate student I was lucky to have more senior friends and mentors in my research group and in this context in particular I want to thank Natacha Altamirano and Robie Hennigar. In particular Robie deserves mention as one of my first ever collaborators. Naty, thanks for your friendship and your advice throughout the various stages of my PhD.

I have been supported by a Vanier Canada Government Scholarship for three years of my PhD; I thank the Canadian people for funding this.

Finally, thanks to the many friends who have made my time in Waterloo (almost five years!) so rewarding and enjoyable, even during this last year of the pandemic. I have learnt more from you all than could ever be written in a PhD thesis, and I couldn't have written this one without a lot of you—in particular I thank Juan Cayuso and Tomáš Gonda who have been there since the very start. I thank my parents, for always giving me their unconditional support, and I thank the teachers I have learnt from at every stage of my education.

Table of Contents

List of Figures

List of Tables

Chapter 1

Introduction

During the 20th Century, cosmology and astrophysics developed into precise sciences with improving observations of the sky driving theory to explain what we see. One of the most important theory developments of this period was the development of General Relativity (GR) by Einstein in 1916. This theory, which relates the presence of mass-energy to the curvature of the spacetime manifold we inhabit, generalized Newton's theory of gravity and allowed us to understand anomolous measurements that had already been made.

The revolutionary nature of GR lay not in its predictions of slight deviations from the previous theory, but the qualitatively new phenomena it predicted, which led to a new era in astrophysics. A black hole solution was discovered by Schwarzschild only months after Einstein developed the central equations of GR (the "Einstein equations"), describing a mass so dense that it cannot allow light to escape and creates a causally disconnected region of spacetime. Wave solutions were found by Einstein, where disturbances in the curvature of spacetime itself radiate energy at the speed of light. Despite seeming exotic when they were introduced, black holes were subsequently found in the sky by astronomers during the 20th century [6], and it is almost taken for granted now that there is a supermassive black hole at the centre of most galaxies. More recently, gravitational radiation from black hole mergers—where two black holes collide—has been detected by the gravitational wave interferometers of LIGO [7], 100 years after Einstein's prediction. We also have our first "photo" of a black hole, from only 2019 [8].

GR is a non-linear theory and the modelling of waveforms from binary black holes is usually done numerically, with significant effort, and requires much computing power. The existence of analytic approximations to gravitational waves is unusual, and interesting especially as it can serve to develop physical intuition as well as to compare with numerical results in situations where we have access to both. Some early work of my PhD related to the development of analytic approximations to gravitational waves; this work is presented in Chapter 3.

The remainder of this thesis focuses on cosmology, the name given to the study of the history and large-scale structure of our universe. As well as the developments in astrophysics precipitated by GR as described above, GR has allowed the field of cosmology to have a mathematical foundation for the first time. We can write down a metric for the spacetime of the universe and use the Einstein equations to understand its behaviour. GR, along with the developments in particle physics of the 20th Century, has allowed us to build precise, quantitative models that describe our universe. The simultaneous developments in observation and instrumentation have allowed us to test those models quantitatively. In particular, the detection of the cosmic microwave background (CMB) radiation in the 1960s [9] and its fluctuations in the 1990s [10] have allowed us to see light that last interacted with matter when the universe was around 380,000 years old. We now have full-sky maps of the CMB temperature on arcminute scales from the *Planck* satellite [11], and the CMB remains most our most important probe of early-universe cosmology.

These developments in observational cosmology have led to a widely accepted model for the universe that we live in: an expanding spacetime, filled with radiation, matter, and "dark energy". Most of the matter is "dark" matter—where by "dark" we mean it does not interact with the electromagnetic force, and so we cannot see directly any of its effects; however, it interacts gravitationally and accounts for the strong gravitational fields we observe that cannot be due to the visible matter alone. Observations indicating that the universe's expansion has recently started to accelerate have motivated the inclusion of the dark energy component, represented by Λ. The name we give to this cosmological model is ΛCDM, with "CDM" standing for "cold dark matter". This theory describes much of what we observe, including the fluctuations of the CMB and the clustering of matter on large scales, with only 6 free parameters, that can be measured precisely by comparison with data.

In the coming decade and further, we will continue to improve the observations we make of the CMB. Higher resolution CMB maps are being made already by the Atacama Cosmology Telescope (ACT) [12, 13] and the South Pole Telescope (SPT) [14, 15]; soon the Simons Observatory (SO) [16] will make high resolution maps on large fractions of the sky, and CMB-S4 [17] will improve even further on this. The smaller angular scales we will access with these experiments will probe a new regime of CMB physics: that where CMB *secondary effects*, processes that have changed the CMB in the late universe, dominate over the *primary* properties that it had upon its release. For example, the scattering of CMB photons from electrons in the late universe, known as the Sunyaev–Zel'dovich (SZ) effect, starts to become important, and so does gravitational interaction between CMB photons and large masses that caused the CMB to be lensed. These effects contain information about the distribution of electrons and masses that cause them, which can be accessed through the CMB map. In this regime, the CMB starts to be a late-universe probe, from which we can learn about the large scale structure of the universe today and its recent evolution.

Measuring and interpreting these secondary effects is a key goal of the upcoming CMB surveys. In particular, high-resolution CMB maps can used to directly map the intervening matter responsible for their lensing, and the SZ effects can be used to map the electron distribution of the late universe. These will have many potential applications, both on their own, and in combination with each other and other late-universe probes. However, a detailed understanding of the signals will be required to achieve these potentials. Much of the work presented in Part II of this Thesis concerns work towards the modelling and applications of these probes.

One late-universe property of relevance is the cosmic infrared background (CIB), a diffuse background which is sourced by the thermal radiation from small dust particles in unresolved star-forming galaxies. As a tracer of these distant galaxies, the CIB is an interesting cosmological probe that contains information about the clustering of these galaxies. The CIB also contains information about astrophysics, as the star formation rate of galaxies is correlated with their dust content and hence their infrared emission. Also, the CIB is important to consider in high resolution measurements of the CMB: on the smallest scales accessed by SO and CMB-S4 it will be brighter than the CMB and its separation will be important to make clean CMB maps. Modelling of the CIB is considered explicitly in this thesis; the work presented in Chapter 7 shows how CMB lensing mass maps can be combined with CIB maps to learn directly about the CIB and improve on current CIB models.

The CIB is also considered in Chapter 8, this time as a cosmological probe that can be combined with the SZ signal from a CMB survey. In particular, the *kinetic* SZ (kSZ) effect is sourced when CMB photons scatter off of a moving electron, and the kSZ signal we receive contains information about the distribution of electrons and also about their velocity. Through the cross-correlation of the kSZ signal with another density tracer, a map of the *large-scale* electron velocity field can be made, turning the small-scale SZ signal into a large-scale probe, which contains information about the primordial universe. In Chapter 8 we show how the CIB can be used as this density tracer and how we can measure the velocity in this way with upcoming experiments.

The final two chapters of this thesis, Chapters 9 and 10, concern the effects of baryons on CMB lensing. In particular, our current models of the clustering matter neglect to include complicated effects due to star formation, gas cooling, and feedback induced baryons—ie, the "ordinary" matter such as protons, electrons, and neutrons. We quantify explicitly in Chapter 9 how this will bias measurements of the neutrino mass from CMB lensing maps, which is an important goal of these upcoming surveys. We present several ways to avoid these baryonic effects to achieve a clean measurement of the neutrino mass. We also consider in Chapter 10 how these effects will bias measurements from the CMB itself, and again show how they can be avoided.

This body of this thesis is presented in two parts. Part I focuses on gravitational waves, with Chapter 2 serving as an introduction of the theory of gravitational waves and black holes, and 3 representing work done early in my PhD to find analytic approximations to gravitational waves in certain configurations. Part II focuses on topics related to cosmology. The first three chapters of this Part serve as backgrounds and summaries of theory found that can be found in various textbooks or review papers. We begin with an introduction to the modern theory of cosmology and perturbation theory in Chapter 4, followed by an introduction to the halo model used to model various observables in Chapter 5. Chapter 6 introduces the likelihood and Fisher formalism used for forecasting errors on parameters inferred from future experiments. We then present the original work done during the latter half of my PhD: in Chapter 7 we discuss the potential of upcoming CMB lensing surveys to improve constraints on CIB models; in Chapter 8 we present an estimator that will extract the large-scale velocity field of the universe from the combination of the small-scale CMB and CIB maps; and in Chapters 9 and 10 we discuss late-universe effects on CMB lensing models and mitigation of modelling uncertainty to constrain fundamental physics parameters in unbiased ways, with Chapter 9 dealing with inference from CMB lensing mass maps and Chapter 10 dealing with inference from lensed CMB maps.

All CMB and linear matter power spectrum calculations throughout are done with CAMB[1] [18].

1.1 Conventions and notation

The following conventions are used throughout the thesis.

- A $(-,+,+,+)$ signature for the spacetime metric.

---

[1] http://camb.info

- Greek indices (eg μ,ν) refer to 4-dimensional (spacetime) quantities; Latin indices (eg i,j,k) refer to 3-dimensional spatial quantities. The spacetime dimensions are indexed by $(0, 1, 2, 3)$ and the spatial ones by $(1, 2, 3)$. The Einstein summation convention is assumed, whereby upper and lower repeated indices are summed over: $x^\mu x_\mu = \sum_{\mu=0}^{3} x^\mu x_\mu$. Greek indices are (raised) lowered with the 4-dimensional (inverse) metric $(g^{\mu\nu})$ $g_{\mu\nu}$: $x^\mu = g^{\mu\nu} x_\nu$, $x_\mu = g_{\mu\nu} x^\nu$, $g^{\mu\alpha} g_{\alpha\nu} = \delta^\mu_\nu$ where δ^μ_ν is the identity.
- Spatial 3-vectors and angular 2-vectors are denoted with bold text and an over-arrow, eg $\vec{\boldsymbol{k}}$, $\vec{\boldsymbol{x}}$, $\vec{\boldsymbol{\alpha}}$. Unit vectors are denoted with bold text and a hat, eg $\hat{\boldsymbol{n}}$.
- Partial derivatives with respect to a coordinate x^α are denoted ∂_α.
- Covariant derivatives with respect to a coordinate x^α are denoted either by ∇_α or with a subscript $_{;\alpha}$.
- For all Fourier transformations,

$$\Phi(\vec{\boldsymbol{k}}) = \int d^3\vec{\boldsymbol{\chi}} e^{-i\vec{\boldsymbol{k}}\cdot\vec{\boldsymbol{\chi}}} \Phi(\vec{\boldsymbol{\chi}}) \tag{1.1}$$

$$\Phi(\vec{\boldsymbol{\chi}}) = \int \frac{d^3\vec{\boldsymbol{k}}}{(2\pi)^3} e^{i\vec{\boldsymbol{k}}\cdot\vec{\boldsymbol{\chi}}} \Phi(\vec{\boldsymbol{k}}). \tag{1.2}$$

- For all spherical harmonic expansions,

$$\phi(\hat{\boldsymbol{n}}) = \sum_{\ell=0}^{\infty} \sum_{m=-\ell}^{m=\ell} \phi_{\ell m} Y_{lm}(\hat{\boldsymbol{n}}) \tag{1.3}$$

$$\phi_{\ell m} = \int d^2\hat{\boldsymbol{n}} Y^*_{\ell m}(\hat{\boldsymbol{n}}) \phi(\hat{\boldsymbol{n}}), \tag{1.4}$$

  where the $Y_{\ell m}$ are the spherical harmonic functions which satisfy the 2-dimensional Laplace equation on the unit sphere (and $*$ refers to complex conjugation). The $Y_{\ell m}$ are normalized as follows:

$$\int d^2\hat{\boldsymbol{n}} Y_{\ell m}(\hat{\boldsymbol{n}}) Y^*_{\ell' m'}(\hat{\boldsymbol{n}}) = \delta_{\ell\ell'} \delta_{mm'}. \tag{1.5}$$

- Subscript 0s refer to quantities at the present day, eg H_0 is the Hubble parameter $H(t)$ today.
- Superscript 0s refer to initial conditions, ie Φ_0 is the value of Φ at $t \to 0$.
- Superscript $^{(0)}$ refers to background quantities, eg $\rho^{(0)}$ is the background (homogeneous) density; while $\delta\rho$ is the perturbation.

Part I

Exact Gravitational Wave Signatures from Extremal Black Holes

Chapter 2

Gravitational waves and black holes

The theory of General Relativity (GR) had not long been introduced before it was realized that it admits wave-like solutions in the vacuum. In this Chapter we will introduce the basics of the linearized gravity that results in this conclusion, and in particular present the quadrupole formula for gravitational radiation. We will also present some common black hole solutions that are relevant for Chapter 3. As a very basic introduction to GR, various of the concepts introduced in this Chapter will be relevant for the cosmological perturbation theory discussed in Part II of this thesis.

The Chapter is organized as follows. In Section 2.1 we present the central equations of GR, the Einstein Equations. In Section 2.2 we present the Einstein Hilbert action, from which the Einstein equations can be derived. In Section 2.3 we present the geodesic equation, the equation for the worldline followed by all particles moving under the influence of gravity alone. In Section 2.4 we linearize the Einstein equations and present the "quadrupole formula" for gravitational radiation. Finally, in Section 2.5 we present various basic black hole solutions.

2.1 The Einstein equations

The idea of GR is that spacetime is a curved manifold with a metric $g_{\mu\nu}$ where the curvature of the spacetime and the distribution of stress-energy are related by the Einstein Equations,

$$G_{\mu\nu} = 8\pi G T_{\mu\nu} \tag{2.1}$$

where $G_{\mu\nu}$ is the Einstein tensor

$$G_{\mu\nu} \equiv R_{\mu\nu} - \frac{1}{2} R g_{\mu\nu} \tag{2.2}$$

with $R_{\mu\nu}$ the Ricci tensor and R the Ricci scalar. $R_{\mu\nu}$ and R can be obtained from the Riemann tensor according to

$$R_{\mu\nu} \equiv R^{\sigma}{}_{\mu\sigma\nu}; \tag{2.3}$$

$$R \equiv R^{\mu}{}_{\mu}. \tag{2.4}$$

The Riemann tensor $R^{\rho}{}_{\mu\sigma\nu}$ can be calculated from the Christoffel symbols

$$R^{\rho}{}_{\mu\sigma\nu} = \partial_{\nu}\Gamma^{\rho}_{\nu\mu} - \partial_{\nu}\Gamma^{\rho}_{\sigma\mu} + \Gamma^{\rho}_{\sigma\lambda}\Gamma^{\lambda}_{\nu\mu} - \Gamma^{\rho}_{\nu\lambda}\Gamma^{\lambda}_{\sigma\mu}, \tag{2.5}$$

where the Christoffel symbols $\Gamma^{\alpha}_{\beta\gamma}$ can be calculated directly from derivatives of the metric

$$\Gamma^{\alpha}_{\beta\gamma} = \frac{g^{\alpha\lambda}}{2} \left(\partial_{\beta} g_{\lambda\gamma} + \partial_{\gamma} g_{\lambda\beta} - \partial_{\lambda} g_{\gamma\beta} \right). \tag{2.6}$$

In Equation (2.1), G is Newton's gravitational constant, which describes the strength of the gravitational interaction.

2.2 The Einstein–Hilbert action

The Einstein equations are derivable from extremizing an action known as the Einstein–Hilbert action. It is given by

$$S_{EH} = \frac{1}{8\pi G} \int R\sqrt{-g}\, d^4x, \tag{2.7}$$

where R is the Ricci scalar and g is the determinant of the metric $g \equiv \det g_{\mu\nu}$.

2.3 The geodesic equation

Objects experiencing no external forces follow geodesics —the "shortest paths"—in the spacetime. That is, their worldlines obey the geodesic equation

$$\frac{d^2 x^{\mu}}{d\lambda^2} + \Gamma^{\mu}_{\alpha\beta} \frac{dx^{\alpha}}{d\lambda} \frac{dx^{\beta}}{d\lambda} = 0 \tag{2.8}$$

where x^μ represents the spacetime coordinates of the object's path (its "worldline"), and λ is an affine parameter that parametrizes its path.

There are three types of geodesics: those on which the interval $ds^2 = g_{\mu\nu}dx^\mu dx^\nu$ is greater than, less than, or equal to zero. Physical particles are constrained to travel on time-like geodesics, for which $ds^2 < 0$. Light travels on light-like geodesics, for which $ds^2 = 0$. Paths along space-like geodesics, for which $ds^2 > 0$, are unphysical. This can be restated as a constraint on the object's 4-velocity $u^\mu \equiv \frac{dx^\mu}{d\tau}$: for light-like geodesics $u^\mu u_\mu = 0$ and for timelike geodesics $u^\mu u_\mu = -1$, where t is the proper time along the particle's trajectory.

2.4 Linearized gravity and wave solutions

The vacuum Einstein equations are given by Equation (2.1) with $T_{\mu\nu} = 0$:

$$G_{\mu\nu} = 0. \tag{2.9}$$

Given a solution $g^{(0)}_{\mu\nu}$ of the Einstein equations—such as the Minowski metric $\eta_{\mu\nu}$, which is a trivial solution to the vacuum equations—one can perform perturbation theory around $g^{(0)}_{\mu\nu}$ to find the behaviour of any perturbation, for example

$$g_{\mu\nu} = \eta_{\mu\nu} + h_{\mu\nu} \tag{2.10}$$

where $|h_{\mu\nu}| \ll |\eta_{\mu\nu}|$. To linear order in perturbations, the Einstein tensor for (2.10) is

$$G_{\mu\nu} = -\frac{1}{2}\partial_\alpha\partial^\alpha\bar{h}_{\mu\nu} \tag{2.11}$$

where $\bar{h}_{\mu\nu}$ is the trace-reversed perturbation $\bar{h}_{\mu\nu} \equiv h_{\mu\nu} - \frac{\eta_{\mu\nu}}{2}h$ with h the trace of $h_{\mu\nu}$, ie $h \equiv h^\mu{}_\nu$, and where $\bar{h}_{\mu\nu}$ is in the Lorentz gauge

$$\partial_\alpha\bar{h}^{\alpha\beta} = 0. \tag{2.12}$$

In a vacuum, the Einstein equations are $G_{\mu\nu} = 0$; for Equation (2.11) this permits wave solutions

$$\bar{h}_{\mu\nu} = \mathrm{Re}\left[A_{\mu\nu}e^{ik_\alpha x^\alpha}\right] \tag{2.13}$$

where k^α is a null vector, ie $k^\alpha k_\alpha = 0$; and it is orthogonal to $A_{\mu\nu}$, ie $k_\alpha A_\mu{}^\alpha = 0$.

If there are perturbations also to the stress-energy, then the Einstein equations require $G_{\mu\nu} = 8\pi G T_{\mu\nu}$, where $T_{\mu\nu}$ are these perturbations. The solution to this, given Equation (2.11), is

$$\bar{h}_{\mu\nu}(t, \vec{\boldsymbol{x}}) = -\frac{2}{3R}\frac{d^2}{dt^2} q_{\mu\nu}(\vec{\boldsymbol{x}}')\bigg|_{t_{\text{ret}}} \tag{2.14}$$

where $R \equiv |\vec{\boldsymbol{x}} - \vec{\boldsymbol{x}}'|$ and $q_{\mu\nu}$ is the mass quadrupole tensor

$$q_{\mu\nu} \equiv 3 \int T^{00} x^{\mu} x^{\nu} d^3x; \tag{2.15}$$

the derivative is calculated at the retarded time $t_{\text{ret}} \equiv t - R$.

From (2.15), we can see that a configuration with a time-varying quadrupole causes gravitational waves at a distance.

2.5 Black hole solutions

Black hole solutions are solutions to the Einstein equations in which there is a region of spacetime in which no time-like or light-like geodesics reach the "asymptotic infinities" of the spacetime. As such, there are no physical paths to leave these regions, even for light. As black holes have been detected in our universe, they are important astrophysically as well as being extremely interesting due to their non-trivial causal structures.

2.5.1 Stationary solutions

Schwarzschild

One of the simplest solutions to the vacuum Einstein equations is the Schwarzschild solution

$$ds^2 = -f(r)dt^2 + \frac{1}{f(r)}dr^2 + r^2 d\Omega^2 \tag{2.16}$$

where $f(r) = \left(1 - \frac{2M}{r}\right)$, M is the mass of the black hole, and $d\Omega^2$ is the standard 2-sphere metric $d\Omega^2 = d\theta^2 + \sin^2\theta d\phi^2$. $f(r) = 0$ defines the presence of a horizon in the spacetime, inside of which no physical matter can leave.

Reissner–Nordström

The Einstein equations can be supplemented with the Maxwell equations for an electromagnetic field potential A_α with field strength

$$F_{\mu\nu} \equiv \nabla_\mu A_\nu - \nabla_\nu A_\mu \tag{2.17}$$

where ∇_μ is the covariant derivative; the Maxwell equations are

$$F^{\mu\nu}{}_{;\mu} = 0 \tag{2.18}$$

$$F_{[\mu\nu;\alpha]} = 0 \tag{2.19}$$

where the square brackets [] indicate that one should antisymettrize the enclosed indices. The combination of the Einstein equations and the Maxwell equations are the Einstein–Maxwell equations; they admit a black hole solution known as the Reissner–Nordström (RN) solution which takes a similar form to (2.16) but with

$$f(r) = 1 - \frac{2M}{r} + \frac{Q^2}{r^2} \tag{2.20}$$

where Q is the charge of the black hole. The electromagnetic field is given by

$$A = -\frac{Q}{r}dt. \tag{2.21}$$

Note that $Q \leq M$, and black holes with $Q = M$ are referred to as "extremal".

Kerr

It is important to note that astrophysical black holes are not expected to have a significant electromagnetic charge Q; however, they can have non-zero have angular momentum, in which case the spherically-symmetric solution (2.16) is not appropriate. In this case, the Kerr metric

$$ds^2 = -\frac{\Delta}{\rho^2}\left(dt - a\sin^2\theta d\phi\right)^2 + \frac{\sin^2\theta}{\rho^2}\left(\left(r^2 + a^2\right)d\phi - adt\right)^2 + \frac{\rho^2}{\Delta}dr^2 + \rho^2 d\theta^2 \tag{2.22}$$

with

$$\rho^2 \equiv r^2 + a^2\cos^2\theta; \tag{2.23}$$

$$\Delta \equiv r^2 - 2Mr + a^2, \tag{2.24}$$

where $a \equiv \frac{J}{M}$ is the angular momentum per unit mass, is a solution that is expected to be a better description for astrophysical black holes; it can also be generalized to include non-zero charge, in which case it is known as the Kerr–Newmann metric.

The black hole solutions introduced in this Section are all *stationary*, and as such they do not have any time-varying quadrupole and do not emit gravitational radiation. To achieve a time-varying quadrupole one typically considers *binary* systems, whereby two (or more) black holes rotate around each other, losing energy (which is emitted as gravitational radiation) and eventually colliding. This is the sort of system that has been observed in the gravitational wave mergers detected by LIGO, and in general they are not analytical solutions but instead must be evolved numerically on a computer with great effort.

Multi-black-hole solution: Majumdar–Papapetrou

While the above solutions have all been for single black holes, Majumdar and Papapetrou introduced a multi-black-hole extension to the Reissner–Nordström solution where all the black holes are extremal and with the same sign charge, and the gravitational attraction is "balanced out" by the electromagnetic repulsion; thus this remains a static solution. This solution will be presented in the following Chapter, and is the basis for the system we consider.

Chapter 3

Dilatonic imprints on exact gravitational wave signatures

3.1 Introduction

The great discovery made by LIGO on September 14, 2015 [7] provided the first direct confirmation that strong gravitational waves are emitted in the process of the coalescence of two black holes. The detection of a neutron star-neutron star collision [19], has also marked the beginning of the age of "multi-messenger astronomy" where we can "see" an event both in electromagnetic (EM) detectors and in gravitational wave detectors.

To understand a black hole merger (or scattering) and the associated emission of gravitational waves is a complicated problem in which strong field dynamical effects play an important role. For this reason, there is little hope for attacking this problem exactly, and various approximations [20] and/or numerical studies [21, 22, 23, 24] have been considered; for example, a number of analytic predictions of gravitational waves have been computed within the Post-Newtonian (PN) approximation (see e.g. [20] and references therein).

In this chapter we calculate the gravitational wave signature of two colliding black holes surrounded by a dilatonic field. Such a problem was recently studied numerically for weakly charged black holes where the dilatonic field vanishes at infinity [25] and in the PN approximation for non-vanishing asymptotic values of the dilaton [26] (see also [27] for a discussion of collisions of dilatonic black holes with angular momentum).

We study this problem from a different perspective, analytically calculating the gravitational wave signature in an approximation that is applicable in the strong field regime and for any black hole mass ratio. To carry out this procedure it is necessary that the two black holes be extremally charged and that the system evolve adiabatically, through a series of approximately static configurations — the so called *moduli space approximation* (MSA) [28, 29]. We thereby generalize recent results for the Einstein-Maxwell case [30], finding imprints of the dilatonic field on the gravitational wavefront. As we shall see, such imprints depend crucially on the value of the dilatonic coupling constant a. Interesting analytic results can be obtained at least in two cases: i) (low energy) string theoretic black holes, characterized by $a = 1$, for which there are no coalescence orbits and only a memory effect is observed; and ii) an intermediate value $a = 1/\sqrt{3}$ of the coupling. We show that the late-time wavefront in the latter case becomes exponentially suppressed, in notable contrast to the polynomial decay in the case without a dilaton [30].

The outline of this Chapter is as follows. In the next Section (Section 3.2), we review the evolution of a black hole binary system in the MSA in Einstein–Maxwell theory. Following [30], the corresponding gravitational wavefront is calculated in Section 3.3. The main results of the chapter are gathered in Section 3.4 where the dilatonic case is studied. We conclude in Section 3.5.

3.2 Black hole merger in moduli space approximation

To describe a black hole merger in the MSA in Einstein–Maxwell theory, we start with the static multi black hole solution due to *Majumdar and Papapetrou* (MP) [31, 32]. The MP solution represents a static configuration of n extremally charged black holes, each of mass m_i and position $\vec{\boldsymbol{x}}_i$; for $n = 1$ it reduces to the familiar extremal Reissner–Nordström spacetime. The solution reads

$$ds^2 = -\psi^{-2}dt^2 + \psi^2 d\vec{\boldsymbol{x}} \cdot d\vec{\boldsymbol{x}}\,, \tag{3.1}$$

$$A = -(1 - \psi^{-1})dt\,. \tag{3.2}$$

Here, A is the Maxwell vector potential, and the metric function ψ is given by

$$\psi = 1 + \sum_{i=1}^{n} \frac{m_i}{r_i}\,. \tag{3.3}$$

In what follows, and in Equation (3.3), we often write $d\vec{\boldsymbol{x}} \cdot d\vec{\boldsymbol{x}} = dr^2 + r^2 d\Omega^2$, with $r = \sqrt{\vec{\boldsymbol{x}} \cdot \vec{\boldsymbol{x}}} = |\vec{\boldsymbol{x}}|$. We also have $r_i = |\vec{\boldsymbol{r}}_i| = |\vec{\boldsymbol{x}} - \vec{\boldsymbol{x}}_i|$.

The MP solution is static. To describe a dynamical system, we promote the black hole positions $\vec{\boldsymbol{x}}_i$ in (3.3) to functions of time, $\vec{\boldsymbol{x}}_i = \vec{\boldsymbol{x}}_i(t)$, and further employ the MSA, requiring that the system moves through configurations with small velocities, always remaining approximately static. This amounts to perturbing the solution and treating the black holes as slowly moving. To second order in velocities one obtains the *moduli space metric*, in which the motion of black holes is geodesic [28, 29]. In particular the following Lagrangian

$$L = \frac{1}{2}\mu\gamma(r_{12})\,\vec{\boldsymbol{v}}\cdot\vec{\boldsymbol{v}} \tag{3.4}$$

describes the centre of mass motion of two black holes, with the centre-of-mass motion subtracted. Here $M \equiv m_1 + m_2$ and $\mu \equiv \frac{m_1 m_2}{M}$ are the total and reduced black hole masses, and $\vec{\boldsymbol{r}}_{12} \equiv \vec{\boldsymbol{x}}_1 - \vec{\boldsymbol{x}}_2$ and $\vec{\boldsymbol{v}} = \frac{d\vec{\boldsymbol{r}}_{12}}{dt}$ are the relative black hole separation and velocity. The conformal factor $\gamma(r_{12})$ takes the form

$$\gamma(r_{12}) = \left(1 + \frac{M}{r_{12}}\right)^3 - \frac{2\mu M^2}{r_{12}^3}. \tag{3.5}$$

The approximation holds for [29]

$$\frac{r_{12}}{M} \gg v_\infty^2\,, \tag{3.6}$$

where v_∞ is the absolute value of the velocity at large $\vec{\boldsymbol{r}}_{12}$, and so will certainly break down in the final stages of the black hole coalescence, although note that by choosing small v_∞ we can get arbitrarily close to the complete merger.

All we have to do to study the black hole merger or scattering is to solve the equations of motion

$$\frac{d\phi_{12}}{dt} - \frac{bv_\infty}{r_{12}^2\gamma(r_{12})} = 0 \tag{3.7}$$

$$\left(\frac{dr_{12}}{dt}\right)^2 + \frac{v_\infty^2}{\gamma(r_{12})}\left(\frac{b^2}{\gamma(r_{12})r_{12}^2} - 1\right) = 0 \tag{3.8}$$

that follow from (3.4). Conservation of energy $E = \frac{1}{2}Mv_\infty^2$ and angular momentum $l = bv_\infty$ follow straightforwardly, with v_∞ the relative velocity at infinite separation of the black holes, and b the impact parameter. Without loss of generality we can confine the motion to a plane $\theta = \frac{\pi}{2}$ due to the spherical symmetry of $\gamma(r_{12})$.

These equations of motion allow for both coalescing and scattering orbits, depending on the value of the impact parameter: if $b > b_{\text{crit}}$, scattering will occur, and for $b < b_{\text{crit}}$

there will be a merger. For any mass ratio, $b_{\rm crit}$ is obtained by computing the degenerate positive root in the effective potential in (3.8), yielding

$$\frac{2b_{\rm crit}^3}{3\sqrt{3}} - b_{\rm crit}^2 M + 2\mu M^2 = 0\,, \tag{3.9}$$

which becomes $b_{\rm crit} = \frac{3+\sqrt{3}}{2}M$ for equal mass black holes.

There are two limiting cases of physical interest for which trajectories can be found: i) $r_{12} \gg M$ when the black holes are widely separated (corresponding to early times of the interaction, $t \to -\infty$, or late times of the black hole scattering, $t \to +\infty$) and ii) $r_{12} \ll M$ for late times for black hole coalescence.

In the first regime, Equations (3.7) and (3.8) become (using an overdot to indicate differentiation with respect to t)

$$\dot{r}_{12} = \mp v_\infty (1 - \frac{3}{2}\epsilon + \dots)\,, \quad \dot{\phi}_{12} = \frac{b v_\infty \epsilon^2}{M^2} + \dots\,, \tag{3.10}$$

where $\epsilon = M/r_{12} \ll 1$, yielding

$$\begin{aligned} r_{12\,\text{early/late}} &= \mp v_\infty t - \frac{3}{2} M \log(\mp v_\infty t/r_0)\,, \\ \phi_{12\,\text{early/late}} &= -\frac{b}{v_\infty t} + \phi_{12\,0}\,, \end{aligned} \tag{3.11}$$

For late time coalescing orbits, equations (3.7) and (3.8) read

$$\dot{r}_{12} = -\frac{v_\infty \epsilon^{3/2}\sqrt{M}}{\sqrt{M - 2\mu}}\,, \quad \dot{\phi}_{12} = \frac{b v_\infty \epsilon}{M(M - 2\mu)}\,, \tag{3.12}$$

where now $\epsilon = r_{12}/M \ll 1$, giving

$$r_{12\,\text{coalescing}} = \frac{4M^2(M - 2\mu)}{v_\infty^2 t^2}\,, \quad \phi_{12\,\text{coalescing}} = -\frac{4b}{v_\infty t}\,, \tag{3.13}$$

disregarding the integration constants.

These simple expressions will allow us to find analytic approximations for the early- and late-time radiation. For the 'intermediate times' we shall solve Eqs. (3.7) and (3.8) numerically, to plot the trajectories for various values of b. We depict the solutions in Figure 3.1, which provides an illustration of trajectories just above and just below the critical impact parameter for a collision.

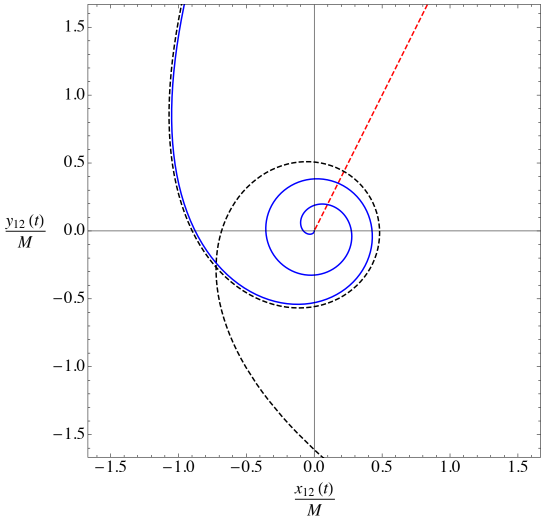

Figure 3.1: **Black hole trajectories for $a = 0$.** Trajectories are illustrated for equal mass black holes and various impact parameters. In red we have plotted a head-on ($b = 0$) collision. The blue solid line corresponds to a slightly-below-critical collision: $b = 0.999 b_{\text{crit}} = 2.36M$, whereas the black dashed line to a slightly-above-critical scattering: $b = 1.01 b_{\text{crit}} = 2.39M$. We set up the two near-critical collisions with otherwise identical initial conditions. Recall that $b_{\text{crit}} = \frac{3+\sqrt{3}}{2}M \approx 2.367M$.

3.3 Gravitational radiation to leading order

Following closely the discussion in [30], let us now study the gravitational radiation from the binary black hole system described by the moduli space approximation.

To leading order, gravitational radiation experienced by an observer at radial coordinate r is given by the quadrupole formula

$$h^{TT} = \frac{2}{r}\frac{d^2}{dt^2}Q^{TT}\bigg|_{t_{\mathrm{ret}}} . \tag{3.14}$$

Here, h is the metric perturbation describing the gravity wave, Q is the mass quadrupole, TT denotes the transverse-traceless projection, and $t_{\mathrm{ret}} = t - r$ is the retarded time. For a metric such as (3.1), it is easy to read off Q due to its *asymptotically Cartesian mass-centred* form (see Section XI of [33] for a definition of this form). In the centre of mass frame, the expansion of g_{tt} gives

$$g_{tt} = -1 + \frac{2M}{r} + \frac{3M^2}{r^2} - \frac{4M^3}{r^3} + \frac{\mu r_{12}^2}{r^3}\sqrt{\frac{6\pi}{5}}\left(e^{-2i\phi_{12}}Y_2{}^2 - \sqrt{\frac{2}{3}}Y_2{}^0 + e^{2i\phi_{12}}Y_2{}^{-2}\right) + \mathcal{O}\left(\frac{1}{r^4}\right) , \tag{3.15}$$

where the mass quadrupole moments I_{2m} are

$$I_{2\pm2} = 2\sqrt{\frac{2\pi}{5}}\mu r_{12}^2 e^{\mp 2i\phi_{12}} ; \tag{3.16}$$

$$I_{20} = -4\sqrt{\frac{\pi}{15}}\mu r_{12}^2 , \tag{3.17}$$

obtained by comparing with equation (11.4a) of [33]. The transverse traceless projection of Q^{TT} is

$$Q^{TT} = \frac{1}{4}\left(I_{22}\ {}_{-2}Y_{22} + I_{20}\ {}_{-2}Y_{20} + I_{2-2}\ {}_{-2}Y_{2-2}\right)\hat{e}_R + c.c., \tag{3.18}$$

where *c.c.* stands for complex conjugate, $\hat{e}_R$ is the circular polarisation tensor

$$\hat{e}_R = \frac{1}{\sqrt{2}}\left(\hat{e}_+ + i\hat{e}_\times\right) , \tag{3.19}$$

and ${}_{-2}Y_{\ell m}$ are the spin-weighted spherical harmonics of spin-weight -2:

$$\begin{aligned} {}_{-2}Y_{22} &= \frac{1}{2}\sqrt{\frac{5}{\pi}}e^{2i\phi}\cos^4\left(\frac{\theta}{2}\right) \,, \\ {}_{-2}Y_{20} &= \frac{1}{4}\sqrt{\frac{15}{2\pi}}\sin^2\theta \,, \\ {}_{-2}Y_{2-2} &= \frac{1}{2}\sqrt{\frac{5}{\pi}}e^{-2i\phi}\sin^4\left(\frac{\theta}{2}\right) \,. \end{aligned} \tag{3.20}$$

$(\theta,\,\phi)$ are the angular coordinates of the observer. To simplify matters, we can choose an observer on the north pole $(\theta,\,\phi) = (0,0)$ (so ${}_{-2}Y_{20} = 0 = {}_{-2}Y_{2-2}$) and

$$h^{TT} = \frac{\mu}{\sqrt{2}r}\frac{d^2}{dt^2}\left(r_{12}^2 e^{-2i\phi_{12}}\right)\hat{e}_R + c.c. \tag{3.21}$$

All that remains to calculate the gravitational radiation is to solve (3.8) for r_{12} and ϕ_{12}. This can easily be done numerically, or, for early and late times, analytically, using the results of the previous section. Using (3.11) we find

$$h^{TT}_{\text{early/late}} = \frac{\sqrt{2}\mu v_\infty^2}{r}\left(1 \pm \frac{3}{2}\frac{M}{v_\infty t}\right)e^{-2i\phi_{12}}\hat{e}_R + c.c.\,, \tag{3.22}$$

where the upper/lower signs correspond to early/late time scattering orbits. As noted in [30], (3.22) provides a clear illustration of the *gravitational memory effect*: h^{TT} takes different values at early and late times and we have

$$\Delta h^{TT} = \frac{\sqrt{2}\mu v_\infty^2}{r}\left(e^{-2i\phi_{12}^f} - e^{-2i\phi_{12}^i}\right)\hat{e}_R + c.c.\,, \tag{3.23}$$

where ϕ_{12}^i and ϕ_{12}^f are the respective initial and final angular separations. For coalescing orbits at late times (3.13) we recover

$$h^{TT}_{\text{coalescing}} = \frac{160\sqrt{2}\mu M^4(M-2\mu)^2}{rt^6 v_\infty^4}e^{-2i\phi_{12}}\hat{e}_R + c.c., \tag{3.24}$$

and we note that, at late times of a coalescence, the t-dependence of ϕ_{12} is too small to appear at this order in h^{TT}. Note also the t^{-6} fall-off, characteristic for Einstein–Maxwell theory. As we shall see in the next section, this becomes very different in the presence of a dilaton.

The h_+^{TT} signatures can be seen in Figure 3.2, where we have plotted the *numerically calculated* signatures for orbits with impact parameters $b = 0$, $b = 0.999b_{\text{crit}}$, and $b = 1.01b_{\text{crit}}$. See also Figure 3.5, where we plot the logarithm of the numerically calculated wavefront for a head-on and a near-critical merger and include the early- and late-time analytic expressions for comparison purposes; the analytic predictions are followed closely.

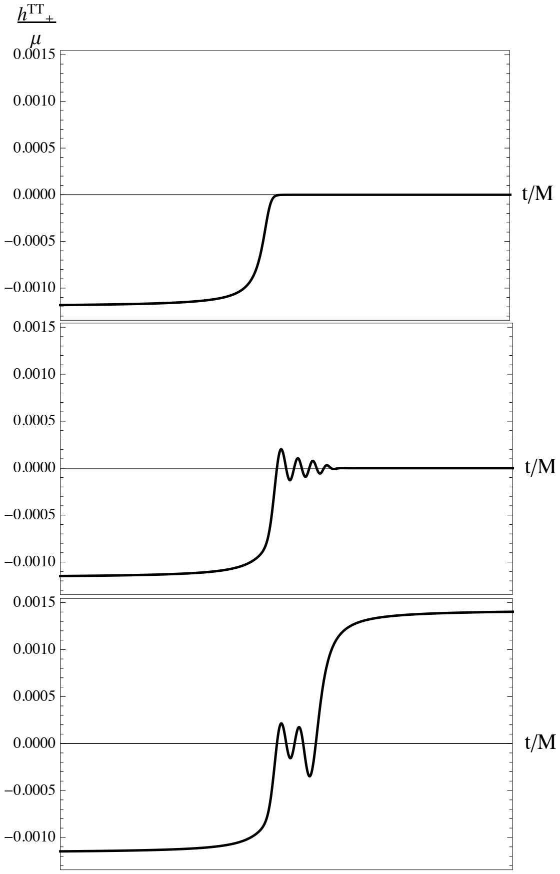

Figure 3.2: **Gravitational wave signatures for $a = 0$.** We have plotted the h_+^{TT} wavefronts for the three different orbits depicted in Figure 3.1. The top graph illustrates the wavefront emitted upon the head-on ($b = 0$) merger, the middle graph the wavefront emitted upon the below-critical coalescence, and the bottom graph the wavefront emitted upon the scattering interaction.

3.4 Coupling to a dilaton

Let us now consider the following generalization of the Einstein–Maxwell theory [34, 35]:

$$S = \int d^4x\sqrt{-g}\left(-R + 2\left(\nabla\phi\right)^2 + e^{-2a\phi}F^2\right)\,, \tag{3.25}$$

with ϕ a dilatonic scalar field and a the corresponding coupling constant. This action describes a broad range of fundamental theories: $a = 0$ yields Einstein–Maxwell theory, $a = 1$ gives the low energy action of string theory, and $a = \sqrt{3}$ corresponds to Kaluza–Klein theory. The corresponding static multi-black hole solution [36] is given by

$$\begin{aligned} ds^2 &= -\psi_a^{-\frac{2}{1+a^2}}dt^2 + \psi_a^{\frac{2}{1+a^2}}d\vec{\boldsymbol{x}}\cdot d\vec{\boldsymbol{x}}\,, \\ A &= \frac{1}{\sqrt{1+a^2}}\psi_a^{-1}dt\,, \quad e^{-2a\phi} = \psi_a^{\frac{2a^2}{1+a^2}}\,. \end{aligned} \tag{3.26}$$

where

$$\psi_a = 1 + (1+a^2)\sum_{i=1}^{n}\frac{m_i}{r_i}\,, \tag{3.27}$$

and reduces to the MP solution (3.3) for $a = 0$.

In order to find the quadrupole moment for this metric, we need to perform an expansion of g_{tt}, similar to (3.15), obtaining in general a-dependent coefficients of expansion. The structures of equation (3.26) and (3.27) ensure that the quadrupole moments are a-independent and are still given by (3.16) and (3.17).

Let us now promote the static metric to a dynamical setting, using the MSA approximation. The corresponding moduli space metric for general a [37] yields a description of the motion of two black holes via the Lagrangian (3.4) where now[1]

$$\gamma_a(r_{12}) = 1 + M\left(\frac{3-a^2}{4\pi}\right)\int d^3\vec{\boldsymbol{x}}\left(\psi_a^{\frac{2(1-a^2)}{1+a^2}}\right)\frac{\vec{\boldsymbol{r}}_1\cdot\vec{\boldsymbol{r}}_2}{r_1^3 r_2^3}\,, \tag{3.28}$$

with the integration variable $\vec{\boldsymbol{x}} \equiv \vec{\boldsymbol{r}}_1 - \vec{\boldsymbol{r}}_2$ and is non-trivial to integrate for generic a. Of course, for $a = 0$ we obtain (3.5). For the Kaluza–Klein case, $a = \sqrt{3}$, the moduli space metric vanishes and there is no interaction between the black holes at this order of expansion—to get non-trivial results one would have to go to higher order in velocities.

---

[1] Note that this reduces to equation (IV.9) in ref. [26] for the weak field $\psi_a \to 1$ approximation.

In what follows we focus on two cases where we can perform analytically the integration in (3.28): the string-theoretic case $a = 1$ for which [37]

$$\gamma_{a=1} = 1 + \frac{2M}{r_{12}}, \tag{3.29}$$

and the case $a = \frac{1}{\sqrt{3}}$, where we find

$$\gamma_{a=\frac{1}{\sqrt{3}}} = 1 + \frac{8}{3}\left(\frac{M}{r_{12}} + \frac{2M^2}{3r_{12}^2}\right) . \tag{3.30}$$

Note that these are both independent of μ, in contrast to what happens in the Einstein-Maxwell case. In other words, in our approximation and for these two special cases the gravitational wave signature will only depend on the total mass of the system but not on the binary mass ratio.

3.4.1 String theory black holes: $a = 1$

When $a = 1$, ψ does not contribute at all to the integral in (3.28). Interestingly, there is no value of b for which the black holes merge. At least within the MSA, all trajectories are scattering, including the head-on collision [37] (although it is not unreasonable to suspect that mergers could happen when the approximation is taken to higher order in v^2). As such, no oscillatory waveforms exist, and we only observe a memory effect, according to

$$\phi_{12\ \text{early/late}} = -\frac{b}{v_\infty t} + \ldots\, , \tag{3.31}$$

$$r_{12\ \text{early/late}} = \mp v_\infty t - M \log\left(\mp v_\infty t\right) + \ldots\, , \tag{3.32}$$

and so

$$h^{TT}_{\text{early/late}} = \frac{\sqrt{2}\mu v_\infty^2}{r}\left(1 \pm \frac{M}{v_\infty t}\right) e^{-2i\phi_{12}}\hat{e}_R + c.c.\, . \tag{3.33}$$

The memory effect can be seen in Figure 3.3.

3.4.2 Intermediate coupling: $a = \frac{1}{\sqrt{3}}$

For $a = \frac{1}{\sqrt{3}}$ the μ-independence of $\gamma(r_{12})$ in (3.30) implies that wavefronts emitted by binary pairs of arbitrary mass ratio yield the same gravitational wave signature, albeit rescaled

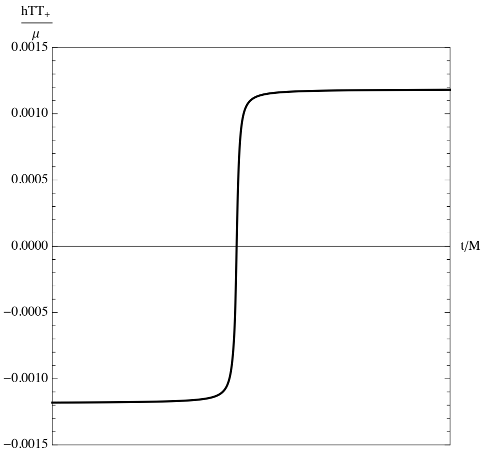

Figure 3.3: **The memory effect for $a = 1$.** For this case there are no merging orbits and no oscillatory behaviour in h^{TT}. However we do see very clearly a memory effect.

by μ; this is not true for $a = 0$, for which the equations of motion explicitly depend on μ. The critical impact parameter b_{crit} is $b_{\text{crit}} = \frac{4}{3}M$.

Using (3.30) to solve (3.8) yields

$$r_{12\ \text{early/late}} = \mp v_\infty t - \frac{4M}{3}\log\left(\mp v_\infty t\right) + \dots\,, \tag{3.34}$$

$$\phi_{12\ \text{early/late}} = -\frac{b}{v_\infty t} + \dots\,, \tag{3.35}$$

for the separation at early and late times, when $r_{12} \gg M$. Hence

$$h^{TT}_{\text{early/late}} = \frac{\sqrt{2}\mu v_\infty^2}{r}\left(1 \pm \frac{4}{3}\frac{M}{v_\infty t}\right) e^{-2i\phi_{12}}\hat{e}_R + c.c.\,. \tag{3.36}$$

For coalescing orbits at late times we find

$$r_{12\ \text{coalescing}} = r_0 \exp\left(-\frac{3q}{16}\frac{v_\infty t}{M}\right), \tag{3.37}$$

$$\phi_{12\ \text{coalescing}} = \frac{9}{16}\frac{b v_\infty t}{M^2} + \dots\,, \tag{3.38}$$

where r_0 is the separation at some t_0, and we abbreviated $q \equiv \sqrt{16 - 9b^2/M^2}$; in particular, note that $\dot{\phi}_{12}$ is no longer small at late times. This implies an exponentially decaying

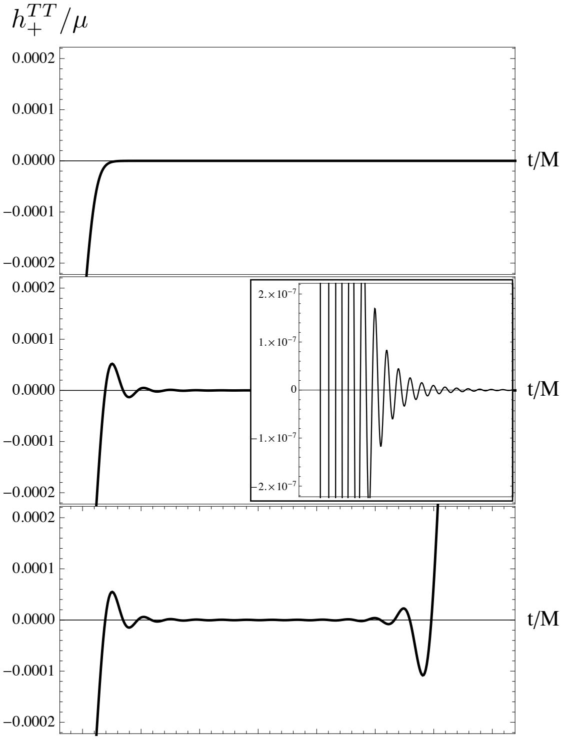

Figure 3.4: **Gravitational wave signatures for $a = \frac{1}{\sqrt{3}}$.** We plot here graphs analagous to those in Figure 3.2. The top graph illustrates the wavefront emitted upon a head-on collision ($b = 0$), the middle a sub-critical case ($b = 0.999 b_{\text{crit}} = 1.332M$), and the bottom a scattering event ($b = 1.01 b_{\text{crit}} = 1.34667M$). The inset in the middle depicts near-critical coalescence to make the exponentially decaying behaviour more explicit.

signature:

$$h^{TT}_{\text{coalescence}} = \frac{9}{64}\frac{\mu\sqrt{2}r_0^2 v_\infty^2}{rM^4}(8M^2 - 9b^2 + 3ibMq)\exp\Big(-\frac{3}{8}\frac{v_\infty t}{M^2}(Mq + 3ib)\Big)\hat{e}_R + c.c.\,. \tag{3.39}$$

We show the logarithm of the wavefront of coalescing orbits for different values of b in Figure 3.5(b), where the b-dependence of the fall-off is seen. The exponential fall-off behaviour is also clearly shown, in contrast to the t^{-6} behaviour evident in Figure 3.5 (a) for the Einstein–Maxwell case. Note that the electromagnetic radiation would also be

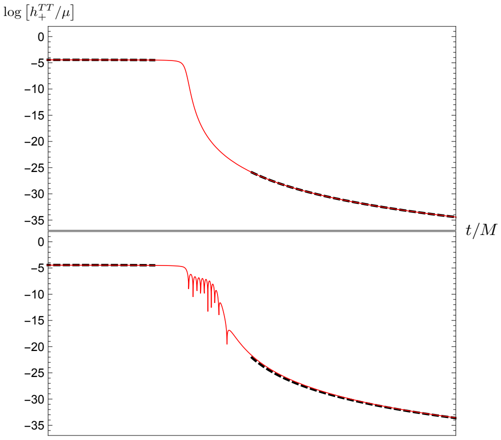

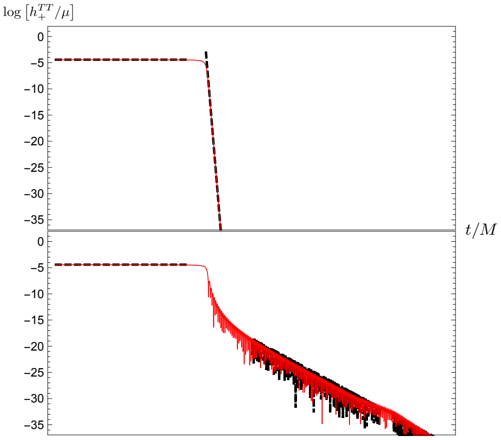

Figure 3.5: **Comparison of analytic expressions with numerical results.** *Left*: $a = 0$. *Right*: $a = \frac{1}{\sqrt{3}}$.

Above we have plotted the behaviour $\log(\left|h_+^{TT}\right|)$ as a function of time for head-on and below-critical collisions, with the numerically calculated solution in red and the analytical predictions for large and small $\frac{m}{r_{12}}$ in black. On the left is $a = 0$ and on the right is for $a = \frac{1}{\sqrt{3}}$. We notice a number of things on the log plot that are difficult to see on the previous graphs: the t^{-6} for $a = 0$ behaviour can be directly contrasted with the e^{-t} behaviour for $a = \frac{1}{\sqrt{3}}$. We also notice the lack of b-dependence for the $a = 0$ case, as predicted, and the obvious b-dependence for $a = \frac{1}{\sqrt{3}}$.

expected to have an exponential fall-off, as it takes a similar form as gravitational radiation (see [30]).

3.5 Conclusion

The presence of a dilaton can make a significant imprint on the gravitational waveforms emitted in black hole collisions and scattering events. By analytically computing expressions for the gravitational wavefronts emitted by the collision of two extremally charged dilatonic black holes, we have been able to compare the general relativistic (Einstein–Maxwell) wavefronts with those occurring in a string-theoretic case ($a = 1$) and a more general dilatonic theory ($a = 1/\sqrt{3}$). In the latter case the gravitational waveforms are exponentially suppressed in time, whereas in general relativity the wavefronts decay with t^{-6}. However the gravitational memory effect for scattering is the same for all values of a, including the $a = 0$ Einstein–Maxwell case.

Our results complement those of recent studies of dilatonic black hole mergers [25, 26], and illustrate a qualitative difference between cases with and without a dilaton.

It would be interesting to develop this technique to spacetimes with general coupling constant a between the dilaton and the Maxwell field as we have only been able to do this so far for the specific values of $a = 0, \frac{1}{\sqrt{3}}, 1, \sqrt{3}$; we leave this question for a future study. Likewise, more detailed studies of non-extremal dilatonic black holes over a broad range of parameter space need to be carried out to see where the most interesting phenomenological possibilities lie.

Part II

Cosmology from CMB secondaries

Chapter 4

Background cosmology, perturbation theory, and power spectra

Much of what we understand about the evolution of the universe comes from linear perturbation theory, whereby the Einstein equations are used to evolve a perturbed FLRW (Friedmann–Lemaître–Robertson–Walker) metric in the presence of scalar perturbations. In this Chapter, we discuss the zeroth order dynamics of our universe, and use perturbation theory to describe the various observables we see.

The Chapter is organized as follows. In Section 4.1 we introduce the FLRW metric and the theory that describes the history of our universe's expansion. In Section 4.2 we give a qualitative history of the thermal properties of our universe. In Section 4.3 we introduce cosmological perturbation theory. We focus first on density perturbations, explicitly introducing the density and velocity power spectra and discussing their properties today; then we discuss the anisotropy spectrum of the observed CMB including primary and secondary effects. We then discuss the secondary effects in more detail, with Section 4.4 focusing on CMB lensing, and Section 4.5 focusing on the Sunyaev–Zel'dovich effects. Most of this Chapter is a summary of standard material that can be found in textbooks; references used in particular throughout are [38, 39, 40].

4.1 Dynamics of a homogeneous universe

The first order FLRW metric is

$$ds^2 = -dt^2 + a(t)^2 dS_3^2 = a(\eta)^2 \left(-d\eta^2 + dS_3^2\right) \tag{4.1}$$

where η is the conformal time (related to the more intuitive coordinate time t by $d\eta = \frac{dt}{a(t)}$) and a is the (time-dependent) scale factor. dS_3^2 describes the spatial geometry of the universe and can take one of three options:

$$dS_3^2 = \frac{dr^2}{1 - k\frac{r^2}{r_0^2}} + r^2 d\Omega^2 \tag{4.2}$$

where r_0 is some (arbitrary) scale radius, with $k \in (-1, 0, 1)$ describing hyperbolic (open), flat, and spherical (closed) space respectively; $d\Omega^2$ is the standard 2-sphere metric $d\Omega^2 = d\theta^2 + \sin^2\theta d\phi^2$.

(4.1) is the most general spherically symmetric homogeneous spacetime; it is required by the assumption of the *cosmological principle* which states that our place in the universe is not special—i.e. that the universe is homogeneous and isotropic so that the it should look the same no matter where we observe it from.

The Einstein equations

$$G_{\mu\nu} = 8\pi G T_{\mu\nu} \tag{4.3}$$

relate the metric $g_{\mu\nu}$ to the presence of stress-energy: the Einstein tensor $G_{\mu\nu}$ is defined in Section 2.1 where we first discussed the Einstein equations. $T_{\mu\nu}$ is the stress energy tensor which describes the presence of any energy, momentum, or shear density.

For a perfect fluid, $T_{\mu\nu}$ takes on a very simple form for an observer with 4-velocity u^μ:

$$T_{\mu\nu} = (\rho + P)\, u_\mu u_\nu + P g_{\mu\nu} \tag{4.4}$$

where ρ is the energy density of the fluid and P is its pressure; in particular for an observer at rest with respect to the fluid $u^\mu = (1, 0, 0, 0)$ so for the metric (4.1)

$$T^\mu{}_\nu = \begin{pmatrix} -\rho & 0 & 0 & 0 \\ 0 & P & 0 & 0 \\ 0 & 0 & P & 0 \\ 0 & 0 & 0 & P \end{pmatrix}. \tag{4.5}$$

In general, the Einstein equations (4.3) for the FLRW metric (4.1), along with a relation $P = P(\rho)$ (the “equation of state”), can be solved to understand the dynamics of a and ρ: relations $a = a(t)$ and $\rho = \rho(a)$. The Einstein equations for the FLRW metric are known as the Friedmann equations:

$$H^2 + \frac{k}{a^2} = \frac{8\pi G}{3}\rho; \tag{4.6}$$

$$\frac{\ddot{a}}{a} = -\frac{4\pi G}{3}\left(\rho + 3P\right) \tag{4.7}$$

where the Hubble parameter $H(t) \equiv \frac{\dot{a}}{a}$. Equation (4.6) is the tt component of the Einstein equations, and equation (4.7) comes from the trace of the Einstein equations.

Equation (4.6) allows us to define a critical density for the universe

$$\rho_c = \frac{3H^2}{8\pi G} \tag{4.8}$$

(note that time dependence of H is assumed on the right hand side and so ρ_c is a time-dependent quantity). If the energy density of the universe ρ is equal to the critical density at any time t, the spatial curvature k of the universe must be exactly 0. We can summarize this by defining a quantity Ω

$$\Omega \equiv \frac{\rho}{\rho_c}; \tag{4.9}$$

if $\Omega = 1$ then k must be 0; $\Omega > 1$ implies $k > 0$; and $\Omega < 1$ implies $k < 0$. Most measurements of the energy density today are consistent with $\Omega = 1$, indicating that the spatial curvature of the universe is close to 0.

Different types of energy (ie, with different equations of state) cause the metric to evolve in different ways by affecting the time-dependence of a; this in turn causes the density of the respective energies to evolve in different ways with time. In particular the a-dependence of common different forms of stress-energy (radiation, non-relativistic matter, and a cosmological constant Λ) are presented in Table 4.1.

Energy type	Equation of State	Evolution of density	Time-evolution of a
Radiation	$P = 1/3\rho$	$\rho \propto a^{-4}$	$a \propto t^{\frac{1}{2}} \propto \eta$
Matter	$P = 0$	$\rho \propto a^{-3}$	$a \propto t^{\frac{2}{3}} \propto \eta^2$
Cosmological Constant (Λ)	$P = -\rho$	$\rho \propto a^0 = \text{const}$	$a \propto e^{Ht}$

Table 4.1: The evolution of energy density and scale factor in a universe containing various different energy components.

In general the energy density of the universe is a combination of these components:

$$\rho = \rho_r + \rho_m + \rho_\Lambda \tag{4.10}$$

where the subscripts $\{r, m, \Lambda\}$ refer to radiation, matter, and Λ respectively. From the properties in Table 4.1 we can understand the history of the expansion of our universe:

given the energy densities today $\rho_0 \equiv \rho_{r0} + \rho_{m0} + \rho_{\Lambda 0}$, and defining the scale factor today to be $a(t_0) = 1$ we can write

$$\rho = \rho_{r0} a^{-4} + \rho_{m0} a^{-3} + \rho_{\Lambda 0}. \tag{4.11}$$

Understanding the evolution of different energy components with a leads us to the inevitable conclusion that in the distant future (as a increases) the energy density of the universe will be completely dominated by ρ_Λ, while in the distant past it was dominated by ρ_r. In between there was a period of matter-domination when ρ_m was the most important energy-density component. Indeed, we have only recently left this era and entered the period of Λ-domination; noting the time-evolution of a in such a universe, we see that this is a period of accelerated expansion where a is beginning to grow exponentially (this should be contrasted with the power-law growth of a during the time of matter and radiation domination).

Note that we can also separate the Ω parameter into its different components:

$$\Omega = \Omega_r + \Omega_m + \Omega_\Lambda \tag{4.12}$$

where $\Omega_x \equiv \frac{\rho_x}{\rho_c}$; the energy contribution due to spatial curvature Ω_k can be defined as $\Omega_k \equiv \Omega - 1$. This also inspires a definition $\rho_k = \frac{8\pi G}{3}\frac{k}{a^2}$, ie the identification of the spatial curvature component of the Friedmann equation (4.6) as an energy density due to spatial curvature that evolves as a^{-2}.

4.1.1 Distance measures

As we look far away, we see the universe as it was in the past. There are a number of quantities we can use to measure distance (or equivalently, age), for example: the scale factor; the coordinate time t; the conformal time η (also known as the "light travel time"); the coordinate distance in Mpc[1] ("comoving distance"); the physical distance; the redshift of a photon emitted a long time ago. These all have 1-to-1 relationships and so are equally valid as distance measures, but in different contexts some are more useful than others. We will discuss some of the most commonly used ones here, and they will be used interchangeably where appropriate throughout.

---

[1] At least in a universe that is always expanding, the coordinate distance has a monotonic relationshipw with the other measurements mentioned; in a universe that recollapses this will not be the case.

Physical distance and coordinate distance

The universe has not always been the same size. Two galaxies that are a certain distance X from each other today were closer together in the past, by a factor of the scale factor a:

$$X(t) = a(t)\chi \tag{4.13}$$

where χ is the comoving distance (which is constant in time) and X is the physical ("proper") distance. As the scale factor is defined to be 1 today, the comoving distance is given by the proper distance today. The comoving distance is the coordinate distance r, for the coordinates (r, θ, ϕ) in Equation (4.1).

When we see a distance galaxy, what is the comoving distance between us and it? We can consider the distance along which the light has travelled. Light travels along geodesics defined by $ds^2 = 0$, so a photon travelling radially obeys the equation $dt = adr = ad\chi$. Integrating the coordinate (comoving) distance gives

$$d\chi = \int \frac{dt}{a} = \int \frac{da}{a}\frac{dt}{da} = \int_0^a \frac{da}{a^2 H(a)}. \tag{4.14}$$

This can be integrated with Equation (4.6), (using the expression (4.11) for ρ to find explicitly $H(a)$), to find the relation $\chi(a)$, which in general is dependent on the values of the ρ_{x0}.

Redshift

The redshift of a photon as it travels in an expanding universe is an extremely useful distance measure, because it can be measured directly by comparing the frequency of photons (if one assumes that all photons of interest are the same frequency when they are emitted).

Because the speed of light is constant, photons are redshifted in an expanding universe as their physical wavelength increases. If a photon is emitted with wavelength λ_e and observed with wavelength λ_o, the redshift z is defined as

$$z \equiv \frac{\lambda_o - \lambda_e}{\lambda_e}. \tag{4.15}$$

With the metric (4.1) for a photon emitted at a_1 and observed at a_2 it is easy to show that

$$z_{a2,a1} = \frac{a_2}{a_1} - 1; \tag{4.16}$$

for photons detected today we have $a_2 = 1$ so the scale factor at which the photon was emitted is given by

$$a = \frac{1}{1+z}. \tag{4.17}$$

So, given a redshift measurement z, we can convert to a and then to comoving distance with Equation (4.14) which is an expression for $\chi(a)$.

4.1.2 The cosmological parameters

Our cosmological model, ΛCDM, has 6 free parameters which must be measured from the data: the expansion rate of the universe today H_0, the density of cold dark matter Ω_c, the density of baryonic matter Ω_b, the initial amplitude of scalar fluctuations A_s, the scalar spectral index n_s, and the optical depth to the CMB τ. At times we will refer to H_0 in terms of the dimensionless parameter h through the definition $H_0 = 100\,h\,\mathrm{km/s/Mpc}$. Throughout, we use the best-fit values of [41]: $\{H_0 = 67.32\ \mathrm{km/s/Mpc}, \Omega_b h^2 = 0.022383, \Omega_c h^2 = 0.12011, n_s = 0.96605, A_s = 2.1 \times 10^{-9}, \tau = 0.0543\}$.

4.2 A qualitative history of the universe

Within the standard cosmological model, the universe has been expanding as described in the previous section since $t \to 0$, perhaps preceded by a period of exponential expansion referred to as *inflation*. With our knowledge of particle physics, we can describe what happened during the expansion with much detail, at least from a time slightly after $t = 0$. In this Section we will briefly describe some of the important events that occured during the expansion.

We model the universe as beginning with all the particles of the Standard Model of particle physics in thermal equilibrium. The particles that contribute to the radiation density ρ_r are the massless particles; in particular, the photons (although the neutrinos also contribute if they are massless). As the universe expands, the temperature of the photons decreases as $T \propto \frac{1}{a}$. While we have good knowledge from particle collider experiments of the standard model interactions up to $T \sim \mathcal{O}(100\,\mathrm{GeV})$, the higher temperature regime is beyond our models.

After the temperature reached $T \sim \mathcal{O}(100\,\mathrm{MeV})$, we have detailed knowledge of the interactions of the standard model and we can understand how the particles interacted with each other. In brief, we expect that at very high temperatures the quarks and gluons were unconfined and the universe consisted of a quark–gluon plasma; but around this time they became confined into the familiar protons and neutrons.

The neutrinos stopped interacting with the remaining particles when the weak interaction rate become lower than the expansion rate of the universe; they have been free-streaming through the universe since then without interacting with the other particles. Within the standard model, the neutrinos are massless, but it is known from flavour oscillation experiments that they must have some small mass; when the temperature reached $T \sim M_\nu$ where M_ν is their mass, the neutrinos started to behave as matter as opposed to radiation, and to contribute to ρ_m instead of ρ_r.

For much of the early universe, the photons and the electrons were coupled through the Compton scattering process whereby photons scatter off of free electrons. During this time, the mean free path of a photon was small. However, as the temperature lowered to below the ionisation energy of Hydrogen, the electrons and the protons formed stable atomic Hydrogen; this event is known as *recombination*. At this point the photons could no longer interact with the electron-proton sector, and they have been travelling without scattering since that time. These photons make up what is known as the Cosmic Microwave Background (CMB), and they have temperature $T \approx 2.7$K today. They contain much information about the early universe and they have been mapped in ever-increasing detail over the past few decades in efforts to access this. We refer to the surface that we "see" when we detect these photons as the *surface of last scattering*, and it is at a redshift of $z \sim 1100$.

For a long time after recombination, the atomic Hydrogen remained neutral and didn't interact with the photons; as we cannot see much from this time it is referred to as the "dark ages", although 21cm Hydrogen line intensity mapping offers a way to potentially probe this era, by taking advantage of the low-energy photon emitted during the hyperfine transition of atomic Hydrogen (a process which occurs at a rate of $\sim 3 \times 10^{-15}\text{s}^{-1}$ for every atom).

As the universe was expanding, the matter was gravitationally clustering and small overdensities were growing and becoming more dense. At some point, the overdensities were such that the first stars formed in them, and at this point the Hydrogen gas became reionized due to the complex interactions occuring in the baryon[2] sector. There were some free electrons and a small number of CMB photons scattered off of these, a process called the Sunyaev–Zel'dovich (SZ) effect. Meanwhile, the overdensities continued to grow and galaxies and galaxy clusters formed. By taking galaxy surveys—mapping the angular positions of galaxies on the sky—we can learn about the properties of the late universe.

---

[2] "Baryon" refers to all the ordinary matter: protons, neutrons, and electrons

We can even make quasi three-dimensional galaxy surveys by measuring the redshift of galaxies we see, either by taking "photometric" redshifts where the overall colour of the galaxy is considered, or more precise (but more difficult) spectroscopic redshifts where the frequency of known atomic emission lines can be measured in the spectrum of the galaxy and compared to the un-redshifted versions.

It is important to note that most of the matter in the universe does not consist of standard model particles, but instead some other component known as cold dark matter (CDM). It does not interact with any other particle except gravitationally, and so does not display the complex behaviour of the ordinary ("baryonic") matter such as the formation of stars and galaxies.

In the following Sections, we will introduce the cosmological perturbation theory used to describe the evolution of fluctuations in the mean energy density. We will describe the spectrum of fluctuations we see today in the matter density field, and in the mean temperature of the CMB.

4.3 Perturbations

The universe is not entirely homogeneous. It contains perturbations seeded by quantum fluctuations stretched during inflation. These perturbations are observed in both the matter density field—as perturbations to the mean density—and in the radiation field (in particular as perturbations to the mean temperature of the CMB).

Due to gravitational instability, perturbations to the background matter density that were initially small ($\sim 10^{-5}$ times the mean density) have grown today to be $\mathcal{O}(1)$ times the mean density, leading to the dramatic inhomogeneities we observe today like galaxies. On the other hand, the perturbations in photon temperature T remain small, $\sim 10^{-5}$ times the mean temperature; despite this, they have been detected and mapped extremely precisely.

While the equations that govern the evolution of perturbations—the Boltzmann equations and the Einstein equations—are generally not soluble analytically, they can be linearized and evolved numerically. Thus we have precise predictions for their evolution, which are valid in the regime that the perturbation is much less than the background quantity. This is true for the CMB, where $\frac{\Delta T}{T} \ll 1$ and the expansion in small $\frac{\Delta T}{T}$ is always valid. For matter overdensities on large scales, this is also true; but on small scales the overdensities have reached the nonlinear regime and linear perturbation theory fails.

4.3.1 Scalar perturbations

First order perturbed metric

Density perturbations induce perturbations induced in the metric. We work in the conformal Newtonian gauge, where the scalar perturbations to the metric are defined by

$$ds^2 = \left(-\left(1+2\Phi\right)dt^2 + \left(1+2\Psi\right)\delta_{ij}a(t)^2 dx^i dx^j\right). \tag{4.18}$$

In this gauge, half of the perturbation to $-g_{00}$, ie $\frac{\delta g_{00}}{2} = \Phi$, is known as the *Newtonian potential.*

First order perturbed stress energy tensor

The entire expression for the first-order perturbed stress-energy tensor (4.4) includes perturbations to ρ, P, and four-velocity u^μ. These can be denoted $\delta\rho$, δP, and $\delta u^\mu = \left(\delta u^0, \frac{v^i}{a(t)}\right)$ respectively, with $u^\mu = \left(1+\delta u^0, \frac{v^i}{a(t)}\right)$.

δu^0 is characterized entirely in terms of the metric perturbations by means of the normalization condition $u^\mu u_\mu = -1$, so

$$\delta u^0 = -\Phi. \tag{4.19}$$

After imposing this, it is easy to show that the perturbation $\delta T_{\mu\nu} \equiv T_{\mu\nu} - T^{(0)}_{\mu\nu}$ (where the background value is $T^{(0)}_{\mu\nu}$, although note that this split into perturbation and background is gauge-dependent) is

$$\delta T^\mu{}_\nu = \begin{pmatrix} -\delta\rho & & a(t)\left(P^{(0)}+\rho^{(0)}\right)\vec{\boldsymbol{v}} & \\ & \delta P & 0 & 0 \\ -\frac{\left(P^{(0)}+\rho^{(0)}\right)\vec{\boldsymbol{v}}}{a(t)} & 0 & \delta P & 0 \\ & 0 & 0 & \delta P \end{pmatrix}. \tag{4.20}$$

where the first index corresponds to the rows and the second index to the columns (thus note that $\delta T^0{}_i \neq \delta T^i{}_0$). We can relate the stress-energy perturbations to the metric perturbations with the Einstein equations.

The density perturbations we are interested in are those of the matter distribution $\delta\rho_m$ and of the radiation distribution $\delta\rho_r$ (with corresponding pressure perturbation $\delta P = \frac{\delta\rho_r}{3}$). In general we can define a dimensionless *overdensity* δ by

$$\delta_x \equiv \frac{\delta\rho_x}{\rho_x^{(0)}} \tag{4.21}$$

where $\rho_x^{(0)}$ is the background value of the density and $\delta\rho$ is the (gauge-dependent) perturbation. We mostly use Equation (4.21) when referring to matter overdensity, so henceforward δ with no subscript refers to the matter overdensity.

Note that the matter overdensity is composed of the perturbation to cold dark matter δ_c and to the baryon density δ_b. These behave qualitatively differently because δ_b is coupled to δ_r, while δ_c evolves independently (other than the coupling due to gravity).

Perturbed Einstein equations

The perturbed metric and the perturbed stress energy tensor can be related with the Einstein equations, which can be solved order-by-order. The first order Einstein equations are

$$-\nabla^2\Psi + 3a^2 H\left(\dot{\Psi} - H\Phi\right) = 4\pi G a^2 \delta\rho, \tag{4.22}$$

$$\frac{1}{a^2}\nabla^2\left(\Psi + \Phi\right) - \frac{1}{a^2}\left(\Psi + \Phi\right)_{,ii} + 6H^2\Phi + 4\Phi\dot{H} + 2H\dot{\Phi} - 6H\dot{\Psi} - 2\ddot{\Psi} = 8\pi G\delta P \tag{4.23}$$

$$\left(\dot{a}\Phi - a\dot{\Psi}\right)_{,i} = 4\pi G a^2\left(\rho^{(0)} + P^{(0)}\right)v^i \tag{4.24}$$

$$-\left(\Psi + \Phi\right)_{,ij} = 8\pi G\delta T_{ij} \tag{4.25}$$

where ∇^2 is the three-dimensional flat-space Laplacian operator. Equation (4.22) is the (t,t) component of the Einstein equations; Equation (4.23) is the (i,j) component for $i=j$; Equation (4.24) is the (t,i) component; and Equation (4.25) is the (i,j) component for $i \neq j$.

In the perfect fluid regime where $\delta T^i_j \propto \delta^i_j$, we have from Equation (4.25) that

$$\Psi = -\Phi. \tag{4.26}$$

Thus Equations (4.22), (4.23), and (4.24) can be written entirely in terms of Φ (after also Fourier transforming so that $\nabla^2 \to -k^2$) as

$$-k^2\Phi - 3a^2 H\left(H\Phi + \dot{\Phi}\right) = 4\pi G a^2\delta\rho, \tag{4.27}$$

$$\ddot{\Phi} + 4H\dot{\Phi} + \left(3H^2 + 2\dot{H}\right)\Phi = 4\pi G\delta P. \tag{4.28}$$

$$\left(a\Phi_{,i}\right)^{\cdot} = 4\pi G a^2\left(\rho^{(0)} + P^{(0)}\right)v^i \tag{4.29}$$

Super- and sub-horizon modes and horizon crossing

Given initial conditions for δ and Φ, we can evolve them with the Einstein equations through radiation and matter domination to understand their distribution today. This can be done numerically to high accuracy, but analytic insight can be gained in some regimes by making approximations. In particular, we can consider the large-scale and small-scale modes separately, where "large" and "small" is meant with respect to the Hubble scale of of the universe. In particular, modes with physical wavelength $\frac{a}{k} \gg H^{-1}$ are large-scale ("super-horizon"), and $\frac{a}{k} \ll H^{-1}$ are small-scale ("sub-horizon"). A general conclusion is that large-scale modes are "frozen out" and do not evolve; but, as the Hubble scale grows faster than a during both matter and radiation domination, modes than initially start super-horizon "cross the horizon" when $\frac{H^{-1}}{a} \sim k$ and begin to evolve.

4.3.2 Power spectrum and two point function

Within the linear regime, given a set of initial conditions and their evolution equations, we can make predictions about the observed anisotropies today. The initial conditions are generally provided by inflation; in particular, many models of inflation predict an almost-scale invariant distribution of inhomogeneities. Note that this is a *statistical statement*, in that we do not have a prediction for the exact distribution of inhomogeneities $\delta(\vec{\boldsymbol{x}})$, but we can say things about their statistics; in particular the mean $\langle\delta(\vec{\boldsymbol{x}})\rangle$ and the variance $\left\langle\delta(\vec{\boldsymbol{x}})\delta(\vec{\boldsymbol{x}}')\right\rangle$. In the simplest case—that of a *Gaussian* distribution—this describes the entire statistics of the field, as higher order statistics such as the bispectrum $\left\langle\delta(\vec{\boldsymbol{x}})\delta(\vec{\boldsymbol{x}}')\delta(\vec{\boldsymbol{x}}'')\right\rangle$, trispectrum, etc... are expressible in terms of the mean and the variance.

In general the mean is not an interesting quantity, as it is just one number and can be subtracted from the quantity one is considering such that its mean is 0 by definition (this has already been done in the definition of δ). The variance (two-point function), however, is an interesting quantity that depends in general on the vector $\vec{\boldsymbol{r}} \equiv \vec{\boldsymbol{x}} - \vec{\boldsymbol{x}}'$; this motivates the definition of the 2-point function

$$\langle\delta(\vec{\boldsymbol{x}})\delta(\vec{\boldsymbol{x}} - \vec{\boldsymbol{r}})\rangle \equiv \xi(\vec{\boldsymbol{r}}) = \xi(r). \tag{4.30}$$

The Fourier transform of $\xi(r)$, the *power spectrum*, is commonly worked with as it is diagonal in Fourier space:

$$\left\langle\delta(\vec{\boldsymbol{k}})\delta^*(\vec{\boldsymbol{k}}')\right\rangle = (2\pi)^3\, P(k)\delta^3(\vec{\boldsymbol{k}} - \vec{\boldsymbol{k}}'). \tag{4.31}$$

Note that $\xi(\vec{\boldsymbol{r}}) = \xi(r)$ and $\left\langle \delta(\vec{\boldsymbol{k}})\delta^*(\vec{\boldsymbol{k}}') \right\rangle = f(k)\delta^3(\vec{\boldsymbol{k}} - \vec{\boldsymbol{k}}')$ are results of the assumptions of statistical homogeneity and isotropy. We can see that, with these definitions, $\xi(r)$ and $P(k)$ are Fourier conjugates by explicitly Fourier transforming and evaluating Equation (4.30):

$$
\begin{aligned}
\xi(r) = \langle \delta(\vec{\boldsymbol{x}})\delta(\vec{\boldsymbol{x}} - \vec{\boldsymbol{r}}) \rangle &= \left\langle \int \frac{d^3\vec{\boldsymbol{k}}}{(2\pi)^3} e^{i\vec{\boldsymbol{k}}\cdot\vec{\boldsymbol{x}}} \delta(\vec{\boldsymbol{k}}) \int \frac{d^3\vec{\boldsymbol{k}}'}{(2\pi)^3} e^{-i\vec{\boldsymbol{k}}'\cdot(\vec{\boldsymbol{x}}-\vec{\boldsymbol{r}})} \delta^*(\vec{\boldsymbol{k}}') \right\rangle \\
&= \int \frac{d^3\vec{\boldsymbol{k}}}{(2\pi)^3} \int \frac{d^3\vec{\boldsymbol{k}}'}{(2\pi)^3} e^{i\vec{\boldsymbol{k}}\cdot\vec{\boldsymbol{x}} - i\vec{\boldsymbol{k}}'\cdot(\vec{\boldsymbol{x}}-\vec{\boldsymbol{r}})} \left\langle \delta(\vec{\boldsymbol{k}})\delta^*(\vec{\boldsymbol{k}}') \right\rangle \\
&= \int \frac{d^3\vec{\boldsymbol{k}}}{(2\pi)^3} \int d^3\vec{\boldsymbol{k}}' e^{i\vec{\boldsymbol{k}}\cdot\vec{\boldsymbol{x}} - i\vec{\boldsymbol{k}}'\cdot(\vec{\boldsymbol{x}}-\vec{\boldsymbol{r}})} P(k)\delta^3\left(\vec{\boldsymbol{k}} - \vec{\boldsymbol{k}}'\right) \\
&= \int \frac{d^3\vec{\boldsymbol{k}}}{(2\pi)^3} e^{i\vec{\boldsymbol{k}}\cdot\vec{\boldsymbol{r}}} P(k), \qquad (4.32)
\end{aligned}
$$

which is the definition of the Fourier transform (see Equation (1.2)).

In order to understand the power spectrum today, we need to understand the initial overdensity spectrum $P(k, t = 0)$; and how the overdensities evolved both through the radiation dominated era and through the matter domination era. We will consider the initial conditions in the next Section, and then consider the evolution in these different regimes.

4.3.3 Initial conditions for $P(k)$: inflation

The initial perturbations in our universe are thought to be seeded by inflation, whereby the universe underwent a rapid exponential increase which resulted in initially small quantum fluctuations being stretched to super-horizon scales. It is these quantum fluctuations which are thought to have seeded the structure of our universe. Inflation has also been invoked as a way of providing the “initial conditions” for the big bang framework—it also solves various other cosmological problems, in particular the **horizon problem**: why do distant parts of the universe, which have seemingly not been in causal contact, seem to have been in thermal equilibrium in the past?; and the **flatness problem**: why is the density of our universe so close to the critical density?

The inflation paradigm posits that before the radiation-domination era of the standard “big bang” paradigm, there was a period of exponential expansion of the scale factor (this is to be contrasted with the $a \propto t^x$ growth of matter- and radiation-domination, see Table

4.1). Exponential expansion allows for a tiny portion of the universe—which could be in thermal equilibrium—to grow at such a rate that, when looked at today, portions of the universe that seem extremely distant in fact used to be much closer together. This solves the horizon problem, as it means that seemingly un-causally-connected regions of spacetime would have been causally connected before inflation; it also solves the flatness problem as any initial spatial curvature would have been stretched super-horizon.

Many theories of inflation predict that the universe was seeded with an almost scale-invariant curvature spectrum

$$\Delta_{\Phi^0}(k) \equiv \frac{k^3 P_{\Phi^0}(k)}{2\pi^2} = A_s \left(\frac{k}{k_0}\right)^{n_s - 1} \tag{4.33}$$

where $P_{\Phi^0}(k)$ is the initial spectrum of inhomogeneities in the Newtonian potential Φ (note that, as we live in three spatial dimensions, $P(k) \propto k^{-3}$ is scale invariant). The scalar spectral index n_s quantifies the departure from scale invariance, with $n_s = 1$ being exactly scale invariant. Many inflation models predict n_s close to but below 1; current constraints from the *Planck* satellite (which combine measurements of the CMB with other late-universe probes) give $n_s = 0.965 \pm 0.004$ [42] (note that exact scale invariance has been ruled out). The amplitude of scalar fluctuations A_s is the name given to the constant of proportionality in (4.33) when the pivot scale k_0 is $0.05\,\mathrm{Mpc}^{-1}$; it is constrained by *Planck* to be $A_s = 2.1^{+0.031}_{-0.034} \times 10^{-9}$.

Initial conditions for δ: adiabaticity

To write the initial spectrum of density perturbations, we need to relate the initial matter and radiation overdensities to Φ^0, for which we have the initial condition (4.33).

We can do this by noting first that all modes of interest today were super-horizon initially, and taking the large-scale relation between Φ and δ from Equation (4.27), which states that

$$-3a^2 H\Phi = 4\pi G a^3 \delta\rho; \tag{4.34}$$

along with the background Friedmann equation (4.6) for $\rho^{(0)}$ we get that, on super-horizon scales,

$$\frac{\delta\rho_{\vec{\boldsymbol{k}}\to 0}}{\rho^{(0)}} = -2\Phi_{\vec{\boldsymbol{k}}\to 0}. \tag{4.35}$$

Initially ρ was dominated by by radiation so we can neglect δ_m and say that the initial condition for δ_r is exactly

$$\delta^0_{r\vec{\boldsymbol{k}}} = -2\Phi^0_{\vec{\boldsymbol{k}}}. \tag{4.36}$$

To get the initial condition for δ, we make the assumption of adiabaticity: constant entropy per baryon $\frac{S}{n_B}$ where S is the entropy and n_B is the baryon number density. This results in the relation

$$\delta_c^0 = \frac{3}{4}\delta_r^0 = -\frac{3}{2}\Phi^0. \tag{4.37}$$

With these initial conditions, we see that the initial matter power spectrum was scale invariant just like $P_{\Phi^0}(k)$:

$$P(k, t \to 0) = \frac{9}{4} P_{\Phi^0}(k). \tag{4.38}$$

We will see below that this scale invariance is preserved until the modes cross the horizon.

4.3.4 Evolution of density perturbations

All density perturbations that we measure today are sub-horizon, and crossed the horizon either during radiation domination or during matter domination (neglecting the very recent period when dark energy started to become relevant). The largest-scale modes we see have only recently crossed the horizon, during the period of matter domination. During this period, we can neglect radiation density and solve the Einstein equations assuming $\rho = \rho_m$.

The radiation-domination period is more complicated, because $\delta\rho$ is dominated by $\delta\rho_r$ and so the Einstein equations give the evolution of δ_r. During this period, we can find the behaviour of δ_c by using the conservation of its the stress-energy tensor $T^{\mu}{}_{\nu;\mu} = 0$, which is conserved independently of the behaviour of radiation as the CDM and the radiation do not interact; although note that the baryon overdensities *are* coupled to the radiation and so this is not true for δ_b (although during this time $T^{\mu}{}_{\nu;\mu} = 0$ is true separately for the radiation+baryon stress energy tensor).

Density inhomogeneities in a matter dominated universe

In a matter dominated universe, the Einstein equations are solved by

$$\Phi_{\vec{k}}(t) = B_{\vec{k}} \tag{4.39}$$

$$\delta_{\vec{k}}(t) = -\frac{3t^{2/3}k^2 B_{\vec{k}}}{2} - 2B_{\vec{k}}. \tag{4.40}$$

where $B_{\vec{\boldsymbol{k}}}$ is the Fourier transform of an arbitrary spatially varying function $B(\vec{\boldsymbol{x}})$. Note that there is no time-dependence on the right hand side of Equation (4.39)[3]: on all scales, the Newtonian potential is constant in matter dominated universes. On superhorizon scales, δ is constant and given by $\delta = -2\Phi$; on small scales, Equation (4.40) becomes

$$\delta_{\vec{\boldsymbol{k}}} = \frac{-3k^2 t^{2/3} B_{\vec{\boldsymbol{k}}}}{2}. \tag{4.41}$$

We see from Equation (4.41) that the small scale overdensity modes grow with time: a gravitational instability. We also see that their spectrum is $\left\langle \delta_{\vec{\boldsymbol{k}}} \delta_{\vec{\boldsymbol{k}}'} \right\rangle \sim t^{4/3} k^4 \left\langle \delta^0_{\vec{\boldsymbol{k}}} \delta^0_{\vec{\boldsymbol{k}}'} \right\rangle = a^2 k^4 \left\langle \delta^0_{\vec{\boldsymbol{k}}} \delta^0_{\vec{\boldsymbol{k}}'} \right\rangle$ (as $a \propto t^{2/3}$ during matter domination) and so modes that crossed the horizon after matter-radiation equality obey a power spectrum

$$P(k,t) \propto a(t)^2 k^4 P_\Phi(k, t \to t_{\rm eq}) \tag{4.42}$$

where we have denoted $\left\langle B_{\vec{\boldsymbol{k}}} B_{\vec{\boldsymbol{k}}'} \right\rangle = P_\Phi(k, t \to t_{\rm eq})$, ie the power spectrum of Φ just after matter-radiation equality. We will see below that the super-horizon behaviour of Φ during radiation domination is scale-independent, and so $P_\Phi(k, t \to t_{\rm eq}) \propto P_{\Phi^0}(k) \propto k^{-3}$. Thus for modes that have crossed the horizon since matter-radiation equality we have

$$P(k) \propto k. \tag{4.43}$$

The Newtonian potential in a radiation dominated universe

To understand the behaviour of CDM perturbations that crossed the horizon during radiation domination, we need to solve the energy-conservation equations ${T^\mu}_{\nu;\mu} = 0$ for the CDM fluid during this time. The Newtonian potential can be considered as an external source that is unaffected by δ_c, but it will be necessary to know how it evolves. In this regime, $\Phi_{\vec{\boldsymbol{k}}}$ is solved by

$$\Phi_{\vec{\boldsymbol{k}}}(t) = 9\Phi^0_{\vec{\boldsymbol{k}}} \left(\frac{\sqrt{3}\sin\left(\frac{2k\sqrt{t}}{\sqrt{3}}\right) - 2k\sqrt{t}\cos\left(\frac{2k\sqrt{t}}{\sqrt{3}}\right)}{8k^3 t^{3/2}} \right). \tag{4.44}$$

where $\Phi^0_{\vec{\boldsymbol{k}}}$ is its value as $t \to 0$.

---

[3] In fact, there is another solution to $\Phi_{\vec{\boldsymbol{k}}}$ which is time-dependent and can be added to the constant solution, but as it decays with time it is of no relevance today.

On super-horizon scales, (4.44) is constant:

$$\Phi_{\vec{\boldsymbol{k}}\to 0} = \Phi^0_{\vec{\boldsymbol{k}}\to 0} \tag{4.45}$$

(this justifies the statement below Equation (4.42) that the superhorizon spectrum of Φ has no scale dependence induced during radiation domination). However, once the mode crosses the horizon - ie, $k\eta \gg 1$, the function (4.44) starts to decay; this is in contrast to the matter-domination case where Φ was constant both super- and sub-horizon.

CDM perturbations in a radiation dominated universe

To understand how δ_c behaved during this radiation domination, we can use the conservation of the energy-momentum tensor

$$T^{\mu}{}_{\nu;\mu} = 0, \tag{4.46}$$

in the metric of (4.18) with Φ obeying Equation (4.44). As the CDM and the baryon/radiation plasma do not interact except gravitationally, conservation of $T_{\mu\nu}$ is true separately for the CDM stress energy tensor—ie, the part that does not interact with radiation—and the stress energy tensor of the fluid composed of the radiation and the baryons.

The conservation of energy-momentum leads to the following equations:

$$\frac{\dot{\delta\rho}}{\rho^{(0)}} + 3H\left(\frac{\delta\rho+\delta P}{\rho^{(0)}}\right) + \left(\frac{\rho^{(0)}+P^{(0)}}{\rho^{(0)}}\right)\frac{\vec{\nabla}\cdot\vec{v}}{a} - 3\left(\frac{\rho^{(0)}+P^{(0)}}{\rho^{(0)}}\right)\dot{\Phi} = 0 \tag{4.47}$$

$$\nabla^2\delta P + \frac{1}{a^3}\partial_t\left(a^4\left(\rho^{(0)}+P^{(0)}\right)\vec{\nabla}\cdot\vec{v}\right) + \left(\rho^{(0)}+P^{(0)}\right)\nabla^2\Phi = 0, \tag{4.48}$$

where Equation (4.47) is the t-component, ie the energy conservation equation; and Equation (4.48) is the spatial divergence of the spatial components, ie the momentum conservation equations (note that in Equation (4.48) ∂_t denotes the partial derivative with respect to the coordinate time t).

For the cold dark matter fluid, $P^{(0)} = 0 = \delta P$ and $\rho^{(0)} \propto a^{-3}$, and Equations (4.47) and (4.48) become

$$\partial_t\left(a^2\left(3\dot{\Phi} - \dot{\delta}_c\right)\right) - k^2\Phi = 0. \tag{4.49}$$

One can solve this to show that the result is that the overdensity modes that cross the horizon during the radiation era modes grow approximately logarithmically:

$$\delta_c \sim \delta_c^0 - 9\Phi^0\log\left(k\eta\right) - 5.75\Phi^0 \tag{4.50}$$

where δ_c^0 is their value at $t \to 0$. Thus the power spectrum of these modes is

$$P(k) \propto P_{\Phi^0}(k)\left(\log k\right)^2 \propto k^{-3}\left(\log k\right)^2. \tag{4.51}$$

4.3.5 The matter power spectrum today

The matter power spectrum today, calculated numerically with CAMB, is shown in Figure 4.1. This is of course much more accurate than the approximations we have made, but the scale behaviour we found in Equations (4.43) and (4.51) is shown on the plot for comparison.

On the largest scales, we see the $P(k) \propto k$ dependence we expect for modes that crossed the horizon during matter domination; on smaller scales we see the $k^{-3} (\log k)^2$ behaviour we expect for modes that crossed during radiation domination. There is a turnover in the power spectrum at the scale corresponding to matter-radiation equality, $\sim 100\,\mathrm{Mpc}$.

For modes that crossed the horizon before recombination, there are slight wiggles in the power spectrum: these are baryonic acoustic oscillations (BAOs), and they result from the interaction between the baryons and the radiation.

4.3.6 The velocity power spectrum

On sub-horizon scales, the Einstein equations (4.22) and (4.24) can be combined to give

$$\dot{\delta} = \frac{ikv}{a} \tag{4.52}$$

Writing δ in terms of a growth factor such that $\delta(t) = D(t)\delta_0$ with δ_0 the overdensity today, we can explicitly write

$$v = \frac{-ia}{k}\frac{\delta}{D}\dot{D}; \tag{4.53}$$

rearranging and switching the derivative with respect to time to one with respect to a, and defining

$$f \equiv \frac{d\ln D}{d\ln a}, \tag{4.54}$$

we can write

$$v = \frac{-ifaH\delta}{k} \tag{4.55}$$

where δ_0 is the matter overdensity today. So the velocity power spectrum is directly related to the matter power spectrum as

$$P_{vv}(k) = \left(\frac{faH}{k}\right)^2 P_{\delta\delta}(k). \tag{4.56}$$

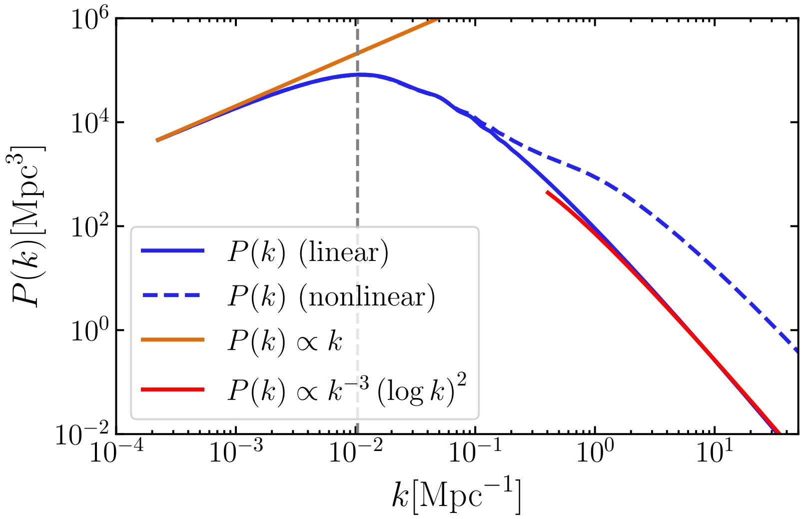

Figure 4.1: The matter power spectrum today. The solid blue line is the linear $P(k)$ calculated with CAMB; overlaid are the analytical approximations $P(k) \propto k$ and $P(k) \propto k^{-3}(\log k)^2$. The modes that crossed the horizon after matter-radiation equality follow $P(k) \propto k$; the modes which crossed before follow $P(k) \propto k^{-3}(\log k)^2$. There is a peak in between these modes corresponding to the scale at matter-radiation equality, indicated with a vertical dashed line on the plot. Also shown for comparison is the nonlinear matter power spectrum, calculated with CAMB using HMCode; large scales remain linear but the smallest scales are expected to have extra power than would be indicated by the linear calculation.

4.3.7 Anisotropies in the CMB

We can probe the perturbations in the radiation field by measuring the temperature fluctuations in the CMB. There are differences, however, in how we probe the radiation field compared to how we probe the matter field. We have some access to probes of the matter perturbations at different redshifts to our own, by—for example—making galaxy surveys of distant galaxies. By contrast, when we map the CMB we are measuring the radiation overdensity at our own position and at our own cosmological time; however, there is information in the different photon propogation directions, as they have mostly been travelling without scattering since they left the surface of last scattering. As such, we can look in different directions and map the photon temperature across the sky.

When we measure the temperature, we are measuring $T(\hat{\boldsymbol{n}}, \vec{\boldsymbol{x}}_0, t_0)$, where $\hat{\boldsymbol{n}}$ is a unit vector describing the direction we look in; and $\vec{\boldsymbol{x}}_0$ and t_0 describe our location in space and time. The analogue of the power spectrum in this case is the angular correlation function (where the $\vec{\boldsymbol{x}}$ and t dependence is now suppressed)

$$C(\theta) = \left\langle \frac{\delta T}{T_0}(\hat{\boldsymbol{n}}) \frac{\delta T}{T_0}(\hat{\boldsymbol{n}}') \right\rangle \tag{4.57}$$

where $\hat{\boldsymbol{n}} \cdot \hat{\boldsymbol{n}}' = \cos\theta$, and T_0 is the mean CMB temperature. Instead of Fourier transforming we project onto spherical harmonics:

$$\frac{\delta T}{T_0}(\hat{\boldsymbol{n}}) = \sum_{\ell=0}^{\infty} \sum_{m=-\ell}^{\ell} a_{\ell m} Y_{\ell m}(\hat{\boldsymbol{n}}). \tag{4.58}$$

This is a very convenient basis because the assumption of statistical homogeneity and anisotropy tells us that

$$\langle a^*_{\ell m} a_{\ell' m'} \rangle = \delta_{\ell \ell'} \delta_{m m'} C_\ell \tag{4.59}$$

where

$$C_\ell = \left\langle |a_{\ell m}|^2 \right\rangle \tag{4.60}$$

encodes the information about fluctuations on angular scales $\theta \sim \frac{\pi}{\ell}$.

4.3.8 The Boltzmann equation

When we look at the CMB, we see photons that have been travelling without scattering since recombination. In this regime, the fluid approximation—in which only two quantities, the spatially dependent density and velocity fields, describe the perturbations—breaks down. As such, we cannot use the conservation of the perfect fluid energy-momentum tensor to describe the evolution of the radiation field since recombination. Instead, we can use the more general Boltzmann equation, which states that for particles that evolve without collisions

$$\frac{df}{dt} = 0 \tag{4.61}$$

where f is the distribution function, that gives the particle density in phase space: the number of particles in a phase-space volume element $d^3x d^3p$ is

$$dN = f(\vec{\boldsymbol{x}}, \vec{\boldsymbol{p}}, t) d^3x d^3p. \tag{4.62}$$

The statement that $\frac{df}{dt} = 0$ states that the number of particles in a phase-space volume is conserved[4].

Equation (4.61) can be generalized to allow for collisions by adding a collision term $C[f]$ on the right hand side. Prior to recombination, the photons interact with the baryons and so $C[f] \neq 0$ and instead should describe Compton scattering. In this regime, however, the photons and baryons act as an (imperfect) fluid, and can be described with a stress-energy tensor T^{μ}_{ν} for an imperfect fluid (a generalization of Equation (4.4) including anisotropic stress terms on the off-diagonal spatial components) which obeys ${T^{\mu}}_{\nu;\mu} = 0$[5]. The initial conditions for radiation in Section 4.3.3 can be evolved with these equations to find a distribution for the radiation overdensity at recombination t_r.

To understand how these overdensities propogate towards us after recombination, we can write down the Boltzmann Equation (4.61) in the perturbed FLRW metric (4.18). The distribution function of the photons is Planckian:

$$f(\vec{\boldsymbol{x}}, \vec{\boldsymbol{p}}, t) = \frac{1}{e^{\frac{E}{T}} - 1}. \tag{4.63}$$

To zeroth order T is homogeneous and decays with time according to $T \propto \frac{1}{a}$. The perturbed distribution function is

$$f(\vec{\boldsymbol{x}}, \vec{\boldsymbol{p}}, t) = \frac{1}{e^{\dfrac{E}{T_0 + \Delta T(\vec{\boldsymbol{x}}, \vec{\boldsymbol{p}}, t)}} - 1} \tag{4.64}$$

where T_0 is the background quantity. ΔT is dependent not only on $\vec{\boldsymbol{x}}$ but on the photons' direction of propagation $\vec{\boldsymbol{p}}$.

For the FLRW metric and the distribution function (4.64), the Boltzmann equation is

$$0 = \left(\frac{\partial}{\partial \eta} + \hat{p}^i \frac{\partial}{\partial x^i}\right)\left(\frac{\Delta T}{T} + \Phi\right) - 2\frac{\partial \Phi}{\partial \eta}. \tag{4.65}$$

Going to Fourier space, and defining $\mu \equiv \hat{\boldsymbol{k}} \cdot \hat{\boldsymbol{p}}$ (where hats indicate unit vectors such that $\vec{\boldsymbol{k}} \equiv k\hat{\boldsymbol{k}}$) , this is

$$0 = \left(\frac{\partial}{\partial \eta} + i\mu k\right)\left(\frac{\Delta T}{T} + \Phi\right) - 2\frac{\partial \Phi}{\partial \eta}. \tag{4.66}$$

---

[4] This follows as the phase-space volume itself is conserved along the path of a particle due to Louiville's theorem.

[5] in this regime, ${T^{\mu}}_{\nu;\mu} = 0$ coincides with the Boltzmann equations for photons and baryons.

The operator $\left(\frac{\partial}{\partial t}+\frac{\hat{p}^i}{a}\frac{\partial}{\partial x^i}\right)$ is a total time derivative along the photon's path, and so we can integrate Equation (4.65):

$$\frac{\Delta T}{T}+\Phi=2\int\frac{\partial\Phi}{\partial\eta}=2\int\frac{\partial\Phi}{\partial t}dt. \tag{4.67}$$

In particular, in a matter-dominated universe, $\frac{\partial\Phi}{\partial t}=0$ and

$$\frac{\Delta T}{T}+\Phi=\text{const.} \tag{4.68}$$

Neglecting the contribution to due time-varying Φ contribution, this means that the photons an observer at $(\eta_0,\boldsymbol{\vec{x}}_0)$ sees in the direction $\boldsymbol{\hat{n}}$ have temperature

$$\frac{\Delta T}{T}(\eta_0,\boldsymbol{\vec{x}}_0,\boldsymbol{\hat{n}})=\frac{\Delta T}{T}(\eta_r,\boldsymbol{\vec{x}}_r,\boldsymbol{\hat{n}})+\Phi(\eta_r,\boldsymbol{\vec{x}}_r)-\Phi(\eta_0,\boldsymbol{\vec{x}}_0). \tag{4.69}$$

The monopole $\Phi(\eta_0,\boldsymbol{\vec{x}}_0)$ is unobservable: it is the same for all photons we detect, and need not be considered. Without this, we see that the temperature perturbations we observe are given by the temperature perturbations plus the Newtonian potential at recombination; this is the Sachs–Wolfe (SW) effect. The contribution due to time-varying Φ is the integrated Sachs–Wolfe (ISW) effect; this is relevant in our universe as the potentials were in fact still varying a small bit at the time of recombination due to the presence of radiation, contributing to an early ISW effect; and as the dark matter has recently started to dominate today, contributing to a late ISW effect.

There is also a Doppler term, which is due to the relative velocity between the observer and the velocity of the photon-baryon fluid at recombination $\boldsymbol{\vec{v}}_b$:

$$\frac{\Delta T}{T}(\eta_0,\boldsymbol{\vec{x}}_0,\boldsymbol{\hat{n}})=\boldsymbol{\hat{n}}\cdot\left(\boldsymbol{\vec{v}}_b(\eta_r,\boldsymbol{\vec{x}}_r)-\boldsymbol{\vec{v}}(\eta_0,\boldsymbol{\vec{x}}_0)\right). \tag{4.70}$$

We see a significantly Doppler-shifted CMB due to our motion with respect to its frame of reference.

4.3.9 The primary CMB power spectrum

The power spectrum of fluctuations in CMB temperature is shown in Fig 4.2. This is an extremely useful probe of the cosmological parameters, as many of them have different effects on the power spectrum. We will discuss the qualitative features below.

Large scales

The fluctuations on large scales are due only to the SW, ISW, and Doppler effects; we expect scale-independence in these scales as these modes were not in causal contact at the time of recombination and as such were super-horizon at that time. Indeed, the flat behaviour at low ℓ is indicative of a scale-independent spectrum (as, in two dimensions, a scale independent spectrum is $\sim \ell^{-2}$; note that $\ell(\ell+1)C_\ell$ is plotted); these modes are still following the scale-independent behaviour seeded by inflation, as these are modes which were superhorizon at the time of release of the CMB.

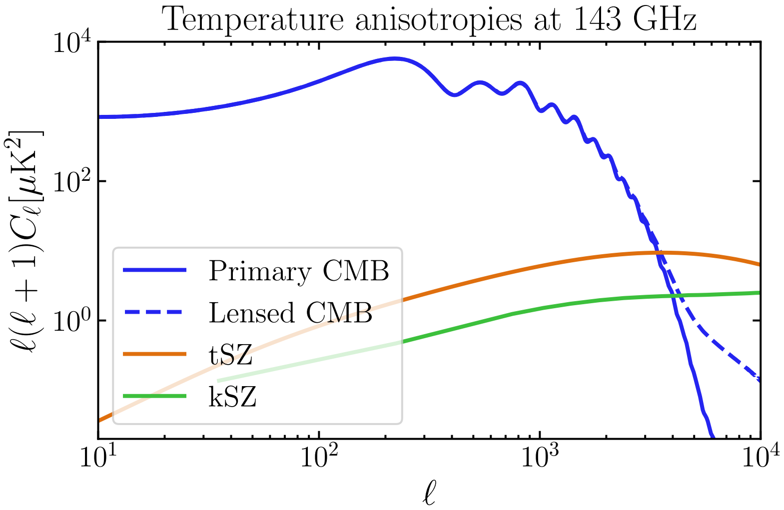

Figure 4.2: The power spectra of the fluctuations in observed CMB temperature C_ℓ^{TT}. Primary anisotropies are indicated in blue (with the lensed spectrum in dashed blue); the secondary kSZ and tSZ anisotropies are indicated in orange and green.

Intermediate scales

On intermediate scales, baryon acoustic oscillations are evident—significantly more so than in the matter power spectrum. This is due to the modulation of δ_γ at recombination by a cosine function, due to the interaction with the baryon fluid prior to recombination. The positions and heights of the Doppler peaks are strongly dependent on the value of the baryon density Ω_b.

Small scales

On the small scales, the CMB power is exponentially suppressed, as the photons had time to come to equilibrium, removing all fluctuations. This is known as Silk damping, and this part of the power spectrum ($\ell \gtrsim$ a few 1000) is sometimes referred to as the "damping tail" of the CMB.

4.3.10 The secondary CMB anisotropies

If there were no other structure in the universe, the CMB that we see would have a power spectrum as described above. However, much happens to the CMB photons as they travel from the surface of last scattering to us. They interact with the structure that has formed in the late universe: they are gravitationally lensed by matter, and they scatter off of the free electrons that start to appear in the universe after their reionization at a redshift of $z \gtrsim 7$, in a process known as the Sunyaev–Zel'dovich (SZ) effect [43]. This leads to observable features in the CMB known as the *secondary CMB anisotropies* (to be contrasted with the *primary CMB anisotropies*, which we would see if it didn't interact after its release at recombination). The sizes of the secondary signals are indicated in Figure 4.2, to compare with the primary signal; in particular the lensed CMB power spectrum, and the thermal and kinetic SZ effects (to be discussed below) are shown.

We will discuss CMB lensing and the SZ effects in the following Sections.

4.4 CMB lensing

As the CMB passes by matter, it is lensed. This induces many changes in the observed CMB, shifting power from large to small scales, and inducing coupling between different modes—ie $C_{\ell\ell'} \not\propto \delta_{\ell\ell'}$. Because this is caused by the clustering of matter, on large scales CMB lensing is mostly a linear effect, with non-linearities becoming important on smaller scales. CMB lensing is a very useful way of probing the matter power spectrum, as it is sensitive to all matter—unlike galaxy surveys, which are not directly sensitive to dark matter—and because its theory is very well understood.

When we measure the temperature in the direction $\hat{\boldsymbol{n}}$ we do not see the temperature emitted at $\hat{\boldsymbol{n}}$ but instead the temperature emitted elsewhere that has been deflected into the path of $\hat{\boldsymbol{n}}$; the deflection angle can be denoted $\vec{\boldsymbol{\alpha}}$ such that the observed (lensed) temperature $\tilde{T}$ is related to the emitted (unlensed) temperature T by

$$\tilde{T}(\hat{\boldsymbol{n}}) = T(\hat{\boldsymbol{n}} + \vec{\boldsymbol{\alpha}}). \tag{4.71}$$

The measured CMB power spectrum is thus the lensed power spectrum $C_\ell^{TT\,\mathrm{lensed}} = C_\ell^{\tilde{T}\tilde{T}}$. The deflection angle can be calculated by explicitly integrating the null geodesic equation in the metric (4.1); in the small-angle regime the integral can be done over the undeflected photon path (the "Born approximation") and the result is that the deflection angle $\vec{\boldsymbol{\alpha}}$ be written as the derivative of a potential ϕ

$$\vec{\boldsymbol{\alpha}} = \vec{\boldsymbol{\nabla}}\phi \tag{4.72}$$

where $\vec{\boldsymbol{\nabla}}$ is the angular gradient, and ϕ is given by a weighted integral over the Newtonian potential along the line of sight[6]

$$\phi(\hat{\boldsymbol{n}}) = -2\int_0^{\chi_S} d\chi W^{\Phi}(\chi)\Phi(\chi\hat{\boldsymbol{n}}, \chi) \tag{4.73}$$

where χ_S is the comoving distance of the surface of last scattering. In a flat universe, the lensing efficiency kernel is

$$W^{\Phi}(\chi) = \frac{\chi_S - \chi}{\chi_S\chi}. \tag{4.74}$$

4.4.1 Qualitative effects on the observed CMB

CMB lensing has many effects on the CMB we observe. It shifts power from large to small scales, blurring the acoustic peaks and inducing mode coupling such that it is no longer true that $\langle a_{\ell m} a_{\ell' m'}\rangle \propto \delta_{\ell\ell'}\delta_{mm'}$. It also significantly changes the observed polarization spectrum of the CMB. In Figure 4.2 it is clear that much of the CMB signal on multipoles $\ell \gtrsim$ a few × 1000 is due to lensing.

The non-Gaussianity induced in the CMB by lensing can be used to reconstruct the lensing potential $\phi(\hat{\boldsymbol{n}})$ from the observed CMB map, for example by the use of quadratic estimators [44]. The effects of lensing can also be "undone" in a process known as "delensing", with high-fidelity measurements of either $\phi(\hat{\boldsymbol{n}})$ or other highly correlated proxies of it, to get access to the underlying unlensed CMB map [45, 46, 47, 48].

As it is a projection of the matter power spectrum, the angular power spectrum of $\phi(\hat{\boldsymbol{n}})$ is a powerful probe of $P(k)$; this will be discussed below.

---

[6] Strictly speaking, ϕ is an integral of the Weyl potential $\Phi - \Psi$, but we work in the regime where $\Psi = -\Phi$.

4.4.2 The CMB lensing power spectrum

CMB lensing is a very useful way to probe the matter power spectrum. In particular, as the CMB is lensed by all the matter between us and the surface of last scattering—all the structures in the universe, essentially—we can use the lensed CMB to make a 2-dimensional map of this integrated mass distribution and study the power spectrum of this, instead of the 3-dimensional matter power spectrum. In this Section we discuss the CMB lensing power spectrum.

Projection of the three-dimensional matter power spectrum to 2 dimensions

The angular power spectrum of ϕ, denoted $C_\ell^{\phi\phi}$, is defined as follows:

$$\langle \phi_{\ell m} \phi^*_{\ell' m'} \rangle \equiv C_\ell^{\phi\phi} \delta_{\ell\ell'} \delta_{mm'} \tag{4.75}$$

where $\phi_{\ell m}$ are the multipole moments of the real-space field $\phi(\hat{\boldsymbol{n}})$ projected onto a spherical harmonic basis. In (4.75), the Kronecker deltas $\delta_{\ell\ell'}\delta_{mm'}$ are a result of the assumption of statistical isotropy (analagously to the appearance of the Dirac delta in the definition of $P(k)$ (4.31)) and the angular power spectrum $C_\ell^{\phi\phi}$ is only a function of the primary wavenumber ℓ and not the angular momentum number m (again analagously to $P(k)$ being a function only of $|\vec{\boldsymbol{k}}|$).

Using the definition Equation (4.73) along with the explicit Fourier and spherical harmonic decompositions allows one to express $C_\ell^{\phi\phi}$ in terms of the three-dimensional power spectrum $P(k)$; the expression is derived explicitly in Appendix A.1 and the result is

$$C_\ell^{\phi\phi} = \frac{2}{\pi} \int d\chi d\chi' W^\Phi(\chi) W^\Phi(\chi') \int k^2 dk P_\Phi(k) j_\ell(k\chi) j_\ell(k\chi'), \tag{4.76}$$

where $P_\Phi(k)$ is the power spectrum of the Newtonian potential Φ and $j_\ell(x)$ are the spherical Bessel functions of degree ℓ.

This can be simplified significantly by taking the Limber approximation [49] (derived in Appendix A.2), which is valid in the large-ℓ limit:

$$C_\ell^{\phi\phi} = \int d\chi \frac{W^\Phi(\chi)^2}{\chi^2} P_\Phi\left(k = \frac{\ell + 1/2}{\chi}, z\right). \tag{4.77}$$

This is much easier to integrate numerically than (4.76), which contains highly oscillatory Bessel functions that require many sampling points for the integration over k.

Note that we can relate $C_\ell^{\phi\phi}$ to an integral directly over the matter power spectrum (as opposed to $P_\Phi(k)$), using the Poisson equation relation between P_δ and P_Φ:

$$C_\ell^{\phi\phi} = \frac{1}{l^4}\int d\chi \chi^2 \left(\frac{3}{2}\frac{H_0^2\Omega_m^0}{a}\right)^2 W^\Phi(\chi)^2 P_\delta\left(k = \frac{\ell+1/2}{\chi}\right) \tag{4.78}$$

where $\left(\ell+\frac{1}{2}\right)^4$ has been replaced by ℓ^4 (which is a valid approximation as we are working already in the high-ℓ limit).

4.4.3 Lensing potential to lensing convergence

As well as the lensing potential ϕ, the CMB lensing convergence κ is also commonly used, where

$$\kappa(\hat{\boldsymbol{n}}) \equiv \frac{-1}{2}\nabla\cdot\vec{\boldsymbol{\alpha}} = -\frac{1}{2}\nabla^2\phi. \tag{4.79}$$

In spherical harmonic space, κ and ϕ are related as follows:

$$\kappa = \frac{-\ell(\ell+1)}{2}\phi. \tag{4.80}$$

Thus, the power spectrum of κ is

$$C_\ell^{\kappa\kappa} = \frac{\left(\ell\left(\ell+1\right)\right)^2}{4}C_\ell^{\phi\phi}; \tag{4.81}$$

in the high-ℓ limit this means that

$$C_l^{\kappa\kappa} = \frac{1}{4}\int d\chi \chi^2 \left(\frac{3}{2}\frac{H_0^2\Omega_m^0}{a}\right)^2 W^\Phi(\chi)^2 P_\delta\left(k = \frac{\ell+1/2}{\chi}\right). \tag{4.82}$$

This allows us to define a new lensing convergence kernel $W^\kappa(\chi)$ such that

$$C_\ell^{\kappa\kappa} = \int \frac{d\chi}{\chi^2} W^\kappa(\chi)^2 P_\delta\left(k = \frac{\ell+1/2}{\chi}\right); \tag{4.83}$$

this is also the power spectrum (in the high-ℓ limit) of the overdensity field projected along a redshift kernel $W^\kappa(\chi)$

$$\kappa = \int d\chi W^\kappa(\chi)\delta(\chi\hat{\boldsymbol{n}},\chi) \tag{4.84}$$

where $W^\kappa(\chi)$ is given by

$$W^\kappa(\chi) = \frac{3}{2}H_0^2\Omega_m^0\frac{\chi}{a}\left(1-\frac{\chi}{\chi_s}\right). \tag{4.85}$$

4.4.4 Redshift distribution

The redshift distribution (4.85) is very well understood, making the interpretation of the convergence map also quite straightforward. The redshift kernel $W^{\kappa}(z)$ is plotted in Figure 4.3; note that $W^{\kappa}(z)$ is defined by

$$\kappa(\hat{\boldsymbol{n}}) = \int dz W^{\kappa}(z)\delta(\chi\hat{\boldsymbol{n}}, \chi), \tag{4.86}$$

and as such differs from $W^{\kappa}(\chi)$ by a factor of $\frac{d\chi}{dz}$. The power spectrum $C_{\ell}^{\kappa\kappa}$ is also shown in Figure 4.3, on the right.

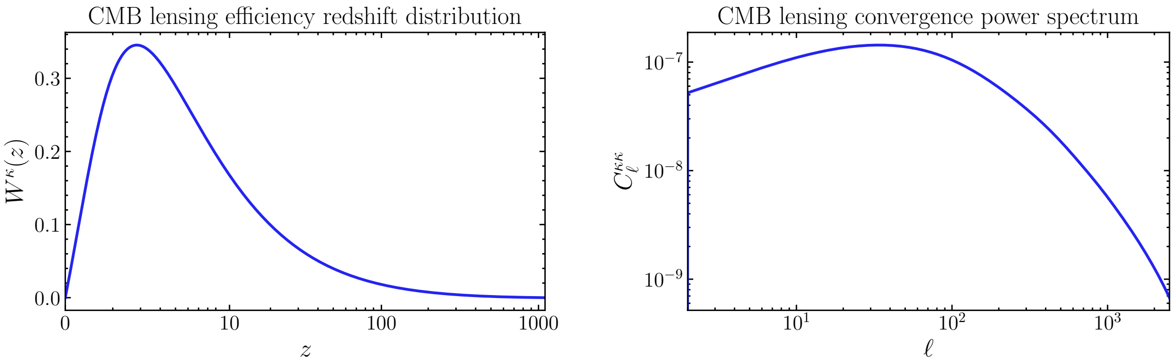

Figure 4.3: *Left*: The redshift distribution of the CMB lensing efficiency; while this peaks at redshift $z \sim 2$ there is a very broad kernel with significant support at much higher redshift than this. (Note that the x-axis scales as $\log(1+z)$.) *Right*: The power spectrum of the CMB lensing convergence.

4.4.5 CMB lensing as a probe of $P(k)$

Because the redshift distribution of ϕ is so well understood, and because it is sensitive to the dark matter as well as ordinary matter, $C_{\ell}^{\phi\phi}$ is a very useful probe of the matter power spectrum $P(k)$. This is in contrast to galaxy surveys, where the modelling of the redshift distribution of galaxies must be considered, along with the differences between the galaxy and the dark matter distributions.

There exist a number of methods to extract $\phi(\hat{\boldsymbol{n}})$ from a CMB map, in particular by exploiting the statistical anisotropy it induces in the $a_{\ell m}$: for a lensed CMB map, it is not true that $\langle a_{\ell m} a_{\ell' m'} \rangle \propto \delta_{\ell\ell'}\delta_{mm'}$. It becomes easier to extract the lensing information from higher-resolution CMB experiments, and signal-dominated $\phi(\hat{\boldsymbol{n}})$ maps are some of the key goals of the upcoming SO and CMB-S4 experiments.

4.5 The Sunyaev–Zel'dovich effects

In the late universe, there are free electrons, and the CMB photons Compton scatter off of them [43, 50]. The Sunyaev–Zel'dovich (SZ) effect is the name given for the scattering of the CMB photons off of these electrons. This induces observable effects in the CMB. The thermal SZ (tSZ) effect, when photons off of high-temperature electrons, induces a spectral distortion the CMB. The kinetic SZ (kSZ) effect, when photons scatter off of electrons moving with some velocity with respect to the CMB, is a blackbody effect that is the dominant blackbody effect on angular scales $\ell \gtrsim 4000$.

4.5.1 The thermal Sunyaev–Zel'dovich effect

The tSZ contribution to the temperature anisotropy is [43]

$$\frac{\Delta T}{T}(\hat{\boldsymbol{n}}, \nu) = g_\nu y(\hat{\boldsymbol{n}}) \tag{4.87}$$

where $y(\hat{\boldsymbol{n}})$ is the Compton y parameter and g_ν is the spectral function of the tSZ effect

$$g_\nu = x \coth\frac{x}{2} - 4 \tag{4.88}$$

where $x \equiv h\nu/k_B T_{CMB}$. $y(\hat{\boldsymbol{n}})$ is given by the integral of the electron pressure over the line of sight at $\hat{\boldsymbol{n}}$, ie

$$y(\hat{\boldsymbol{n}}) = \frac{\sigma_T}{m_e c^2}\int a(\chi)\, d\chi\, P_e(\chi, \hat{\boldsymbol{n}}) \equiv \int a(\chi)\, d\chi\, y_{3D}(\chi, \hat{\boldsymbol{n}}) \tag{4.89}$$

where σ_T is the Thompson scattering cross section, m_e is the mass of the electron, c is the speed of light, and $P_e(\chi, \hat{\boldsymbol{n}})$ is the electron pressure; the three-dimensional Compton-y field is defined as the rescaling of the electron pressure field $y_{3D} \equiv \frac{\sigma_T}{m_e c^2} P_e(\chi, \hat{\boldsymbol{n}})$.

4.5.2 The kinetic Sunyaev–Zel'dovich effect

The kSZ temperature anisotropy is given by

$$\frac{\Delta T(\hat{\boldsymbol{n}})}{T} = \sigma_T \int d\chi e^{-\tau(\chi)} a(\chi) n_e(\chi, \hat{\boldsymbol{n}}) \vec{\boldsymbol{v}}(\chi, \hat{\boldsymbol{n}}) \cdot \hat{\boldsymbol{n}} \tag{4.90}$$

where σ_T is the Thompson scattering cross section, $\tau(\chi)$ is the optical depth to χ, $n_e(\chi, \hat{\boldsymbol{n}})$ is the electron density at $\chi\hat{\boldsymbol{n}}$, and $\vec{\boldsymbol{v}}$ is the velocity of the electron at $(\chi, \hat{\boldsymbol{n}})$; note that the kSZ temperature anisotropy is not sensitive to the transverse velocity field but instead only the radial velocity field $v_r \equiv \vec{\boldsymbol{v}} \cdot \hat{\boldsymbol{n}}$.

On linear scales, the velocity field is related to the matter overdensity field by (see Section 4.3.6)

$$v = \frac{ifaH}{k}\delta \tag{4.91}$$

where $f \equiv \frac{d \ln D}{d \ln a}$ with D the growth factor. The *radial* velocity field is thus given by

$$v_r = \mu \frac{ifaH}{k}\delta \tag{4.92}$$

where $\mu \equiv \frac{k_r}{k}$.

Because the kSZ temperature anisotropy is sourced both by the velocity field and the electron density, its power spectrum is a 4-point function $\sim \langle v_r v_r \delta_e \delta_e \rangle$ where δ_e is the electron overdensity defined by $n_e(\chi, \hat{\boldsymbol{n}}) = \bar{n}_e(\chi)\left(1 + \delta_e(\chi, \hat{\boldsymbol{n}})\right)$. As such, its power spectrum is not as straightforward to write down as the two-point quantities we have considered elsewhere.

At large ℓ, kSZ power spectrum is dominated by an integral over the transverse momentum power spectrum $P_{q\perp}$ as follows [51]:

$$C_\ell = \frac{1}{2}\left(\frac{\sigma_T \bar{n}_{e0}}{c}\right)^2 \int \frac{d\chi}{\chi^2 a^4} e^{-2\tau} P_{q\perp}\left(k = \frac{\ell + 1/2}{\chi}, z(\chi)\right) \tag{4.93}$$

where $P_{q\perp}$ depends on the four-point function $P_{\delta\delta vv}$ but can be approximated by [52]

$$P_{q\perp}(k, z) = \dot{a}^2 f \int_{-1}^{1} d\mu \int \frac{d^3k'}{(2\pi)^3} P_{ee}^{\text{nonlin}}(|\vec{\boldsymbol{k}} - \vec{\boldsymbol{k}}'|, z) P_{\delta\delta}^{\text{lin}}(k', z) \frac{k(k - 2k'\mu)(1-\mu^2)}{k'^2\left(k^2 + k'^2 - 2kk'\mu\right)}. \tag{4.94}$$

The kSZ and tSZ effects probe the electron distribution and (in the case of kSZ) the velocity distribution of the universe. However, they are non-linear effects, and modelling the electron power spectrum requires going beyond perturbation theory. They will be discussed further in Chapter 5.

Figure 4.2 indicates the scale dependence of the secondary CMB signals at 143 GHz. The tSZ effect can be separated from the primary CMB by means of it spectral dependence, by taking measurements at different frequencies; however, just like the primary CMB, the kSZ effect is a black-body effect and can't be subtracted in this way. It becomes the dominant signal on angular scales of $\ell \gtrsim 4000$.

Chapter 5

Nonlinear power spectra: the halo model

The most straightforward way to calculate power spectra is to do so with perturbation theory, where calculations can be done by expanding in small perturbations δ. However, at late times and on small scales, this does not suffice as the gravitational instability that leads to structure formation causes the matter overdensities δ to increase with time, to the point where $\delta \ll 1$ is no longer true and the small-δ linear expansion fails. The linear power spectrum is thus expected to be inaccurate on scales smaller than some (time-dependent) scale k_{NL} and we must model the power spectrum another way. To this end, in this Chapter we introduce the halo model and discuss its use for modelling non-linear power spectra. In Figure 4.1, both the linear power spectrum and a non-linear model of the power spectrum (calculated using CAMB [18] with HMCode [53]) are shown; as expected, we see that on scales with $k \gtrsim 0.1\text{Mpc}^{-1}$ the linear power spectrum is significantly smaller than the non-linear power spectrum.

As well as this, some quantities that we are interested in modelling are intrinsically non-linear; for these quantities the halo model is also very useful. One of the most obvious observables we have access to are maps of galaxy density, and indeed in upcoming years there will be many higher-density galaxy surveys over large fractions of the sky such as the Legacy Survey of Space and Time (LSST) by the Rubin Observatory [54].

The halo model provides a useful prescription for calculating matter and galaxy power spectra, and other quantities of interest such as the electron distribution (which is relevant for the SZ effects) and the cosmic infrared background (CIB), on large and also on non-linear scales. The main idea behind the halo model is to consider, instead of the smooth overdensity field δ, just the *peaks* of δ. Within this model, all of the matter in the universe is placed in these peaks—the "halos". The correlations between observables can then be split into the large-scale correlations between two different halos, and the small-scale correlations within a single halo (as the distance between halos is larger than the typical size of a halo):

$$P^{XY}(k,z) = P^{XY}(k,z)^{2h} + P^{XY}(k,z)^{1h}, \tag{5.1}$$

where P^{2h} refers to the inter-halo correlations ("the two-halo term") and P^{1h} to the intra-halo correlations ("the one-halo term"). This Chapter is organized as follows. In Section 5.1 we will introduce some of the functions used to model halo distributions. In Section 5.2 we will present the halo power spectrum and express the matter power spectrum using the halo model. In Section 5.3 we will discuss the modelling of the galaxy distribution within the halo model. In Section 5.4 we will discuss the modelling of the CIB, and in Section 5.5 we will discuss the modelling of electron distributions. Finally in Section 5.6 we state expressions the cross power spectra of the quantities we have discussed.

5.1 Properties of halos

Halos formed from the gravitational evolution and collapse of overdensities in the initial density field of the universe. As these are objects that evolve in time, their properties will have some dependence on their age; as such we can label the halos by their redshift z. It is also useful to label halos by their mass, as their number density depends on their mass: more massive peaks in δ are rarer than less massive peaks.

A review of the halo model is given in [55]. In this Section we introduce the halo mass function, the halo bias, and the halo density profile, and we refer to [55] and references therein for further details.

5.1.1 The halo mass function

The distribution of halos of different masses is described by the halo mass function $\frac{dN}{dM}(M,z)$ which gives the differential number density of halos of mass M at redshift z. The integral over all masses gives the total number density $N(z)$ of halos at z:

$$N(z) = \int dM \frac{dN}{dM}(M,z)^{1}. \tag{5.2}$$

---

[1] With these conventions, $\frac{dN}{dM}$ has dimensions of [mass^{-1}][distance^{-3}].

Note that $\frac{dN}{dM}$ depends on the mass M and the redshift of the halo.

Forms of $\frac{dN}{dM}$ were first calculated by Press and Schechter [56] whose formalism was generalized by Sheth and Torman [57]. Within these formalisms, $\frac{dN}{dM}$ is not parametrized by the mass of the halo but instead by the peak height, defined by

$$\nu \equiv \frac{\delta_c}{\sigma(M)} \tag{5.3}$$

where $\delta_c \sim 1.686$ is the critical density required for collapse, and $\sigma^2(M)$ is the variance of the initial density field smoothed with a tophat filter of a size similar to the the radius of the halo:

$$\sigma^2(M, z) = \int \frac{dk}{k} \frac{k^3 P(k, z)}{2\pi^2} |W(kR)|^2 \tag{5.4}$$

where $W(kR)$ is the Fourier transform of a tophat function

$$W(x) = \frac{3}{x^3} (\sin x - x \cos x) \tag{5.5}$$

and R is given by

$$R = \left(\frac{3M}{4\pi \bar{\rho}_m} \right)^{\frac{1}{3}} \tag{5.6}$$

where $\bar{\rho}_m$ is the comoving matter density (which is constant with z). The halo mass function can then be expressed in terms of the *halo multiplicity function* $f(\nu)$ through

$$\frac{dN}{dM} \equiv \frac{\bar{\rho}_m}{M} f(\nu) \frac{d \ln \nu}{dM}. \tag{5.7}$$

Various prescriptions have been given for $f(\nu)$. Press and Schechter [56] gave

$$f(\nu) = \frac{\nu}{\sqrt{2\pi}} \exp\left(-\frac{\nu^2}{2} \right). \tag{5.8}$$

Sheth and Torman generalized this to [57]:

$$f(\nu) = \frac{2A}{\sqrt{\pi}} \left(1 + \frac{1}{(a\nu^2)^p} \right) \left(\frac{a\nu^2}{2} \right)^{\frac{1}{2}} \exp\left(-\frac{a\nu^2}{2} \right) \tag{5.9}$$

where $A \sim 0.322$, $a = 0.707$, and $p = 0.3$, or, following [58, 59],

$$f(\nu) = \nu\alpha \left(1 + (\beta\nu)^{-2\phi} \right) \nu^{2\eta} e^{-\left(\frac{\gamma\nu^2}{2} \right)} \tag{5.10}$$

In all calculations, we use the halo mass function of Tinker [58]; in this reference the authors fit to N-body simulations to find the values of the parameters $\{\alpha, \beta, \phi, \eta, \gamma\}$ of Equation (5.10); the values of the parameters are presented in Appendix B.

5.1.2 Halo bias

We have linear perturbation theory predictions about the evolution of and statistics of the continuous dark matter overdensity δ. However, within the halo model, we are interested not in describing δ but in describing the density of discrete halos δ_h. These form where there are peaks in δ, and in general the peaks of a field are biased with respect to the underlying field:

$$\delta_h = b\delta \tag{5.11}$$

where the bias b is some number. For dark matter halos, the bias is scale-dependent (on large scales) and dependent on the mass and redshift of a halo

$$\delta_h(M, z) = b(M, z)\delta. \tag{5.12}$$

It is a requirement that dark matter is *unbiased with respect to itself*:

$$\int dM \frac{dN}{dM} \frac{M}{\bar{\rho}} b(M, z) = 1, \tag{5.13}$$

which is equivalent to the assumption that *all of the dark matter is contained within the halos*. Note that this can also be written as

$$\int d\ln\nu b(\nu) f(\nu) = 1. \tag{5.14}$$

As Equation (5.14) contains both $f(\nu)$ and $b(M, z)$ it is essential that these quantities are defined consistently with respect to each other. We use the halo bias of Tinker [58], in which

$$b(\nu) = 1 - A\frac{\nu^a}{\nu^a + \delta_c^a} + B\nu^b + C\nu^c. \tag{5.15}$$

where $\delta_c \sim 1.686$ is again the critical density required for collapse; the values of the parameters $\{A, a, B, b, C, c\}$ in Equation (5.15) are given in Appendix B.

5.1.3 The halo density profile

Knowledge of the halo density profile $\rho(r)$, which describes the density at a distance r from the centre of a halo, is essential for understanding halo properties and behaviour on scales around the size of the halo. A common parametrization is the Navarro–Frenk–White (NFW) [60] profile

$$\rho(r) = \frac{\rho_S}{(r/r_s)\left(1 + r/r_s\right)^2} \tag{5.16}$$

which is parametrized by the scale radius r_s and the density at r_s, ρ_s. In practice r_s is replaced by the concentration parameter $c \equiv \frac{R}{r_S}$ where R is the halo radius.

The Fourier transform of $\rho(r)$ is necessary for the computation of power spectra (which are the Fourier transforms of the 2-point correlation function):

$$\begin{aligned} u(k, M) &\equiv \frac{\int d^3\vec{\boldsymbol{x}}\rho(\vec{\boldsymbol{x}})e^{-i\vec{\boldsymbol{k}}\cdot\vec{\boldsymbol{x}}}}{\int d^3\vec{\boldsymbol{x}}\rho(\vec{\boldsymbol{x}})} && (5.17) \\ &= \frac{1}{M}\int_0^R dr 4\pi r^2 \frac{\sin kr}{kr}\rho(r), && (5.18) \end{aligned}$$

where R is the radius at which you truncate the halo. The integral (5.18) can be done exactly for the NFW profile:

$$\begin{aligned} u(k, M) = \frac{1}{\left[\ln(1+c) - \frac{c}{1+c}\right]}\Bigg[&\sin(kR)\left[\mathrm{Si}([1+c]kR) - \mathrm{Si}(kR)\right] - \frac{\sin(ckR)}{(1+c)kR} \\ &+ \cos(kR)\left[\mathrm{Ci}([1+c]kR) - \mathrm{Ci}(kR)\right]\Bigg] \qquad (5.19) \end{aligned}$$

where

$$\begin{aligned} \mathrm{Ci}(x) &\equiv -\int_x^\infty \frac{\cos x}{x}dx; && (5.20) \\ \mathrm{Si}(x) &\equiv \int_x^\infty \frac{\sin x}{x}dx. && (5.21) \end{aligned}$$

In all calculations throughout, to calculate $u(k, M)$ we use the parametric concentration relations of [61], which are described in further detail in Appendix B.

5.2 The halo power spectrum and the matter power spectrum

Within the halo model, power spectra split into large scale 2-halo power spectra—describing inter-halo correlations (ie, between two different halos)—and small scale 1-halo power spectra—describing intra-halo correlations (ie, within a single halo).

The 2-halo power spectra are computed from the underlying linear dark matter power spectrum $P_{\mathrm{lin}}(k)$—ie, the power spectrum of the continuous underlying dark matter field, computed with linear perturbation theory. From Equation (5.12) we see the power spectrum between two halos of masses M_1 and M_2 is

$$P_{hh}(M_1, M_2, z_1, z_2) = b(M_1, z_1)b(M_2, z_2)P_{\text{lin}}(k, z_1, z_2). \tag{5.22}$$

Extending this to halos of all masses—the halo power spectrum—gives

$$P_{hh}(k, z) = \left(\int dM \frac{dN}{dM}(M, z)b(M, z)\right)^2 P_{\text{lin}}(k, z) \tag{5.23}$$

5.2.1 Matter power spectrum

To calculate the mass power spectrum we weight the halos by mass and also include the radial density profile of the halo:

$$P^{2h}_{mm}(k) = \left(\int dM \frac{dN}{dM} b(M) \frac{M}{\bar{\rho}_m} u(k, M)\right)^2 P_{\text{lin}}(k) \tag{5.24}$$

(where the z-dependence has been suppressed). The 1-halo term is

$$P^{1h}_{mm}(k) = \int dM \frac{dN}{dM} \left(\frac{M}{\bar{\rho}_m} u(k, M)\right)^2 . \tag{5.25}$$

The matter power spectrum computed with the halo model is shown in Figure 5.1. The linear and non-linear matter spectra computed with CAMB are shown on the same plot for comparison.

5.3 Galaxies and the halo occupation distribution

5.3.1 Galaxy properties from halo properties

In order to describe observables related to galaxies, such as the galaxy power spectrum, using the halo model, we need to connect the properties of galaxies to the properties of the halos they form in. Within the halo model, we assume that galaxies form in halos, with one galaxy per parent halo. Galaxy formation is a complicated and highly non-linear process, the understanding of which is currently an area of active study. However, a general conclusion is that many galaxy properties (such as galaxy luminosity) depend on the stellar

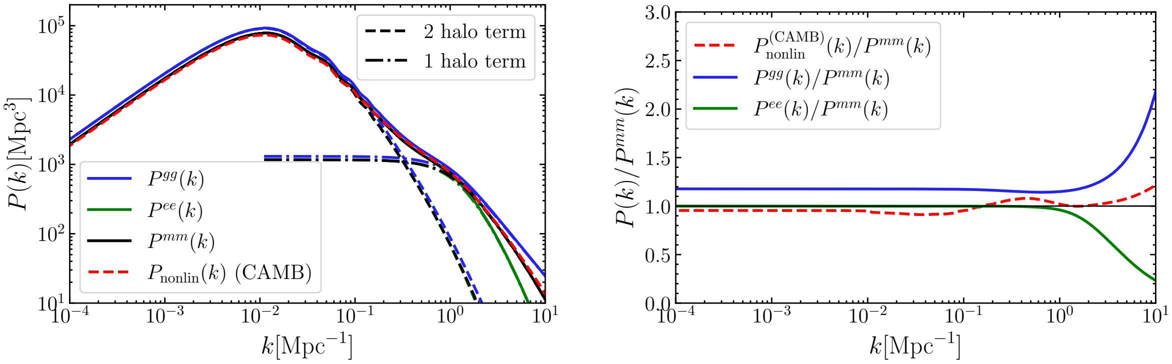

Figure 5.1: Matter, galaxy, and electron power spectra (at $z = 0$) from the halo model. The 1-halo and 2-halo terms are shown separately (although note that the 1-halo power spectra have been artificially set to zero on scales larger than $k = 10^{-2}\,\mathrm{Mpc}^{-1}$). On large scales $P^{gg}(k)$ is a scale-dependent multiple of the $P^{mm}(k)$, ie $P^{gg} = b_g^2 P^{mm}(k)$, although this fails on small scales. The nonlinear matter power spectrum computed with HMCode in CAMB is also shown in dashed red for comparison with the matter power spectrum, although it is hard to distinguish as they agree to ∼percent levels. Note that on small scales, the electrons are suppressed with respect to the matter power spectrum.

mass of the galaxy M_*. These galaxy masses are correlated with the host halo mass M. Thus we can relate galaxy properties to the host halo mass, although note that there is some scatter in any $M - M_*$ relation due to their imperfect correlation, in particular because M_* will depend on the history of the galaxy formation such as any mergers it has undergone, its angular momentum, and baryonic processes such as feedback.

The mass of a host halo is a few orders of magnitude greater than the stellar mass of its galaxy. For instance, a typical halo mass today is around $M \sim 10^{13} M_\odot$, where $M_\odot$ is the stellar mass of our Sun; a typical galactic mass corresponding to this would be $M_* \sim 10^{11} M_\odot$. Also, as halos are formed mostly of dark matter, they can be modelled and studied with N-body simulations; galaxies are more complicated.

Abundance Matching

Stellar mass can be related to halo mass via *abundance matching*, whereby it is assumed that the $M_* - M$ relation is monotonic, and a halo mass function that describes the number density of halos of mass M is related to a galactic stellar mass function, which describes the number density of galaxies of mass M_*. With the assumption that each halo (above a certain minimum threshold mass) hosts exactly one galaxy, the *total* number density of galaxies and halos should be equal, and $M_* - M$ relation can be constructed from the galactic mass function and the halo mass function. In particular, we can write

$$\int_0^M dM' \frac{dN}{dM}(M') = \int_0^{M_*} \Phi(M'_*) dM'_* \tag{5.26}$$

where$\frac{dN}{dM}$ is the halo mass function and $\Phi(M_*)$ is the galactic stellar mass function. The left hand side of Equation (5.26) defines a function $\Phi_h(M)$ and the right hand side $\Phi_*(M_*)$; the $M_* - M$ relation is

$$M(M_*) = \Phi_h^{-1}(\Phi_*(M_*)) \tag{5.27}$$

$$M_*(M) = \Phi_*^{-1}(\Phi_h(M)). \tag{5.28}$$

The real $M_* - M$ relation is expected to not be truly monotonic, due to the imperfect correlation between M_* and M; this can be accounted for by including a scatter in the abundance matching (for more details see the discussion of scatter in [62]).

Knowledge of both the halo mass function and the galactic stellar mass function is required for abundance matching. Halo mass functions can be measured from N-body simulations, while galactic stellar mass functions must be measured by directly taking measurements; a scatter can be included in the abundance-matching process. In particular, [62] gives an $M_* - M$ relation that relates the halo mass function of [58] to measured galactic stellar mass functions. This is the relation that we use throughout when we calculate $M_*(M)$.

Subhalos and satellite galaxies

In N-body simulations, large halos are found to contain smaller bound density peaks within their virial radii. These are referred to as subhalos, and galaxies that form within them are referred to as *satellite* galaxies of the larger parent halo (the galaxy that forms at the centre of the parent halo is referred to by contrast as a "central galaxy"). The subhalos formed separately and are accreted onto the larger halos, and the properties of the satellite galaxies are found to correlate with the mass of the subhalo at the time of accretion (the total mass of the subhalo is found to decrease after accretion due to tidal effects, which are not expected to affect the stellar mass of the satellite galaxy M_*), and so they are labeled by this M.

Thus the total number of galaxies within a halo of mass M is

$$N^{\rm gal}(M,z) = N^{\rm cen}(M,z) + N^{\rm sat}(M,z), \tag{5.29}$$

where the number of central galaxies $N^{\rm cen}$ is either 0 or 1 and $N^{\rm sat}$ depends on the number of subhalos that host galaxies.

5.3.2 The halo occupation distribution

The specific relations $N^{\rm cen}(M,z)$ and $N^{\rm sat}(M,z)$ is known as the halo occupation distribution (HOD) [63]. In general, it is expected that there is some threshold stellar mass $M_*^{\rm thresh}$ below which galaxies cannot form. If this were true, we could write

$$N^{\rm cen}(M) = \Theta(M_* - M_*^{\rm thresh}) \tag{5.30}$$

where $\Theta(x)$ is the Heavisde step function and here (and in all equations to follow) by M_* we mean $M_*(M)$. To allow for a smooth transition between 0 and 1 galaxies, and for realistic effects, scatter can be included, and we can write the mean number of central galaxies in a galaxy of mass M as [64]

$$\bar{N}^{\rm cen}(M) = \frac{1}{2} - \frac{1}{2}{\rm erf}\left(\frac{\log_{10} M_*^{\rm thresh} - \log_{10} M_*(M)}{\sqrt{2}\sigma_{\log M_*}}\right) \tag{5.31}$$

where ${\rm erf}(x)$ is the error function, ie the Gaussian integral from 0 to x, and the parameter $\sigma_{\log M_*}$ describes the scatter around the threshold stellar mass; $\sigma_{\log M_*} = 0$ corresponds to $\bar{N}_c(M) = 1$ for $M_*(M) > M_*^{\rm thresh}$ and $\bar{N}_c(M) = 0$ for $M_*(M) < M_*^{\rm thresh}$. Note that, for *power-law* stellar mass functions, Equation (5.31) can be simplified to be of the form

$$\bar{N}^{\rm cen}(M) = \frac{1}{2} - \frac{1}{2}{\rm erf}\left(\frac{\log_{10} M_{\rm min} - \log_{10} M}{\sqrt{2}\tilde{\sigma}_{\log M}}\right) \tag{5.32}$$

where $M_{\rm min}$ is the halo mass corresponding to a stellar mass of $M_*^{\rm thresh}$ and $\tilde{\sigma}_{\log M}$ is the scatter in halo mass as opposed to in stellar mass.

$N^{\rm sat}(M)$ depends on the number of subhalos hosted by a parent halo that are large enough to host a satellite galaxy. [64] gives the following functional form for $\bar{N}^{\rm sat}(M)$:

$$\bar{N}^{\rm sat}(M) = \bar{N}^{\rm cen}(M)\left(\frac{M}{M_{\rm sat}}\right)^{\alpha_{\rm sat}} e^{-M_{\rm cut}/M}, \tag{5.33}$$

where $M_{\rm sat}$, $\alpha_{\rm sat}$, and $M_{\rm cut}$ are parameters that depend on $M_*^{\rm thresh}$. Note that is an expression for the total number of satellite galaxies, and any information about their masses is lost; if we want to know the mass distribution of these galaxies, the subhalo mass function $\frac{dN}{dM_S}$ is a useful quantity, where

$$N_S(M) = \int \frac{dN}{dM_S}(M, M_S) dM_S \tag{5.34}$$

is the number of subhalos hosted by a halo of mass M. [65] fits a parametric form to $\frac{dN}{dM_S}$ and finds that for a host halo of mass M

$$\frac{dN}{dM_S}(M_S, M) = 0.3 \left(\frac{M_S}{M}\right)^{-0.7} \exp\left(-9.9\left(\frac{M_S}{M}\right)^{2.5}\right). \tag{5.35}$$

The threshold mass M_*

Galaxy surveys do not detect every single galaxy, but instead all galaxies above a certain luminosity. This is a z-dependent quantity, as distant galaxies must be more luminous to be detected. This can be incorporated into the HOD to find the galaxy distribution detected by a given survey, by adjusting the threshold mass M_* (with the assumption that the most luminous galaxies are also the most massive, such that a threshold luminosity corresponds to a threshold mass).

$M_*^{\rm thresh}$ can be chosen to match a given galaxy survey with knowledge of the expected redshift distribution $\frac{dN}{dz}$ of the survey. For example, for the LSST gold sample [54] we expect [66]

$$\frac{dN}{dz} = n_s z^{1.24} \exp\left(-\left(\frac{z}{0.5}\right)^{1.01}\right) \tag{5.36}$$

where $n_s = 26\,\text{arcmin}^{-2}$. This can be related to the total number density $\bar{n}_g(z)$ through

$$4\pi \frac{dN}{dz} = \chi^2 \frac{d\chi}{dz} \bar{n}_{\rm g}; \tag{5.37}$$

choosing the z-dependent $M_*^{\rm thresh}$ so that Equation (5.37) is satisfied specifies $M_*^{\rm thresh}$ for the LSST survey.

5.3.3 Galaxy power spectra

For a galaxy survey the galaxy clustering power spectra are

$$P_{gg}^{2h} = \left(\int dM \frac{dN}{dM} b(M) \frac{\bar{N}^{\rm cen}(M) + \bar{N}^{\rm sat}(M) u(k,M)}{\bar{n}_g(z)} \right)^2 P_{\rm lin}(k) \tag{5.38}$$

$$P_{gg}^{1h} = \left(\int dM \frac{dN}{dM} \frac{2\left\langle N^{\rm cen}(M) N^{\rm sat}(M) \right\rangle u(k,M) + \left\langle N^{\rm sat}(M)(N^{\rm sat}(M)-1) \right\rangle u(k,M)^2}{\bar{n}_g(z)^2} \right) \tag{5.39}$$

where

$$\bar{n}_{\rm gal} = \int dM \frac{dN}{dM} \left(N^{\rm cen}(M) + N^{\rm sat}(M) \right) \tag{5.40}$$

is the mean number density of galaxies at z. The angular brackets indicate the expectations of the quantities inside them; we take [55]

$$\left\langle N^{\rm cen}(M) N^{\rm sat}(M) \right\rangle = \bar{N}^{\rm cen}(M) \bar{N}^{\rm sat}(M); \tag{5.41}$$

$$\left\langle N^{\rm sat}(M)(N^{\rm sat}(M)-1) \right\rangle = \bar{N}^{\rm sat}(M)^2. \tag{5.42}$$

Note that there is no term $\propto \bar{N}^{\rm cen}(M)^2$ in the 1-halo term Equation (5.39). However, this term *is* present in measured power—it is the "Poissonian" term sourced by self-pairs of galaxies, and is constant (ie, independent of k). It can also be referred to as the "shot noise" of the power spectrum, and decreases with higher number density of galaxies $\bar{n}_g$.

The galaxy power spectrum at $z = 0$ expected from LSST is shown in Figure 5.1, along with the ratio P^{gg}/P^{mm}, where we see that on large scales the galaxy power spectrum is a constant multiple of the matter power spectrum, with this bias becoming scale-dependent on small scales.

5.4 The cosmic infrared background

Small particles of dust in star-forming galaxies absorb light and emit thermally in the infrared. We detect this emission as a diffuse background in the infrared, and refer to it as the cosmic infrared background (CIB). Anisotropies in the CIB trace the anisotropies of the dusty star-forming galaxies, which are found at all redshifts since reionization, although the emissivity peaks at $z \sim 2$, when the star formation rate density of the universe was highest. To model the CIB correlations within the halo model, we use the prescription of [67] wherein halos are assigned infrared luminosities in a mass-dependent way.

The CIB intensity density at frequency ν is given by [68]

$$I_\nu(\hat{\boldsymbol{n}}) = \int d\chi a(\chi) j_\nu(\chi, \hat{\boldsymbol{n}}) \tag{5.43}$$

where $j_\nu(\chi, \hat{\boldsymbol{n}})$ is the emissivity density at $(\chi, \hat{\boldsymbol{n}})$. in general it is given by

$$j_\nu(\chi, \hat{\boldsymbol{n}}) = \bar{j}_\nu(\chi)\left(1 + \delta j_\nu(\chi, \hat{\boldsymbol{n}})\right) \tag{5.44}$$

where $\bar{j}_\nu(\chi)$ is the mean emissivity density at χ and δj_ν are the fluctuations. The mean can be calculated by assigning a mass-dependent luminosity density $L_\nu(M, z)$ to all halos and integrating over halo mass:

$$\bar{j}_\nu(z) = \int dM \frac{dN}{dM} \frac{L_{(1+z)\nu}(M, z)}{4\pi}. \tag{5.45}$$

Note that emission we detect at frequency ν is redshifted from its frequency at emission $(1 + z)\nu$.

Assigning luminosity density to halos

By using $L_\nu^{\text{gal}}(M_*, z)$ to denote the luminosity of a galaxy with stellar mass M_*, we can write explicitly

$$L_\nu^{\text{cen/sat}}(M, z) = \int dM_* \frac{dN^{\text{cen/sat}}}{dM_*}(M, M_*) L_\nu^{\text{gal}}(M_*, z) \tag{5.46}$$

where $\frac{dN^{\text{cen/sat}}(M,M_*)}{dM_*} dM_*$ is the number of central or satellite galaxies of stellar mass between M_* and $M_* + dM_*$ hosted by a halo of mass M (an assumption has been made in Equation (5.46) that satellite galaxies and central galaxies obey the same stellar mass-luminosity density relation $L_\nu^{\text{gal}}(M_*, z)$).

The central luminosity has a simple expression: galaxies only host one or zero central galaxies, of stellar mass M_*, and so

$$L_\nu^{\text{cen}}(M, z) = N^{\text{cen}}(M) L_\nu^{\text{gal}}(M_*, z) \tag{5.47}$$

where N^{cen} is given by Equation (5.31).

To calculate the satellite luminosity, it is helpful to assign the satellite galaxies to subhalos of mass M_S, which have accreted onto the host halo. These satellite galaxies host centrals whose galaxies properties correlate to M_S in the same way that the central galaxies correlate to M. In that case we can write

$$L_\nu^{\rm sat}(M,z) = \int dM_S \frac{dN}{dM_S} N^{\rm cen}(M_S) L_\nu^{\rm gal}(M_*,z) \tag{5.48}$$

where M_* is $f_{SHMR}(M_S)$ and $\frac{dN}{dM_S}$ is the subhalo mass function.

5.4.1 A parametric model for $L_\nu(M,z)$

A host of models for $L_\nu^{\rm gal}(M_*,z)$ exist in the literature. A prescription introduced in [67] that assigns luminosity to halos based on halo mass separates the dependence on M, z, and ν, according to

$$L^{\rm gal}_{(1+z)\nu}(M,z) = L_0 \Phi(z) \Sigma(M) \Theta((1+z)\nu) \tag{5.49}$$

where $\Phi(z)$ and $\Sigma(M)$ are parametric functions that control the z- and M-dependence of $L_\nu(M,z)$ respectively; $\Theta((1+z)\nu)$ is the spectral energy distribution (SED) which is usually given by a modified black body spectrum which may be tempered by a power-law tail at high frequency; and L_0 is an overall normalization factor. This model is useful as it bypasses the need for modelling $M_*(M)$ by assigning luminosity based on host halo mass as opposed to stellar mass. This model has been fit to the power spectrum of the observed CIB both by the *Planck* satellite and by the *Herschel* satellite. We discuss the parametric forms of the functions in Equation (5.49) below.

Redshift evolution: $\Phi(z)$

$\Phi(z)$ controls the redshift dependence of the normalization of the $L-M$ relation and should be increasing with redshift, motivated by observations that the star formation rate was increases with redshift. It is parametrized as

$$\Phi(z) = (1+z)^\delta. \tag{5.50}$$

In the fit to *Planck* CIB power spectra, $\delta = 3.6$ was found [69].

Various implementations [67, 70] of this parametric model also consider another parameter z_p at which the $L-M$ relation plateaus; in such a case

$$\Phi(z) = \begin{cases} (1+z)^\delta & z < z_p \\ (1+z_p)^\delta & z \geq z_p \end{cases}. \tag{5.51}$$

This break is motivated by observational evidence of such a plateau in the $L-M$ relation, at $z \sim 2$.

Mass dependence: $\Sigma(M)$

$\Sigma(M)$ controls the dependence of luminosity on halo mass. Motivated by observations that star formation is suppressed at low and high masses, and taking the simplifying assumption that L/M takes a log-normal form, $\Sigma(M)$ is given by

$$\Sigma(M) = \frac{M}{\sqrt{2\pi\sigma^2_{L/M}}} e^{-(\log_{10} M - \log_{10} M_{\rm eff})^2/2\sigma^2_{L/M}}. \tag{5.52}$$

$\Sigma(M)$ is specified by two parameters: $M_{\rm eff}$, the peak of the specific IR emissivity (L/M); and $\sigma^2_{L/M}$, which controls the range of halo masses that produce the emissivity. [69] found that $M_{\rm eff} = 10^{12.6} M_\odot$ and $\sigma^2_{L/M} = 0.5$.

IR SEDs: $\Theta(\nu, z)$

Finally, the SED Θ is a modified black body, which may be tempered by a power-law tail at high frequencies

$$\Theta \propto \begin{cases} \nu^\beta B_\nu(T_d(z)) & \nu < \nu_0 \\ \nu^{-\gamma} & \nu \geq \nu_0, \end{cases} \tag{5.53}$$

where $B_\nu(T)$ is the Planck function at temperature T and $T_d(z)$ is the dust temperature at redshift z, parametrized as

$$T_d = T_0 \left(1+z\right)^\alpha. \tag{5.54}$$

The power-law tail accounts for the gray-body emission from dust at higher temperatures than T_d [71, 72]. In (5.53), ν_0 is the (z-dependent) frequency satisfying the continuous derivative relation

$$\left.\frac{d\ln\Theta(\nu,z)}{d\ln\nu}\right|_{\nu=\nu_0} = -\gamma \tag{5.55}$$

[69], which used the normalization condition

$$\Theta = \begin{cases} \left(\frac{\nu}{\nu_0}\right)^\beta \frac{B_\nu(T_d(z))}{B_{\nu_0}(T_d(z))} & \nu < \nu_0 \\ \left(\frac{\nu}{\nu_0}\right)^{-\gamma} & \nu \geq \nu_0, \end{cases} \tag{5.56}$$

found $\beta = 1.75$, $\gamma = 1.7$, $T_0 = 24.4\,\mathrm{K}$ and $\alpha = 0.36$.

Thus there are four parameters that control the SED: the gray-body emissivity factor β, the high-frequency power-law exponent γ, the dust temperature today T_0, and α, which controls the redshift evolution of the temperature.

5.4.2 Other models for $L_\nu(M, z)$

Other models take advantage of the relationship between star formation rate (SFR) and luminosity. The Kennicutt relation states that [73]

$$SFR = K L_{IR} \tag{5.57}$$

where L_{IR} is the total infrared luminosity (integrated over all wavelengths, ie $L_{IR} = \int d\nu L_\nu$). Some models parametrize SFR instead of L_ν; additionally, the model of [74] is notable in that it requires no parametrization and fitting to any CIB data and instead uses externally measured SFR models to model the CIB power spectra, with good agreement to the *Planck* CIB power spectra found.

5.4.3 The CIB power spectrum

The angular power spectrum of the CIB is given, from Equation (5.43), as a Limber integral over the emmissivity power spectrum

$$C_\ell^{\nu\nu'} = \int d\chi \frac{a^2(\chi)}{\chi^2} \bar{j}_\nu(\chi)^2 P_{jj}^{\nu\nu'}\left(k = \frac{\ell + 1/2}{\chi}, z(\chi)\right) \tag{5.58}$$

where $P_{jj}^{\nu\nu'}(k, z)$ is the power spectrum of fluctuations δj; this we can model with the halo model in a similar way to how we wrote the galaxy power spectrum, by comparing the expression (5.45) for emissivity density to the expression (5.40) for galaxy number density. In particular, by defining a CIB luminosity profile according to

$$u_{j_\nu}(M, z) = \frac{L_\nu^{\mathrm{cen}}(M) + L_\nu^{\mathrm{sat}}(M) u(k, M)}{4\pi \bar{j}_\nu(z)} \tag{5.59}$$

we can write

$$P_{jj}^{2h}(k, z) = D_\nu(z) D_{\nu'}(z) P_{\mathrm{lin}}(k); \tag{5.60}$$

$$P_{gg}^{1h}(k, z) = \left(\int dM \frac{dN}{dM} u_{j_\nu}(M, z) u_{j_{\nu'}}(M, z)\right) \tag{5.61}$$

where

$$D_\nu(z) = \left(\int dM \frac{dN}{dM} b(M) u_{j_\nu}(M,z) \right) \tag{5.62}$$

and where the $L^{\rm cen} - L^{\rm cen}$ term in Equation (5.61) contributes to shot noise as opposed to a clustering term.

The CIB power spectra computed within the halo model using the models of [74] (see Section 5.4.2) and [69] (see Section 5.4.1) are shown in Figure 5.2. The power spectra calculated directly from the CIB maps from [75] are also shown for comparison; in this work the high frequency *Planck* data was used to make maps of the CIB on large ($\sim 25\%$) of the sky.

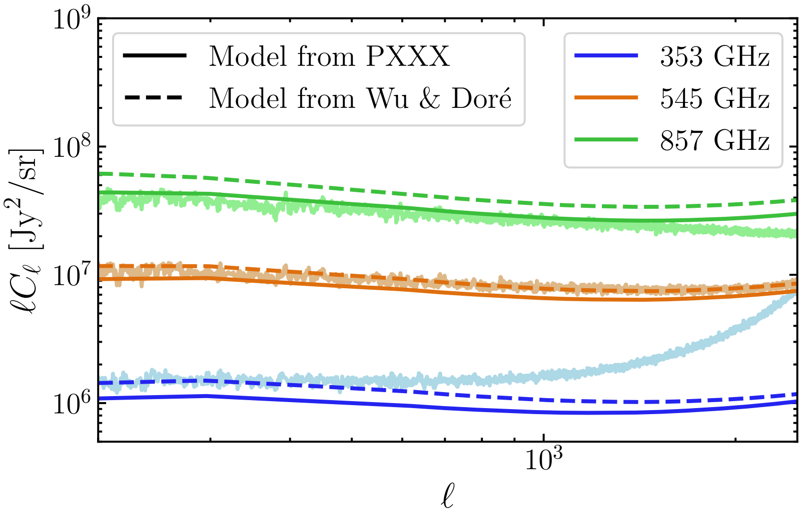

Figure 5.2: The CIB power spectrum at 353, 545, and 857 GHz, with the model from [69] (PXXX) in solid lines and from [74] (Wu & Doré) in dashed lines. The power spectra measured directly from the CIB maps in [75] are shown in paler colours, although note that the instrumental noise dominates over the signal on the smallest scales, especially at 353 GHz.

5.5 Electron distributions

We can model the tSZ and kSZ effects within the halo model by assigning radially-dependent electron density profiles to a halo.

5.5.1 The electron distribution for kSZ

The power spectrum of the kSZ effect is given in Equation (4.93). From Equation (4.94), it is clear that one needs to model the non-linear electron power spectrum to calculate the kSZ power; in addition, this is necessary for kSZ cross-correlations such as those to be discussed in Chapter 8.

A radially-dependent electron gas profile $\rho_{\rm gas}(k, M, z)$ can be assigned to halos in a mass dependent way; in particular, parametric fits to various different models are given in [76]. When we calculate the electron power spectrum throughout, we use the "AGN" profiles of this reference. The electron power spectrum is given by expressions similar to the matter power spectrum, Equations (5.24) and (5.25), but with $u(k, M)$ modified to account for the different distribution of electrons; in particular

$$P^{2h}_{ee}(k) = \left(\int dM \frac{dN}{dM} b(M) \frac{M}{\bar{\rho}_m} u_{\rm gas}(k, M)\right)^2 P_{\rm lin}(k) \tag{5.63}$$

(where the z-dependence has been suppressed). The 1-halo term is

$$P^{1h}_{ee}(k) = \int dM \frac{dN}{dM} \left(\frac{M}{\bar{\rho}_m} u_{\rm gas}(k, M)\right)^2 . \tag{5.64}$$

where $u_{\rm gas}(k, M, z)$ is the Fourier transform of $\rho_{\rm gas}(k, M, z)$.

The electron power spectrum at $z = 0$ is plotted in Figure 5.1 and compared to the matter power spectrum. On large scales, the electrons trace the matter, but on small scales baryonic effects become relevant and the electrons are suppressed relative to the DM.

5.5.2 The tSZ effect

The tSZ effect is sourced by electrons with high temperature and requires different profiles to those used in the kSZ effect, which is not affected by electron temperature.

The Compton y-parameter was given in Section 4.5.1 as

$$y(\hat{\boldsymbol{n}}) = \int a(\chi)\, d\chi\, y_{3D}(\chi, \hat{\boldsymbol{n}}) \tag{5.65}$$

where the three-dimensional Compton-y field a rescaling electron pressure field given by $y_{3D} \equiv \frac{\sigma_T}{m_e c^2} P_e(\chi, \hat{\boldsymbol{n}})$. The angular power spectrum of $y(\hat{\boldsymbol{n}})$ can then be computed via a

Limber integral (see Appendix A.2) [77, 78]

$$C_\ell^{yy} = \int \frac{a^2 d\chi}{\chi^2} P_{yy}\left(k = \frac{\ell + 1/2}{\chi}, z(\chi)\right) \tag{5.66}$$

where $P_{yy}(k,z)$ is the three-dimensional power spectrum of y_{3D}.

$P_{yy}(k,z)$ can be computed within the halo model by assigning to each halo a radially dependent pressure profile $P_e(r)$ and Fourier transforming this; in particular

$$P_{yy}^{2h}(k,z) = \left(\int dM \frac{dN}{dM} b(M) u_y(k,M,z)\right)^2 P_{\text{lin}}(k,z) \tag{5.67}$$

$$P_{yy}^{1h}(k,z) = \int dM \frac{dN}{dM} u_y(k,M,z)^2 \tag{5.68}$$

where

$$u_y = \int d^3\vec{\boldsymbol{r}} e^{-i\vec{\boldsymbol{k}}\cdot\vec{\boldsymbol{r}}} y(\vec{\boldsymbol{r}}, M) = \int dr 4\pi r^2 \frac{\sin{(kr)}}{kr} y(r,M) \tag{5.69}$$

where in the last line we assumed spherical symmetry of $y(\vec{\boldsymbol{r}})$.

The tSZ power spectrum, computed using the parametric pressure profiles of [79], is shown in Figure 5.3. The tSZ is dominated by high mass halos at low redshift, and as such its power spectrum is predominantly a 1-halo signal except for at the very largest scales. Note that to get the tSZ power spectrum from C_ℓ^{yy} one must multiply by the spectral function of the tSZ given by Equation (4.88).

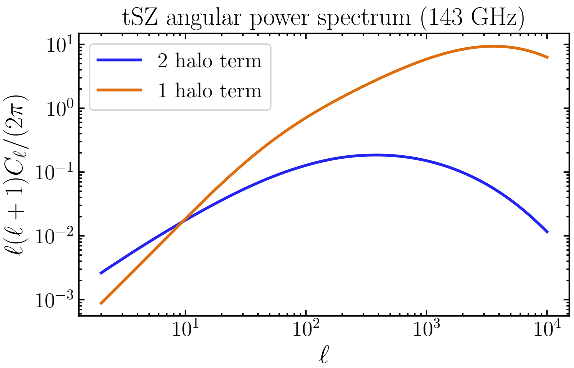

Figure 5.3: The tSZ power spectrum, computed with the parametric pressure profiles of [79]

5.6 Cross power spectra

The power spectra we have discussed in the above sections are of the form

$$P^{2h}_{XX}(k,z) = D_X(k,z)D_X(k,z)P_{\rm lin}(k,z) \tag{5.70}$$

spectrum and $D_X(k,z)$ is

$$D_X(k,z) = \int dM \frac{dN}{dM} b_h(M,z) u_X(M,k,z). \tag{5.71}$$

$u_X(M,k,z)$ is specific to the observable X and describes the (Fourier-transformed) radial profile of X within the halo. The 1-halo power spectra are given by

$$P^{1h}_{XX} = \int dM \frac{dN}{dM} u_X(M,k,z)^2, \tag{5.72}$$

where for the correlation of two discrete sources the k-independent term can be moved into a separate shot-noise term as it does not provide information about clustering. We can write the cross power as

$$P^{2h}_{XY}(k,z) = D_X(k,z)D_Y(k,z)P_{\rm lin}(k,z) \tag{5.73}$$

and

$$P^{1h}_{XX} = \int dM \frac{dN}{dM} u_X(M,k,z) u_Y(M,k,z). \tag{5.74}$$

The profiles for the different observables are

$$u_m(M,k,z) = \left(\frac{M}{\rho_m}\right) u(k,M,z) \tag{5.75}$$

$$u_g(M,k,z) = \frac{N^{\rm cen}(M,z) + N^{\rm sat}(M,z)u(k,m,z)}{\bar{n}_g(z)} \tag{5.76}$$

$$u_e(M,k,z) = \left(\frac{M}{\rho_m}\right) u_{\rm gas}(k,M,z) \tag{5.77}$$

$$u_{j_\nu}(M,k,z) = \frac{L^{\rm cen}_\nu(M) + L^{\rm sat}_\nu(M)u(k,M)}{4\pi\bar{j}_\nu(z)}. \tag{5.78}$$

Chapter 6

Likelihoods and the Fisher formalism

Many cosmological experiments take measurements of observables—such as the CMB or the matter power spectrum—not just out of interest in mapping these quantities but with the hope of using them to say something about the underlying physical theory, such as the value of a set of parameters or to compare different models. This has led to many developments in the statistics of these observational experiments, in particular with regards to Bayesian statistics whereby we take data and construct a probability distribution for the parameters of a theory. The value of the parameter can be expected to be somewhere where the probability distribution is peaked, and the width of the distribution gives an idea of the "error" on the parameter.

This Chapter is organized as follows. In Section 6.1 we introduce the commonly-used likelihood function, which gives the probability for measuring certain data given an underlying cosmological theory and we discuss Bayes' theorem whereby the likelihood function can be converted into a probability distribution for the parameters of a theory given the measurement of certain data. In Section 6.2 we introduce the Fisher formalism whereby the errors on parameters can be predicted by understanding the curvature space of a theory, without taking any data, and we discuss explicitly of the calculations of the mode and bandpower Fisher matrices in Section 6.3. Finally in Section 6.4 we discuss the noise power spectrum for intensity experiments.

6.1 Bayes' theorem and the likelihood function

The likelihood $\mathcal{L}(d|\Pi)$ is the probability of measuring a set of data d given an underlying theory described by the parameters Π:

$$P(d|\Pi) = \mathcal{L}(d|\Pi). \tag{6.1}$$

Bayes' theorem states that the probability of two events A and B occuring, $P(A \cap B)$, is given by the probability that B occurs times the probability that A occurs given B has occurred (denoted $P(A|B)$), and vice versa:

$$P(A|B)P(B) = P(B|A)P(A). \tag{6.2}$$

Given a likelihood for data given a theory, we can construct the probability of a theory given some data using Equation (6.2):

$$P(\Pi|d) = \frac{P(d|\Pi)P(\Pi)}{P(d)}. \tag{6.3}$$

The denominator is not important as it does not depend on Π, and indeed we can write

$$P(\Pi|d) \propto \mathcal{L} \tag{6.4}$$

in the case where the *prior* probability $P(\Pi)$ is uniform; note that this might not be the case though, and in general the prior is relevant. In particular, one can put external knowledge about the theory there.

If a likelihood can be constructed that will be a function of some parameters Π and d, one can measure d and find the values of Π that maximize $\mathcal{L}(d|\Pi)P(\Pi)$; these represent the peak of the probability distribution $P(\Pi|d)$.

The simplest form of a likelihood is Gaussian. Consider a theory that predicts data points $\bar{d}$, and some measurements $\hat{d}$; we would like the likelihood to be maximized around $\bar{d} = \hat{d}$ and so we write

$$\mathcal{L} = \frac{1}{\sqrt{2\pi|C|}} \exp\left(-\frac{1}{2}\left(\hat{d} - \bar{d}\right) \cdot C^{-1} \cdot \left(\hat{d} - \bar{d}\right)\right) \tag{6.5}$$

where C is the covariance of the data points, which encodes (for example) the errors of the measurements. $|C|$ is the determinant of C; it appears in the prefactor of $\mathcal{L}$ to ensure that the integral over Π is 1, as required by probability theory.

6.2 Fisher matrix

The likelihood function (6.5) can only be maximized with knowledge of the data $\hat{d}$. However, when fitting parameters, the values of Π that maximize $\mathcal{L}$ is not the only quantity of interest: one also wants to know the *errors* on Π, ie the size of the region $\Pi \pm \sigma$ in which one can move about in parameter space and have confidence that the values still represent the "true" underlying values of Π.

For Gaussian likelihoods, this region σ turns out to be calculable *without the data*, as it is dependent only on the size of the curvature of the likelihood in parameter space. More intuitively—we want to maximize the likelihood, or equivalently minimize the χ^2 (pronounced "chi-squared") where χ^2 is the related to the term in the exponent of Equation (6.5) according to

$$\mathcal{L} = \frac{1}{\sqrt{2\pi C}} \exp\left(-\frac{1}{2}\chi^2\right) \tag{6.6}$$

If the minimum is very sharp (ie spans a small region in parameter space) this will be much easier than if it is shallow (see Figure 6.1). The data can tell us the position of the minimum, but we can learn about the curvature without them.

With this in mind, the error on the parameter Π^i can be calculated *in advance of taking any data* by computing the curvature of the likelihood. Allowing for a multidimensional parameter space, this is given by the inverse of the Fisher matrix, which is defined by

$$F_{ij} = \frac{1}{2} \operatorname{Tr}\left[\frac{\partial C}{\partial \Pi^i} C^{-1} \frac{\partial C}{\partial \Pi^j} C^{-1}\right] \tag{6.7}$$

where the covariance matrix C includes both signal and noise; although note that the noise is usually independent of the model parameters Π such that the derivatives are only taken of the signal covariance matrix (not the noise). From Equation (6.7), the error on a parameter i is

$$\sigma(\Pi_i) = \sqrt{F^{-1}_{ii}} \tag{6.8}$$

and the covariance between two parameters i and j is

$$\sigma_{ij} = \left(F^{-1}\right)_{ij}. \tag{6.9}$$

Note that this gives a *lower bound* for the error from the true experiment (which may not achieve this lower bound due to, eg, non-Gaussianities in the likelihood function). Also, it is important that in (6.12) the Fisher matrix must be inverted *before* taking the square root of the diagonal, which is not equivalent to taking $\frac{1}{\sqrt{F_{ii}}}$. This is due to degeneracies

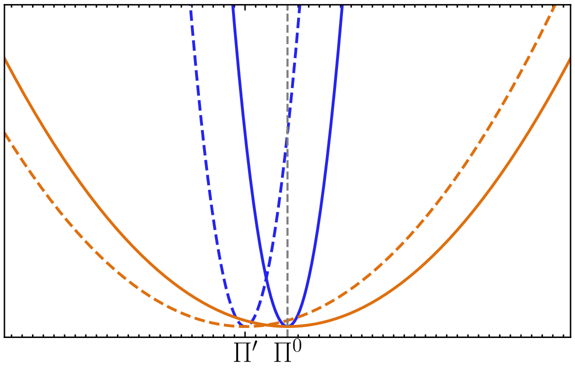

Figure 6.1: χ^2 for a model with high curvature (blue) and small curvature (orange). it is much easier to constrain the blue model; the two minima Π^0 and Π' are clearly distinguishable with little overlap between the two curves. The same cannot be said of the orange model; it is much easier to "move around" in parameter space (the x-axis without changing much the value of the likelihood (in particular the value of $\chi^2(\Pi')$ is much closer to the value of $\chi^2(\Pi^0)$) for the orange model than the blue model. This translates into a larger error on the parameters of the orange model than the blue model, independently of the location of the minimum.

between the parameters, which must be taken into account; this is known as *marginalizing* over the other parameters in Π.

It is useful to be able to calculate the errors in advance of taking data, as one can know what to look for before constructing an experiment, which is useful because experiments are expensive.

6.3 Calculating Fisher matrices

6.3.1 Mode Fisher matrix

Many measurements we take are 2-dimensional spherical maps, such as the CMB temperature $\Delta T(\hat{\boldsymbol{n}})$; or the angular galaxy density $\delta^g(\hat{\boldsymbol{n}})$. When we write these as spherical harmonic expansions, the data one considers can thus be labeled $\{a^i_{\ell m}\}$ (where i runs from 1 to the total number of fields considered N); in this case the covariances are given by the angular power spectra:

$$\left\langle a^i_{\ell_1 m_1} a^j_{\ell_2 m_2} \right\rangle = C^{ij}_{\ell_1} \delta_{\ell_1 \ell_2} \delta_{m_1 m_2} + N^{ij}_{\ell_1 \ell_2 m_1 m_2} \tag{6.10}$$

Conveniently, (assuming $N^{ij}_{\ell_1 \ell_2 m_1 m_2} \propto \delta_{\ell_1 \ell_2} \delta_{m_1 m_2}$), the covariance C is diagonal in this basis, and the Fisher matrix is given by

$$F_{ij} = \sum_\ell \frac{(2\ell+1)}{2} \operatorname{Tr} \left[\frac{\partial C_\ell}{\partial \Pi^i} C_\ell^{-1} \frac{\partial C_\ell}{\partial \Pi^j} C_\ell^{-1} \right] \tag{6.11}$$

where the factor of $2\ell + 1$ appears due to the the sum over m from $-\ell$ to ℓ. Note that the trace is taken of an $N \times N$ matrix at each l, where N is the number of fields considered.

The expression (6.11) is true for a field that is measured on the whole sky. It is easy to modify for the case of partial sky coverage: we can simply multiply by the sky fraction $f_{\rm sky}$ that we expect to have access to—the assumption being that we only have access to a proportion $f_{\rm sky}$ of the modes, which are independent. This assumption breaks down on the largest scales (scales $\sim$ the area of the survey), where mode coupling effects correlate the different $a_{\ell m}$s and it is no longer true that $\left\langle a^i_{\ell_1 m_1} a^j_{\ell_2 m_2} \right\rangle \propto \delta_{\ell_1 \ell_2} \delta_{m_1 m_2}$.

From the Fisher matrix (6.11) the parameter errors can be calculated:

$$\sigma(\Pi^i) = \sqrt{(F^{-1})_{ii}}. \tag{6.12}$$

6.3.2 Bandpower Fisher matrix

In the mode Fisher formalism, one considers as data the fields $a^i_{\ell m}$. In the bandpower Fisher formalism, one instead measures the fields, calculates their power spectra, and uses these *power spectra* as data. In this case, the $N \times N$ covariance matrices C^{ij}_ℓ between N fields at each l are replaced by $\frac{N(N+1)}{2} \times \frac{N(N+1)}{2}$ covariance matrices

$$\mathbb{C}\left(\hat{C}^{\alpha\beta}_\ell, \hat{C}^{\gamma\delta}_\ell\right) = \frac{1}{(2\ell+1) f_{\rm sky}} \left(C^{\alpha\gamma}_\ell C^{\beta\delta}_\ell + C^{\alpha\delta}_\ell C^{\beta\gamma}_\ell \right) \tag{6.13}$$

where all the C_ℓ on the right hand side include noise; F_{ij} is now given by

$$F_{ij} = \sum_\ell \frac{\partial C^T_\ell}{\partial \Pi^i} \mathbb{C}^{-1}_\ell \frac{\partial C_\ell}{\partial \Pi^j} \tag{6.14}$$

where C^T_ℓ denotes the transpose of C_ℓ. The usefulness of this method is that one can explicity consider only the cross-correlation between two fields without considering their auto-correlation; this is useful when there are some biases we may not understand in the auto power spectra. For example, we measure the power spectrum of the CMB temperature C_ℓ^{TT} and its E-mode polarization C_ℓ^{EE}, with covariance C_ℓ^{TE}. In this case the data vector would be

$$\Delta = \{T_{\ell m}, E_{\ell m}\} \tag{6.15}$$

with covariance matrix

$$C_\ell = \begin{pmatrix} C_\ell^{TT} & C_\ell^{TE} \\ C_\ell^{TE} & C_\ell^{EE} \end{pmatrix}. \tag{6.16}$$

There are some foregrounds to the T field that add power on small scales that are not issues with the E field; we can avoid these by removing small-scale information in T. In the mode formalism this means that we must remove all T information and the data vector becomes just $\{E_{\ell m}\}$ with covariance matrix C_ℓ^{EE}. However, in the bandpower formalism, the data vector is

$$\Delta = \left\{C_\ell^{TT}, C_\ell^{TE}, C_\ell^{EE}\right\} \tag{6.17}$$

with covariance matrix

$$\mathbb{C}_\ell = \begin{pmatrix} \mathbb{C}\left(C_\ell^{TT}, C_\ell^{TT}\right), \mathbb{C}\left(C_\ell^{TT}, C_\ell^{TE}\right), \mathbb{C}\left(C_\ell^{TT}, C_\ell^{EE}\right) \\ \mathbb{C}\left(C_\ell^{TE}, C_\ell^{TT}\right), \mathbb{C}\left(C_\ell^{TE}, C_\ell^{TE}\right), \mathbb{C}\left(C_\ell^{TE}, C_\ell^{EE}\right) \\ \mathbb{C}\left(C_\ell^{EE}, C_\ell^{TT}\right), \mathbb{C}\left(C_\ell^{EE}, C_\ell^{TE}\right), \mathbb{C}\left(C_\ell^{EE}, C_\ell^{EE}\right) \end{pmatrix}. \tag{6.18}$$

The Fisher matrix calculated from (6.14) for (6.18) agrees with the one calculated from (6.11) for (6.16); however now we have the ability to remove C_ℓ^{TT} on small scales while still using some T information through keeping C_ℓ^{TE}, where there are no biases as the foregrounds in T are uncorellated with those in E.

6.4 Instrumental Noise

In general, when we measure a field $a_{\ell m}$ there will be some noise with the measurement: we will not measure precisely the underlying $a_{\ell m}$. Ideally the noise should be uncorrelated with the signal and it should not mimic the signal one is looking for, as it would bias the inferences.

Many signals are measured—for example the CMB or the CIB—by taking an intensity map of the sky. As well as noise, there are beam effects, due to the finite resolution of any experiment. As such, our data is not $a_{\ell m}$ but instead we measure

$$\hat{a}_{\ell m} = B_{\ell m} a_{\ell m} + n_{\ell m} \tag{6.19}$$

where $B_{\ell m}$ is the beam window function and $n_{\ell m}$ is the noise. Thus, assuming that the noise is uncorrelated with the signal, and assuming for simplicity that $B_{\ell m} = B_\ell$ (ie the beam is only a function of ℓ, which is not an unreasonable assumption) the variance is

$$\langle \hat{a}_{\ell m} \hat{a}_{\ell' m'} \rangle = B_\ell^2 C_\ell + \langle n_{\ell m} n_{\ell' m'} \rangle \, . \tag{6.20}$$

For noise that is uncorrelated between pixels, the noise is diagonal and this can be written

$$\langle \hat{a}_{\ell m} \hat{a}_{\ell' m'} \rangle = B_\ell^2 C_\ell + N_\ell . \tag{6.21}$$

For symmetrical Gaussian beams with a full width at half maximum (FWHM) of Θ, B_ℓ is given by

$$B_\ell^2 = \exp\left(\frac{-\ell^2 \Theta^2}{8 \log 2} \right) , \tag{6.22}$$

and so it falls off exponentially at high angular scales. After beam-deconvolving, the signal is

$$\langle \hat{a}_{\ell m} \hat{a}_{\ell' m'} \rangle = C_\ell + \exp\left(\frac{\ell^2 \Theta^2}{8 \log 2} \right) N_\ell , \tag{6.23}$$

and so any noise will swamp the signal on small scales. In particular, beam deconvolved white noise—where N_ℓ is constant—grows exponentially up at high ℓ, and dominates over all underlying signals.

The SO and CMBS4 experiments will improve over *Planck* by having smaller beam sizes as well as lower white noise levels; although they will have higher noise on very large scales as they are ground-based and experience atmospheric effects which *Planck*, being a space-based satellite, did not. The noise levels expected from SO [16] and CMBS4 [80] are shown on Figure 6.2; they have been calculated by combining the noise at different frequencies using an internal linear combination (ILC) (e.g., [81, 82]) and include both instrumental and atmospheric noise as well as contributions from foregrounds such as the and tSZ, kSZ effects and the CIB (full details can be found in [16, 80]). For comparison with the *Planck* experiment, the beam-deconvolved white noise in the 143 GHz *Planck* channel is shown.

The noise expected on the measurement of the $C_\ell^{\kappa\kappa}$ is more complicated to calculate than by a simple procedure such as that in Equation (6.23). We show on the right hand side of Figure 6.2 the noise on the CMB lensing convergence power spectrum expected from the upcoming experiments, along with the noise power spectrum from the *Planck* measurement. Future experiments will bring much better measurement of the $C_\ell^{\kappa\kappa}$, with many modes being measured with signal-to-noise greater than 1.

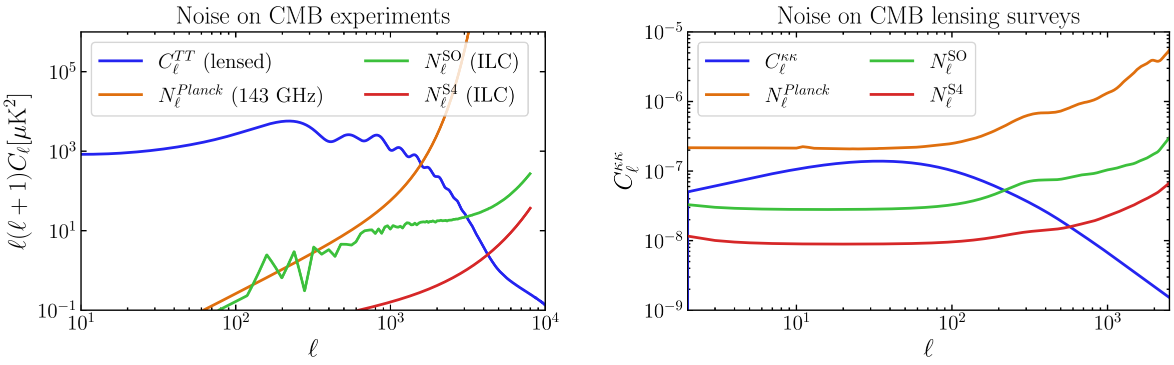

Figure 6.2: *Left*: The CMB signal and the noise expected from the SO and CMBS4 experiments. *Right*: The CMB lensing signal and the nosie expected from the SO and CMBS4 experiments.

Chapter 7

Improving CIB models with CMB lensing maps

7.1 Introduction

Star forming galaxies contain particles of dust that absorb ultraviolet light and emit thermally in the infrared (IR). This IR emission sources the cosmic infrared background (CIB), a diffuse, unresolved background that traces star-forming galaxies. Dust content in galaxies is correlated with the star formation rate, and the CIB emissivity peaks at around redshift $z \sim 2$ where the star formation rate is high. Anisotropies in the CIB trace anisotropies in the star-forming galaxy distribution [68] and give insight into the physics of star formation. The CIB, and the CIB anisotropies, have been detected at numerous wavelengths [83] by IRIS [84], Herschel [70], SPT [72], *Planck* [85, 69] and ACT [86, 87]. Various theoretically motivated parametric models have been fit to the data measuring the CIB (e.g. [74, 88, 69, 70, 89]). Improving these models is not just useful for understanding star formation history itself, but also because the CIB appears as a foreground to the cosmic microwave background (CMB) at lower frequencies.

Gravitational lensing of the CMB offers an unbiased probe of the total matter content of the universe. While the CMB is sourced at very high redshift $z \sim 1100$, it is well known that the CMB we detect has been lensed by intervening matter [90]. The lensing kernel of the CMB peaks at $z \sim 2$, close to where the CIB intensity density peaks (see Figure 7.1), and as the galaxies sourcing the CIB trace the dark matter primarily responsible for CMB lensing, it is expected (and confirmed empirically e.g. [91, 92, 93]) that the CMB lensing potential and the CIB are correlated. This high degree of correlation has been exploited for improving the science return from CMB experiments, e.g., by using the CIB as (or as part of) a template [94] for the lensing signal itself, allowing one to undo the effect of the lensing signal. Delensing the CMB in this way [95, 48] allows us to more clearly reveal underlying cosmological signals of interest, e.g. B-modes from primordial gravitational waves [96] or new relativistic species [48].

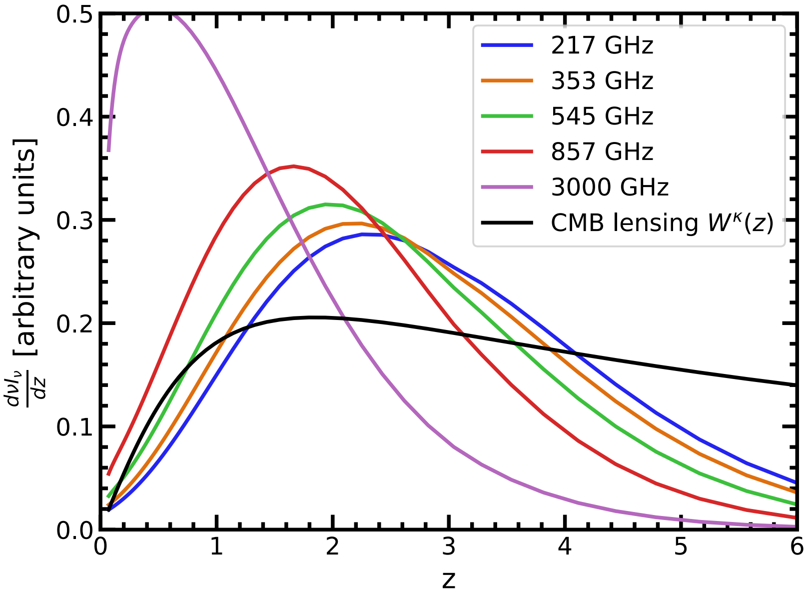

Figure 7.1: *Left:* The redshift distribution of the CMB lensing kernel and the CIB. The redshift distribution of the CIB monopole $\frac{d\nu I_\nu}{dz}$ is shown with all kernels normalized so that $\int_0^6 W(z)dz = 1$; the (similarly normalized) CMB lensing efficiency kernel $W^{\kappa}(z)$ is also shown in black.

In this chapter, we explore the potential for obtaining improved models of the CIB from cross-correlations of the CMB lensing signal with existing measurements of the CIB from *Planck* and future high-resolution measurements from CCAT-prime [97, 98]. Such improvements will enhance our understanding of high-redshift star formation and will relax degeneracies encountered in the damping tail of the CMB temperature power spectrum. As an example of the latter, inferences of the amplitude of the kinetic Sunyaev-Zeldovich effect (e.g. [99]) can be affected by model bias in the CIB contribution.

The CMB lensing potential can be reconstructed from statistical anisotropies in the

CMB [44]: the *Planck* collaboration has reconstructed the lensing potential on about 70% percent of the sky [100] with signal-to-noise per mode close to unity near the peak of the power spectrum, but otherwise generally noise-dominated. High-resolution ground-based CMB experiments like ACT and SPT are now making CMB maps that are significantly signal dominated over a larger range of scales (albeit currently on small fractions of the sky) [93, 101].

Over the next decade however, the CMB lensing potential will be imaged with high fidelity to even higher L than at present over large fractions of the sky [16, 17]. We also expect improvements in CIB measurements in coming years, with experiments such as CCAT-prime [97, 98], and Simons Observatory in its highest frequency channels [16], measuring the small-scale CIB to higher accuracy. The CMB lensing / CIB cross correlation has already been used to fit large-scale (linear) models of the CIB [91, 88, 102]; our work here forecasts the improved parameter constraints on the parametric halo model for the CIB introduced in [67], which was fit to *Planck*+IRIS CIB power spectrum data in [69]. While the CMB lensing potential does not depend on the CIB model parameters, we expect improvements due to the cross-correlation depending on the redshift distribution of the CIB as well as due to sample-variance cancellation (see e.g. [103]), where measuring the CMB lensing potential on the same patch of sky as the CIB intensity can afford improvements in the CIB model due to their high correlation.

CIB models have previously been cross-correlated with CMB lensing maps to infer CIB model parameters [91, 88, 102] and also with other external large-scale-structure probes such as the Sloan Digital Sky Survey (SDSS) galaxies [104]. In this work we quantify the potential improvements of employing such external cross-correlations in particular as we get access to better CMB lensing data.

In all calculations in this Chapter, we use the cosmology of [105]:$\{\Omega_m, \Omega_\Lambda, \Omega_b h^2, 10^9 A_s, h, n_s\} = \{0.3175, 0.6825, 0.022068, 2.2, 0.6711, 0.9624\}$. We explore constraints from subsets of measurements of the CIB made by *Planck* at 217, 353, 545, 857 GHz, IRIS at 3000 GHz [84] and future CCAT-prime measurements [97, 98] at $\{220, 280, 350, 410, 850\}$ GHz , with improvements from CMB lensing measured by *Planck* or future Simons Observatory-like [16] and CMB-S4-like [17] experiments. For all CMB lensing fields, we impose a maximum multipole of $L = 1000$; for *Planck*+IRIS CIB forecasts we use a multipole range of $186 \leq L \leq 2649$, and for CCAT-prime we include $L \leq 10000$. Our baseline forecasts are on 2240 square degrees of sky, with the 3000 GHz IRIS field only included on 183 square degrees, mimicking the analysis of [69]. CMB lensing reconstruction maps are assumed to have full overlap with these 2240 square degrees, but we also explore the possibility of including the CIB / CMB lensing cross-correlations over larger fractions of the sky without including the CIB auto-spectrum (which may have larger systematics due to Galactic dust).

7.2 The CIB-CIB and CIB-CMB lensing power spectra within the halo model

7.2.1 CIB emissivity power spectrum

We model the CIB emission power spectrum with the halo model of Chapter 5.4, where the CIB intensity density was expressed as

$$I_\nu(\hat{\mathbf{n}}) = \int_0^{\chi_{re}} d\chi\, a(\chi) j_\nu\left(\chi, \hat{\mathbf{n}}\right). \tag{7.1}$$

with angular power spectrum

$$C_L^{\nu\nu'} = \int \frac{d\chi}{\chi^2} a^2 \bar{j}_\nu(z) \bar{j}_{\nu'}(z) P_j^{\nu\nu'}\left(k = \frac{L}{\chi}, z\right) \tag{7.2}$$

where $P_j^{\nu\nu'}(k,z)$ is the three-dimensional power spectrum of the fluctuations in j_ν. The power spectrum is presented explicitly in Chapter 5.4.3, and can be split into a 1- and 2-halo term

$$P_j^{\nu\nu'}(k,z) = P_j^{\nu\nu'\,2-\mathrm{halo}}(k,z) + P_j^{\nu\nu'\,1-\mathrm{halo}}(k,z). \tag{7.3}$$

The 2-halo term is given by

$$\bar{j}_\nu(z)\bar{j}_{\nu'}(z) P_j^{\nu\nu'\,2-\mathrm{halo}}(k,z) = D_\nu(z) D_{\nu'}(z) P_{\mathrm{lin}}(k,z) \tag{7.4}$$

where

$$D_\nu(z,k) \equiv \int dM \frac{dN}{dM} b(M,z) \left(\frac{L^{\mathrm{cen}}_{(1+z)\nu}(M,z) + L^{\mathrm{sat}}_{(1+z)\nu}(M,z) u(k,M,z)}{4\pi} \right) \tag{7.5}$$

with $u(k,M,z)$ the normalized Fourier transform of the halo density profile, and L^{cen} and L^{sat} the total luminosity due to central and satellite galaxies respectively. The 1-halo term is

$$\begin{aligned} \bar{j}_\nu(z)\bar{j}_{\nu'}(z) P_j^{\nu\nu'\,1-\mathrm{halo}}(k,z) = \int dM \frac{dN}{dM} \frac{1}{(4\pi)^2} \Big(& L^{\mathrm{cen}}_{(1+z)\nu} L^{\mathrm{sat}}_{(1+z)\nu'} u(k,M,z) \\ & + L^{\mathrm{cen}}_{(1+z)\nu'} L^{\mathrm{sat}}_{(1+z)\nu} u(k,M,z) + L^{\mathrm{sat}}_{(1+z)\nu} L^{\mathrm{sat}}_{(1+z)\nu'} u^2(k,M,z) \Big). \end{aligned} \tag{7.6}$$

Note that the auto-correlations ($\sim {L^{\rm cen}_{(1+z)\nu}}^2$) have not been included in the 1-halo term; these instead contribute to a scale-independent shot noise term to be discussed below.

Poissonian term: shot noise

There is also a shot noise component in the power spectrum, arising from the discrete nature of the sources. This is present in both the $\nu = \nu'$ power spectra and the $\nu\nu'$ spectra with $\nu \neq \nu'$, as the same source can contribute to the intensity at different frequencies.

The shot noise is scale independent and is given by an integral over the flux density S_ν of all sources at frequency ν up to a cutoff flux $S_{\rm cut}$ at which point sources are removed:

$$C_L = \int_0^{S_{\rm cut}} S_\nu^2 \frac{dN}{dS_\nu} dS_\nu. \tag{7.7}$$

$\frac{dN}{dS_\nu}$ is the distribution of flux densities such that $\frac{dN}{dS_\nu}\Delta S_\nu$ is the (angular) number density of sources with flux between S_ν and $S_\nu + \Delta S_\nu$.

The shot noise can be calculated from the CIB emissivity model and Eq. (7.7). However, as this term is more sensitive to scatter in the $L-M$ relation, there is more error induced in the step going between the integration over S_ν (or equivalently $L_{(1+z)\nu}$ than for the 1-halo and 2-halo power spectra. In practice, this can be dealt with by introducing explicitly a term to describe that scatter (see e.g. Appendix A of [106]):

$$\frac{dN}{d\ln S} = \int \frac{dN}{d\ln M} P(\ln S|\ln M) \tag{7.8}$$

where $P(\ln S|\ln M)$ follows a normal distribution with some width σ; $\sigma \to 0$ recovers $\frac{dN}{dS} \to \frac{dN}{dM}$. σ could be chosen to fit the observed shot noise in a data set. However, in [69], due to the increased modelling uncertainty in computing the shot noise, the values of the shot noise were not calculated from the halo model prescription and instead were calculated from the model of [107] and also included radio point source contributions from [108]. As such, the calculated shot noise had no dependence on the CIB model parameters that were being varied in the analysis; *moreover*, the shot noise contribution at each frequency pair was marginalized over by allowing the value to vary in the analysis. With this in mind, we perform no calculations for the shot noise, and instead use as our fiducial values for the shot noise the best-fit values of [69] (see Table 7.1), and marginalize over these values in our Fisher forecasts.

ν, ν'	217	353	545	857	3000
217	21	54	121	181	95
353		262	626	953	411
545			1690	2702	1449
857				5364	4158
3000					9585

Table 7.1: Shot noise values of [69], in Jy^2/sr. The frequencies are in GHz and are the frequencies for which the CIB power spectra were measured and used to fit the model.

Point source removal and S_{cut}

At current angular resolutions, the CIB is a diffuse, unresolved emission; however it is composed of discrete point sources—galaxies. If a single galaxy is bright enough, it can appear in a map as a point source and be removed. In each CIB map there is a (frequency-dependent) threshold flux density S_{cut} above which the point sources can be removed. Considering that flux S_ν can be expressed in terms of luminosity $L_{(1+z)\nu}$ by

$$S_\nu = \frac{L_{(1+z)\nu}}{4\pi(1+z)\chi^2}, \tag{7.9}$$

a flux-cut is equivalent to a z-dependent luminosity cut, which should be imposed in the calculations of C_L. We implement the flux cut by removing all halos with total luminosity greater than that corresponding to the flux limit in Equation (7.9) where S^ν is replaced by the flux cut of the experiment in question.

7.2.2 The CIB-CMB lensing cross power spectrum

The angular power spectrum of the CMB lensing potential ϕ is discussed in detail in Section 4.4.2. It is given in the Limber approximation by

$$C_L^{\phi\phi} = \frac{4}{L^4} \int \frac{d\chi}{\chi^2} W^\kappa(\chi)^2 P_{mm}\left(k = \frac{L}{\chi}, z\right) \tag{7.10}$$

with the lensing efficiency kernel $W^\kappa(\chi)$ given by

$$W^\kappa(\chi) = \frac{3}{2}\left(\frac{H_0}{c}\right)^2 \frac{\Omega_m}{a} \chi \left(1 - \frac{\chi}{\chi_S}\right) \tag{7.11}$$

where χ_S is the comoving distance of the source of the CMB at $z \sim 1080$ and $P_{\rm mm}(k,z)$ is the matter power spectrum. The matter power spectrum can be computed within the halo model by

$$P^{2h}_{mm}(k,z) = \left(\int dM \frac{dn}{dM}\frac{M}{\rho_m} b(M,z) u(k,M,z)\right)^2 P_{\rm lin}(k,z) \tag{7.12}$$

(with ρ_m the matter density today); the 1-halo term can also be written:

$$P^{1h}_{mm}(k,z) = \int dM \frac{dn}{dM}\left(\frac{M}{\rho_m} u(k,M,z)\right)^2 . \tag{7.13}$$

The cross power between ϕ and the CIB is given by a Limber integration over the emissivity-matter cross-power spectrum $P^{\nu}_{mj}(k,z)$

$$C^{\phi\nu}_L = \frac{2}{L^2}\int \frac{d\chi}{\chi^2} W_\kappa(\chi) a(\chi) \bar{j}_\nu(z) P^{\nu}_{mj}\left(k = \frac{L}{\chi}, z\right), \tag{7.14}$$

where

$$\bar{j}^{\nu}(z) P^{\nu}_{mj}(k,z)^{2-\rm halo} = D_\nu(z)\left(\int dM \frac{dn}{dM}\frac{M}{\rho_m} b(M,z) u(k,M,z)\right) P_{\rm lin}(k,z) \tag{7.15}$$

and

$$\bar{j}^{\nu}(z) P^{\nu}_{mj}(k,z)^{1-\rm halo} = \int dM \frac{dn}{dM}\frac{M}{\rho_m} u(k,M,z) \frac{1}{4\pi}\left(L^{\rm cen}_{(1+z)\nu} + L^{\rm sat}_{(1+z)\nu} u(k,M,z)\right). \tag{7.16}$$

7.3 A parametric $L - M$ relation

We use the parametric $L_\nu(M,z)$ model described in Section 5.4.1, using the best-fit values of *Planck* [69] in our fiducial model. We also parametrize the number of central galaxies hosted by a halo as

$$N^{\rm cen}(M,z) = \begin{cases} 0 & M < M_{\rm min} \\ 1 & M \geq M_{\rm min} \end{cases} \tag{7.17}$$

where $M_{\rm min}$, the minimum halo mass to host a galaxy, is one of the parameters of the model; in the fiducial model, we use $M_{\rm min} = 10^{10} M_\odot$.

This luminosity-mass relation we consider was introduced in [67]. The parametric model has been fit to several data sets with various subsets of the parameters allowed to vary; for fits to SPIRE data see [70] and for fits to *Planck* data see [69].

The $L - M$ relation is parameterized by making the simplifying assumption that its dependence on mass and redshift can be separated and specifying

$$L^{\rm gal}_{(1+z)\nu} = L_0 \Phi(z) \Sigma(M) \Theta((1+z)\nu); \tag{7.18}$$

L_0 is an overall normalization factor, which can be allowed to vary as a parameter in the model; $\Phi(z)$ determines the redshift evolution of the $L-M$ relation; $\Sigma(M)$ determines the mass dependence; and Θ is the spectral energy distribution (SED). Their explicit forms are given in Section 5.4.2. The fiducial values we use for the CIB model parameters are the best-fit ones of [69][1]. These values are summarized in Section 7.3 and Table 7.2.

Parameter	Parameter description	Value
α	Redshift evolution of dust temperature	0.36 ± 0.05
T_0	Dust temperature at $z = 0$	24.4 ± 1.9 K
β	Emissivity index of SED	1.75 ± 0.06
γ	Power law index of SED at high frequency	1.7 ± 0.2
δ	Redshift evolution of $L - M$ normalization	3.6 ± 0.2
$\log_{10} M_{\rm eff}/M_\odot$	Most efficient halo mass	12.6 ± 0.1
$\log_{10} M_{\rm min}/M_\odot$	Minimum halo mass to host a galaxy	unconstrained
L_0	normalization of $L - M$ relation	6.4×10^{-8}Jy MPc$^2/M_\odot$
$\sigma^2_{L/M}$	Size of halo masses sourcing CIB emission	0.5 (not varied)

Table 7.2: Best-fit parameters for the luminosity model of [69]

Fiducial values of the parameters

We consider the model of [69], which was fit to the CIB power spectra at {217, 353, 545, 857, 3000} GHz. In this model, the parameters δ, β, T_0, γ, α, $\log_{10} M_{\rm min}$, $\log_{10} M_{\rm eff}$, and L_0 were varied; $\sigma^2_{L/M}$ was fixed at 0.5. There is no plateau in the $L - M$ relation: $\Phi(z)$ behaves as $(1+z)^\delta$ at all redshifts. The parameters are summarized and their values are

---

[1] The value of L_0 is not listed in [69] and so we choose a value that reproduces the amplitude of the CIB power spectra and intensities therein.

given in Table 7.2. The values of the shot noises in the power spectra were also allowed vary as parameters, and marginalized over; their best-fit values are given in Table 7.1. With the SED normalized as in Equation (5.56), the fiducial value we use for L_0 is $L_0 = 6.4 \times 10^{-8}$Jy MPc$^2/M_\odot = 1.49 \times 10^{-15} L_\odot/M_\odot$.

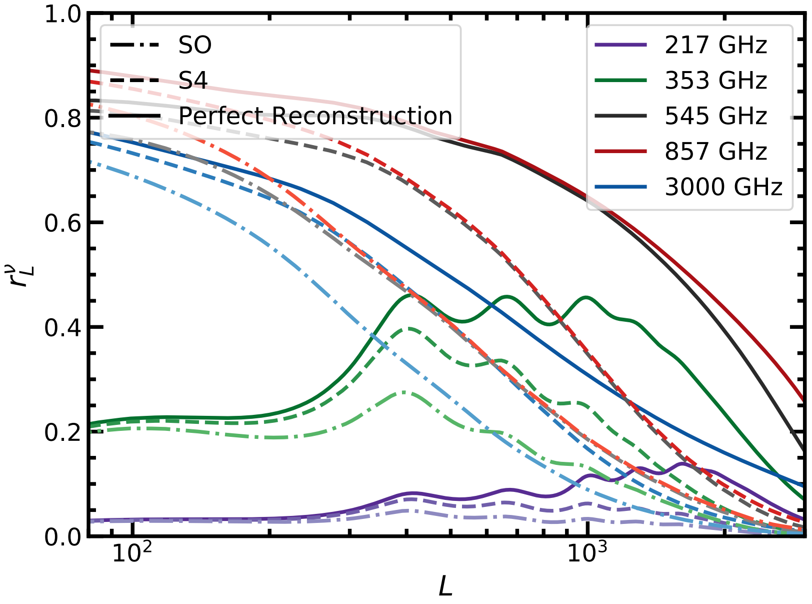

Figure 7.2: The correlation coefficients between the CIB maps from *Planck*+IRIS with CMB lensing maps from various experiments. The calculation includes instrumental and foreground noise in the CIB maps. The perfect reconstruction case corresponds to no noise on the CMB lensing reconstruction.

7.4 Fisher forecasts

We perform various Fisher forecasts to investigate whether inclusion of CIB/CMB lensing data has power to improve constraints on CIB models. We consider two experimental configurations for the CIB: one corresponding to the *Planck*+IRIS experiments, at {217, 353, 545, 857, 3000} GHz, and one corresponding to the upcoming CCAT-prime [98] survey, which will measure the CIB on small angular scales at {220, 280, 350, 410, 850} GHz.

We are considering improvements in only the parameters of the CIB model; the CMB lensing power spectrum is not dependent on any of the parameters we are including in our forecast[2]. However, the CMB lensing power spectrum and the CIB power spectra are correlated; see Figure 7.2 for plots of the correlation coefficients $r_L^\nu \equiv \frac{C_L^{\nu\phi}}{\sqrt{C_L^{\nu\nu} C_L^{\phi\phi}}}$. Due to the high correlation coefficient, measuring these two fields *on the same patch of sky* can yield improvements in a model describing one field even if the other is not dependent on this model through the cancellation of sample-variance shared by the two fields [103]. Additionally, knowledge of the redshift distribution of the CIB is contained in the correlation or lack thereof [109] with the CMB lensing matter distribution, whose redshift dependence is precisely known. Due to this, we expect the inclusion of CMB lensing in the CIB analysis to yield improvements in the CIB parameters.

7.4.1 Fisher matrix formalism

We consider at each L an $(N+1) \times (N+1)$ covariance matrix , where N is the number of frequency channels at which the CIB is measured:

$$C_L = \left(\begin{array}{cc} C_L^{\nu\nu'} & C_L^{\nu\phi} \\ C_L^{\nu\phi} & C_L^{\phi\phi} \end{array} \right). \tag{7.19}$$

$C_L^{\nu\nu'}$ is an $N \times N$ covariance matrix of the auto- and cross-power spectra of the CIB, $C_L^{\nu\phi}$ is an N-dimensional vector of the cross power spectra between the CIB and CMB lensing, and $C_L^{\phi\phi}$ is the CMB lensing power spectrum.

We consider a vector of parameters

$$\Pi^i = (\alpha, T_0, \beta, \gamma, \delta, \log_{10} M_{\text{eff}}/M_\odot, \log_{10} M_{\text{min}}/M_\odot, L_0, S^{\nu\times\nu'}) \tag{7.20}$$

where $S^{\nu\times\nu'}$ denotes the $\frac{N(N+1)}{2}$ shot noise parameters. The Fisher matrix for the parameters is

$$F_{ij} = \sum_L \frac{(2L+1)}{2} f_{\text{sky}} \, \text{Tr} \left[C_L^{-1} \frac{\partial C_L}{\partial \Pi^i} C_L^{-1} \frac{\partial C_L}{\partial \Pi^j} \right] \tag{7.21}$$

where f_{sky} is the sky fraction covered by the experiment. C_L^{-1} includes both signal and noise. Within this setup, the fully marginalized forecast 1σ error on a parameter i is given by $\sqrt{(F^{-1})_{ii}}$.

---

[2] In particular, we assume cosmological parameters are known to much better precision than the CIB model parameters considered here.

At times, we refer to forecasts where we remove the CIB auto power spectra from our forecasts, and consider only the cross power spectra $C_L^{\phi\nu}$ and the lensing auto-power $C_L^{\phi\phi}$. We do this by instead employing the bandpower Fisher formalism, where the Fisher matrix is computed from the covariance of the power spectra; in this case the data is considered to be the power spectra (as opposed to the fields themselves) and we consider the data vector

$$C_L = \left(C_L^{\nu,\nu'}, C_L^{\nu,\phi}, C_L^{\phi\phi}\right) \tag{7.22}$$

with covariance matrix

$$\mathbb{C}\left(\hat{C}_L^{\alpha\beta}, \hat{C}_L^{\gamma\delta}\right) = \frac{1}{(2L+1)f_{\text{sky}}}\left[\left(C_L^{\alpha\gamma} + N_L^{\alpha\gamma}\right)\left(C_L^{\beta\delta} + N_L^{\beta\delta}\right) + \left(C_L^{\alpha\delta} + N_L^{\alpha\delta}\right)\left(C_L^{\beta\gamma} + N_L^{\beta\gamma}\right)\right]; \tag{7.23}$$

F_{ij} is now given by

$$F_{ij} = \sum_L \frac{\partial C_L^T}{\partial \Pi^i}\mathbb{C}_L^{-1}\frac{\partial C_L}{\partial \Pi^j} \tag{7.24}$$

(where C_L^T denotes the transpose of C_L). This Fisher formalism is equivalent to the one that results in Equation (7.21); however, it allows us to explicitly remove power spectra from the analysis by taking only the entries we are interested in in (7.22), something is not possible when we are computing Equation (7.21).

7.4.2 The CIB power spectra and CMB lensing: signal and noise

CIB noise specifications

There is instrumental noise in the $\nu = \nu'$ power spectra, which we include as

$$N_L = N(L)e^{\frac{L(L+1)\Theta_{\text{FWHM}}^2}{8\ln 2}} \tag{7.25}$$

where $N(L)$ is the value of the noise and Θ_{FWHM} is the beam Full Width at Half Maximum in radians. For *Planck* and IRIS we use only white noise $N(L) = N_{\text{white}}$. The values of N_{white} and Θ_{FWHM} are given in Table 7.3. For CCAT-prime we consider both large-scale frequency dependent "red" noise and white noise corresponding to the specifications given in [98]:

$$N(L) = N_{\text{red}}\left(\frac{L}{L_{\text{knee}}}\right)^{\alpha_{\text{knee}}} + N_{\text{white}}, \tag{7.26}$$

where L_{knee} is 1000 and α_{knee} is 3.5. We emphasize that just as with Simons Observatory and CMB-S4 configurations considered below, the noise specifications correspond to one of many possible configurations that CCAT-prime could observe in. The values of N_{red}, N_{white}, and Θ_{FWHM} are given in Table 7.3 [3] (note that we consider the noise levels corresponding to the configuration in which CCAT-prime observes 15,000 sq. deg., but we only use 2240 sq. deg. of these). We show in Figure 7.3 the signal and noise at the frequencies measured by *Planck*. We show in Figure 7.4 a summary of the signal and noise at all of the CCAT-prime frequencies.

Frequency	Beam (arcmin)	Noise	
		Jy^2/sr	μK-arcmin
217 GHz	5.01	72	60.12
353 GHz	4.86	305	208.98
545 GHz	4.84	369	1137
857 GHz	4.63	369	29075
3000 GHz	4.3	305	6.7×10^{18}

Frequency	Beam (arcmin)	White noise		'Red' noise	
		Jy^2/sr	μK-arcmin	Jy^2/sr	μK-arcmin
220 GHz	57	4.2	14.6	3.7×10^3	435
280 GHz	45	11.8	27.5	2.0×10^4	1140
350 GHz	35	85.1	105	2.5×10^5	5648.8
410 GHz	30	468	377	6.6×10^5	14174
850 GHz	14	69483	575000	1.5×10^7	8.5×10^6

Table 7.3: Noise levels and beam sizes for the *Planck* [111] , IRIS [84], and one of many possible CCAT-prime [98] configurations.

CMB lensing noise specifications

The lensing potential can be reconstructed from CMB temperature and polarization maps [44]. We consider various reconstruction noise scenarios including reconstruction noise in line with that of *Planck*, with a Simons Observatory-like scenario (specifically the 'goal' configuration from [16]), and a Stage-4 (S4) like scenario such as [17]. Additionally,

---

[3] At *Planck* frequencies, we change between μK and Jy using the conversion factors in [110]. See Appendix C for more details.

we also compare to the case when there is no noise on the lensing reconstruction out to $L = 1000$. The signal and noise for the various lensing scenarios are plotted on the right of Figure 7.4. In all cases we assume that the CMB lensing potential is measured reliably in the multipole region $186 \leq L \leq 1000$.

With the signal and noise expected from these experiments, we can calculate the forecast errors on the measurement of the CIB/lensing cross correlation. The error-bars on $C_L^{\phi\nu}$ can be calculated from the bandpower covariance matrix of Equation (10.8) with $\alpha = \gamma = \kappa$ and $\delta = \beta = \nu$. Assuming independence of the L-modes measured (which may be slightly optimistic due to mode-coupling induced by partial-sky effects) we can calculate the covariance of the $C_L^{\phi\nu}$

$$\left(\Delta C_L^{\phi\nu}\right)^2 = \frac{1}{\Delta L(2L+1) f_{\text{sky}}} \left[\left(C_L^{\nu\nu} + N_L^{\nu\nu}\right) \left(C_L^{\phi\phi} + N_L^{\phi\phi}\right) + \left(C_L^{\nu\phi}\right)^2 \right] \tag{7.27}$$

where ΔL is the width of the bins over which $C_L^{\nu\phi}$ is measured; in [91] the bandpowers are given in bins of width $\Delta L = 126$. See Figure 7.5 for plots of the predicted errors, the fiducial model, and the data of [91].

7.4.3 Foregrounds

We include contributions from foregrounds as noise in the covariance matrices. The dominant foreground at high frequencies is emission from Galactic dust; however by restricting our baseline analysis to the cleanest 2240 sq. deg. used in [69] and to angular scales with $L > 186$, we substantially reduce the noise contribution from dust, and therefore do not include it in our forecasts. The main contaminant at low frequencies is the CMB, which is dominant over the CIB at 217 and 353 GHz. Note, however, that for the analysis in [69] the CMB was subtracted from these maps, using a template of the CMB measured at 143 GHz.

We include the entire CMB power (computed with CAMB) in our forecasts at all frequencies, and find this has little effect on our forecast except for the predicted errors on the measured cross-power at CMB-dominated frequencies (see Figure 7.5). We also include the early- and late-time kinetic Sunyaev–Zeldovich (kSZ) effect, the thermal Sunyaev–Zeldovich (tSZ) effect, and radio point sources as foregrounds [86, 112, 16].

7.5 Forecast results

7.5.1 Constraints on CIB model parameters

First we consider only *Planck*+IRIS-like CIB data: $\nu = \{217, 353, 545, 857, 3000\}$ GHz, with noise specifications corresponding to those in Table 7.3. For the CIB power spectra, we sum over all multipoles $186 \leq L \leq 2649$, corresponding to the multipoles used to fit the data in [69]; for the CMB lensing power spectra we sum only over $186 \leq L \leq 1000$. We consider a sky fraction of 2240 square degrees for the *Planck* frequencies $\nu = \{217, 353, 545, 857\}$ GHz, and 183 square degrees for the 3000 GHz IRIS data, corresponding to the sky areas used in the *Planck* analysis [69]. We assume full overlap between all maps, and the CMB lensing potential reconstruction. Motivated by the priors used in [69], we include Gaussian priors in the Fisher matrix with widths of 20 K for T_0 and 0.5 for β; we also include Gaussian priors on the shot noise parameters with widths given by the 1σ errors in Tables 6 and 7 of [69]. We assume the flux cuts in Table 1 of [69]

The forecast constraints on the parameters, and improvements upon including the different lensing scenarios, are given in Table 7.4. A bar graph of the improvement factors is also presented in Figure 7.6. Triangle plots of the covariances of the parameters are given in Figure 7.7.

Parameter	Reported Constraint		CIB only	Forecast Improvement				
			Forecast σ	$N_L^{\kappa\kappa}$ *Planck*	$N_L^{\kappa\kappa}$ SO	$N_L^{\kappa\kappa}$ $S4$		$N_L^{\kappa\kappa} = 0$
	Value	Percentage	σ_{CIB}	$\sigma_{\mathrm{CIB}}/\sigma$	$\sigma_{\mathrm{CIB}}/\sigma$	$\sigma_{\mathrm{CIB}}/\sigma$	Percentage	$\sigma_{\mathrm{CIB}}/\sigma$
α	0.05	13.89 %	0.03	1.11	1.63	2.47	2.96 %	3.34
T_0[K]	1.9	7.79 %	1.04	1.22	1.89	2.46	1.73 %	2.88
β	0.06	3.43 %	0.02	1.03	1.14	1.25	1.04 %	1.34
γ	0.2	11.76 %	0.06	1.04	1.1	1.14	2.86 %	1.18
δ	0.2	5.56 %	0.29	1.17	1.59	1.85	4.42 %	2.02
$\log_{10}(M_{\mathrm{eff}})$	0.1	0.79 %	0.17	1.08	1.2	1.28	1.05 %	1.37
$\frac{L_0}{L_0^{\mathrm{fid}}}$	None		0.23	1.19	1.62	1.87	12.45 %	2.04
$\log_{10}(M_{\mathrm{min}})$	unconstrained		47.81	1.06	1.38	1.87	255.99 %	2.36

Table 7.4: Constraints and improvement factors $\sigma_{\mathrm{CIB}}/\sigma$ on this model when only incorporating *Planck* data. In the columns labelled 'Percentage' we report the size of the constraint as a percentage of the fiducial parameter value.

Second we consider CCAT-prime+IRIS-like data. As CCAT-prime is noise dominated at low L, we include the low-L data from *Planck* in this forecast as well. Thus we consider a forecast at $\nu = \{220, 280, 350, 410, 545, 850, 3000\}$ GHz, although the 545 and 3000 GHz data is only signal-dominated at low L, and the 410 and 280 GHz data are only signal

Parameter	CIB: $N_L^{\nu\nu'}{}_{\text{CCAT}-\text{prime}}$	Forecast Improvement				
	Forecast Constraint	$N_L^{\kappa\kappa}{}_{Planck}$	$N_L^{\kappa\kappa}{}_{\text{SO}}$	$N_L^{\kappa\kappa}{}_{S4}$		$N_L^{\kappa\kappa}=0$
	σ_{CIB}	$\sigma_{\text{CIB}}/\sigma$	$\sigma_{\text{CIB}}/\sigma$	$\sigma_{\text{CIB}}/\sigma$	Percentage	$\sigma_{\text{CIB}}/\sigma$
α	0.02	1.06	1.38	1.99	2.66 %	2.75
T_0[K]	0.72	1.1	1.54	2.06	1.42 %	2.52
β	0.02	1.01	1.08	1.14	0.78 %	1.18
γ	0.05	1.01	1.06	1.09	2.61 %	1.12
δ	0.22	1.1	1.52	1.96	3.12 %	2.29
$\log_{10}(M_{\text{eff}})$	0.13	1.08	1.34	1.55	0.67 %	1.69
L_0	0.17	1.1	1.53	1.95	8.84 %	2.26
$\log_{10}(M_{\text{min}})$	37.67	1.05	1.33	1.88	200.05 %	2.58

Table 7.5: 1σ constraints and improvement factors on the parameters when including both *Planck* and CCAT-prime data.

dominated at high L. At 220, 350, and 850 GHz respectively we consider *Planck* noise levels appropriate to 217, 353, and 857 GHz.

We must also include shot noise values in the CCAT-prime forecast. We consider flux cuts similar to the *Planck* experiment; as the flux cuts could be smaller and the shot noises lower, our forecast is conservative in this regard. We choose the shot noise parameters from those in Table 7.1, where we have in every case rounded up the relevant CCAT-prime frequency if it does not appear in the table. Forecast 1σ constraints are shown in Table 7.5.

7.5.2 Impact of the high-frequency data

The forecasts in Section 7.5 included 3000 GHz data on around 8% of the sky area on which the low-frequency fields are measured. The 3000 GHz field is qualitatively different to the low frequency fields: it probes the high-frequency end of the SED (5.53) and as such informs the parameter γ while the lower frequency fields do not. It is also sourced at lower redshift (see Figure 7.1) and thus is less correlated with the rest of the CIB and can provide more independent information. As well as providing all the information on γ, including the 3000 GHz field on even this small sky fraction provides significant constraining power on the parameters relating to the dust temperature (α, T_0), improving the constraints on these parameters by up to 100%. Because of this, it is important to include the high-frequency information in any CIB model fitting.

7.5.3 Galaxies as an external tracer

The Rubin Observatory [54] will measure the clustering of billions of galaxies and their photometric redshifts in their LSST (Legacy Survey of Space and Time) survey. While the CMB lensing kernel is highly correlated with the CIB, both peaking at redshift $z \sim 2$, it is interesting to see what low-redshift information can add to the CIB, particularly as the 3000 GHz field (which is sourced at lower redshift) helps significantly with some parameters (as discussed in Section 7.5.2). In this Section we consider how a low-redshift galaxy sample from the Rubin Observatory can help improve parameter constraints. A similar analysis was done in [104] where a CIB halo model was fit to the cross power spectra of the CIB and SDSS galaxies in a narrow redshift bin, in order to isolate redshift behaviour of the CIB.

The angular galaxy clustering power-spectrum for a photometric redshift bin between redshifts z_i and z_f (comoving distances χ_i and χ_f)

$$C_L^{gg} = \frac{1}{\Delta\chi^2}\int_{\chi_i}^{\chi_f}\frac{d\chi}{\chi^2}P_{gg}\left(k=\frac{L}{\chi},z\right), \tag{7.28}$$

where $\Delta\chi = \chi_f - \chi_i$ is the extent of the bin in comoving distance and P^{gg} is the galaxy power spectrum. We choose to consider only one photometric redshift bin, from $z = 0$ to $z = 1$, and use only the two-halo galaxy power spectrum, which can be written as

$$P_{gg}^{2-\mathrm{halo}}(k,z) = b_g^2 P_{\mathrm{lin}}(k,z), \tag{7.29}$$

where the galaxy bias b_g is defined as

$$b_g(z) = \int dM \frac{dN}{dM}\frac{N^{\mathrm{gal}}(M,z)}{\bar{n}_{\mathrm{gal}}(z)}b(M,z). \tag{7.30}$$

For the galaxy density field predicted for the LSST Gold sample [54]

$$\frac{dn}{dz} \propto z^2 \exp\left(-\frac{z}{0.5}\right) \tag{7.31}$$

with a total number density of 40 arcmin^{-2}. We calculate N^{gal} with the model described in Chapter 5.3.2, with the threshold stellar mass for galaxy detection chosen to reproduce the distribution (7.31).

As we do not wish to focus on uncertainties in the non-linear galaxy HOD, we restrict our galaxy clustering information to scales where only the two-halo term is relevant by using an L_{max} of 500 for the galaxy survey and neglecting the 1-halo terms.

We can write the two-halo cross-power spectrum between galaxies and the CIB emissivity as

$$\bar{j}(z)P_{jg}^{\nu\,2-\mathrm{halo}}(k,z) = b_g(z)D_\nu(z)P_{\mathrm{lin}}(k,z) \tag{7.32}$$

with $D_\nu(z)$ the CIB bias. The angular power spectra can be computed from the Limber approximation

$$C_L^{\nu g} = \frac{1}{\Delta\chi}\int_{\chi_i}^{\chi_f}\frac{d\chi}{\chi^2}j(z)P_{jg}^{\nu}\left(k=\frac{L}{\chi},z\right). \tag{7.33}$$

We perform a forecast with the same formalism as in Section 10.3 where we now consider a covariance matrix with galaxy clustering included:

$$C_L = \begin{pmatrix} C_L^{\nu\nu'} & C_L^{\nu\phi} & C_L^{\nu g} \\ C_L^{\nu\phi} & C_L^{\phi\phi} & C_L^{\phi g} \\ C_L^{\nu g} & C_L^{\phi g} & C_L^{gg} \end{pmatrix}. \tag{7.34}$$

The cross-power spectra between lensing and galaxies $C_L^{g\phi}$ is

$$C_L^{\phi g} = \frac{1}{\Delta\chi l^2}\int\frac{d\chi}{\chi^2}a(\chi)b_g(\chi)W_\kappa(\chi)P_{\mathrm{lin}}\left(k=\frac{L}{\chi},z\right). \tag{7.35}$$

To account for the uncertainties in the modelling of our galaxy power spectra, when we include galaxies in the forecast we marginalize over the galaxy bias by introducing a parameter A such that $C_L^{gg} = A^2C_L^{gg}$, $C_L^{g\phi} = AC_L^{g\phi}$, and $C_L^{g\nu} = AC_L^{g\nu}$ with $A = 1$ in the fiducial case.

We assume full overlap between the galaxy field, the CIB fields, and the CMB lensing field (although we restrict the 3000 GHz field to 183 square degrees as before). We find that some CIB model parameters can be constrained much more strongly when including galaxies; similarly to when the 3000 GHz field was included, the CIB dust temperature parameters α and T_0 are improved significantly, as well as the parameter controlling the redshift evolution of the $L-M$ normalization δ, indicating that the low-redshift information helps to inform these parameters.

7.6 Constraints on star formation history

The source of the energy of the dust particles emitting the CIB is irradiation by ultraviolet (UV) light emitted by the star-forming galaxies. The star formation rate (SFR) can be measured directly with UV detections; however these measurements must be corrected for the dust attenuation, as much of the UV emission is indeed absorbed and re-emitted in the IR (see [113] for a review of cosmic star formation history). In [114], UV measurements are used to constrain the SFRD at redshifts up to $z = 4.5$. Direct measurements of total IR emission of galaxies are also used to constrain SFR [115, 116]. As the CIB emission traces all galaxies (not just those luminous enough to be resolved as sources), it can provide a complementary probe of the SFR, particularly at high redshift.

The star formation rate (SFR) can be related very simply to the total infrared luminosity of galaxies through the Kennicutt relation [73]:

$$\mathrm{SFR} = K L_{\mathrm{IR}} \tag{7.36}$$

with K the Kennicutt constant $K = 1.7 \times 10^{-10} M_{\odot}\mathrm{yr}^{-1}$. The total infrared luminosity is simply the luminosity density integrated over its entire IR emission spectrum:

$$L_{\mathrm{IR}} = \int d\nu L_{\nu} \tag{7.37}$$

—as the only ν-dependence is in the SED this can be written equivalently as

$$L_{\nu} = \Theta_{\nu} L_{\mathrm{IR}} \tag{7.38}$$

with the SED $\Theta(\nu)$ normalized such that $\int d\nu\, \Theta(\nu) = 1$[4]. The definition of emissivity (5.45) can then be written

$$j_{\nu}(z) = \Theta_{(1+z)\nu} \int dL_{\mathrm{IR}} \frac{dN}{dL_{\mathrm{IR}}} \frac{L_{\mathrm{IR}}}{4\pi} \tag{7.39}$$

with $\frac{dN}{dL_{\mathrm{IR}}}$ the IR luminosity function such that $\frac{dN}{dL_{\mathrm{IR}}} dL_{\mathrm{IR}}$ gives the number density of halos with total IR luminosity between L_{IR} and $L_{\mathrm{IR}} + dL_{\mathrm{IR}}$. Due to the Kennicutt relation, the integral in (7.39) gives the mean star formation rate density (SFRD) ρ_{SFR}:

$$j_{\nu}(z) = \frac{\Theta_{(1+z)\nu}}{4\pi} \frac{\rho_{\mathrm{SFR}}(z)}{K}. \tag{7.40}$$

This can be written in terms of the effective SED $s_{\nu,\mathrm{eff}}$, the flux density from a halo with luminosity of $1L_{\odot}$

$$s_{\nu,\mathrm{eff}} = \Theta_{(1+z)\nu} \frac{1L_{\odot}}{4\pi\chi^2(1+z)} \tag{7.41}$$

such that

$$j_{\nu}(z) = \frac{\rho_{\mathrm{SFR}}(z) s_{\nu,\mathrm{eff}} \chi^2 (1+z)}{K}. \tag{7.42}$$

---

[4] Note that this is a different normalization to the SED in Section 5.4.1.

In modelling the star formation rate, an alternative approach to using a parametric SED is to use for $s_{\nu,\mathrm{eff}}$ externally measured SEDs such as those of [107]. Indeed, in [88] CIB and CMB lensing data are used to constrain the ρ_{SFR} in this way. This approach has the advantages of being able to incorporate different types of galaxies with different SEDs [117] such as those undergoing a starburst phase or the more common main sequence galaxies.

We can use the parametric halo model to compute $\rho_{\mathrm{SFR}}(z)$ by using for the parametric SED of Equation (5.53) in (7.41) to compute $s_{\nu,\mathrm{eff}}$ (note it must be normalized to integrate to 1 over all frequencies). We can then forecast the constraints on $\rho_{\mathrm{SFR}}(z)$ by drawing parameters from the covariance matrix defined by F^{-1}, the inverse of the Fisher matrices discussed above. We show in Figure 7.8 how the inclusion of lensing data improve constraints on ρ_{SFR} through this model; as it is difficult to see the improvements on a logarithmic scale we include a linear plot of the constraints divided by the fiducial value of ρ_{SFR}. We define the 1σ errors as the area within which 68% of 1000 realisations fell, centered on the median value.

7.7 Discussion

In this Chapter, we explored the possibility of using cross-correlations of CMB lensing mass maps with maps of the CIB to improve physical models of the latter. We have shown that inclusion of CMB lensing data can lead to up to $2\times$ improvement in constraints on the dust temperature and its redshift evolution, and on the redshift evolution of the relation between CIB galaxy luminosity and mass, in particular. Since cosmological parameters like the amplitude of matter fluctuations are known to much better precision than the astrophysical parameters of interest here, we have not varied them in our forecasts (although see [118] for a CIB-only forecast which varies the cosmological parameters along with the CIB parameters). Therefore, the CMB lensing potential does not depend on the parameters under consideration. Due to this, improvements in parameter constraints will come from either the redshift overlap or cancellation of sample variance, as described below.

We have calculated explicitly the constraints for a CIB-only scenario with zero foregrounds and instrumental noise, and we find that in the realistic forecast, while not all of the parameters have reached their sample variance limit, for many of them the inclusion of SO- or S4-like lensing improves the constraint to such an extent that they are better than the “perfect” sample-variance limited CIB-only case. However, we note that this effect might not be due solely to sample variance cancellation, but that the well-understood redshift kernel of the CMB lensing field may be helping to constrain the redshift dependence of the CIB fields by breaking parameter degeneracies.

In order to be conservative and facilitate comparisons with earlier work, the improvements we have presented are calculated for the small sky areas ($\sim 5\%$) used for the analysis in [69]. It is possible to consider larger sky areas for the CIB maps than was done here; [75] produced maps with improved treatment of galactic dust using HI data and recommended sky fractions of {18.7%, 16.3%, 14.4%} at {353, 545, 857} GHz for auto-power spectrum analysis. Accounting for the partial sky covered by typical ground-based surveys however reduces the area available for cross-correlation (necessary for improvements from sample variance cancellation) to {6.4%, 8.4%, 9.8%}, respectively.

The requirements on foreground cleaning for the CIB maps are more stringent for an auto-power-spectrum analysis than for a cross-correlation with CMB lensing. Much of the foreground contamination is sourced by Galactic dust, which will introduce spurious correlations in the auto-spectrum from the spatially dependent two-point correlation of Galactic emission, which can be significantly brighter than the CIB. On the other hand, in a cross-correlation of CMB lensing (calculated through quadratic estimators of the form $\langle T^{150} T^{150} \rangle$, where T^{150} is the CMB temperature field as measured at 150 GHz that dominates near-term experiments) with the CIB biases enter through bispectra of the form $\langle T_G^{150} T_G^{150} T_G^{\rm high} \rangle$ where T_G^{150} is the Galactic dust emission at 150 GHz and $T_G^{\rm high}$ is the Galactic emission at high frequencies used for CIB maps. These are suppressed relative to the biases in the CIB auto-spectrum for several reasons that include (1) the SED of dust being such that T_G^{150} is significantly smaller than $T_G^{\rm high}$ and (2) contributions from Galactic dust blobs being further reduced in the high-resolution CMB map through mitigation techniques like point source bias hardening [119]. As such, the sky area available for the cross-correlation between the CIB and CMB lensing is larger; the largest maps of [75] have a total sky area of 34.2% with roughly 20% overlap with typical wide-area ground based high-resolution CMB experiments from which CMB lensing maps will be available. To understand the impact of sky area, we show in Figure 7.9 the improvement in the constraints as the lensing field is added on top of the baseline forecast. The area on which the CIB auto power spectrum is measured is not changed in Figure 7.9, and the lensing field is added first on the IRIS+*Planck* fields, then on the *Planck* fields, and then on extra sky but without any CIB auto-power spectrum measured beyond the baseline 2240 sq. deg. We find that for some parameters like the SED emissivity index β, substantial improvements can be obtained by including CIB/lensing cross-correlations in larger fractions of the sky, without having to measure the CIB auto-spectrum beyond 2240 sq. deg. We note however that our forecasts do not include the increased scatter on large scales from Galactic dust contamination that is encountered when including larger sky areas [75].

We have checked that forecasts with the auto-spectrum of the CMB lensing map removed—i.e., with only $C_L^{\nu\nu'}$ and $C_L^{\nu\kappa}$ as data—and have found that there is negligible degradation in the forecast parameter improvements. As such, one will not need to measure the auto-spectrum of the lensing potential to achieve model improvements.

We find that the inclusion of the 3000 GHz field, even on a small fraction of the sky area, is key for constraining the CIB model. This is not only due to the fact that it is the only field that informs the high-frequency part of the SED, but also because it is the only low-redshift tracer included in the survey, as evidenced in Figure 7.1. As such, it provides information that is independent of the low-frequency fields. We have also demonstrated that the inclusion of another low-redshift tracer (such as galaxy clustering out to $z \sim 1$, say from the Rubin Observatory [54, 120]) can improve parameters even further. As in the case for when lensing is included, the galaxy density must be measured on the same patch of sky to provide improvement. This is an interesting possibility; however, we note that we have presented rough optimistic forecasts as an illustrative example of the power of correlating the CIB with other low z tracers to improve the CIB model.

For robustness, our baseline forecasts have restricted analyses mostly to the mostly two-halo regime by using the multipole range $186 \leq L \leq 2649$. We have however also considered improvements to a CIB model made with CIB maps of higher angular resolution exploring the one-halo regime, in particular those that will be made by CCAT-prime. While the HOD we use is not expected to be very accurate on such small scales, it is interesting that there is still improvement factors up to ~ 2 for the S4 case in these forecasts when the large-scale lensing cross-correlation is included.

Studying the CIB is interesting for a variety of reasons. First, from an astrophysical perspective, it contains interesting information about star formation history. We have shown what improvements can be made to measurements of the star formation rate density through including lensing data in Section 7.6. While the model we use as our fiducial model may not reproduce very accurately other measurements of the star formation rate (perhaps due to the crude parametric SED used), it is possible that alternative models of the CIB, such as the simpler single-parameter halo model used in [89] (which uses externally measured SEDs) will be improved similarly by including lensing data. The CIB is also an interesting cosmological signal: as a tracer of large scale structure, the CIB carries interesting information [121, 3] and having a more accurate model can allow us to exploit further its cosmological information.

Secondly, the CIB is important to understand as a foreground to other signals of interest. The CIB is a significant foreground to the CMB at small angular scales and its accurate modelling is necessary to make unbiased measurements of signals that are relevant to the small-scale CMB such as the kSZ power-spectrum [99], as well as extensions to the

ΛCDM model deriving significant information from the damping tail[5]. We leave detailed exploration of the potential improvements to physics in the temperature damping tail to future work. The tSZ effect is also a significant foreground to the CMB at small angular resolution, and must also be mitigated or modeled; as discussed in [89], the tSZ/CIB correlations can be consistently modelled with the halo model approach presented in Section 7.2. As we find that significantly more accurate models of the CIB can be built by including external tracers, in particular the CMB lensing potential, in the data analysis, this method of constraining models of the CIB will be of great use in improving our knowledge of star formation as well as potentially physics in the damping tail.

---

[5] It should be noted that as the polarization sensitivity of ground-based experiments improves, parameters like the number of relativistic species N_{eff} will increasingly derive their information from the polarization TE and EE spectra. Thus, CIB-related model bias to extensions of the ΛCDM model (like N_{eff}) will likely be less of an issue, since the CIB is not significantly polarized.

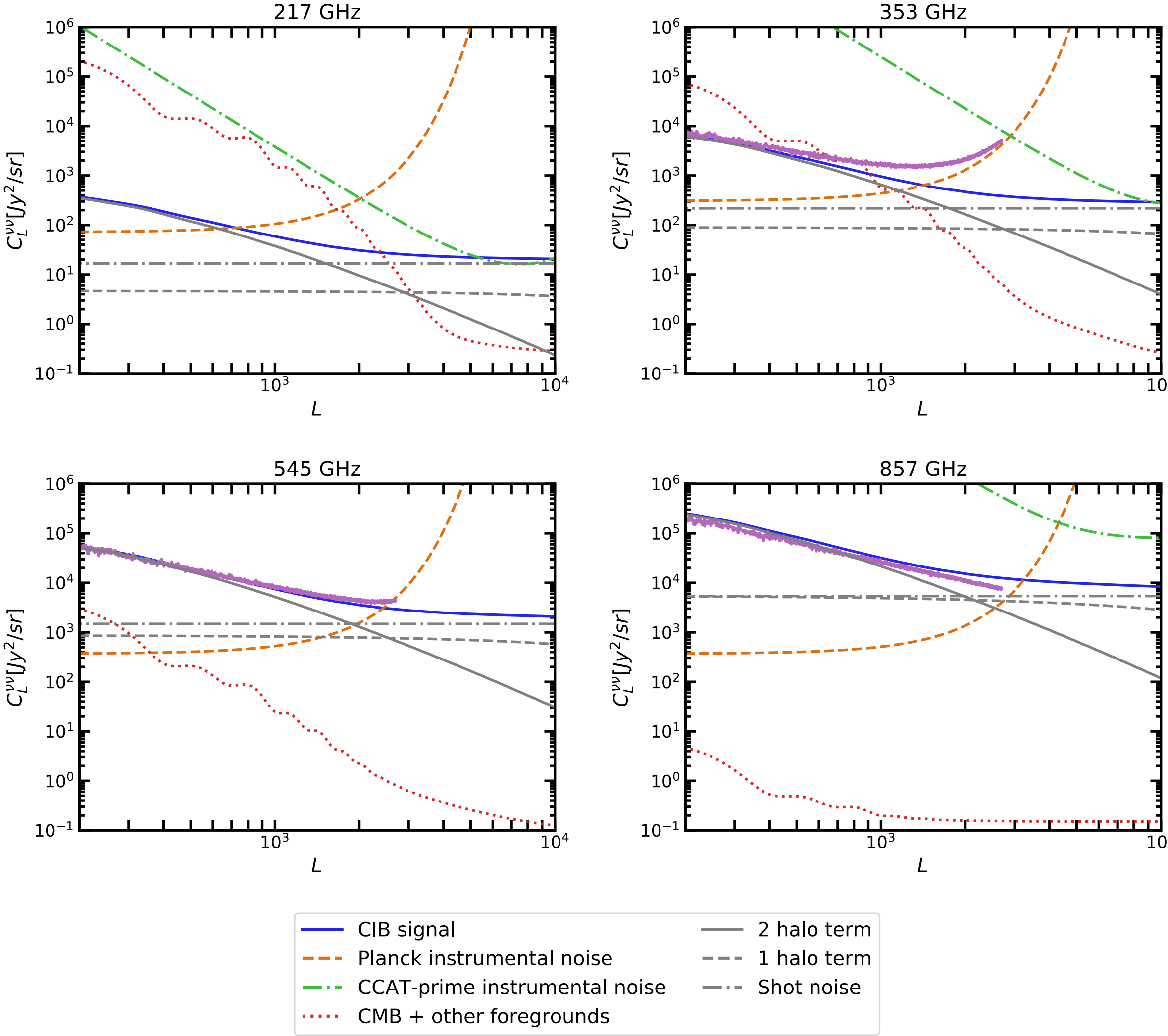

Figure 7.3: The predicted CIB signal at *Planck* frequencies is shown here in solid blue along with beam-deconvolved instrumental noise (orange dashed) and total foreground power (red dotted). Also shown in purple are the power spectra of the CIB maps of [75] (for 353, 545 and 857 GHz), corrected for the beam and partial sky coverage. When available at a nearby frequency, the beam-deconvolved CCAT-prime instrumental noise (one of many possible configurations) is also shown. This Figure shows that our signal and noise power spectra account fairly well for the observed CIB power in [75].

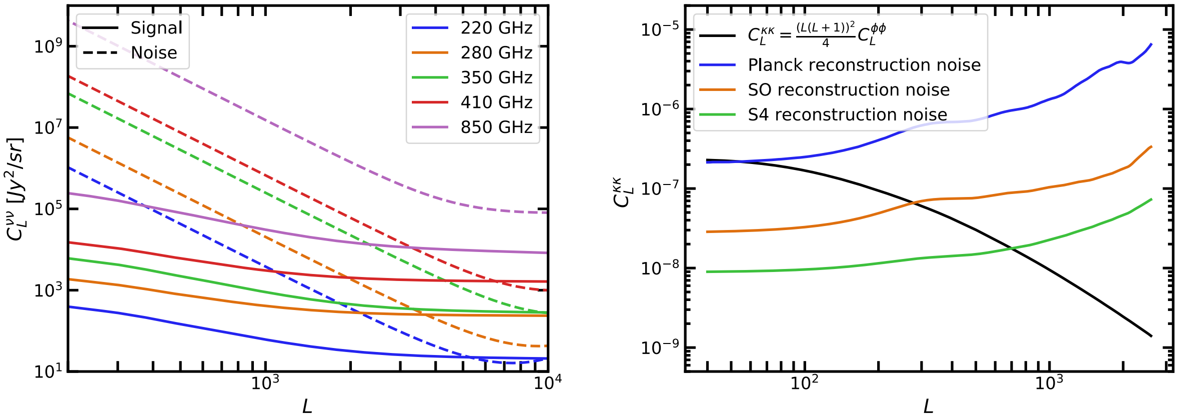

Figure 7.4: *Left:* The CIB signal at CCAT-prime frequencies (solid) shown against the beam-deconvolved instrument noise for one of many possible configurations of CCAT-prime, corresponding to the values in Table 7.3. *Right:* The CMB lensing convergence power spectrum shown against various reconstruction noise levels from the *Planck* satellite, a Simons Observatory-like configuration and a CMB-S4-like configuration (note that we plot the lensing convergence power spectrum which is related to the lensing potential power spectrum through $C_L^{\kappa\kappa} = \frac{(L(L+1))^2}{4} C_L^{\phi\phi}$).

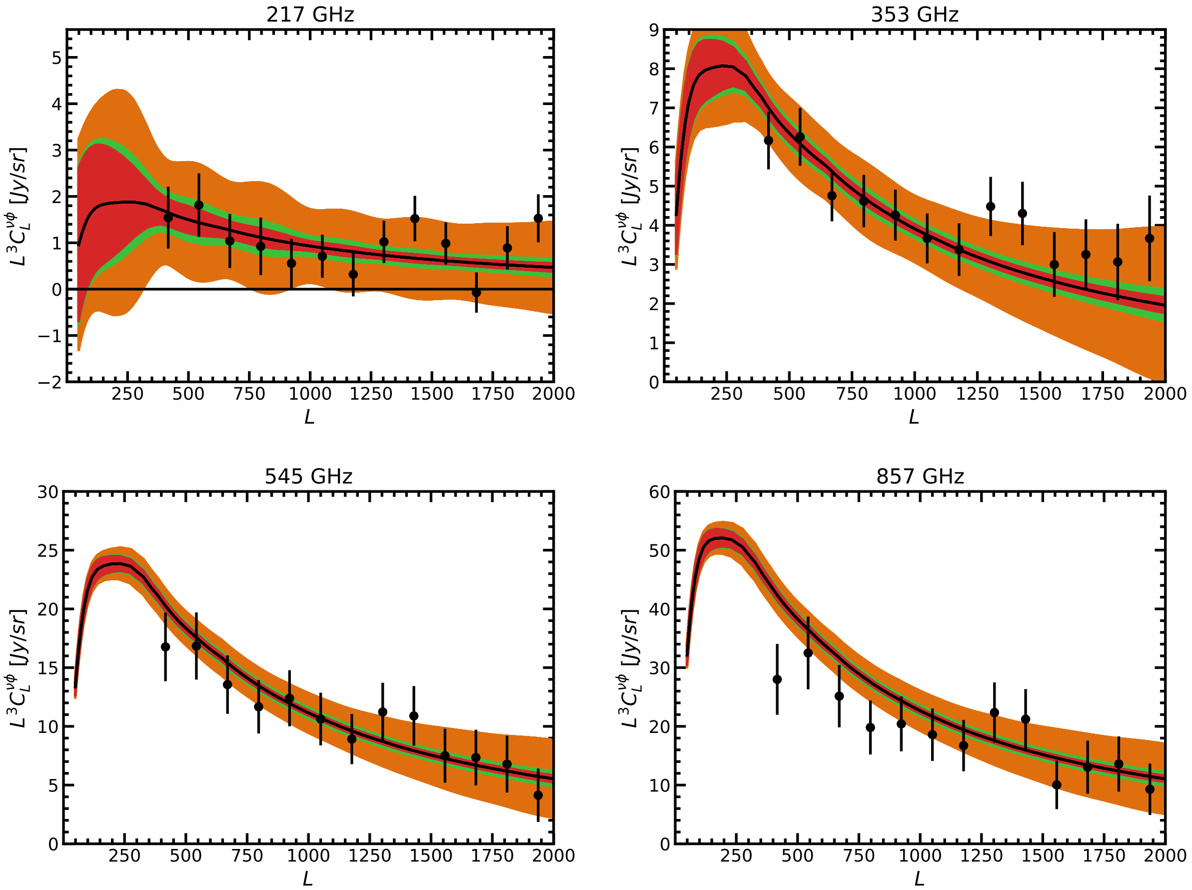

Figure 7.5: The cross-power spectrum between CMB lensing and the CIB measured by *Planck* at various frequencies. The model prediction for $L^3C_L^{\phi\nu}$ is plotted in black. The data points show the measurements using *Planck* lensing from [91]. The predicted 1-σ uncertainty lensing reconstruction noise and our CIB model is shown in orange for *Planck*, in bins of width $\Delta L = 126$; in red for a Simons Observatory-like lensing reconstruction, and in green for a CMB-S4-like lensing reconstruction. Note that the error bars on the *Planck* data points are smaller than predicted at low frequency, as our analysis (conservatively) does not assume that the CMB is cleaned using lower frequency data.

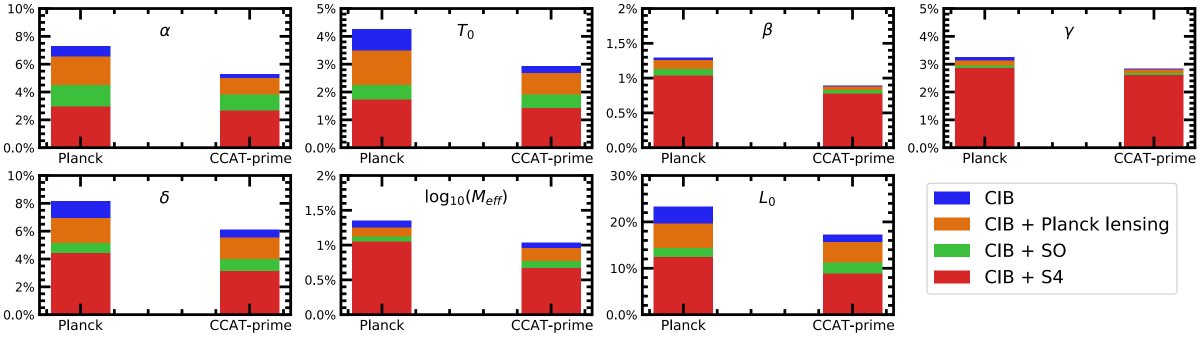

Figure 7.6: Percentage constraints on various CIB halo model parameters and their improvement with the incorporation of CMB lensing, for the CIB as measured by *Planck* and by CCAT-prime. We show improvements when including lensing reconstruction from *Planck* itself or from a future Simons Observatory-like or CMB-S4-like survey configuration.

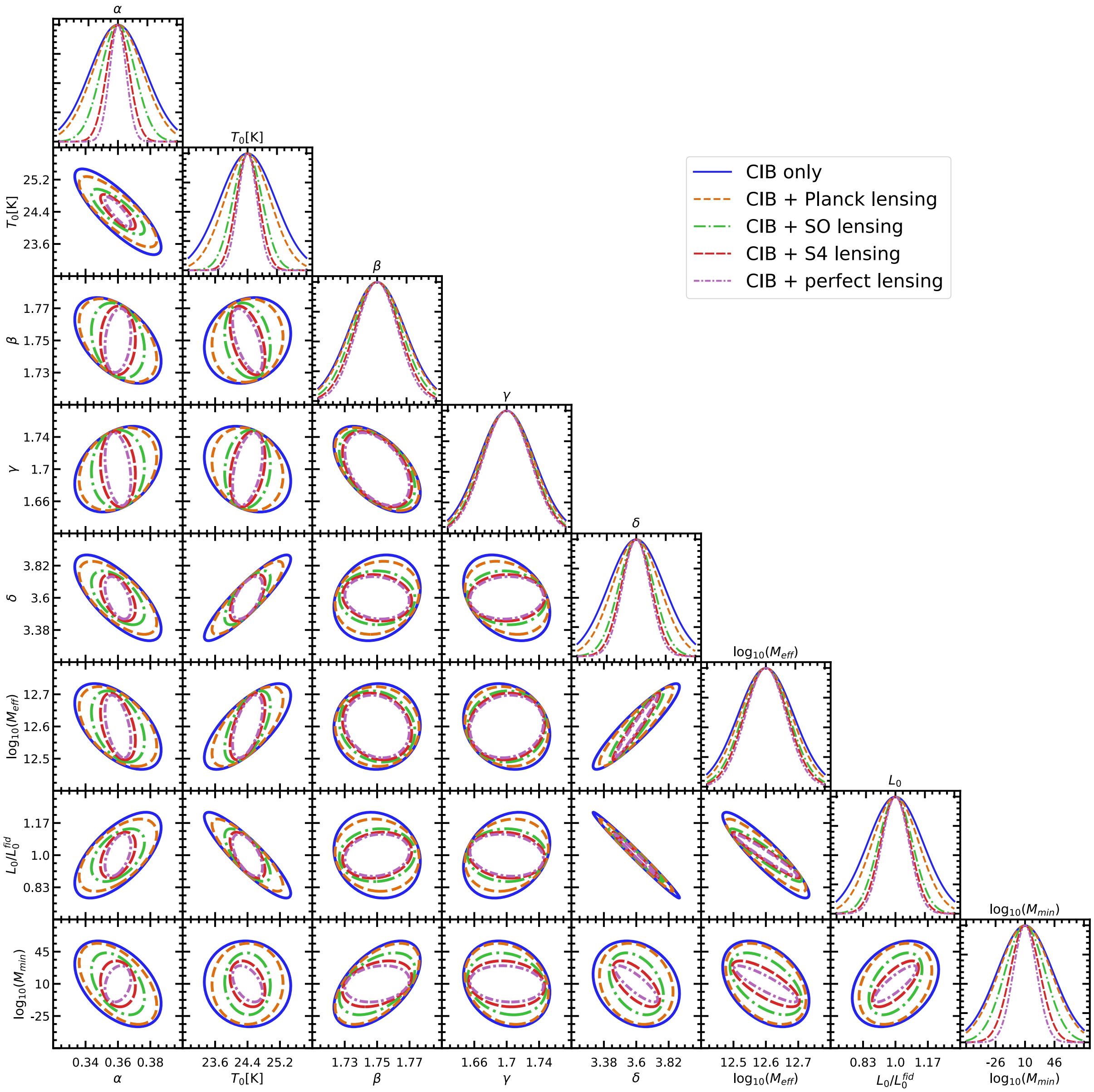

Figure 7.7: Forecast 1-σ confidence ellipses for various parameters of the CIB model, with and without CMB lensing information: in blue solid, we show constraints when only including *Planck* CIB measurements. In orange dashed, we show constraints when including *Planck* lensing reconstruction in addition. In green (dot-dashed) and red (dashed), the constraints when adding a Simons Observatory-like and CMB-S4-like lensing reconstruction are shown respectively. In purple dot-dashed, we show constraints when adding a noiseless CMB lensing reconstruction.

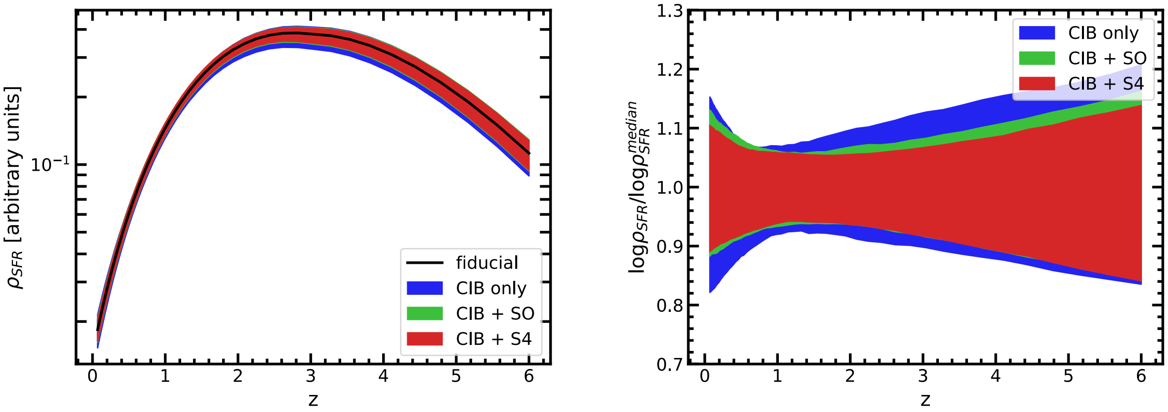

Figure 7.8: Star formation rate constraints for *Planck*-like CIB data with various lensing scenarios. On the left ρ_{SFR} is plotted in arbitrary units on a log scale, and the fiducial value is also shown. On the right we show a linear scale, and we divide by the median value of each set of realisations to make the improvements more visible. Note that we only consider *Planck*-like CIB data, specifically the no-lensing scenario (blue), the SO-lensing scenario (green), and the S4-like lensing scenario (red).

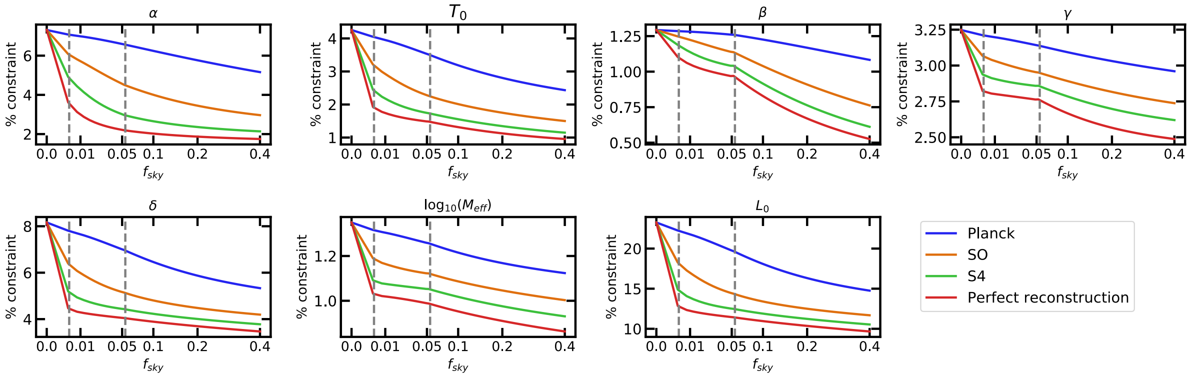

Figure 7.9: The improvement in CIB model constraints with the area of the CIB-lensing cross correlation included in the analysis. In all cases the CIB auto power spectrum is measured on the fiducial 2240 square degrees (183 square degrees for 3000 GHz), and the lensing field is introduced first on the small 183 square degree patch where we have the entire *Planck*+IRIS fields, then onto the 2240 square degrees where we have the *Planck* fields, and finally it is included without the CIB auto power spectra measured on the same patch. The two dashed grey lines denote these transitions. The x-axis has been transformed such that it is linear in $\sqrt{f_{\rm sky}}$.

Chapter 8

Velocity reconstruction with the CIB and the kSZ effect

8.1 Introduction

The Cosmic Microwave Background (CMB) temperature anisotropies have been measured with ever-improving angular resolution and sentitivity, from COBE's [10, 122] measurements of $\sim 10\mu K$ fluctuations on angular scales of $\sim 10^\circ$, to the *Planck* satellite [123] and ground-based CMB experiments such as SPT and ACT measuring $\sim 10^{-2}\mu K$ fluctuations on $\sim 1'$ scales. These experiments have extracted almost all of the information from the *primary* CMB — anisotropies sourced primarily at the surface of last scattering, where the CMB was released. However, there remains much information to be extracted from CMB *secondaries*: anisotropies generated through the interaction of CMB photons with mass (lensing) or charges (the Sunyaev–Zel'dovich (SZ) effect) throughout the universe. These effects are on the resolution/sensitivity frontier, and while they have been detected with moderate significance thus far, future experiments such as Simons Observatory [16] (S), CCAT-prime [124], CMB-S4 [17], PICO [125], or CMB-HD [126] will provide highly significant measurements of the secondary CMB.

The kinetic Sunyaev Zel'dovich (kSZ) effect is one such secondary temperature anisotropy, induced by the scattering of CMB photons off electrons with non-zero CMB dipole in their rest frame [50]. The kSZ effect is the dominant blackbody component of the CMB on angular scales corresponding to $l \gtrsim 4000$, and has been detected at the $> 4\sigma$ level [127, 128, 129, 130, 131, 132, 133]. The kSZ effect is interesting from a cosmological perspective because of its dependence on the remote dipole field, the CMB dipole observed at different locations in the universe. The remote dipole field can be reconstructed using the correlations between CMB temperature and a tracer of density, a technique known as tomography [134, 135, 136, 137, 138, 139, 140, 141, 142]. Forecasts [140, 141, 142] indicate that the remote dipole field can be reconstructed with high signal-to-noise through cross-correlation of next-generation CMB experiments and a large redshift survey such as LSST [54]. These measurements of the remote dipole field have the potential to improve constraints on primordial non-Gaussianity [143], determine the physical nature of various anomalies in the primary CMB [144] (e.g. the lack of power on large scales, the hemispherical power asymmetry, the alignment of low multipoles), provide precision tests of gravity [145, 146], and constrain the state of the universe before inflation [138].

In this Chapter we adapt the techniques of Ref. [140] to define a quadratic estimator for the remote dipole field from a *2-dimensional* tracer of structure in cross-correlation with CMB temperature maps. In particular we consider as the 2-dimensional tracer the Cosmic Infrared Background (CIB), infrared radiation from dusty star-forming galaxies. The anisotropies in the CIB trace the distribution of large scale structure (LSS), and have been measured with increasing accuracy from balloon (e.g. BLAST [147]) and ground-based facilities (e.g. SPT [72, 133] and ACT [148]) as well as satellite missions (e.g. Herschel [70] and *Planck* [69]) over a wide range of frequencies ($\sim 100-1200$ GHz). In principle, the CIB can provide constraints on cosmology. However, the main obstruction to using the CIB as a competitive cosmological probe (e.g. to measure primordial non-Gaussianity [149]) is the lack of maps on large fractions of the sky with sufficiently low foreground residuals (see e.g. [75]). Although, by virtue of its large correlation with the lensing potential [150], the CIB has proven to be a useful tool for de-lensing CMB polarization maps to obtain improved constraints on primordial gravitation waves [151].

To obtain a high fidelity reconstruction of the remote dipole field, it is necessary to measure the clustered component of the tracer (here the CIB) on angular scales of $\ell \sim 3000-4000$, where kSZ becomes comparable in amplitude to the primary CMB [140, 142]. This resolution/sensitivity has been achieved for the CIB with existing experiments, e.g. SPT [133], albeit on small areas of the sky. The CIB at a fixed frequency samples structure over a wide range of redshifts, and only a significantly coarse-grained reconstruction of the remote dipole field can be obtained using kSZ tomography. This coarse-grained dipole field has structure primarily on large angular scales, which means that measurements of the CIB on large fractions of the sky are necessary for kSZ tomography. If future measurements can achieve this, the course-grained remote dipole field provided by kSZ tomography will probe the homogeneity of the universe on the very largest scales. This can be used to constrain various models of early-universe physics [144, 138].

To assess the utility of the CIB for kSZ tomography, we perform a set of simplified forecasts for the *Planck* satellite and for a future experiment with specifications similar to a stage-4 CMB experiment [17]. In our forecasts, we assume that the CIB can be perfectly separated from the blackbody component (the lensed primary CMB and kSZ) in each channel, as well as from other foregrounds. We further assume data on the full sky, Gaussian beam, and white instrumental noise. We perform a principal component analysis to identify which modes of the CMB dipole field we can hope to reconstruct from the CIB and find that reconstruction of a linear combination (in redshift space) of the remote dipole will be possible for modes with redshift-weightings corresponding to that of the CIB integration kernel. Under these assumptions, we find that the remote dipole can be reconstructed with an overall signal-to-noise of order one using *Planck*-quality data. We also perform a forecast for a next-generation experiment; for an idealistic case with no foregrounds, we find that a full-sky survey could in principle perform a mode-by-mode reconstruction of the remote dipole field on large-scales with high signal-to-noise ($> \mathcal{O}(10)$ for $\ell < 10$), and obtain an overall signal-to-noise of $\mathcal{O}(1000 - 10000)$.

The remote dipole field can also be reconstructed using future galaxy redshift surveys. We demonstrate that the CIB-based reconstruction of the remote dipole field is highly correlated with the galaxy-based reconstruction. While this implies that there is limited additional cosmological information to mine from the CIB-based reconstruction, the methods developed in this Chapter to obtain CIB information are interesting nevertheless. First, as we wait for LSST-like galaxy surveys to become available to use for tomography, alternative methods are worth investigating as the density tracer maps might become available earlier than LSST. Secondly, the large correlation can be used to address the optical depth degeneracy [76, 152, 142]: the modelling uncertainty in the correlation between electrons and the tracer used for the reconstruction. The optical depth degeneracy manifests as a redshift-dependent bias on the reconstructed dipole field, different for each tracer. By correlating the CIB-based and galaxy-based reconstructions, it is possible to measure the ratio of optical depth bias parameters with arbitrary accuracy. Such a measurement could both help extract cosmology from reconstructions of the remote dipole field, as well as provide insight into physical models of both the CIB and electron distribution.

This Chapter is organized as follows. In Section 8.2 we derive the quadratic estimators we use; in Section 8.3 we will describe our forecast; in Section 8.4 we will present the results of our forecasts for *Planck*-quality data and a next-generation experiment; in Section 8.5 we explore the correlations between the CIB-based and galaxy-based remote dipole reconstructions; we conclude in section 8.7.

8.2 KSZ tomography: reconstruction via a 2-dimensional field

We wish to reconstruct the remote dipole field by cross-correlating the CMB temperature anisotropies with the CIB intensity, which is a two-dimensional field defined by the line-of-site integral over the 3-dimensional CIB emissivity density. Ref. [140] derived a minimum variance quadratic estimator for the remote dipole field using a 3-dimensional tracer (galaxy redshifts) and the CMB temperature anisotropies. Here, we adapt this analysis for the 2-dimensional case. Following [140], we use the cross-correlation between the kSZ-induced CMB temperature and our tracer to derive this estimator.

Neglecting optical depth effects, the kSZ-induced temperature anisotropy in the direction $\hat{\mathbf{n}}$ is given by

$$\left.\frac{\Delta T}{T}\right|_{\mathrm{kSZ}}(\hat{\mathbf{n}}) = \int_0^{\chi_{\mathrm{re}}} d\chi\ \dot{\tau}\left(\hat{\mathbf{n}},\chi\right) v_{\mathrm{eff}}\left(\hat{\mathbf{n}},\chi\right) \tag{8.1}$$

The integral over comoving radial distance χ is done out to reionization at χ_{re}. The remote dipole field $v_{\mathrm{eff}}\left(\hat{\mathbf{n}},\chi\right)$ is defined by

$$v_{\mathrm{eff}}\left(\hat{\mathbf{n}},\chi\right) \equiv \sum_{m=-1}^{1} \Theta_1^m\left(\hat{\mathbf{n}},\chi\right) Y_{1m}\left(\hat{\mathbf{n}}\right), \tag{8.2}$$

$$\Theta_1^m\left(\hat{\mathbf{n}},\chi\right) \equiv \int d^2\hat{\mathbf{n}}'\ \Theta(\hat{\mathbf{n}},\chi,\hat{\mathbf{n}}')Y_{1m}(\hat{\mathbf{n}}') \tag{8.3}$$

where $\Theta(\hat{\mathbf{n}},\chi,\hat{\mathbf{n}}')$ is the CMB temperature the electron at $(\hat{\mathbf{n}},\chi)$ sees along direction $\hat{\mathbf{n}}'$, $\Theta(\hat{\mathbf{n}},\chi,\hat{\mathbf{n}}') = \Theta_{\mathrm{SW}} + \Theta_{\mathrm{ISW}} + \Theta_{\mathrm{Dop}}$, with the usual contributions from Sachs-Wolfe (SW), Integrated Sachs-Wolfe (ISW), and Doppler (Dop) effects. The dominant contribution to the remote dipole field at any point in spacetime is the Doppler effect from the peculiar velocity field, and therefore one can approximate $v_{\mathrm{eff}} \simeq \vec{\boldsymbol{v}}\cdot\hat{\mathbf{n}}$ unless long-distance correlations of the remote dipole field are considered. Such correlations will be relevant to our discussion below, and so we consider all contributions to the remote dipole field. A more detailed description of the properties of the remote dipole field can be found in Refs. [139, 140]. The differential optical depth $\dot{\tau}(\chi,\hat{\mathbf{n}})$ is defined by

$$\dot{\tau}\left(\chi,\hat{\mathbf{n}}\right) = -\sigma_T a(\chi) n_e\left(\chi,\hat{\mathbf{n}}\right); \tag{8.4}$$

here σ_T is the Thompson scattering cross section, which governs the rate of the scattering of the photons and electrons; $a(\chi)$ is the scale factor at comoving distance χ; $n_e\left(\chi,\hat{\mathbf{n}}\right)$ is the comoving electron number density.

We proceed by defining N redshift bins, labelled by α where $\alpha \in 1 \cdots N$, each with comoving-distance boundaries $\chi^\alpha_{\rm min}, \chi^\alpha_{\rm max}$. The optical depth τ^α in each bin is thus defined as

$$\tau^\alpha(\hat{\mathbf{n}}) \equiv \int_{\chi^\alpha_{\rm min}}^{\chi^\alpha_{\rm max}} d\chi \dot{\tau}\left(\chi, \hat{\mathbf{n}}\right). \tag{8.5}$$

The bin-averaged dipole field is

$$\bar{v}^\alpha_{\rm eff}(\hat{\mathbf{n}}) = \frac{1}{\chi^\alpha_{\rm max} - \chi^\alpha_{\rm min}} \int_{\chi^\alpha_{\rm min}}^{\chi^\alpha_{\rm max}} d\chi\, v_{\rm eff}\left(\chi, \hat{\mathbf{n}}\right) \tag{8.6}$$

with

$$v_{\rm eff}\left(\chi^\alpha, \hat{\mathbf{n}}\right) = \bar{v}^\alpha_{\rm eff}(\hat{\mathbf{n}})\left(1 + \delta v_{\rm eff}\left(\chi^\alpha, \hat{\mathbf{n}}\right)\right). \tag{8.7}$$

Contributions from $\delta v_{\rm eff}$ are small, due to cancelations along the line-of-sight, and we therefore have

$$\frac{\Delta T}{T}(\hat{\mathbf{n}}) \simeq \sum_\alpha \tau^\alpha(\hat{\mathbf{n}})\bar{v}^\alpha_{\rm eff}(\hat{\mathbf{n}}). \tag{8.8}$$

The CIB brightness $I_\nu(\hat{\mathbf{n}})$ at frequency ν is given by a line-of-sight integral over emissivity density $j_\nu(\chi, \hat{\mathbf{n}})$ (see e.g. [68]):

$$I_\nu(\hat{\mathbf{n}}) = \int_0^{\chi_{\rm re}} d\chi\, a(\chi) j_\nu\left(\chi, \hat{\mathbf{n}}\right). \tag{8.9}$$

We model the CIB with the halo model following the "minimally empirical" model for the mean emissivity density of [74]; for further details see Chapter 5.4.3.

We now compute the cross-correlation between the kSZ temperature anisotropy (8.8) and CIB brightness (8.9). We work in spherical harmonic space with the conventions

$$O(\hat{\mathbf{n}}) = \sum_{lm} o_{\ell m} Y_{\ell m}(\hat{\mathbf{n}}); \tag{8.10}$$

$$o_{\ell m} = \int d^2\hat{\mathbf{n}}\, O(\hat{\mathbf{n}}) Y^*_{\ell m}(\hat{\mathbf{n}}); \tag{8.11}$$

$o_{\ell m}$ are the coefficients of the expansion, which we denote for temperature as $a^T_{\ell m}$ and CIB intensity as $j^\nu_{\ell m}$. The cross-correlation is given by

$$\begin{aligned}\left\langle a^T_{\ell_1 m_1} I^\nu_{\ell_2 m_2}\right\rangle = &\sum_\alpha \sum_{L_1 M_1 L_2 M_2} \bar{v}^\alpha_{L_2 M_2}\left\langle \tau^\alpha_{L_1 M_1} j^\nu_{\ell_2 m_2}\right\rangle \\ &\int d^2\hat{\mathbf{n}}\, Y^*_{\ell_1 m_1}(\hat{\mathbf{n}}) Y_{L_1 M_1}(\hat{\mathbf{n}}) Y_{L_2 M_2}(\hat{\mathbf{n}}).\end{aligned} \tag{8.12}$$

We take the v_{LM} term out of the ensemble average because the dominant contribution to $\left\langle \tau^{\alpha}_{L_1 M_1} \bar{v}^{\alpha}_{L_2 M_2} j^{\nu}_{\ell_2 m_2} \right\rangle$ comes from $\bar{v}_{L_2 M_2} \left\langle \tau^{\alpha}_{L_1 M_1} j^{\nu}_{\ell_2 m_2} \right\rangle$ [139]. Using statistical isotropy to write angular power $\left\langle \tau^{\alpha}_{L_1 M_1} j^{\nu *}_{\ell_2 m_2} \right\rangle$ as

$$\left\langle \tau^{\alpha}_{\ell_1 m_1} I^{\nu *}_{\ell_2 m_2} \right\rangle \equiv C^{\tau \nu \alpha}_{\ell_1} \delta_{\ell_1 \ell_2} \delta_{m_1 m_2}, \tag{8.13}$$

or $\left\langle \tau^{\alpha}_{\ell_1 m_1} j^{\nu}_{\ell_2 m_2} \right\rangle = (-1)^{m_2} C^{\tau \nu \alpha}_{\ell_1} \delta_{\ell_1 \ell_2} \delta_{m_1, -m_2}$, and performing the angular integration in (8.12), gives us

$$\begin{aligned} \left\langle a^{T}_{\ell_1 m_1} j^{\nu}_{\ell_2 m_2} \right\rangle = \sum_{\alpha; L_2 M_2} (-1)^{m_1 + m_2} \sqrt{\frac{(2\ell_1 + 1)(2\ell_2 + 1)(2L_2 + 1)}{4\pi}} \begin{pmatrix} l_1 & l_2 & L \\ 0 & 0 & 0 \end{pmatrix} \\ \begin{pmatrix} \ell_1 & \ell_2 & L \\ -m_1 & -m_2 & M_2 \end{pmatrix} \bar{v}^{\alpha}_{L M_2} C^{\tau \nu \alpha}_{\ell_2} \end{aligned} \tag{8.14}$$

where $\begin{pmatrix} \ell & \ell_1 & \ell_2 \\ m & m_1 & m_2 \end{pmatrix}$ are the Wigner 3J symbols. We then define

$$\Gamma^{\alpha}_{\ell_1 \ell_2 L} \equiv \sqrt{\frac{(2\ell_1 + 1)\,(2\ell_2 + 1)\,(2L + 1)}{4\pi}} \begin{pmatrix} \ell_1 & \ell_2 & L \\ 0 & 0 & 0 \end{pmatrix} C^{\tau \nu \alpha}_{\ell_2} \tag{8.15}$$

such that

$$\left\langle a^{T}_{\ell_1 m_1} j^{\nu}_{\ell_2 m_2} \right\rangle = \sum_{\alpha; LM} (-1)^{m_1 + m_2} \Gamma^{\alpha}_{\ell_1 \ell_2 L} \begin{pmatrix} \ell_1 & \ell_2 & L \\ -m_1 & -m_2 & M \end{pmatrix} \bar{v}^{\alpha}_{LM}. \tag{8.16}$$

8.2.1 Defining an estimator for the dipole field

We want to define a minimum variance quadratic estimator for $\bar{v}$ as in [140]. Note, however, the key difference that in [140] the CMB temperature was being cross-correlated with a 3-D field that *could itself be binned into redshift bins* just as we bin the optical depth, and constrast this to the case we have here, where we cross-correlate the CMB temperature field with a 2-D field that cannot be redshift-binned. This difference manifests itself in the sum over α on the right hand side of (8.16).

We can proceed by defining an estimator

$$\hat{v}^{\alpha}_{LM} = \sum_{\ell_1 m_1 \ell_2 m_2} W^{\alpha}_{LM \ell_1 m_1 \ell_2 m_2} a^{T}_{\ell_1 m_1} j^{\nu *}_{\ell_2 m_2} \tag{8.17}$$

that minimizes the variance, but dropping the constraint that it must be unbiased; i.e. we have

$$\langle \hat{v}^{\alpha}_{LM} \rangle \neq \bar{v}^{\alpha}_{LM}. \tag{8.18}$$

We can then build unbiased estimators from linear combinations of $\hat{v}^{\alpha}$, using the techniques of [153]; we will find that

$$\langle \hat{v}^{\alpha}_{LM} \rangle = R_{\alpha\beta} \bar{v}^{\beta}_{LM} \tag{8.19}$$

for some rotation matrix $R_{\alpha\beta}$. This will allow us to define an *unbiased* quadratic estimator $\hat{v}'^{\alpha}_{LM}$ by

$$\hat{v}'^{\alpha}_{LM} = \left(R^{-1}\right)_{\alpha\beta} \hat{v}^{\beta}_{LM} \tag{8.20}$$

which will have

$$\langle \hat{v}'^{\alpha}_{LM} \rangle = \bar{v}^{\alpha}_{LM}. \tag{8.21}$$

Of course, this will not necessarily be a minimum variance estimator; it will have variance

$$\left\langle \hat{v}'^{\alpha}_{LM} \hat{v}'^{\beta}_{L'M'} \right\rangle = \left(R^{-1}\right)_{\alpha\gamma} \left(R^{-1}\right)_{\beta\delta} N^{\bar{v}\bar{v}}_{\gamma\delta L} \delta_{LL'} \delta_{MM'} \tag{8.22}$$

where the variance of the original estimator $\hat{v}^{\alpha}_{LM}$ is given by

$$\left\langle \hat{v}^{\alpha}_{LM} \hat{v}^{\beta}_{L'M'} \right\rangle = N^{\bar{v}\bar{v}}_{\alpha\beta L} \delta_{LL'} \delta_{MM'}. \tag{8.23}$$

To find the (biased) minimum variance estimator for each bin, we can follow [44] and rewrite the M-dependence of the weights $W^{\alpha}_{LM\ell_1 m_1 \ell_2 m_2}$ in terms of the Wigner 3J-symbols along with a normalization A^{α}_{L} and ℓ-coupling term $w^{\alpha}_{\ell_1\ell_2 L}$ such that

$$\hat{v}^{\alpha}_{LM} = A^{\alpha}_{L} (-1)^{M} \sum_{\ell_1 m_1 \ell_2 m_2} \begin{pmatrix} \ell_1 & \ell_2 & L \\ m_1 & m_2 & -M \end{pmatrix} w^{\alpha}_{\ell_1 \ell_2 L}\, a^{T}_{\ell_1 m_1} j^{\nu}_{\ell_2 m_2}; \tag{8.24}$$

we find (using (8.16)) that the mean is

$$\langle \hat{v}^{\alpha}_{LM} \rangle = \frac{A^{\alpha}_{L}}{2L+1} \sum_{\beta;\ell_1\ell_2} w^{\alpha}_{\ell_1\ell_2 L}\, \Gamma^{\beta}_{\ell_1\ell_2 L}\; \bar{v}^{\beta}_{LM}. \tag{8.25}$$

As we have no requirements on what the mean should be, we can choose to "ignore" the contributions to the mean from the terms in the sum over β where $\beta \neq \alpha$ and, so that we can follow closely the standard procedure of [140], define the normalization A^{α} as

$$A^{\alpha}_{L} = \frac{2L+1}{\sum_{\ell_1\ell_2} w^{\alpha}_{\ell_1\ell_2 L} \Gamma^{\alpha}_{\ell_1\ell_2 L}}. \tag{8.26}$$

We can now proceed to minimize the variance of the estimator to solve for $w^\alpha_{\ell_1\ell_2L}$; we find that

$$w^\alpha_{\ell_1\ell_2L} = \frac{\Gamma^\alpha_{\ell_1\ell_2L}}{C^{TT}_{\ell_1}C^{\nu\nu}_{\ell_2}}, \tag{8.27}$$

where C^{TT}_ℓ is the temperature angular power spectrum and $C^{\nu\nu}_\ell$ is the angular power spectrum of the CIB brightness. Thus the (biased) minimum variance estimator in each bin is

$$\hat{v}^\alpha_{LM} = A^\alpha_L(-1)^M \sum_{\ell_1 m_1 \ell_2 m_2} \begin{pmatrix} \ell_1 & \ell_2 & L \\ m_1 & m_2 & -M \end{pmatrix} \Gamma^\alpha_{\ell_1\ell_2L} \frac{a^T_{\ell_1 m_1} j^\nu_{\ell_2 m_2}}{C^{TT}_{\ell_1}C^{\nu\nu}_{\ell_2}} \tag{8.28}$$

where

$$\frac{1}{A^\alpha_L} = \frac{1}{2L+1} \sum_{\ell_1\ell_2} \frac{\Gamma^\alpha_{\ell_1\ell_2L}\Gamma^\alpha_{\ell_1\ell_2L}}{C^{TT}_{\ell_1}C^{\nu\nu}_{\ell_2}}. \tag{8.29}$$

We define the noise $N^{\bar{v}\bar{v}}_{\alpha\beta L}$ as the variance in the absence of signal $\left\langle \hat{v}^\alpha_{LM} \hat{v}^{*\beta}_{L'M'} \right\rangle$; we find

$$N^{\bar{v}\bar{v}}_{\alpha\beta L} = \frac{A^\alpha_L A^\beta_L}{2L+1} \sum_{\ell_1\ell_2} \frac{\Gamma^\alpha_{\ell_1\ell_2L}\Gamma^\beta_{\ell_1\ell_2L}}{C^{TT}_{\ell_1}C^{\nu\nu}_{\ell_2}}. \tag{8.30}$$

8.2.2 Debiasing $\hat{v}^\alpha$

$\hat{v}^\alpha$ is biased since $\langle \hat{v}^\alpha_{LM} \rangle \neq \bar{v}^\alpha_{LM}$; indeed, we find that its mean is

$$\langle \hat{v}^\alpha_{LM} \rangle = \frac{1}{\sum_{\ell_1\ell_2} \left(\frac{\Gamma^\alpha_{\ell_1\ell_2L}}{C^{TT}_{\ell_1}C^{\nu\nu}_{\ell_2}} \right)^2} \sum_{\ell_1\ell_2} \frac{\Gamma^\alpha_{\ell_1\ell_2L}\Gamma^\beta_{\ell_1\ell_2L}}{C^{TT}_{\ell_1}C^{\nu\nu}_{\ell_2}} \bar{v}^\beta_{LM}. \tag{8.31}$$

This allows us to read off the "rotation matrix" $R_{\alpha\beta}$ of (8.19) as

$$R_{\alpha\beta} = \frac{1}{\sum_{\ell_1\ell_2} \left(\frac{\Gamma^\alpha_{\ell_1\ell_2L}}{C^{TT}_{\ell_1}C^{\nu\nu}_{\ell_2}} \right)^2} \sum_{\ell_1\ell_2} \frac{\Gamma^\alpha_{\ell_1\ell_2L}\Gamma^\beta_{\ell_1\ell_2L}}{C^{TT}_{\ell_1}C^{\nu\nu}_{\ell_2}}; \tag{8.32}$$

we can then define an estimator $\hat{v}'^\alpha$ via (8.20), with variance given by (8.22).

Henceforward we will drop the prime and refer to the set of unbiased estimators as $\hat{v}^\alpha$.

8.3 Signal-to-noise forecasts

8.3.1 Signal model

Our signal model follows [139]. We wish to compute the bin-averaged dipole field power spectrum $C_L^{\bar{v}\bar{v}}$, which is given by

$$C_{\alpha\beta L}^{\bar{v}\bar{v}} = \int \frac{dk}{(2\pi)^3} k^2 P(k) \bar{\Delta}_{\alpha L}(k) \bar{\Delta}_{\beta L}(k) \tag{8.33}$$

with $\bar{\Delta}_{\alpha L}^{v}$ the bin-averaged dipole field transfer function

$$\bar{\Delta}_{\alpha L}^{v}(k) = \frac{1}{\chi_{\text{max}}^{\alpha} - \chi_{\text{min}}^{\alpha}} \int_{\chi_{\text{min}}^{\alpha}}^{\chi_{\text{max}}^{\alpha}} d\chi \Delta_L^v(k, \chi) \tag{8.34}$$

and $\Delta_L^v(k, \chi)$ defined by

$$v_{LM}^{\alpha} = \int \frac{d^3\mathbf{k}}{(2\pi)^3} \Delta_L^v(k, \chi) \Psi_i(\mathbf{k}) Y_{LM}(\hat{\mathbf{k}}). \tag{8.35}$$

$\Delta_L^v(k, \chi)$ has contributions from a Sachs–Wolfe (SW), integrated Sachs–Wolfe (ISW), and Doppler term as given in References [139, 140]. As we will see below, it is necessary to include all contributions to properly model the bin-averaged remote dipole reconstructed using the CIB.

8.3.2 Noise model

The reconstruction noise depends on models for C_ℓ^{TT}, $C_\ell^{\nu\nu}$, and $C_\ell^{\tau\nu}$ (which appear in (8.30) and (8.32) via $\Gamma_{\ell_1 \ell_2 L}^{\alpha}$). We assume that the blackbody contribution to the CMB can be perfectly separated from the CIB, and that all foregrounds for both the CMB and CIB can be perfectly removed.

The CMB temperature anisotropy power spectrum C_ℓ^{TT} is a sum of the lensed primary CMB, the kSZ contribution, and the instrumental noise:

$$C_\ell^{TT} = C_\ell^{\text{lensed}} + C_\ell^{kSZ} + N_\ell^{TT}. \tag{8.36}$$

C_ℓ^{lensed} is computed with CAMB [154] and C_ℓ^{kSZ} is computed using the model described in Ref. [142]. The instrumental noise N_ℓ is given by

$$N_\ell = N_T \exp\left(\frac{\ell(\ell+1)\Theta^2}{8\ln 2}\right) \tag{8.37}$$

where N_T is the noise per pixel squared and Θ is the (Gaussian) beam Full Width at Half Maximum.

Within the halo model-based approach we follow (see e.g. Ref. [55] for a review of the halo model), $C_\ell^{\nu\nu}$ comprises four terms: a one-halo term, a two-halo term, a "shot-noise" term corresponding to self-pairs of galaxies, and an instrumental noise term:

$$C_\ell^{\nu\nu} = C_\ell^{\nu\nu 1h} + C_\ell^{\nu\nu 2h} + C_\ell^{\nu\nu \text{Shot Noise}} + N_\ell^{\nu\nu}. \tag{8.38}$$

The instrumental noise is as in (8.37). The shot noise depends on the flux cut for removing point sources, which is a function of the resolution and sensitivity of an experiment. The optical depth-CIB correlation function $C_\ell^{\tau\nu}$ is also computed within the halo model; details are in Chapter 5.6.

8.3.3 Signal-to-noise

Because the reconstruction noise $N_{\alpha\beta L}^{\bar{v}\bar{v}}$ and signal $C_{\alpha\beta L}^{\bar{v}\bar{v}}$ are both correlated between redshift bins, we perform a Principal Component Analysis (PCA) to isolate uncorrelated modes $\hat{v}'^{\alpha}$. The PCA consists of changing our basis from $\hat{v}^{\alpha}$ to $\hat{v}'^{\alpha}$ via a linear transformation $A^{\alpha\beta}$ such that $\mathbf{C}'^{\bar{v}'\bar{v}'}_L = \mathbf{A}\mathbf{C}^{\bar{v}\bar{v}}_L\mathbf{A}^{-1}$ is diagonal with entries equal to the signal-to-noise of each principal component. We then define the signal-to-noise per mode of the remote dipole field for each principal component α as

$$(S/N)^{\alpha}_{LM} = \left(\frac{f_{\text{sky}}}{2}\left(C'^{\bar{v}'\bar{v}'}_{\alpha\alpha L}\right)^2\right)^{\frac{1}{2}}; \tag{8.39}$$

the total signal-to-noise for the reconstructed remote dipole field is

$$S/N = \left(\sum_{\alpha;L}\frac{f_{\text{sky}}}{2}\left(2L+1\right)\left(C'^{\bar{v}'\bar{v}'}_{\alpha\alpha L}\right)^2\right)^{\frac{1}{2}}. \tag{8.40}$$

Note that the total signal-to-noise is simply the Fisher information, which is a basis-independent quantity unaffected by our PCA; we have confirmed that an identical total signal-to-noise is obtained using the original, non-diagonal basis.

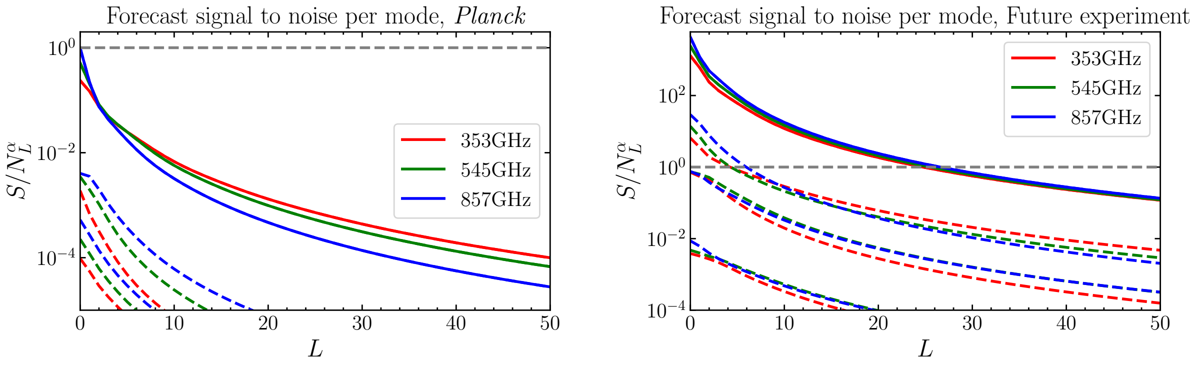

Figure 8.1: The signal-to-noise per mode of the first few principal components of the remote dipole field on the full sky. The dashed grey line corresponds to a signal-to-noise of 1. Left is *Planck*-quality data, right is the future experiment No mode can be reconstructed at signal-to-noise greater than 1 using *Planck*, while for the future experiments it is possible to perform reconstruction at high fidelity for the large-angular scale modes.

Frequency	143 GHz	353 GHz	545 GHz	857 GHz
Noise (μK^2_{CMB})	4.8×10^{-5}	1.30×10^{-3}	4.10×10^{-2}	23.5
Θ_{FWHM}(arcmin)	7.3	4.94	4.83	4.64

Table 8.1: Noise and resolution used for the *Planck* forecast, from [155].

8.4 Forecast results

8.4.1 *Planck*

We first perform a signal-to-noise forecast using values for the experimental noise (8.37) appropriate for the *Planck* experiment, to see if there is in principle sufficient statistical power in existing data to reconstruct the remote dipole field using the CIB. As such, we use the specifications for the High-Frequency Instrument from Table 12 of [155]. We choose the 143-GHz channel for the CMB and we consider the CIB at 353, 545, and 857 GHz. We further assume data on the full sky, neglect foregrounds, and assume that the CIB and CMB can be perfectly separated. Our noise values are given in Table 8.1.

For our redshift-binning scheme, we employ 12 bins of equal comoving width between $0.1 < z < 6$. This choice of redshift range includes most of the signal in the CIB and kSZ anisotropies. Increasing the number of bins does not increase the total signal-to-noise. For

Planck-quality data, we find that the signal-to-noise per mode is below one for all principal components; see Figure 8.1. Summing over all modes and principal components, the total signal-to-noise for the 353, 545, and 857 GHz channels the total signal-to-noise ratios are (0.63, 0.97, 1.5) respectively. We note that the contribution from the monopole ($l = 0$) of the reconstructed dipole field accounts for up to half the cumulative signal-to-noise. Since the different frequency bands of the CIB are highly correlated, it is unlikely that these can be combined to reach a signal-to-noise greater than 1.

To date, the largest foreground-cleaned CIB maps [75] have $f_{\rm sky} \sim 0.25$. Naively, from Eq. (8.40), this reduces the total signal-to-noise by a factor of two. An alternative measure of the degradation in total signal-to-noise due to partial sky coverage is to assume that the dipole field can only be reconstructed above a minimum multipole $L_{\rm min}$. In Figure 8.2, we plot the total signal-to-noise as a function of a minimum multipole $L_{\rm min}$ in the sum over L in (8.40). However, because most of the signal-to-noise is on the largest angular scales, the penalty can be significantly larger than expected from $f_{\rm sky}$, especially at high frequencies. We note, however, that because kSZ tomography uses small angular scale modes of the CIB to reconstruct the remote dipole field on large angular scales, it may be possible to use less aggressive sky cuts and retain a larger fraction of the CIB than has been used in previous analyses.

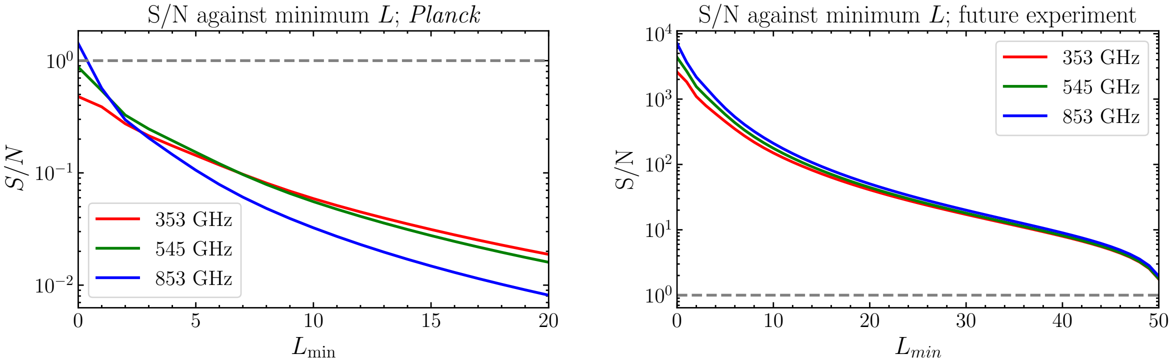

Figure 8.2: Total signal-to-noise as a function of the minimum multipole $L_{\rm min}$ of the first principal component of the remote dipole field that can be reconstructed. Left is for *Planck*-quality data, right is for the future experiment. We see that as we lose access to the remote dipole field on large angular scales (say by having partial-sky data) the total signal-to-noise drops significantly. However, for the future experiments the high signal-to-noise even with low $L_{\rm min}$ indicates it would be possible to make a detection even for significant sky cuts.

It is interesting that there is one principal component that is reconstructed with significantly higher signal-to-noise than the rest (see Figure 8.1). To get insight into what this linear combination is, we can plot the (normalized) components of this mode in the original basis against redshift; see Figure 8.3. We also plot the power contributed to the CIB from each redshift $W_\ell^{CIB}(\chi)$, defined by $C_\ell^{II} = \int d\chi W_\ell^{CIB}(\chi)$, at the relevant frequencies. The first principal component closely traces $W_\ell^{CIB}(\chi)$, with the lower frequency getting information from more distant redshifts. This is as expected, since the ability to reconstruct the remote dipole field at given redshift using kSZ tomography depends on the presence of measurable CIB fluctuations from that redshift.

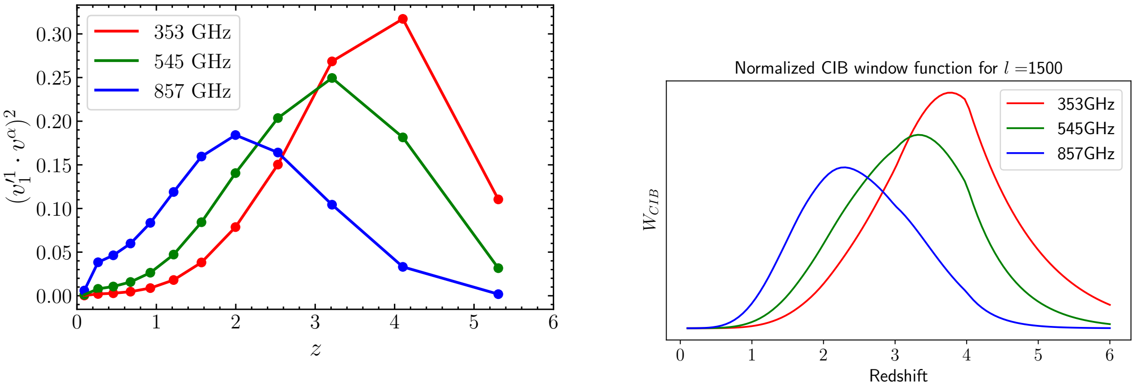

Figure 8.3: The first principal component of the remote dipole field $\hat{v}'^{\alpha}$ in the original $\hat{v}^{\alpha}$ basis for *Planck*-quality data at $L = 1$ (left). For comparison, we plot the power contributed from each redshift to the CIB at $\ell = 1500$ (curves do not strongly depend on the choice of ℓ), defined by $C_\ell^{II} = \int d\chi W_\ell^{CIB}(\chi)$. As expected, the principal components appropriately weight redshift bins according to their contribution to the observed CIB.

8.4.2 Future experiments

Although *Planck*-quality data is not sufficient to reconstruct the remote dipole field using the correlation between the CIB and kSZ temperature anisotropies, future experiments stand to greatly improve these measurements. Here, we consider a hypothetical experiment that measures the CMB and CIB at *Planck* frequencies with noise a factor of 10 lower than the values in Table 8.1 at a resolution of 1 arcminute. This is roughly consistent with proposals such as CMB-S4 and CMB-HD. We also lower the flux cuts above which point sources will be removed by a factor of 10 in the calculation of the shot noise, thus (in principle) lowering the shot noise on the CIB, although the effect is negligible. For comparison, flux cuts used for SPT analysis [133] are a factor of ~ 50 lower than *Planck* [69].

Upon considering these noise specifications, we find clear improvements in our signal-to-noise forecasts. For 12 redshift bins, and assuming full-sky data, no foregrounds, and perfect separation of the CMB and CIB, the total signal-to-noise at (353, 545, 857) GHz goes from (0.63, 0.97, 1.5) to (2600, 4366, 7100). For data of this quality, it is possible to achieve signal-to-noise per mode far greater than one on large angular scales. We plot the signal-to-noise per mode S/N_L^{α} in Figure 8.1 (right hand side) for the first four principal components. A high-fidelity map of the first principal component could be reconstructed up to $L \sim 20$. The shape of the first principal component in the redshift basis is shown in Figure 8.4. Comparing with Figure 8.3, we see that there is relatively more weight at lower redshift for the high frequency channels than for *Planck*-quality data. We also explore the dependence of the total signal-to-noise on the minimum multipole $L_{\rm min}$ that can be reconstructed in Figure 8.2. Even for relatively large $L_{\rm min}$, it is still possible to obtain a total signal-to-noise greater than one with a future experiment. We conclude that achievable future experiments will in principle have the statistical power to perform kSZ tomography using the CIB.

The modes that can be reconstructed with the highest fidelity are on the largest angular scales. To properly interpret the reconstruction on these scales, it is important to include all of the contributions to the remote dipole field, as described in Section 8.2. In particular, it is not a good approximation to replace $v_{\rm eff} \simeq \vec{\boldsymbol{v}} \cdot \hat{\mathbf{n}}$. For the monopole and dipole of the first principal component, the doppler contribution is of the same order as the SW and ISW terms. The SW and ISW contributions reach the percent-level only for $\ell > 5$. Any analysis using the largest angular scales of the CIB-based reconstruction should therefore include all contributions to the remote dipole field.

8.5 Correlations with remote dipole reconstruction from a galaxy redshift survey

8.5.1 Information content

Previous work [139, 140, 142, 141] demonstrated that a high fidelity reconstruction of the remote dipole field over a range of redshifts will be possible using future CMB experiments in concert with large galaxy redshift surveys, such as LSST. The constraining power of these future measurements for a variety of cosmological scenarios was subsequently explored

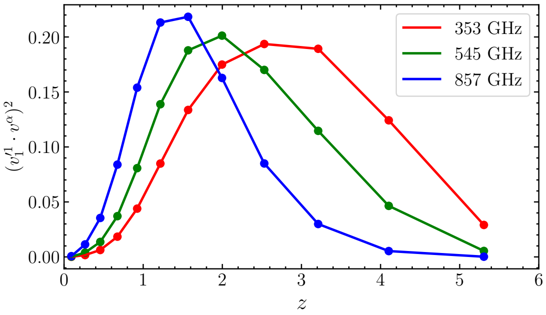

Figure 8.4: The first principal component of the dipole field computed using noise properties of a future experiment; compare with Figure 8.3.

in Refs. [138, 143, 152, 144, 145, 146]. Given that the remote dipole field will already be reconstructed quite well, it is natural to ask if the very coarse-grained reconstruction provided by the CIB will provide any useful new information. A quantitative measure of the information content in a set of correlated observables is given by the Fisher information:

$$F = \sum_L \frac{2L+1}{2} \mathrm{Tr}\left[\mathbf{C}_L(\mathbf{C}_L + \mathbf{N}_L)^{-1}\mathbf{C}_L(\mathbf{C}_L + \mathbf{N}_L)^{-1}\right]. \tag{8.41}$$

We construct an $(N_{\rm bin}+1)\times(N_{\rm bin}+1)$ covariance matrix $\mathbf{C}_L$ which includes the auto- and cross-correlation between v^{α}_{LM} in $N_{\rm bin}$ redshift bins reconstructed using a galaxy survey and the first principal component v'^{1}_{LM} from the reconstruction using the CIB (other principal components have far lower signal-to-noise). We assume that the noise covariance matrix $\mathbf{N}_L$ is diagonal, with the reconstruction noise on v'^{1}_{LM} calculated using the specs for the future experiment from above and reconstruction noise on the v^{α}_{LM} computed using LSST [54] as our proxy for a galaxy survey, as in Ref. [140] [1]. We project out various observables by sending the corresponding noise to infinity.

The Fisher information Eq. (8.41) for the CIB-based reconstruction at 353 GHz is $F_{\rm CIB} = 19.3$. The Fisher information for the galaxy-based reconstruction is significantly larger, $F_{\rm g} = 74.3$, due to the larger number of modes that are reconstructed at appreciable signal-to-noise. If the information in the CIB-based reconstruction were independent of that in the galaxy-based reconstruction (as might be expected from the redshift weighting of the first principal component, as in Figure 8.4), the combined Fisher information

---

[1] The reconstruction noise depends on our model of the galaxy bias and the shot noise for LSST. We assume the galaxy bias is $b = 0.95/D(z)$, where $D(z)$ is the growth function, and that the number density of galaxies per arcmin^2 is $n(z) = (n_{\rm gal}/2z_0)(z/z_0)^2 \exp(-z/z_0)$ with $z_0 = 0.3$ and $n_{\rm gal} = 40$ arcmin^{-2}

would simply be the sum of these two. However, at the large angular scales on which it can be reconstructed, the remote dipole field has a significant correlation length (see e.g. Ref. [140]). Accounting for these correlations, the Fisher information using the full set of observables is $F_{\rm g+CIB} = 76.5$, implying that only roughly 11% of the information in the CIB-based reconstruction is independent. We therefore expect the CIB-based reconstruction to offer limited improvements in the constraints on cosmological models beyond what is possible using the galaxy-based reconstruction. However, we emphasize that this analysis only accounts for statistical error, and that the systematics associated with the CIB-based reconstruction could be less severe, or complementary, to the galaxy-based reconstruction. In this case, the additional information from the CIB-based reconstruction could be important for deriving cosmological constraints from the remote dipole field. A study of mock data, which we refer to future work, will be able to quantify better the effect of systematics on each case.

8.5.2 Optical depth degeneracy

A significant obstruction to using kSZ tomography for cosmology arises from the inability to perfectly model the correlations between the optical depth and the tracer being used in the reconstruction, in this case the CIB intensity (e.g. the power spectrum Eq. (8.13), which is a necessary component for the dipole field estimator). This model uncertainty manifests itself as a redshift-dependent linear bias on the reconstructed dipole field, and is known as the "optical depth degeneracy"; see Refs. [76, 142, 152] for a detailed discussion. This optical depth bias is degenerate with the amplitude and growth of structure, making it difficult to derive cosmological constraints from the reconstructed dipole field alone. However, we can utilize the fact that both the galaxy-based and CIB-based reconstructions trace the same realization of the remote dipole field to measure the ratio of the optical depth bias of the two tracers as a function of redshift. This is an example of sample variance cancelation [103, 156], and in principle the ratio of bias parameters can be measured arbitrarily well in the limit of vanishing reconstruction noise – e.g. without cosmic variance.

We can investigate this by considering again the $(N_{\rm bin}+1)\times(N_{\rm bin}+1)$ covariance matrix $\mathbf{C}_\ell$, with N_{bins} columns corresponding to galaxy reconstruction and the remaining column to the first principal component. We include the optical depth modelling-bias parameters b_g^α and b_{CIB}^α in the covariance matrix using the definitions:

$$v_g^\alpha = b_g^\alpha \bar{v}^\alpha, \quad v'_{CIB} = \sum_\alpha c^\alpha b_{CIB}^\alpha \bar{v}^\alpha \tag{8.42}$$

where $\bar{v}^\alpha$ is the true dipole field in bin α and c^α is the eigenvector of the first principal component. The introduced optical-depth "bias" b^α parameters (which are unrelated to the bias that appears in the power spectrum) quantify modelling uncertainties in the electron—galaxy or electron—CIB cross-corellations.

We consider a simplified analysis, where the amplitude of the primordial power spectrum A_s is allowed to vary, but the other ΛCDM parameters are held fixed. The bias parameters are each totally degenerate with A_s, which is the manifestation of the optical depth degeneracy. We therefore define a reduced parameter space characterized by:

$$\gamma^\alpha \equiv b^\alpha_{CIB}/b^\alpha_g \qquad \beta^\alpha \equiv b^\alpha_g A_s \tag{8.43}$$

We compute the forecaste 1-sigma constraints on β^α and γ^α from the Fisher matrix:

$$F_{AB} = \sum_L \frac{2L+1}{2} \operatorname{Tr}\left[(\mathbf{C}_L + \mathbf{N}_L)^{-1} \frac{\partial \mathbf{C}_L}{\partial \Pi^A} (\mathbf{C}_L + \mathbf{N}_L)^{-1} \frac{\partial \mathbf{C}_L}{\partial \Pi^B} \right] \tag{8.44}$$

where Π^A is our $2N_{\rm bin}$-dimensional parameter vector. We use 12 bins and assume fiducial values of $b^\alpha_g = 1$, $b^\alpha_{CIB} = 1$, and $A_s = 2.2$ (the factor of 10^{-9} is absorbed into the definition of the dipole field), translating to $\gamma^\alpha = 1$ and $\beta^\alpha = 2.2$. The 1-sigma marginalized constraints $\sqrt{(F^{-1})_{AA}}$ for β^α and γ^α are shown in Figure 8.5. We have assumed the noise properties of the future experiment described above, along with galaxy number densities consistent with those expected from LSST. Note that we have not included the covariance between the different frequency channels, presenting each as a separate forecast. For all frequencies, the constraint on γ^α is order $\sim 10\%$ in the redshift range $1 \lesssim z \lesssim 3$, which is where the galaxy-based reconstruction noise is lowest. The best constraint on γ^α reaches the $\sim 3\%$-level, for the 857 GHz channel at $z \sim 1$. This is expected, since the first principal component of the dipole field reconstructed using the 857 GHz channel has the highest correlation coefficient with the galaxy-based reconstruction, peaking around $z \sim 1$. Percent level constraints on b^α_g can be obtained by correlating the remote dipole field with another tracer, such as the distribution of fast radio bursts [152] or the large-scale modes of a galaxy survey [145]. It therefore seems likely that percent-level measurements of b^α_{CIB} itself will be possible, allowing for cosmological information to be harvested from the CIB-based dipole field reconstruction. Such measurements would also provide information on galaxy formation and evolution, e.g. through constraints on the parameters in the halo model.

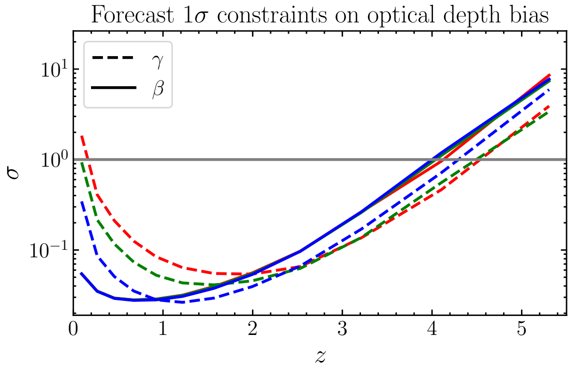

Figure 8.5: 1σ constraints on the optical depth bias. We plot the results of our Fisher forecast for the $1-\sigma$ constraints on the bias parameters $\beta^{\alpha} = b_g^{\alpha} A_S$ (solid line) and $\gamma^{\alpha} = b_{CIB}^{\alpha}/b_g^{\alpha}$ (dashed line). We performed three separate forecasts, one at each frequency.

8.6 Reconstruction on mock data

As an illustration of our technique, we can apply our estimator to mock (simulated) data. In particular, we consider the Websky simulations [157], which provides a three-dimensional halo catalogue out to $z = 4.6$ and converts these to intensity maps corresponding to kSZ emission, CIB emission, and various other processes. The velocities of each halo are also provided from the halo catalogue. As such, we can apply our estimator to the CIB and kSZ maps provided, and check its fidelity by comparing the reconstructed velocity with the "true" velocity field of the simulation.

Note that the model used for the CIB in the Websky simulations differs slightly from that we have used previously, in that it uses the parametric fit of [70]. As such, we use this model to compute the $C_\ell^{\dot{\tau}\nu}$ when computing the filters in the estimators.

We take 6 bins in our reconstruction, with boundaries $z = (0.01, 0.32, 0.71, 1.2, 1.9, 2.9, 3.7, 4.6)$. The signal in each bin is plotted in Figure 8.6. The power spectrum of the mode we expect to reconstruct—ie, the principal component with high signal to noise—is also shown in this Figure in Figure 8.6, along with its redshift distribution (on the right). The map of the velocity field itself is shown in Figure 8.7.

After applying our estimator, we reconstruct the map on the right hand side of Figure 8.7. It is clear that, by eye, there is a high correlation between these maps. Their correlation coefficient is shown in Figure 8.10; a correlation coefficient of $r_L = 1$ corresponds to exact reconstruction. Note that it is clear from the left hand side Figure 8.10,

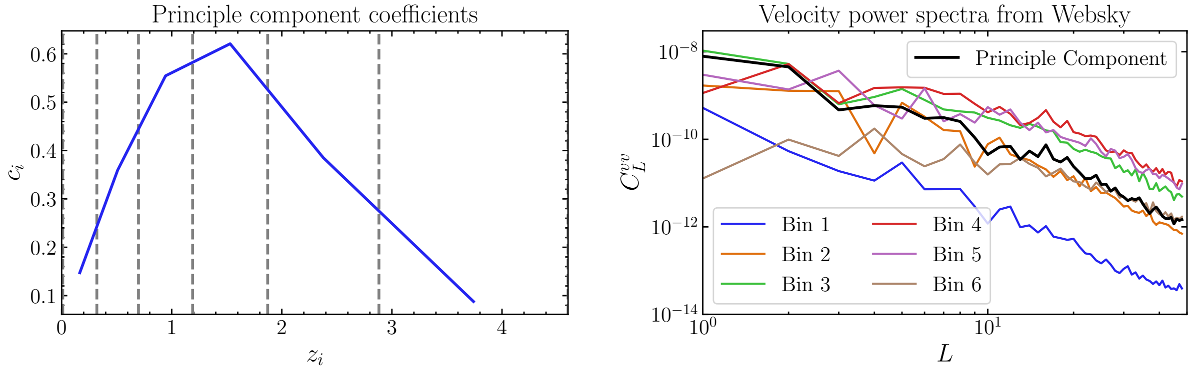

Figure 8.6: *Left*: The coefficients c_i corresponding to the well-reconstructed mode from the Websky analysis (with the 545 GHz CIB map). The mean redshift of each bin is plotted on the x axis, with vertical gray lines indicating the bin boundaries. We expect to reconstruct $\sum_{i=1}^{6} c_i v_i$ where c_i is plotted on the y axis. *Right*: The power spectra of the signal we want to reconstruct from Websky. The velocity power spectrum of each bin is shown, along with the power spectrum of the principal component we expect to reconstruct from the CIB, ie the power spectrum of the field $\sum c_i v_i$.

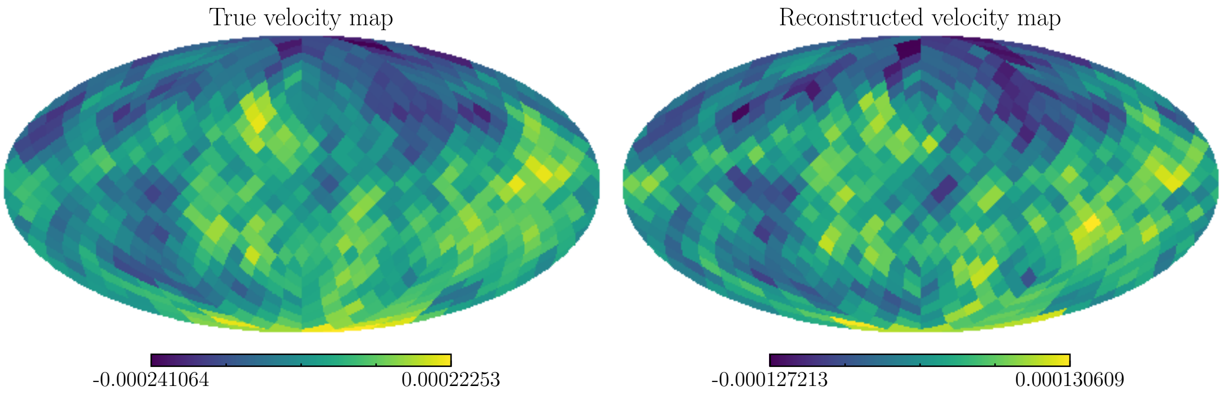

Figure 8.7: *Left:* The large scale mode of the velocity field, as read directly from the simulations *Right:* The recovered density field, as reconstructed with the quadratic estimator. By-eye, a strong correlation is seen between the two on large scales, indicating that the estimator is indeed recovering the signal we expect it to.

where the power spectra of each map is plotted, that we are not recovering the true field exactly; we expect this to be due to an issue in the modelling of our binned cross power spectra between the electrons and the CIB; these uncertainties should be incorporated by the b_{CIB} formalism we considered in Section 8.5.2. Indeed, given the true velocities, we can attempt to fit for the six b^{α}_{CIB} parameters using a Markov–Chain–Monte–Carlo (MCMC) process; in particular we explore the likelihood

$$\mathcal{L} = \frac{1}{2\sqrt{|C|}} \exp -\frac{1}{2}\left(\left(\sum_{i=1}^{6} c^i b^i_{CIB} v^i_t - \sum_{i=1}^{6} c^i \hat{v}^i\right) C^{-1} \left(\sum_{i=1}^{6} c^i b^i_{CIB} v^i_t - \sum_{i=1}^{6} c^i \hat{v}^i\right)\right) \tag{8.45}$$

where C^{-1} is given by the estimator noise

$$C_{LL'MM'} = N_L \delta_{LL'} \delta_{MM'}. \tag{8.46}$$

to find the 6 parameters b_i, and their 1-σ errors, where v^i_t is the true velocity map in bin i, and $\hat{v}^i$ is the reconstruction. These are shown in Figure 8.9. The power spectrum of the field $\sum_i b^i_{CIB} v^i_t$ is shown in Figure 8.10, along with is correlation coefficient with the true velocity map.

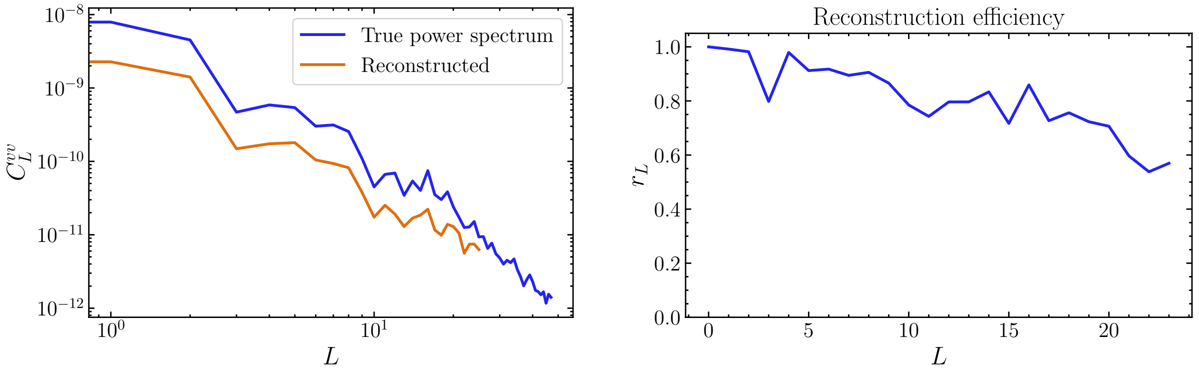

Figure 8.8: The correlation coefficient between the maps in Figure 8.7, ie the reconstructed and the true velocity maps. A correlation coefficient of $r_L = 1$ indicates 100% fidelity in the reconstruction.

We find that the bias parameters are not equal to 1—this is indicative that there is some modelling issue in $C^{\tau v}_{\ell}$. Of course, this is surprising in the case where we are using simulations and so should have a full understanding of the modelling; however we note that we do not have access to the binned CIB, and so we cannot test our models, although we find that we can reproduce the measured power spectrum. Thus, while this serves as a useful proof-of-principle, further tests on simpler simulations will be required; this is ongoing work.

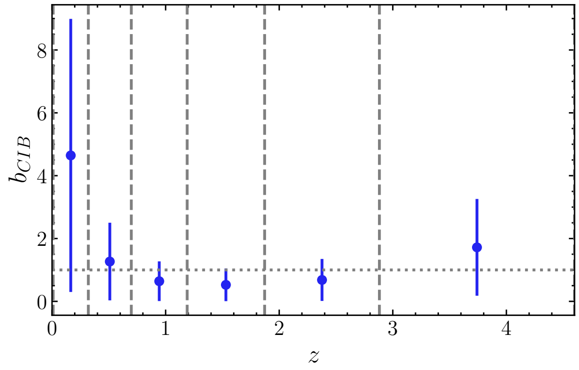

Figure 8.9: The bias parameters b^i_{CIB} for each redshift bin i. There is a dotted line representing the unbiased scenario where $b_{CIB} = 1$. The error bars are calculated by computing the interquartile range of the MCMC chain. The dots represent the values that minimize the likelihood (8.45)

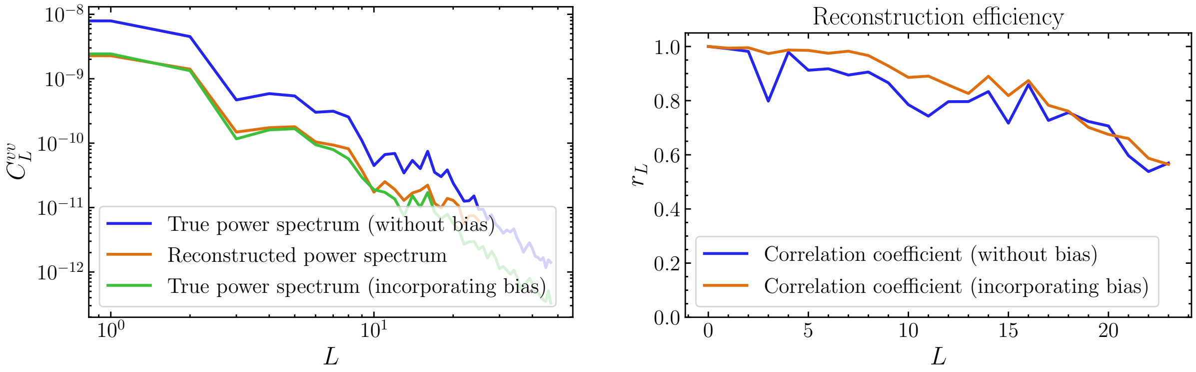

Figure 8.10: The correlation coefficient between the maps in Figure 8.7, ie the reconstructed and the true velocity maps, when the best-fit biases are incorporated. A correlation coefficient of $r_L = 1$ indicates 100% fidelity in the reconstruction.

8.7 Conclusions

We have constructed a quadratic estimator for the remote dipole field based on the CIB and CMB temperature, generalizing previous work on kSZ tomography to two-dimensional tracers of large scale structure. Existing datasets of the CMB and CIB nearly have the sensitivity, resolution, and sky coverage to make a statistically significant detection of the remote dipole field. Our forecast for datasets with comparable sensitivity and resolution to the *Planck* satellite indicate that a detection of signal-to-noise of order one could be made in the absence of foregrounds and sky cuts. However, an idealised future experiment with roughly an order of magnitude better sensitivity, a beam of one arcminute, and lower flux-cut for point-source removal could in principle make a detection with total signal-to-noise of $\mathcal{O}(1000)$. Next-generation experiments such as Simons Observatory [16], CCAT-prime [124], CMB-S4 [17], PICO [125], or CMB-HD [126] fall somewhere between *Planck* and such a future instrument, making it likely that even with complications such as foreground removal, partial sky coverage, instrumental systematics etc. that a high-fidelity CIB-based reconstruction of the coarse-grained remote dipole field will be achievable.

Because of the wide redshift window sampled by the CIB at a fixed frequency, it is only possible to reconstruct the remote dipole field averaged over a very large volume. When considering correlations over such large scales, it is not sufficient to approximate the remote dipole field by the local Doppler shift induced by peculiar velocities – the Sachs Wolfe, Integrated Sachs Wolfe, and primordial Doppler components must be retained. The remote dipole field on such large scales contains information about early-universe physics, and future experiments could meaningfully constrain a number of scenarios, as considered in Ref. [144]. The CIB samples a different range of redshifts at different frequencies, allowing the remote dipole field to be reconstructed over different, overlapping volumes/redshifts. Although the reconstructed fields will be significantly correlated, if the CIB could be sampled densely in frequency, it may be possible to extract some information about the growth rate of structure from the remote dipole field or contribute meaningful constraints on primordial non-Gaussianity [143] and modified gravity [146]. In addition, it may be possible to use the reconstructed remote dipole field to isolate General Relativistic corrections to the observed CIB on the largest angular scales [149, 145].

There is significant model uncertainty in the reconstructed remote dipole field, arising from our imperfect knowledge of the CIB-optical depth cross-spectrum $C_{\ell\alpha}^{I\tau}$ (which is a function of redshift). This manifests itself as a bias on the amplitude of the reconstructed remote dipole field, known as the optical depth bias (see Ref. [142] for a detailed overview). Correlations with a galaxy-based reconstruction of the remote dipole field can be used to constrain the optical depth bias at the $\sim$ 10%-level over a range of redshifts, yielding information on the CIB and distribution of electrons.

Given the potential high-significance reconstruction of the remote dipole field using kSZ tomography with the CIB, the present investigation motivates preliminary investigation with existing data to obtain constraints, and analysis of future data to obtain high fidelity reconstructions.

Chapter 9

Avoiding baryonic feedback effects on neutrino mass measurements from CMB lensing

9.1 Introduction

With improving measurements of the CMB, a cosmological measurement of the sum of the neutrino masses is envisioned within the next decade. Within the standard model of particle physics, the three neutrinos are massless particles; thus, the first measurements of neutrino flavour oscillations [158, 159], a process that only occurs if there exist mass differences between the species, were key developments in the search for beyond-standard-model physics. Neutrino oscillation experiments are sensitive to the difference in the squares of the masses of neutrinos, $\Delta m^2_{ij} \equiv m^2_i - m^2_j$; however, a cosmological neutrino detection will be sensitive to the sum of the neutrino masses $M_\nu \equiv \sum_{i=1}^{3} m_i$, and thus will be important in setting the overall scale of the neutrino masses. The current lower limit on M_ν (from neutrino oscillation experiments) is $M_\nu \gtrsim 60\,\mathrm{meV}$ [160]. Until now, cosmological experiments have only placed upper limits on M_ν; the best is that of the *Planck* survey [42], which gives $M_\nu < 120\,\mathrm{meV}$.

Massive neutrinos have a well-understood effect on the matter power spectrum $P_m(k,z)$. After becoming non-relativistic when their temperature T_ν was comparable to their mass, they started contributing to $P_m(k,z)$; however, due to their small masses, they do not cluster on small scales, instead free-streaming, leading to a suppression of power on small scales. See [161, 162] for reviews on the cosmological effects of neutrinos.

Planck's upper bound on the neutrino mass was obtained from a joint analysis of the CMB temperature and polarisation maps, CMB lensing maps, and baryonic acoustic oscillation (BAO) measurements. As the neutrinos were still relativistic at the time of recombination when the CMB was released, the majority of a CMB survey's constraining power on M_ν comes from the CMB lensing information, which is sensitive to large-scale structure at all redshifts. In coming years, experiments such as the Simons Observatory (SO) [16], SPT-3G [15], and, further in the future, CMB-S4 [17], will make better measurements of the CMB lensing power spectrum, and have been forecast to measure the neutrino mass to between 20 and 30 meV [16, 163, 17].

To be able to reach this level of constraint, the CMB lensing power spectrum must be well understood theoretically. In particular, the lensing power spectrum is a projection of the matter power spectrum $P_m(k, z)$ over all redshifts; however, there are certain effects that currently limit our understanding of $P_m(k, z)$, in particular effects due to baryonic processes (such as gas cooling and feedback from supernovae and active galactic nuclei (AGN)) in the universe. Most predictions of $P_m(k, z)$ only account for gravitational forces, neglecting the complex baryonic interactions that we know exist; our current best method for understanding $P_m(k, z)$ including baryonic physics is to perform large hydrodynamical simulations. Measurements of $P_m(k, z)$ from different simulations differ due to different numerical schemes and phenomenological implementations of baryonic processes that cannot be directly simulated at a given resolution. While the "true" impact of baryonic effects on the matter power spectrum is not known, a general conclusion is that baryons contribute to a suppression of power on small scales (e.g. $0.1 \lesssim k \lesssim \mathcal{O}(\text{few} \times 10)$ at $z = 0$).

Uncertainty due to baryonic feedback has been extensively studied in the context of cosmic shear surveys [164, 165, 166, 167, 168, 169, 170, 171], as the scales affected by feedback directly correspond to the scales that current shear surveys are most sensitive to. However, Ref. [169] and recently Ref. [172] found that uncertainty from baryonic effects can also be important in the search for neutrino masses from CMB lensing, in spite of the higher redshifts and larger length scales involved. If we are to trust a measurement of M_ν from CMB lensing, it will be important to have an inference that is robust to these baryonic effects. Furthermore, the sensitivity of CMB lensing to baryonic effects implies that we could learn about the latter from observations of the former, an avenue explored for cosmic shear in Refs. [173, 174, 175, 176].

Ref. [172] explored the lensing power spectrum suppression and associated bias on neutrino mass from a suite of recent hydrodynamic simulations, finding that the range in possible biases is non-negligible comapared with expected statistical uncertainties. They found a significant scatter between different simulations, comparable to the statistical uncertainty in the measurement. In this paper, we consider various methods of mitigating this bias on the inference of M_ν from CMB lensing surveys similar to SO and CMB-S4. We describe various techniques to remove the sensitivity to the relevant baryonic processes and test, using Fisher forecasts, how these techniques will reduce the bias for the series of simulations examined by Ref. [172]. The first mitigation method we consider is a simple scale cut, where the smallest scales of the CMB lensing convergence (which are most sensitive to baryonic effects) are removed from the analysis. Second, we consider a method of using external cosmic shear measurements to estimate and subtract the low-z contribution to the CMB lensing potential—as baryonic effects are relatively late-universe phenomena, we expect the high-z portion of the CMB lensing potential to be less sensitive to them, while still retaining sensitivity to M_ν. Finally, we ask whether marginalizing over the parameters of a general model for baryonic effects will reduce the bias while preserving the M_ν constraints.

We find that imposing a scale cut of $L_{\rm max} \sim 1000$ on the lensing multipoles used for constraining M_ν can reduce the bias from baryonic effects by up to a factor of 2, with more aggressive cuts significantly increasing the statistical uncertainty. On the other hand, combining this scale cut with subtraction of a low-z tracer, or marginalizing over a baryonic model (with or without a scale cut) will be much more effective in eliminating the bias, reducing it by at least a factor of 5 in the first case and 10 in the second case for all simulations we consider. The maximum residual bias associated with these simulations is $\sim$3 meV in either case, well below the level that would interfere with a high-significance detection of the minimum allowed neutrino mass sum.

This Chapter is organized as follows. In Section 9.2 we discuss the CMB lensing power spectrum $C_L^{\kappa\kappa}$ and review the range of possible baryonic effects as represented by current hydrodynamical simulations. In Section 9.3 we present our Fisher forecast formalism for calculating the forecast constraint and biases on the inference of M_ν from these simulations. In Section 9.4 we discuss the effects of a small angular-scale cutoff in $C_L^{\kappa\kappa}$. In Section 9.5 we discuss the effect of "subtracting" a low-z tracer to isolate the high-z contribution to the CMB lensing map. In Section 9.6 we discuss the effect of marginalizing over parameters that describe the baryonic effects on the matter power spectrum. We discuss our results in Section 10.5.

9.2 CMB Lensing and baryons

The CMB photons we detect have been gravitationally lensed by any matter they encounter along the paths they have travelled since their "release" during recombination, at $z \sim 1100$. Structures at any redshift after recombination can act as lenses, making CMB lensing a powerful probe of the evolution of the matter content of the universe. We mainly quantify this information via the convergence power spectrum $C_L^{\kappa\kappa}$, which is a line-of-sight integral over the matter power spectrum $P_m(k,z)$ (see e.g. [90]),

$$C_L^{\kappa\kappa} = \int_0^{\chi_{\rm CMB}} d\chi \frac{W_{\rm CMB}^{\kappa}(\chi)^2}{\chi^2} P_m\left(k = \frac{L+1/2}{\chi}, z\right), \tag{9.1}$$

where $W_{\rm CMB}^{\kappa}(\chi)$ is the CMB lensing efficiency kernel

$$W_{\rm CMB}^{\kappa}(\chi) = \frac{3}{2}\Omega_m \left(\frac{H_0}{c}\right)^2 \frac{\chi}{a(\chi)} \frac{\chi_{\rm CMB} - \chi}{\chi_{\rm CMB}} \tag{9.2}$$

with H_0 the Hubble constant today, c the speed of light, Ω_m the density of matter today, $\chi_{\rm CMB}$ the comoving distance to the surface of last scattering (at which the CMB was released), and $a(\chi) = \frac{1}{1+z(\chi)}$ the scale factor at comoving distance χ. Equation (9.1) assumes the Limber approximation [49], which is valid in the small-scale, flat-sky limit; and the Born approximation, where the integral is taken over the photon's undeflected path, valid in the small-deflection limit [177, 178].

To make an accurate inference of M_ν from a CMB lensing survey, we need to trust our theoretical model of the lensing convergence; i.e., we need to understand every component of Equation (9.1). The cosmological ingredients that enter CMB lensing kernel $W^\kappa(\chi)$ are well understood. On the other hand, $P_m(k,z)$ is most commonly computed from linear gravitational perturbation theory on large scales, supplemented on small scales by non-linear extensions of gravitational perturbation theory, phenomenological models, N-body simulations, or emulators. Generally, these only account for gravitational interactions between the matter; i.e. they treat all matter as "dark".

However, about 15% of matter is not dark but baryonic, and has complex interactions with itself and with light. These interactions effect changes to how matter clusters on ∼Mpc and smaller scales: as examples, gas cooling and AGN feedback cause matter to condense and expand respectively (e.g. [179]). Our models currently lack a first-principles calculation of the power spectrum $P_m(k,z)$ incorporating these interactions, and they are typically neglected when considering CMB lensing surveys. However, some of the baryonic effects on $P_m(k,z)$—particularly the suppression of power on small scales—mimic the effects of massive neutrinos, and neglecting these in the theoretical modelling of $C_L^{\kappa\kappa}$ can lead to significant biases on the neutrino mass inference [169, 172].

In Figure 9.1, we illustrate the suppression of the CMB lensing power spectrum by baryonic effects, as computed in Ref. [172][1] for a selection of recent hydrodynamical simulations (see Section 9.3.3). At large scales, the power spectra coincide, while the baryonic

---

[1] These computations are available from `http://github.com/sjforeman/cmblensing_baryons`.

suppression becomes relevant at $L \gtrsim 1000$. We also show the effect of a non-zero neutrino mass on the lensing power spectrum, by plotting the ratio of the fiducial $M_\nu = 60\,\mathrm{meV}$ power spectrum to one where $M_\nu = 0\,\mathrm{meV}$ (with all other cosmological parameters unchanged). In this case, we see a power suppression with much milder scale-dependence than for baryonic effects. This difference indicates that it may be possible to disentangle the two types of suppression, motivating the methods we consider in this Chapter.

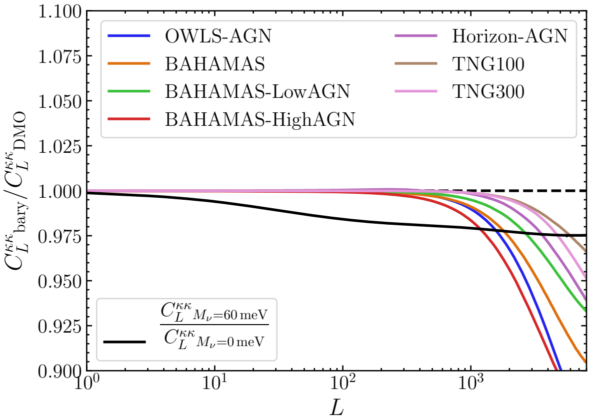

Figure 9.1: The effect of baryons on the CMB lensing power spectrum $C_L^{\kappa\kappa}|_{\mathrm{bary}}$ in a selection of large hydrodynamical simulations (see Section 9.3.3), as computed in Ref. [172], shown as a ratio with the spectrum for dark matter only, $C_L^{\kappa\kappa}|_{\mathrm{DMO}}$. The effect of non-zero M_ν is also shown. The different scale dependences of baryonic and neutrino-mass effects indicate that it may be possible to distinguish between the two in lensing measurements.

9.3 Neutrino mass: constraints and bias

9.3.1 Forecasting the 1σ constraints

We consider an analysis where M_ν is allowed to vary along with other cosmological parameters; as such we consider a parameter vector

$$\vec{\theta} = \left(h, \Omega_b h^2, \Omega_c h^2, \tau, n_s, A_s, M_\nu\right) \tag{9.3}$$

with fiducial values $\{h = 0.675, \Omega_b h^2 = 0.0222, \Omega_c h^2 = 0.1197, \tau = 0.06, n_s = 0.9655, A_s = 2.2 \times 10^{-9}, M_\nu = 0.06\ \mathrm{eV}\}$ corresponding to the best-fit parameters of the *Planck* analysis [42] for the first six parameters, namely, the Hubble parameter in units of $100\,\mathrm{km\,s^{-1}\,Mpc^{-1}}$, the physical baryon density, the physical cold dark matter density, the optical depth to recombination, the primordial scalar fluctuation slope and amplitude (with a pivot scale of 0.05 Mpc^{-1}). We take a fiducial value of 60 meV (the minimum allowed value) for the sum of the neutrino mass M_ν. We compute the fiducial matter power spectrum with CAMB [154], with the nonlinearities and treatment of neutrinos given by the extended halo model from Ref. [53].

As the cosmological parameters will also be constrained from the primary CMB, we include information from the primary CMB temperature and polarization as measured by the experiment we are forecasting for (see Section 9.3.4), as well as a prior from BAO measurements from DESI [180], which improves the analysis by breaking the geometric degeneracy in the CMB.

To compute the information from the CMB and CMB lensing, we use the Fisher formalism, in which the Fisher matrix F approximates the inverse covariance matrix of the parameters, with the diagonals of F^{-1} giving the squares of the expected 1σ uncertainties on each parameter (with all other parameters marginalized over). We calculate F according to

$$F_{ij}^{\mathrm{CMB}} = \sum_{\ell} \frac{2\ell+1}{2} f_{\mathrm{sky}} \,\mathrm{Tr}\left[\frac{\partial C_\ell^{\mathrm{CMB}}}{\partial \theta^i} \left(C_\ell^{\mathrm{CMB}}\right)^{-1} \frac{\partial C_\ell^{\mathrm{CMB}}}{\partial \theta^j} \left(C_\ell^{\mathrm{CMB}}\right)^{-1} \right]. \tag{9.4}$$

In Equation (9.4), f_{sky} is the fraction of sky area which the surveys cover and C_ℓ^{CMB} is the covariance matrix of the CMB:

$$C_\ell^{\mathrm{CMB}} = \begin{pmatrix} C_\ell^{TT} & C_\ell^{TE} & C_\ell^{T\kappa} \\ C_\ell^{TE} & C_\ell^{EE} & C_\ell^{E\kappa} \\ C_\ell^{T\kappa} & C_\ell^{E\kappa} & C_\ell^{\kappa\kappa} \end{pmatrix} \tag{9.5}$$

where C_ℓ^{TT} is the power spectrum of the observed temperature anisotropies (including noise); C_ℓ^{EE} is the power spectrum of the observed E-mode polarisation anisotropies (also including noise); and C_ℓ^{TE} is their cross power spectrum. $C_\ell^{\kappa\kappa}$ includes the reconstruction noise for CMB lensing. Although the CMB we measure is lensed, we use the *unlensed* primary CMB power spectra C_ℓ^{TT}, C_ℓ^{EE} and C_ℓ^{TE} to avoid double-counting of the lensing information. A proper treatment including lensed CMB power spectra would involve including the covariances between the CMB power spectra induced by lensing, and also the covariances between the lensing convergence and the CMB power spectra [181, 182]; neglecting the extra information on M_ν that comes from the lensed CMB power spectra makes our calculation conservative. $C_\ell^{T\kappa}$ and $C_\ell^{E\kappa}$, the cross power spectra of CMB lensing with CMB temperature and E-mode polarization respectively, are non-zero only on very large scales due to correlations induced by the late-universe effects on the CMB such as the Integrated Sachs–Wolfe (ISW) effect [183] and polarization generated after reionization [184], but can be neglected in our analysis as we restrict to multipoles $\ell > 300$ for the primary CMB.

We also include a prior on τ, the optical depth to reionization, which will be an important limiting factor in the inference of M_ν from lensing surveys [163]. We consider two different scenarios: the *Planck* design sensitivity $\sigma_{\text{prior}}(\tau) = 0.006$ (equal to the value achieved by the analysis of *Planck* data in Ref. [185]) and the cosmic variance limit $\sigma_{\text{prior}}(\tau) = 0.002$ [17]. We include this as a Gaussian prior with width $\sigma_{\text{prior}}(\tau)$. The final Fisher matrix we use for forecasting is

$$F = F^{\text{CMB}} + C_{\text{prior}}^{-1} \tag{9.6}$$

where C_{prior} is the sum of the BAO prior and the τ prior. Note that F^{CMB} contains both primary CMB and lensing information, as it is calculated from the covariance matrix in Equation (9.5); however, as the cross power spectra between the primary CMB and the CMB lensing potential are set to zero, this can be separated as a sum of an inverse prior from the primary CMB and a Fisher matrix due to lensing alone.

Within this setup, the lower bound on the marginalized constraint on parameter i is

$$\sigma_i = \sqrt{(F^{-1})_{ii}}. \tag{9.7}$$

9.3.2 Calculating the baryonic bias

Predictions for the CMB lensing power spectrum are typically computed with the dark-matter-only[2] (DMO) nonlinear matter power spectrum $P_{\text{DMO}}(k, z)$. However, since the true power spectrum includes (unknown) baryonic effects, the deviation from the DMO prediction that these effects induce might mimic the neutrino mass signal and result in an incorrect ("biased") inference of the mass. If we can compute the power spectrum incorporating a given model of baryonic effects ($P_{\text{bary}}(k, z)$), we can calculate the bias that would be induced in the inference of the parameter θ^i by (e.g. [169])

$$B_i = F^{-1} \sum_\ell \frac{2\ell+1}{2} f_{\text{sky}} \, \text{Tr}\left[\frac{\partial C_\ell^{\text{CMB}}}{\partial \theta^i} \left(C_\ell^{\text{CMB}}\right)^{-1} \Delta C_\ell \left(C_\ell^{\text{CMB}}\right)^{-1}\right], \tag{9.8}$$

---

[2] "Dark-matter-only" computations could perhaps be more accurately described as "gravity-only", since these computations do not neglect the baryonic contribution to the universe's matter content, but instead treat baryonic identically to dark matter, with only gravitational forces at play. However, "dark-matter-only" is the term most commonly seen in the literature, so we also adopt it.

where ΔC_ℓ is the change in the covariance matrix due to baryonic effects

$$\Delta C_\ell \equiv C_\ell|_{\text{bary}} - C_\ell|_{\text{DMO}}. \tag{9.9}$$

Note that of all the power spectra in the covariance matrix (9.5), only $C_\ell^{\kappa\kappa}$ is affected by the baryons, and $\Delta C_\ell^{XY} = 0$ for $XY \neq \kappa\kappa$ (the κT and κE correlations are too small to be relevant). Thus, Equation (9.8) simplifies to

$$B_i = F^{-1} \sum_\ell \frac{2\ell+1}{2} f_{\text{sky}} \frac{\partial C_\ell^{\kappa\kappa}}{d\theta^i} \frac{1}{(C_\ell^{\kappa\kappa})^2} \Delta C_\ell^{\kappa\kappa} \ . \tag{9.10}$$

We use the forecasting code from Ref. [186][3] to compute the Fisher matrices and biases in our forecasts.

To obtain a range of possible forms for P_{bary}, and therefore $\Delta C_\ell^{\kappa\kappa}$, we turn to hydrodynamical simulations, as described in the next subsection.

9.3.3 Simulations

We use $C_L^{\kappa\kappa}$ computations from Ref. [172], which considers 7 baryonic scenarios from 4 different families of large hydrodynamical simulations (see Ref. [172] for further descriptions):

- the "AGN" member of the OWLS simulation suite [187, 188, 189];
- the base BAHAMAS simulation [190, 191, 189], along with the "Low-AGN" and "High-AGN" versions that respectively contain weaker and stronger AGN feedback than the base simulation;
- the "AGN" member of the Horizon simulation suite [192, 193, 194]; and
- the TNG100 and TNG300 runs of the IllustrisTNG simulations [195, 196, 197, 198, 199, 200].

The matter power spectrum $\hat{P}(k, z)$ is measured from the simulation outputs at several different redshifts, both from DMO runs (which treat baryons and dark matter identically) and from runs that include baryonic processes along with gravity. The measured power spectra have considerable uncertainty due to sample variance arising from the finite number of modes within each simulated volume, but the majority of this sample variance arises

---

[3] https://github.com/msyriac/pyfisher

from randomness in the initial conditions that manifests primarily at large scales. Each pair of DMO and full-hydro runs begins with the same initial conditions (i.e. amplitudes and phases of modes at the initial time), and therefore the sample variance errors mostly cancel[4] in the ratio

$$\hat{R}(k,z) \equiv \frac{\hat{P}_{\rm bary}(k,z)}{\hat{P}_{\rm DMO}(k,z)} \ . \tag{9.11}$$

The corresponding CMB lensing power spectrum $C_\ell^{\kappa\kappa}|_{\rm bary}$ can then be computed by using

$$P_{\rm bary}(k,z) = P_{\rm fid}(k,z)\hat{R}(k,z) \tag{9.12}$$

in Equation (9.1), where $P_{\rm fid}(k,z)$ is the fiducial DMO prediction for the matter power spectrum. Note that the different simulations have been run with different cosmological models, while we compute $P_{\rm fid}$ using a single cosmology in our forecasts. Refs. [202, 203, 189] have found that $\hat{R}(k,z)$ has only a weak dependence on background cosmology, so Equation (9.12) is sufficient for our forecasts, while for work requiring percent-level accuracy, the cosmology-dependence of $\hat{R}(k,z)$ should be carefully accounted for.

9.3.4 Experimental configurations

Several CMB experiments are planned or being built that will begin observations this decade and that are aimed at measuring CMB fluctuations on small scales, for gravitational lensing reconstruction and other secondary anisotropies. Here, we consider an experiment similar to the Simons Observatory (SO) [16], due to begin taking data in the first half of the 2020s. The large aperture telescope for this experiment will have a 6 m diameter and will observe large fractions of the sky at high angular resolution in six frequency channels. We also consider an experiment like CMB-S4 [17, 204], which will have comparable angular resolution and frequency coverage, but higher sensitivity; it is expected to begin taking data on a later timeline than SO. We include Gaussian instrumental white noise on the CMB power spectra:

$$N_\ell = N_T e^{\frac{\ell(\ell+1)\Theta^2_{\rm FWHM}}{8\ln 2}} , \tag{9.13}$$

---

[4] The ratio $\hat{R}(k,z)$ will itself have some sample variance, because it is dominated by baryonic effects on the highest-mass halos within a given simulation volume, and the set of such halos will depend on the initial conditions. Ref. [201] quantified the sample variance in $\hat{R}(k,z)$ for a subset of the simulations considered in this Chapter, finding it to be at the few-percent level for $k \lesssim 20$ (Refs. [194, 189] reached similar conclusions.). This is acceptable for our work, which is focused on the range of $\hat{R}(k,z)$ between different simulations rather than the absolute precision of any one simulation.

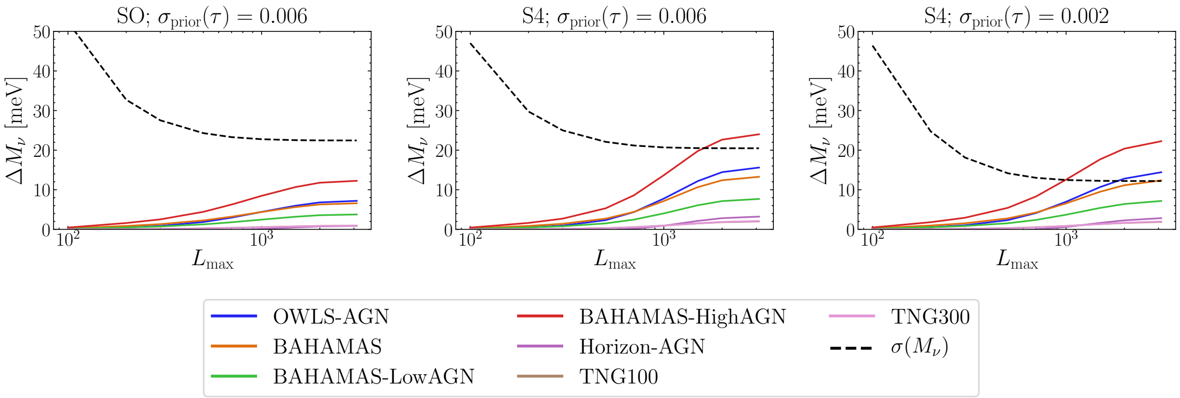

Figure 9.2: Demonstrating mitigation strategy 1: the calculated biases on M_ν plotted against the maximum CMB lensing multipole $L_{\rm max}$ included in the forecast for the different simulations. In each case the 1σ constraint is shown as a dotted line. Note that the TNG100 and TNG300 lines are almost identical.

where N_T is the noise variance and $\Theta_{\rm FWHM}$ is the beam size of the experiment. For both experiments, we use $\Theta_{\rm FWHM} = 1.4'$; for SO, we use N_T corresponding to a map noise level of $6\,\mu$K-arcmin and for S4 we use N_T corresponding to $1\,\mu$K-arcmin.

For $C_L^{\kappa\kappa}$, we include reconstruction noise $N_L^{\kappa\kappa}$ corresponding to the minimum-variance reconstruction of Ref. [44] relevant to the experiment we are considering (SO or S4). We include multipoles $90 \leq L \leq 3100$ in the lensing power spectra, with the upper limit chosen based on where the statistical sensitivity drops off, and the lower limit having negligible impact on the results. For the primary CMB, we include multipoles $300 \leq \ell \leq 3000$ for C_ℓ^{TT} and $300 \leq \ell \leq 5000$ for C_ℓ^{EE}, with the upper limits based on where uncleaned foregrounds are expected to become significant in the lensing reconstruction [205, 206].

9.4 Strategy 1: Small angular-scale cut-off

The forecasts in Ref. [172] considered all scales over which future CMB surveys will have appreciable sensitivity to the lensing power spectrum—ie, a summation over multipoles $90 < L < 3100$. However, baryonic effects are concentrated at a different (though not disjoint) range of scales than the neutrino mass constraint (see Figure 9.1).

With this in mind, the first mitigation strategy we implement is a simple $L_{\rm max}$ cut-off, where $L_{\rm max}$ is the maximum lensing multipole included in the analysis. In Figure 9.2, we show the behaviour of the 1σ constraint on M_ν as well as the biases from different models of baryonic effects as we introduce this cut-off. It is clear that for all of the experimental setups, the constraints saturate at around $L_{\max} \sim 1000$ and there is no benefit to including multipoles $L \gtrsim 1000$; this happens because the suppression of $C_L^{\kappa\kappa}$ is roughly constant for $L \gtrsim 1000$, while the experimental errorbars on $C_L^{\kappa\kappa}$ increase with L over the same range (compare Figure 9.1 of this work with Figure 1 of Ref. [172]). Meanwhile, we see that including higher multipoles does indeed increase the bias, and imposing $L_{\max} \sim 1000$ can reduce the bias by a factor of ~ 2 in some cases. However, in particular for the most advanced experimental configuration, the biases can still be of the same order of magnitude as the expected constraint, and so further mitigation methods will be needed to reduce the bias to an acceptable level.

9.5 Strategy 2: Subtraction of external tracers

9.5.1 Isolating the low-z contribution to the CMB lensing potential

Baryonic phenomena begin to imprint themselves on structure formation at a much later time in cosmological history than neutrino mass effects. As the CMB lensing kernel is an integral over all redshifts, we receive (weighted) information from all of cosmological history since recombination. However, if we could "subtract" the low-z contribution to the lensing map to isolate the high-z effects, we could potentially remove most of the bias while still being sensitive to M_ν.

To illustrate the ideal outcome of such a procedure, we define a high-z CMB lensing field by where $\chi_{\min}$ is some lower bound of the integration; $\chi_{\min} = 0$ corresponds to the standard CMB lensing scenario. We forecast the 1σ errors and baryonic biases on M_ν as in Section 9.3 but replacing $C_L^{\kappa\kappa}$ with $C_L^{\kappa_h\kappa_h}$, and we consider their dependences on the lower limit of integration $\chi_{\min}$.

We show in Figure 9.3 the behaviour of the constraints and the biases plotted against $z_{\min} = z(\chi_{\min})$. Here we see explicitly that the biases are introduced in the late universe at around $z \lesssim 2$, while the constraints on M_ν come from a much larger redshift range. It is clear that if we could isolate the portion of the lensing map that is sourced at $z \gtrsim 2$ we could remove a significant portion of the baryonic bias on M_ν without sacrificing much constraining power on M_ν.

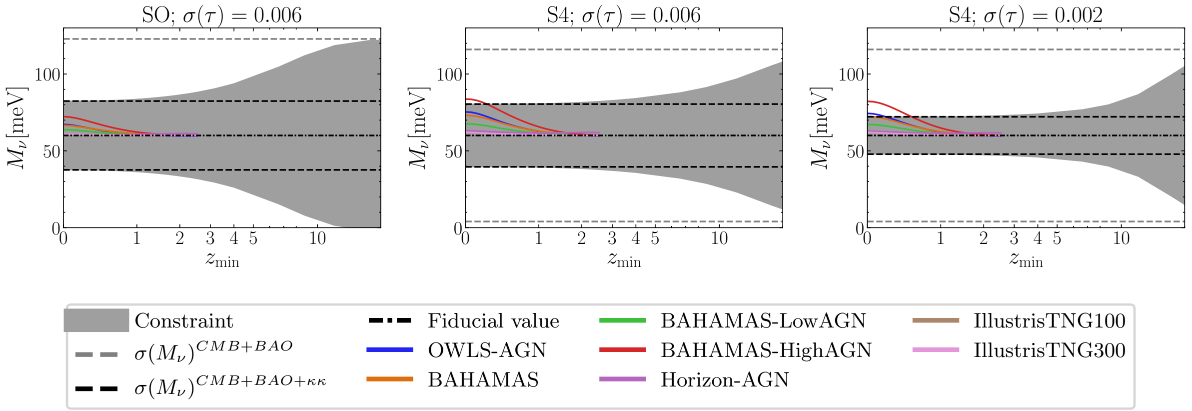

Figure 9.3: The biases (solid lines) and the forecast 1σ constraints on M_ν, plotted against the minimum z $z_{\min}$ used to integrate the CMB lensing kernel, assuming that perfect removal of the $z < z_{\min}$ contribution is possible. We see that the baryonic bias starts to become relevant at $z_{\min} \sim 2$. However, constraining information for M_ν comes from higher z. Note that the x-axis is scaled logarithmically in $(1 + z)$.

Of course, we do not have direct access to measurements of the field κ_h and so the configuration in Figure 9.3 is simply a toy model for illustrative purposes. However, through cross-correlation with a low-z external tracer $\hat{X}$ (such as a cosmic shear map), we could remove the low-z portion of the CMB lensing field by defining a new field

$$\hat{\kappa}^{\text{sub}}(\boldsymbol{L}) = \hat{\kappa}(\boldsymbol{L}) - \frac{C_L^{X\kappa} + N_L^{X\kappa}}{C_L^{XX} + N_L^{XX}} \hat{X}(\boldsymbol{L}), \tag{9.14}$$

where $\hat{\kappa}(\boldsymbol{L})$ is the original CMB lensing convergence, and in this subsection we use hats to denote quantities that include noise (i.e. $C_L^{\hat{A}\hat{B}} = C_L^{AB} + N_L^{AB}$). In Equation (9.14), we weight $\hat{X}$ with a matched filter designed to extract the portion of X correlated with κ, assuming that this correlation is dominated by low redshifts. Note that in our implementation, we will assume that the filter is computed using theoretical expressions with the fixed fiducial cosmological parameters, such that it is not varied in our Fisher calculations.

To see how Equation (9.14) accomplishes our goal, observe that if the weights perfectly match the true statistics of $\hat{X}$ and $\hat{\kappa}$, the power spectrum of $\hat{\kappa}_{\text{sub}}$ reduces to

$$C_L^{\hat{\kappa}_{\text{sub}}\hat{\kappa}_{\text{sub}}} = C_L^{\kappa\kappa} + N_L^{\kappa\kappa} - \frac{\left(C_L^{X\kappa} + N_L^{X\kappa}\right)^2}{C_L^{XX} + N_L^{XX}}. \tag{9.15}$$

Furthermore, if we decompose κ into uncorrelated pieces sourced by low and high redshifts, $\kappa = \kappa_{\rm low} + \kappa_{\rm high}$, and assume that $X(\boldsymbol{L}) = T(L)\kappa_{\rm low}(\boldsymbol{L})$, so that X is perfectly correlated with $\kappa_{\rm low}$ with a transfer function $T(L)$, Equation (9.15) becomes

$$\begin{aligned} C_L^{\hat{\kappa}_{\rm sub}\hat{\kappa}_{\rm sub}} &= C_L^{\kappa_{\rm low}\kappa_{\rm low}} + C_L^{\kappa_{\rm high}\kappa_{\rm high}} + N_L^{\kappa\kappa} \\ &\quad - \frac{\left(T(L)C_L^{\kappa_{\rm low}\kappa_{\rm low}} + N_L^{X\kappa}\right)^2}{T(L)^2 C_L^{\kappa_{\rm low}\kappa_{\rm low}} + N_L^{XX}}. \end{aligned} \tag{9.16}$$

With high noise on X, we recover $C_L^{\hat{\kappa}\hat{\kappa}}$, but in the low-noise limit ($N_L^{X\kappa}, N_L^{XX} \to 0$), we obtain

$$C_L^{\hat{\kappa}_{\rm sub}\hat{\kappa}_{\rm sub}} = C_L^{\kappa_{\rm high}\kappa_{\rm high}} + N_L^{\kappa\kappa}, \tag{9.17}$$

and therefore the low-z contribution to the lensing power spectrum is perfectly subtracted.[5]

In reality, for a tracer we can directly measure, such as cosmic shear, the assumption of perfect and exclusive correlation with the low-z contribution to CMB lensing does not exactly hold; however, if this correlation is sufficiently high, we expect that we can still subtract a significant portion of the unwanted low-z contribution to a lensing map. We consider an explicit example in the following sections.

9.5.2 Cosmic shear from the Rubin Observatory

Cosmic shear is an ideal candidate for an external tracer $\hat{X}$ that we can use to isolate and subtract the low-redshift contribution to CMB lensing maps. As light rays from distant galaxies travel through the universe, their paths are deflected by the intervening matter (just as the CMB is lensed), and this introduces correlated ellipticities in the observed images of these galaxies. These correlations, either amongst these galaxies or between the galaxies and another tracer of large-scale structure, are most commonly measured directly from catalogs of observed galaxy shapes. In our forecasts, we will assume that these catalogs can be converted into lensing convergence maps[6], and take $\hat{X}$ to refer to such a map constructed from galaxies in a given redshift bin.

---

[5] An alternative strategy to the map-level subtraction we have considered here would be to perform the forecasts when including all auto- and cross-power spectra between the lensing map and the other tracer, as performed in, e.g., Refs.[207, 208, 209] in the context of using CMB lensing to mitigate systematic effects seen in cosmic shear surveys. However, this method is *more* sensitive to the baryonic biases sourced at low-z, and should be implemented with a mechanism for marginalizing over baryonic models, which we do not consider in this section for simplicity (although we will consider such a mechanism for the CMB-lensing alone case in Section 9.6).

[6] For recent work on such "mass-mapping" techniques for cosmic shear, see Refs. [210, 211, 212, 213], several of which are extensions to the method first presented in Ref. [214].

The lensing efficiency for a source galaxy at comoving distance χ_S is given by Equation (10.3) with χ_{CMB} replaced by χ_S:

$$W^{\kappa}(\chi, \chi_S) = \frac{3}{2}\Omega_m \left(\frac{H_0}{c}\right)^2 \frac{\chi}{a(\chi)} \frac{\chi_S - \chi}{\chi_S}. \tag{9.18}$$

In practice, galaxies are binned into photometric redshift bins with a finite extent in redshift space, and so we measure the cosmic shear from galaxies at a range of sources. To calculate the shear efficiency for such a bin of galaxies, we integrate over the redshift extent of the bin and weight by the galaxy distribution $\frac{dn}{d\chi}$:

$$W^i(\chi) = \frac{1}{n_i} \int_{\chi_i^i}^{\chi_i^f} d\chi_S \frac{dn}{d\chi_S} W^{\kappa}(\chi, \chi_S) \tag{9.19}$$

for a bin i between χ_i^i and χ_i^f, where n_i is the total number density of the bin $n_i = \int_{\chi_i^i}^{\chi_i^f} d\chi \frac{dn}{d\chi}$. We consider explicitly the distribution predicted for the Rubin Observatory's LSST (Legacy Survey of Space and Time) Gold sample of galaxies [54], a sample that will be used to measure cosmic shear. We take the distribution from Ref. [66]

$$\frac{dn}{dz} = n_s z^{1.24} \exp\left[-\left(\frac{z}{0.5}\right)^{1.01}\right], \tag{9.20}$$

with a total number density $n_s = 26$ arcmin^{-2}. $\frac{dn}{d\chi}$ can be found from Equation (9.20) by computing $\frac{dn}{d\chi} = \frac{dn}{dz}\frac{dz}{d\chi}$.

The shear power spectrum of bin i is given by

$$C_L^{\kappa_i \kappa_i} = \int_0^{\chi_i^f} d\chi \frac{W^i(\chi)^2}{\chi^2} P_m\left(k = \frac{L + 1/2}{\chi}, z\right). \tag{9.21}$$

We consider a survey with N source bins containing equal numbers of galaxies for the cosmic shear fields, and as we wish to use them to subtract as much of the low-z contribution to the CMB lensing kernel as possible, we combine them in such a way to maximize their correlation with the CMB lensing convergence. As such, we consider a linear combination of shear fields

$$\hat{X} = \sum_i c_i \hat{X}_i \tag{9.22}$$

where $\hat{X}_i$ is the convergence map of bin i. The coefficients c_i are chosen to maximize the correlation coefficient between $\hat{X}$ and the CMB lensing potential; we compute them following the linear-algebraic methods of Ref. [46] (see their Appendix A)[7]. The c_i that maximize the correlation coefficient of $\hat{X}$ with the CMB lensing potential $r_L \equiv \frac{C_L^{X\kappa}}{\sqrt{C_L^{XX} C_L^{\kappa\kappa}}}$ are

$$c_i = \sum_j (C_L^{\kappa_A \kappa_B})^{-1}_{ij} \, C_L^{\kappa_j \kappa_{\rm CMB}}, \tag{9.23}$$

where $C_L^{\kappa_A \kappa_B}$ is the covariance matrix of the cosmic shear fields (including noise), and $C_L^{\kappa_j \kappa_{\rm CMB}}$ is the cross-power spectrum between the cosmic shear field j and the CMB lensing convergence. The elements of $C_L^{\kappa_A \kappa_B}$ are

$$C_L^{\kappa_A \kappa_B}{}_{ij} = \int d\chi \frac{W^i(\chi) W^j(\chi)}{\chi^2} P_m\left(k = \frac{L + 1/2}{\chi}, z\right) + N_L^{\kappa_i \kappa_j}, \tag{9.24}$$

with shear noise power spectrum $N_L^{\kappa_i \kappa_j}$ given by

$$N_L^{\kappa_i \kappa_j} = \delta_{ij} \frac{\sigma_\epsilon^2}{n_i} \tag{9.25}$$

where σ_ϵ is the intrinsic shape noise (we take $\sigma_\epsilon = 0.26$ [66]) and n_i is the total angular number density of bin i. The cross power spectrum between CMB lensing convergence and cosmic shear in bin i is given by

$$C_L^{\kappa_j \kappa_{\rm CMB}} = \int d\chi \frac{W^j(\chi) W^\kappa_{\rm CMB}(\chi)}{\chi^2} P_m\left(k = \frac{L + 1/2}{\chi}, z\right) \tag{9.26}$$

where $W^\kappa_{\rm CMB}(\chi)$ is the CMB lensing efficiency kernel given in Equation (10.3).

9.5.3 Intrinsic alignments

It is a non-trivial exercise to separate the apparent ellipticities induced by cosmic shear from the inherent ellipticities of galaxies. Under the assumption that the galaxies have a random distribution of ellipticities, this is not a problem, as taking a high number of galaxies in the sample ensures that the average intrinsic alignment averages to zero and there is no bias to the signal (although Poissonian noise remains). However, if there is an intrinsic alignment to the galaxies' true ellipticities (e.g. as caused by alignment with the large-scale tidal field), this will bias one's inference of a lensing signal. With this in mind,

---

[7] Such a map, combining samples in the mid-infrared and far-infrared from *WISE* and *Planck* to be maximally correlated with CMB lensing, was generated in Ref. [215].

we introduce an intrinsic alignment contribution to our forecasts involving cosmic shear to ensure that the effect of intrinsic alignments on the ability of cosmic shear to subtract the low-z information of the CMB lensing kernel is accounted for.

To quantify the intrinsic alignment contribution, the observed ellipticity γ can be separated into a part induced by gravity γ^G and a part that is intrinsic γ^I,

$$\gamma = \gamma^G + \gamma^I, \tag{9.27}$$

such that the two-point correlation of γ with itself is

$$\langle \gamma\gamma \rangle = \left\langle \gamma^G\gamma^G \right\rangle + \left\langle \gamma^G\gamma^I \right\rangle + \left\langle \gamma^I\gamma^G \right\rangle + \left\langle \gamma^I\gamma^I \right\rangle. \tag{9.28}$$

In terms of the angular power spectra between the ellipticities of galaxies in two redshift bins labelled by i and j, we can write

$$C_L^{\gamma^i\gamma^j} = C_L^{G_iG_j} + C_L^{G_iI_j} + C_L^{G_jI_i} + C_L^{I_iI_j}. \tag{9.29}$$

Correlations between the tidal field responsible for the intrinsic alignments of foreground galaxies and the gravitational field lensing the images of distant galaxies can cause $C_L^{G_iI_j}$ to be non-zero when the redshift bin j is in front of bin i (negligibly small contributions, which are exactly zero in the Limber approximation, come in the case when i is in front of j). This extra contribution to the correlation is also present in the CMB lensing-cosmic shear cross power spectra:

$$C_L^{\kappa_j\kappa_{\mathrm{CMB}}} = C_L^{G_j\kappa_{\mathrm{CMB}}} + C_L^{I_j\kappa_{\mathrm{CMB}}}. \tag{9.30}$$

The gravitational contributions $C_\ell^{G_iG_j}$ and $C_\ell^{G_j\kappa_{\mathrm{CMB}}}$ are the cosmic shear expressions given in Eqs. (9.24) and (9.26). For the other terms, the power spectrum of intrinsic shear $P_{II}(k,z)$ must be introduced. Then, the $I-I$ correlations in redshift bin i are given (within the Limber approximation) by an integral over the redshift bin, weighted by the galaxy density:

$$C_L^{I_iI_i} = \frac{1}{n_i^2}\int_{\chi_j^i}^{\chi_j^f} d\chi \left(\frac{dn}{d\chi_S}\right)^2 P_{II}\left(k = \frac{L+1/2}{\chi}, z\right). \tag{9.31}$$

The cross power spectra between bins $C_L^{I_iI_j}$ is zero (within the Limber approximation) for $i \neq j$, as the redshift window functions do not overlap. For the cross-term C_L^{GI} we introduce the cross power spectrum between matter and intrinsic ellipticities $P_{I,m}(k,z)$ such that

$$C_L^{G_iI_j} = \frac{1}{n_j}\int_{\chi_j^i}^{\chi_j^f} d\chi \left(\frac{dn}{d\chi_S}\right) \frac{W^i(\chi)}{\chi^2} P_{I,m}\left(k = \frac{L+1/2}{\chi}, z\right), \tag{9.32}$$

where $W^i(\chi)$ can be replaced by $W^{\kappa}_{\rm CMB}(\chi)$ to get $C_L^{I_j \kappa_{\rm CMB}}$. As mentioned earlier, this is only non-zero for j in front of i as $W^i(\chi)$ is zero for $\chi > \chi_i^f$, ie over the integration range of Equation (9.32) if bin j is behind bin i.

A simple model for the power spectrum $P_{II}(k,z)$ assumes that (on large scales) galaxies are aligned with their host dark matter halos, which are given ellipticities by their local tidal field, implying that, in the linear regime [216, 217],

$$P_{II}^{\rm lin}(k,z) = \left(\frac{A_{IA} C_1 \bar{\rho} a^2}{\bar{D}}\right)^2 P_m^{\rm lin}(k,z) \tag{9.33}$$

where $\bar{\rho}$ is the mean matter density of the universe at redshift z, $\bar{D} = \frac{D(z)}{a}$ where $D(z)$ is the growth factor normalized to 1 today; and $P_m^{\rm lin}(k,z)$ is the *linear* matter power spectrum. C_1 is a constant amplitude $C_1 = 5 \times 10^{-14} h^{-2} M_\odot^{-1} {\rm Mpc}^3$, chosen to match the IA amplitude of superCOSMOS in [218] and A_{IA} is an overall normalization parameter with a fiducial value of unity which should be marginalized over due to uncertainty in the overall amplitude of the intrinsic alignment power. The cross spectrum between the intrinsic ellipticities and the matter power spectrum $P_{I,m}(k,z)$ is given (again in the linear regime) by

$$P_{I,m}^{\rm lin}(k,z) = -\left(\frac{A_{IA} C_1 \bar{\rho} a^2}{\bar{D}}\right) P_m^{\rm lin}(k,z). \tag{9.34}$$

In [217] this linear alignment model was extended to a "non-linear linear alignment model" by replacing $P_m^{\rm lin}(k,z)$ with the non-linear $P_m(k,z)$. We use this latter model in our forecasts.

In cosmic shear analyses, it is customary to use a very wide prior on the normalization A_{IA}. However, recent shear surveys have been successful in constraining this parameter in combination with photometric or spectroscopic galaxy clustering: for example, when ignoring galaxy colors, the Dark Energy Survey obtained $\sigma(A_{IA}) \approx 0.33$ with its year-1 data [219], and the KiDS survey achieved $\sigma(A_{IA}) \approx 0.5$ in Ref. [220], with both surveys also able to distinguish the amount of intrinsic alignments associated with red and blue galaxies (see also Ref. [221]). Future shear surveys are expected to improve upon this, especially if accompanied by coordinated wide-field spectroscopy (e.g. [222]). Thus, in our baseline forecasts we include a prior of 25% of the fiducial value of A_{IA}, but we also explore the dependence of our results on this choice.

9.5.4 Impact of shear subtraction on neutrino mass inference

Subtracting the optimally-combined shear map of Section 9.5.2 from the CMB lensing map results in a significant reduction of the baryonic bias on M_ν without an appreciable

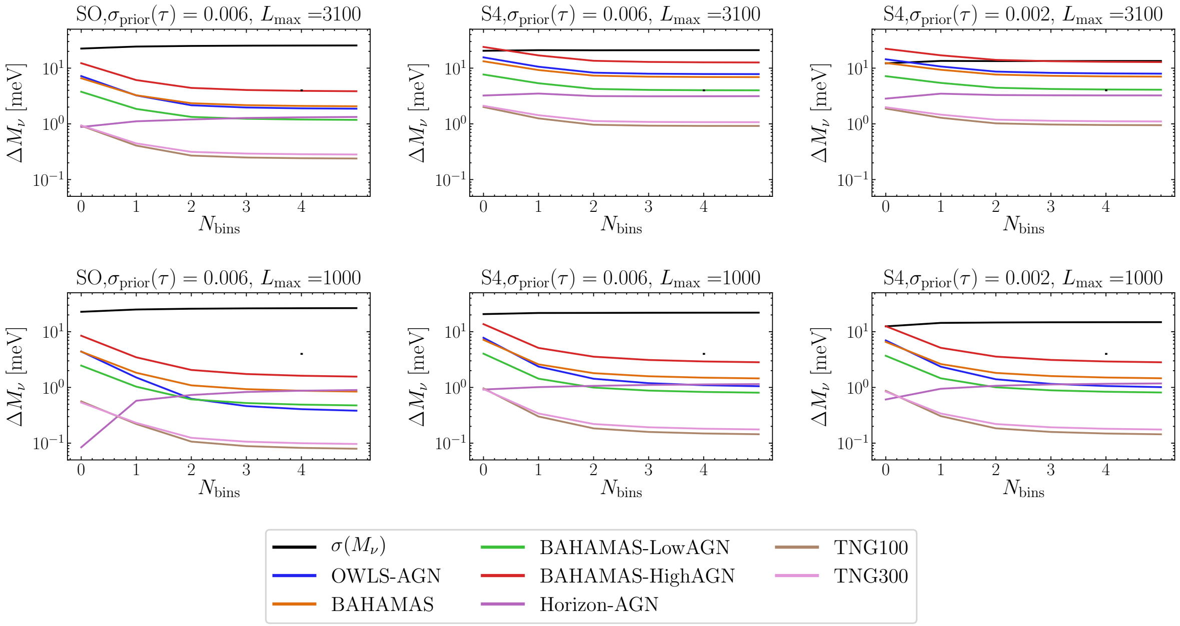

Figure 9.4: Demonstrating mitigation strategy 2: the decrease in the bias when an optimal combination of $N_{\rm bins}$ cosmic shear bins is subtracted from the CMB lensing map. With the exception of $N_{\rm bins} = 0$ (which corresponds to the no-subtraction case), the total redshift extent and number of galaxies are held constant, with $N_{\rm bins}$ controlling the slice thickness. On top is for an analysis with $L_{\rm max}$ of 3100; on bottom we have applied a scale cut of $L_{\rm max} = 1000$ (as well as subtracting cosmic shear). All curves shown include marginalization over intrinsic alignments for cosmic shear, with a 25% prior on the intrinsic alignment amplitude. It is clear that the bias on M_ν can be reduced significantly in the latter case, without appreciably loosening the constraint on M_ν.

increase in the statistical uncertainty. We show some results in Figure 9.4, where we plot the constraints and bias on M_ν against $N_{\rm bins}$, the number of galaxy redshift bins we use to construct $\hat{X}$. Increasing $N_{\rm bins}$ does not increase the number of galaxies in the analysis, but it does have the effect of increasing our redshift resolution and allowing us to weight the galaxy kernels to match the CMB lensing kernel better. Note, however, that at some value of $N_{\rm bins}$, photometric redshift errors will not allow for increasing $N_{\rm bins}$ to give us better redshift resolution, and we expect the curves to saturate around this point in a treatment where photometric redshifts are included. However, for the redshift errors expected of the Rubin Observatory's LSST, we expect to be able to significantly subtract the bias on M_ν

with this method even with a small number of bins, in which case photometric redshift errors will likely be insignificant due to the wide extents of the bins.

Figure 9.4 shows that, with $L_{\rm max} = 3100$ for CMB lensing, implementing the shear subtraction generally decreases the bias on M_ν associated with all but one simulation by factors of 3 to 7 for SO, and a factor of ∼2 for S4 (we denote the no-subtraction case by $N_{\rm bins} = 0$ in the figure). With $L_{\rm max} = 1000$, we similar improvements for SO, but closer to a factor of 5 improvement for S4, in addition to the factor of 2 improvement arising from the $L_{\rm max}$ cut. In all cases, the bulk of the improvement can be obtained with only 2 shear redshift bins (with boundaries $z = [0, 0.93, 4]$) for the LSST specifications we use. Concurrent with the decrease in bias is an increase in the statistical uncertainty on M_ν, by at most ∼20%.

Most simulations in Figure 9.4 display similar behavior, with the bias on M_ν decreasing with $N_{\rm bins}$, but Horizon-AGN exhibits the opposite trend, with the bias *increasing* as more redshift bins are used for the subtraction. This is due to the stronger effect of baryons on high-redshift ($z \gtrsim 3$) clustering observed in Horizon-AGN as compared to the other simulations (contrast Figure 2 of Ref. [194] with results from other simulations summarized in Refs. [189, 201]). If the high-redshift clustering in Horizon-AGN (primarily driven by gas pressure delaying the collapse of dark matter into halos, rather than AGN feedback [194]), as opposed to that in the other simulations (in which the effect of baryons at high z is much more mild) is reproduced in the actual universe, isolating the high-z part of a CMB lensing map will not be sufficient to mitigate the impact of baryons on a neutrino mass constraint.

In Figure 9.5, we show the effect of varying the prior on the intrinsic alignment amplitude A_{IA} on the uncertainty and bias on M_ν, for $N_{\rm bins} = 5$ and the bias associated with the OWLS-AGN simulation. For CMB-S4 with the tighter τ prior, loosening $\sigma(A_{IA})$ from 0.25 to 3 degrades the expected errorbar on M_ν by 15% for $L_{\rm max} = 3100$ or 40% for $L_{\rm max} = 1000$, and increases the bias on M_ν by a factor of ∼2 compared to the $\sigma(A_{IA}) = 0.25$ case. Thus, with the wider A_{IA} prior, the shear subtraction combined with the $L_{\rm max}$ cut is generally still able to reduce the bias on M_ν by a factor of ∼5-6 compared to the case with no mitigation strategy. On the other hand, exact knowledge of A_{IA} leads to improvements in the uncertainty and bias on M_ν of a few tens of percents. Note that the nonlinear alignment model we have used for intrinsic alignments will likely be superseded by more detailed models for future shear surveys (e.g. [223, 224]), but our exploration of priors on A_{IA} can be taken as indicative of how one's knowledge of intrinsic alignments affects the shear subtraction procedure we have described.

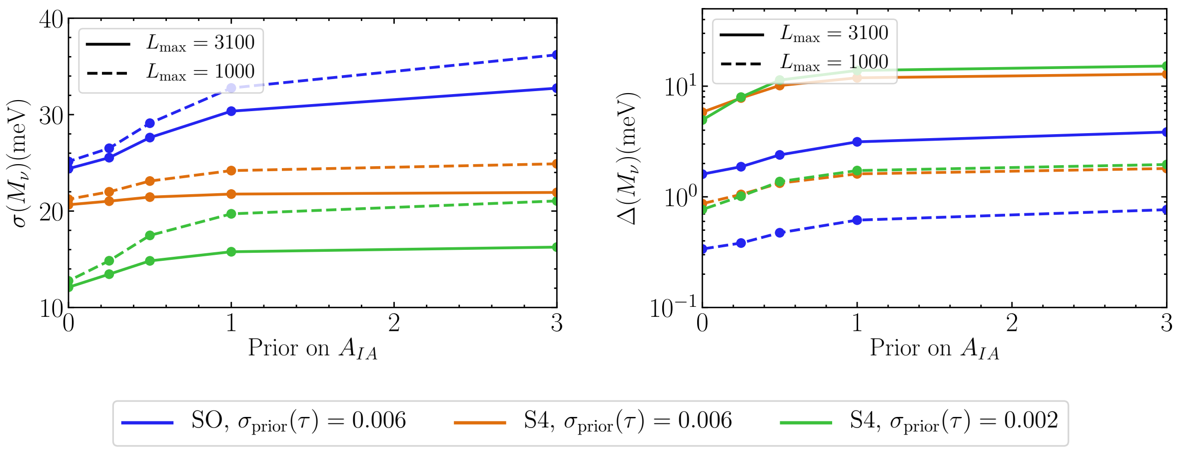

Figure 9.5: The effect of marginalizing over the intrinsic alignment amplitude. If a prior is not included the constraint on $\sigma(M_\nu)$ can increase significantly, as is shown on the left; the bias also increases, as is shown on the right for OWLS-AGN.

9.6 Strategy 3: marginalization over additional parameters

The mitigation strategies we considered above involved removing portions of the data most sensitive to baryons, via scale cuts and/or subtracting proxies for low-redshift information in CMB lensing, while retaining as much constraining power on M_ν as possible. However, as biased constraints on M_ν arise from neglecting baryonic effects in the theoretical modelling of the matter power spectrum, one can instead incorporate a model for these effects; by marginalizing over the associated parameters, we can hope to reduce the bias on M_ν without requiring precise knowledge of the impact of baryons. Examples of such models include perturbation theory [225, 226, 227], extended halo models [228, 202, 53, 229, 230, 231], empirical fitting functions [173, 189] or principal-component decompositions [232, 233, 234] for the matter power spectrum from simulations, “baryonification” algorithms that modify the outputs of N-body simulations [235, 236, 237, 238], emulators [239], or approaches based on machine learning [240, 241].

We choose to test this marginalization approach using the model from Ref. [53]. This model is based on the halo model (e.g. [55]), with a modified 1-halo term for the matter power spectrum. Baryonic effects are parameterized by two parameters. The first, A, is the amplitude of the halo concentration-mass relationship $c(M, z)$:

$$c(M, z) = A\frac{1 + z_{\rm f}(M)}{1 + z}, \tag{9.35}$$

where $z_{\rm f}(M)$ is the formation redshift of halos of mass M; this is designed to capture the effects of processes such as gas cooling, which can cause increased halo concentration. The second parameter, η, alters the (Fourier-transformed) halo density profile $u(k, M)$ via

$$u(k, M) \to u(\nu^\eta k, M), \tag{9.36}$$

where $\nu = \frac{\delta_c}{\sigma(M)}$ with δ_c the critical density required for spherical collapse and $\sigma(M)$ variance in the initial density fluctuation field when smoothed with a tophat filter with the size of the virial radius of the halo. For positive η, the modification (9.36) "puffs out" higher-mass halos ($\nu > 1$) and contracts lower mass halos, and as such η is referred to as the "halo bloating parameter". This is intended to capture some of the effects of AGN feedback on halo profiles. By fitting A and η to the OWLS simulations, Ref. [202] found that it was adequate to use a single redshift-independent value for A, while the redshift dependence of η was well-captured by

$$\eta(z) = \eta_0 - 0.3\sigma_8(z) \tag{9.37}$$

with a single η_0, where σ_8 is the variance of density fluctuations over a sphere with radius 8, and we use those choices in our calculations.

To ensure that the parameter space of A and η_0 sufficiently describes the baryonic effects in the simulations we are considering, in Appendix D we fit these parameters to the $P_{\rm bary}/P_{\rm DMO}$ ratios from each simulation, and compare the "best-fit" predictions with the simulations' measurements. We indeed find that the model is able to reproduce all simulation results with a precision of $\sim$5% over the scales we are concerned with, which is an acceptable level since we are more concerned with the range of simulation results rather than exactly reproducing any one simulation. This agreement also justifies our use of the model from Ref. [53] as opposed to turning to more recent updates (e.g. [229, 230]).

To include this model in our forecasts, we use the same formalism as in Section 9.3, but expanding the vector of parameters in Equation (9.3) to include A and η_0:

$$\vec{\theta} = \left(h, \Omega_b h^2, \Omega_c h^2, \tau, n_s, A_s, M_\nu; A, \eta_0\right). \tag{9.38}$$

The fiducial values we use for A and η_0 are $A = 3.13$ and $\eta_0 = 0.60$, corresponding to those fit to the DMO run of OWLS in Ref. [202]. We do not assume any prior knowledge of

Expt	$\sigma_{\rm prior}(\tau)$	$\sigma(M_\nu)$ [meV]		Simulation	Bias ΔM_ν [meV]		$\Delta M_\nu/\sigma(M_\nu)$	
		no marg.	after marg.		no marg.	after marg.	no marg.	after marg.
SO	0.006	22	24	OWLS-AGN	7.2	0.14	0.32	0.0060
				BAHAMAS	6.6	0.74	0.29	0.031
				BAHAMAS-LowAGN	3.8	0.43	0.17	0.018
				BAHAMAS-HighAGN	12	1.4	0.55	0.059
				Horizon-AGN	0.88	-0.81	0.039	-0.033
				TNG100	0.92	0.090	0.041	0.0038
				TNG300	0.92	0.088	0.042	0.0037
S4	0.006	20	22	OWLS-AGN	16	0.39	0.76	0.018
				BAHAMAS	13	1.1	0.65	0.052
				BAHAMAS-LowAGN	7.7	0.67	0.38	0.031
				BAHAMAS-HighAGN	24	2.4	1.2	0.11
				Horizon-AGN	3.2	-0.78	0.16	-0.036
				TNG100	2.0	0.22	0.098	0.010
				TNG300	2.1	0.20	0.10	0.0091
S4	0.002	12	14	OWLS-AGN	14	0.37	1.2	0.027
				BAHAMAS	12	1.2	1.0	0.083
				BAHAMAS-LowAGN	7.2	0.68	0.59	0.049
				BAHAMAS-HighAGN	22	2.4	1.8	0.18
				Horizon-AGN	2.8	-0.89	0.23	-0.064
				TNG100	1.9	0.21	0.15	0.015
				TNG300	2.0	0.19	0.16	0.014

Table 9.1: Expected uncertainty and bias on M_ν with and without marginalization over the A and η_0 parameters of modified halo model from Ref. [53], using CMB lensing multipoles up to $L_{\rm max} = 3100$. With marginalization, the biases are reduced by a factor of ∼10 in most cases, while the uncertainty is only degraded by ∼15% at most.

the true values of these parameters, which is a conservative choice given the multitude of other datasets which could likely constrain them at some level. Upon marginalizing over A and η_0, along with the other cosmological parameters, we find the results in Table 9.1. In particular, we find that the uncertainty on M_ν is degraded by only $\sim$10% compared to the case where baryonic effects are ignored in the modelling (equivalent to fixing A and η_0 to their fiducial values), while the biases on M_ν are drastically reduced, by factors of $\sim$10 or more. In particular, for CMB-S4 with the tightest τ prior, the bias corresponding to BAHAMAS-HighAGN is roughly 0.2σ, while for all other simulations it is less than 0.1σ; without marginalization, there are 3 simulations that induce a bias exceeding 1σ.

To understand why this prescription works so well at removing the bias while preserving the constraining power, it is helpful to plot the derivatives of $C_L^{\kappa\kappa}$ with respect to A, η_0, and M_ν; see Figure 9.6. We see that A and η_0 have significantly different effects on the shape of the lensing power spectrum than M_ν: since they only modify the 1-halo term in the matter power spectrum, they have the strongest impact at small scales, while neutrino mass suppresses structure growth over a wider range of scales (recall Figure 9.1). This lack of degeneracy implies that the M_ν constraint is not degraded when A and η_0 are marginalized over; furthermore, since the model covers the space of baryonic effects well, the marginalization is effective at removing the associated bias from a determination of M_ν. These conclusions are consistent with other studies of cosmic shear [170, 171, 242], which have found that when priors from the primary CMB or other observations are included, marginalizing over a baryonic model with only a few parameters enables unbiased constraints on neutrino mass without large increases in uncertainty.

9.7 Discussion & Conclusion

Upcoming measurements of CMB lensing have great promise to measure the sum of neutrino masses (M_ν), but this measurement will only be possible if each of several systematic effects are tightly controlled. In this Chapter, we considered one such systematic, related to the impact of "baryonic effects" (the name given to astrophysical processes like gas cooling and AGN feedback) on the lensing power spectrum. Recent simulations indicate that uncertainty in these effects can bias a neutrino mass measurement from CMB lensing by a sizeable fraction of the statistical errorbar if they are not incorporated in the modelling or mitigated in some other way [172].

We investigated three strategies for mitigating this bias, using Fisher forecasts that combine expected CMB lensing and primary CMB measurements from upcoming experiments, BAO constraints expected from DESI, and a prior on the mean optical depth τ,

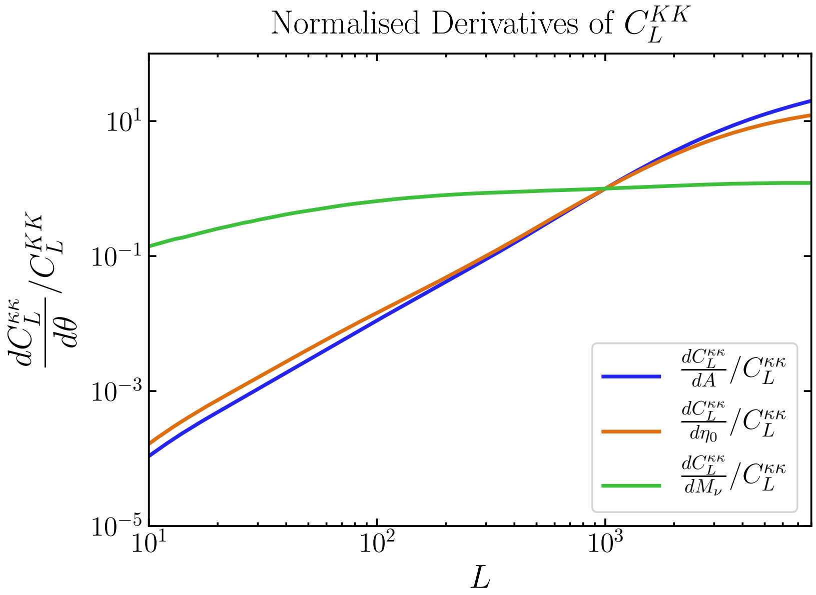

Figure 9.6: The derivatives of the lensing power spectrum with respect to the parameters of the model for baryonic effects from Ref. [53], and also M_ν, all normalized by their own values at $L = 1000$. M_ν is tending towards a scale-independent effect on $C_L^{\kappa\kappa}$ across a wide range of scales, while A and η_0 are significantly scale dependent, becoming increasingly important on small scales.

either from current *Planck* constraints or assuming a cosmic-variance-limited measurement. Our chosen strategies and results are as follows:

1. **Decreasing the largest multipole $L_{\max}$ (smallest physical distance) used for neutrino mass constraints (Section 9.4)**: Baryonic effects are stronger at smaller scales, so one can attempt to reduce sensitivity to these effects by excluding smaller scales from an analysis. We found that keeping $L_{\max} \gtrsim 1000$ is necessary to avoid sacrificing significant constraining power on M_ν, and that setting $L_{\max} = 1000$ can reduce the bias on M_ν by as much as a factor of 2 (compared to our fiducial forecast with $L_{\max} = 3100$). However, this reduction still allows the bias be of the same order as the statistical errorbar on M_ν, so further mitigation is needed.

2. **Removing the low-redshift contribution to the lensing map using external tracers (Section 9.5)**: CMB lensing probes structures over a wide redshift range,

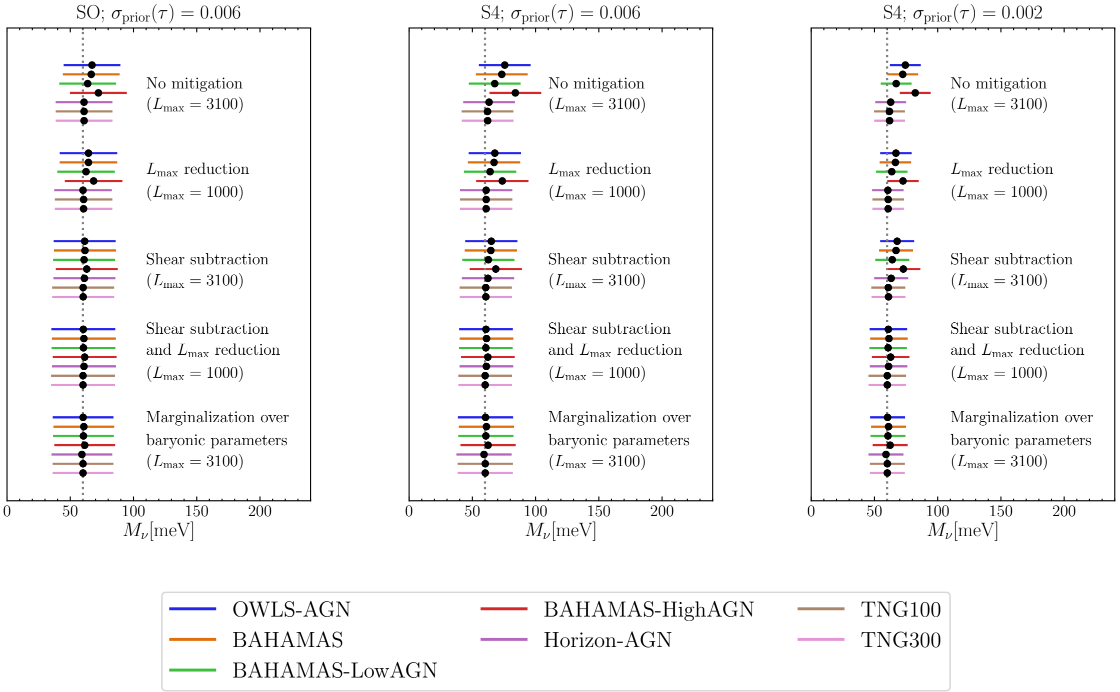

Figure 9.7: A summary of the efficacy of our mitigation methods. For each experimental configuration and each mitigation method, we show the forecast error bars for M_ν, centred on the fiducial value of 60 meV but offset by the bias forecast for each simulation. Without any mitigation, the biases are substantial and have differing values for different simulations [172]. However, it can be seen that $L_{\max}$ reduction and shear subtraction each reduce the biases to some extent, and that when both methods are performed the biases are almost completely removed. Marginalization over baryonic parameters also does an excellent job of almost completely removing the biases.

while simulations indicate that baryonic effects should only have a sizeable effect on clustering at the lower end of this range. Thus, one can attempt to remove the low-z contribution from a CMB lensing map, and use the resulting map for a neutrino mass analysis. We have implemented this proposal using a weighted sum of cosmic shear measurements in different source redshift bins. We found that, with $L_{\max} = 1000$, subtracting a combination of 2 shear redshift bins (modeled on the Rubin Observatory's LSST) from a CMB lensing map is sufficient to reduce the bias on M_ν by factors of 5 or more, down to 3 meV for the most extreme simulation we consider. We also considered the effect of intrinsic alignments in the LSST-like data on this procedure, and found a minor impact, when assuming the priors that are expected.

3. **Marginalizing over a parameterization of baryonic effects (Section 9.6)**: If the effects of neutrino mass and baryonic processes are sufficiently nondegenerate in the lensing power spectrum, one can consider including a simple parameterization of the latter in the matter power spectrum model, and marginalizing over the corresponding parameters. After checking that the modified halo model from Ref. [53] can describe our set of simulations with appropriate accuracy, we found that marginalizing over the model's two parameters only degrades the constraining power on M_ν by about 15%, while reducing the bias on M_ν by factors of 10 or more, down to $\sim$2 meV for the most extreme simulation. This is true even without a reduction in $L_{\rm max}$.

We conclude that either of strategies 2 or 3 should be sufficient to reduce the bias in M_ν from baryons to an acceptable level ($\Delta M_\nu \lesssim 0.2\sigma(M_\nu)$) for CMB-S4. These results are summarized in Figure 9.7.

There is a fourth mitigation strategy that we have not explored in this Chapter: using external measurements to constrain or fix the form of baryonic effects on CMB lensing. It has been shown that the matter power spectrum suppression seen in a range of hydrodynamical simulations is strongly correlated with the mean baryon fraction of group- and cluster-scale halos ($M_{\rm halo} \sim 10^{14} h^{-1} M_\odot$) [189, 231], so an external constraint on this quantity would likely give a much sharper picture of how much power suppression to include in the modelling. This constraint may be achievable with future X-ray observations of groups and clusters (e.g. [243]). For example, when using the model for baryonic effects from Ref. [236], Ref. [171] finds that gas fraction measurements by the upcoming *eROSITA* telescope [244], combined with cluster mass estimates from Euclid weak lensing, will significantly reduce the uncertainty on M_ν from a combination of cosmic shear and *Planck* CMB measurements. However, inference of gas fractions from X-ray measurements requires a measure of the total halo mass, and the various methods to obtain this (e.g. assuming hydrostatic equilibrium or using weak lensing of background galaxies) each come with their own caveats. Furthermore, X-ray measurements are most sensitive to hot gas in a halo's interior, while Refs. [235, 231] have shown that gas at the outskirts of groups and clusters has an important effect on the matter power spectrum.

This fainter, more diffuse gas can be probed using the thermal and kinetic Sunyaev-Zel'dovich (SZ) effects. Mean gas fractions can be extracted from cross-correlations between CMB maps and group/cluster catalogs [130, 245, 246, 247], or more generally, stacked gas and pressure profiles can be measured directly from these cross-correlations [248, 249, 250, 251], with upcoming surveys promising to provide much more powerful measurements [252, 253]. Further constraints are possible by correlating thermal SZ maps and cosmic shear [254, 255] or CMB lensing itself [256], helping to break degeneracies between baryonic effects and neutrino mass. Clearly, there are many avenues for independent constraints of baryonic effects, which can be incorporated into an analysis of CMB lensing. However, the strategies presented in this paper do not depend on any such constraints, and therefore represent a promising approach to pursue in parallel.

Finally, it is worth noting that we have made specific choices when implementing these strategies in our forecasts, but other choices are possible. For instance, one could choose a low-redshift tracer other than cosmic shear to implement the map-level subtraction from Section 9.5; another option would be to use spectroscopic or photometric galaxy catalogs, although galaxy bias and selection effects would need to be carefully accounted for in the subtraction procedure. One could also consider marginalizing over other models for baryonic effects, such as effective-field-theory–based perturbation theory, which Ref. [227] found to be capable of describing baryonic effects on CMB lensing at $L \lesssim 2000$ with suitable accuracy for CMB-S4. Regardless of these specific choices, we expect our general conclusions about these strategies to hold. Therefore, it appears that baryonic effects on a neutrino mass constraint from CMB lensing can be straightforwardly reduced to a negligible level.

Chapter 10

Primary CMB measurements without baryon bias

10.1 Introduction

Measurements of the cosmic microwave background (CMB) temperature and polarization anisotropy power spectra have revolutionized our understanding of cosmology in the past few decades (e.g., [257, 123, 13, 258]). Upcoming CMB anisotropy measurements promise to build upon this success, with unprecedented sensitivity to signals of new physics in the early universe [16, 80]. Key to this success is the robust theoretical foundation upon which CMB anisotropy power spectrum calculations rest. In particular, the primary CMB fluctuations are described to very high accuracy by linear cosmological perturbation theory. As first recognized long ago (e.g., [259, 260, 261, 262]), high-precision measurements combined with this robust theoretical foundation allow constraints on all of the fundamental cosmological parameters (in ΛCDM) to be inferred solely from the CMB. Upcoming experiments will utilize this power to put leading constraints on many new-physics parameters, including the effective number of relativistic species ($N_{\rm eff}$), the sum of the neutrino masses (M_ν), the running of the spectral index of primordial perturbations, models to resolve the H_0 tension, and many other scenarios. All of these constraints rely on the precise modeling of the CMB power spectra within linear perturbation theory.

However, on small angular scales in the CMB, crucial assumptions in this picture begin to break down. Gravitational lensing of CMB photons, which distorts their paths as they travel from the surface of last scatter to our telescopes, leads to subtle but non-negligible changes to the CMB power spectra (for a comprehensive review of CMB lensing, see [90]).

In particular, gravitational lensing smooths the acoustic peaks and pushes anisotropy power into the high-multipole "Silk damping tail" of the CMB power spectra [263, 264, 265]. Thus, due to lensing, the primary CMB is influenced by the properties of the matter density field at low redshifts, as captured in the CMB lensing potential field, which is a particular redshift-weighted projection of the density field along the line-of-sight (LOS). The CMB lensing potential field is well-described by linear perturbation theory on angular scales greater than ~ 10 arcmin [90], but on smaller scales it is affected by nonlinear gravitational evolution and processes associated with baryons, such as feedback from active galactic nuclei (AGN) [266, 267, 268, 187, 269, 270, 271, 272, 273, 274, 4]. Thus, one may wonder to what extent these highly nonlinear processes could affect the primary CMB itself through gravitational lensing, and whether these effects could influence cosmological parameter inference from upcoming high-resolution CMB experiments.

In this Chapter, we show that nonlinear and baryonic effects can indeed produce significant biases in the analysis of data from upcoming CMB experiments. The small-scale (multipoles $\ell \gtrsim 3000$) CMB receives sufficiently large contributions from the small-scale ($L \gtrsim 2000$) CMB lensing potential field that these effects cannot be ignored. We consider a range of models for the effects of nonlinear evolution and baryonic feedback on the small-scale CMB lensing power spectrum, and compute their effects on the primary CMB power spectra. We then propagate these models through a Fisher analysis to forecast biases on cosmological parameters that would be inferred when assuming an incorrect (but currently standard) model. To be concise, we focus on the ΛCDM and ΛCDM+$N_{\rm eff}$ models, where $N_{\rm eff}$ is the effective number of relativistic species. The latter is of particular interest, as constraints on $N_{\rm eff}$ are strongly driven by measurements of the damping tail in the primary CMB power spectra, which is also the region most altered by the effects identified in this Chapter. However, similar biases for other parameters (e.g., the sum of the neutrino masses or the running of the spectral index) are also likely to exist, and should be considered (and mitigated) in upcoming CMB data analyses.

A brief summary of our results is as follows. We show that constraints on $N_{\rm eff}$ from the upcoming Simons Observatory (SO) [16] and CMB-S4 [80] experiments could be biased by up to 0.4σ and 1.2σ, respectively, due to the neglect of baryonic feedback in modeling of the primary CMB power spectra. Similarly, constraints on the physical cold dark matter density, $\Omega_c h^2$, could be biased by up to 1.0σ (SO) and 1.6σ (CMB-S4) in ΛCDM, or up to 0.8σ (SO) and 2.0σ (CMB-S4) in ΛCDM+$N_{\rm eff}$. The Hubble constant H_0, which is a derived parameter in the analysis of CMB data, could be biased by up to 1.0σ (SO) and 1.6σ (CMB-S4) in ΛCDM. In general, the bias on a given parameter depends on the model under consideration, as parameter degeneracies will change. Table 10.1 summarizes the biases on the cosmological parameters for SO and CMB-S4 in the ΛCDM and ΛCDM+$N_{\rm eff}$

	SO		CMB-S4	
	ΛCDM	ΛCDM+$N_{\rm eff}$	ΛCDM	ΛCDM+$N_{\rm eff}$
H_0	0.96	0.15	1.6	0.035
$\Omega_b h^2$	0.070	0.27	0.44	0.56
$\Omega_c h^2$	1.0	0.96	1.6	2.0
τ	0.37	0.42	0.28	0.42
A_s	0.57	0.68	0.52	0.81
n_s	0.36	0.16	0.48	0.69
$N_{\rm eff}$		0.44		1.2

Table 10.1: Fractional biases (in units of the forecast 1σ statistical error bar) on each of the parameters in the various setups, if baryonic effects are ignored. Note that the biases are different for the same parameters in the ΛCDM and ΛCDM+$N_{\rm eff}$ models due to effects of the marginalization over $N_{\rm eff}$. We assume a maximum multipole $\ell_{\rm max} = 5000$ here, with noise power spectra for SO and CMB-S4 shown in Figure 10.1. The OWLS-AGN [187, 189] baryonic model is assumed here.

models.

We suggest multiple mitigation strategies to avoid these potentially significant baryonic feedback-induced biases. The simplest approach is to explicitly discard all high-ℓ TT power spectrum data. At a fixed multipole in the damping tail, the small-scale TT power spectrum is most affected by the lensing contributions described above (compared to TE or EE), due to the larger gradient in the unlensed T field as compared to E. Moreover, due to the much larger amplitude of the TT signal, CMB experiments measure more signal-dominated modes in the TT damping tail than in TE or EE (even after accounting for foregrounds). Thus, the biases that we compute are generally driven most strongly by TT. Explicitly, we find that biases on all parameters investigated here can be kept to $\lesssim 0.3\sigma$ if all TT data at $\ell \gtrsim 3000$ are discarded (see Figure 10.6 and Table 10.2). However, discarding the TT data comes at the price of increased statistical error bars on cosmological parameters. Fortunately, the increase is not dramatic: at most $\sim 21\%$ for $\Omega_c h^2$ and $\sim 13\%$ for $N_{\rm eff}$.

Another mitigation approach is to explicitly parameterize the nonlinear/baryonic effects on the CMB lensing power spectrum, and subsequently marginalize over these parameters in the cosmological analysis of the primary CMB power spectra (e.g., as done in Chapter 9 for the cosmological analysis of the CMB lensing power spectrum). We perform this exercise in our Fisher calculations below. We find that this approach can successfully mitigate the biases, but, like the approach suggested above, comes at the price of increased error bars on cosmological parameters. However, we note that this can likely be improved by performing a joint analysis of the primary CMB power spectra with the reconstructed CMB lensing potential power spectrum itself. This will require a precise treatment of the joint covariance between these probes [275].

Finally, the most data-driven approach would be to "delens" the temperature and polarization anisotropy maps using the measured CMB lensing potential, e.g., as reconstructed using quadratic estimators [276, 277] or maximum-likelihood methods [278, 279], or as traced by external probes like the cosmic infrared background [45, 46, 95, 94]. If the delensing operation were 100% efficient, then because delensing uses the observed (true) lensing potential field to undo the lensing effects, it is clear that all biases related to modeling of the late-time density field would be removed in the primary CMB power spectra (since no such modeling would be required). Assessing the fidelity of this operation for realistic experimental configurations, which will yield less-than-perfect delensing efficiencies, will be a useful exercise in upcoming work. In particular, the feasibility of delensing on such small scales has not yet been explored. It is interesting to note that due to the effects identified here, in addition to statistical optimality arguments identified in earlier work [280], delensing now appears to be an important operation not only for enabling precise constraints on the tensor-to-scalar ratio r [45, 281, 16, 80], but also for enabling unbiased constraints on $N_{\rm eff}$ and other new-physics parameters in upcoming CMB experiments.

The remainder of this Chapter is organized as follows. In Section 10.2 we discuss gravitational lensing of the CMB and how uncertainties in the lensing power spectrum can propagate to uncertainties in the *lensed* power spectra. In Section 10.3 we introduce the Fisher formalism we use to forecast error bars and systematic biases. In Section 10.4 we discuss biases from the mismodeling of unknown baryonic effects, and present several ways to remove these biases. We discuss our results and conclude in Section 10.5.

All of our power spectrum calculations are performed with CAMB [18]. We assume a fiducial cosmology throughout of $\{H_0 = 67.32\ \mathrm{km/s/Mpc}, \Omega_b h^2 = 0.022383, \Omega_c h^2 = 0.12011, n_s = 0.96605, A_s = 2.1 \times 10^{-9}, \tau = 0.0543, M_\nu = 0.06\ \mathrm{eV}, N_{\rm eff} = 3.046\}$, corresponding to the best-fit values of the six primary ΛCDM parameters found in Table 1 of [41] along with the minimum allowed value of the neutrino mass M_ν and the standard value of the effective number of neutrino species $N_{\rm eff}$ (which are the values assumed in [41]).

10.2 The lensed CMB power spectra

Significant cosmological analysis is performed with the two-point statistics of the observed CMB, for which we have well-understood theoretical predictions. In particular, we consider the power spectrum of the CMB intensity anisotropies, C_ℓ^{TT}, and the power spectrum of the E-mode CMB polarization anisotropies, C_ℓ^{EE}. As these probes are not fully independent (the CMB is roughly 10% polarized), we also consider their cross-power spectrum, C_ℓ^{TE}. The effect of gravitational lensing on these quantities is shown in Figure 10.1. We provide a brief summary of the relevant physics here, and refer the reader to Ref. [90] for full details.

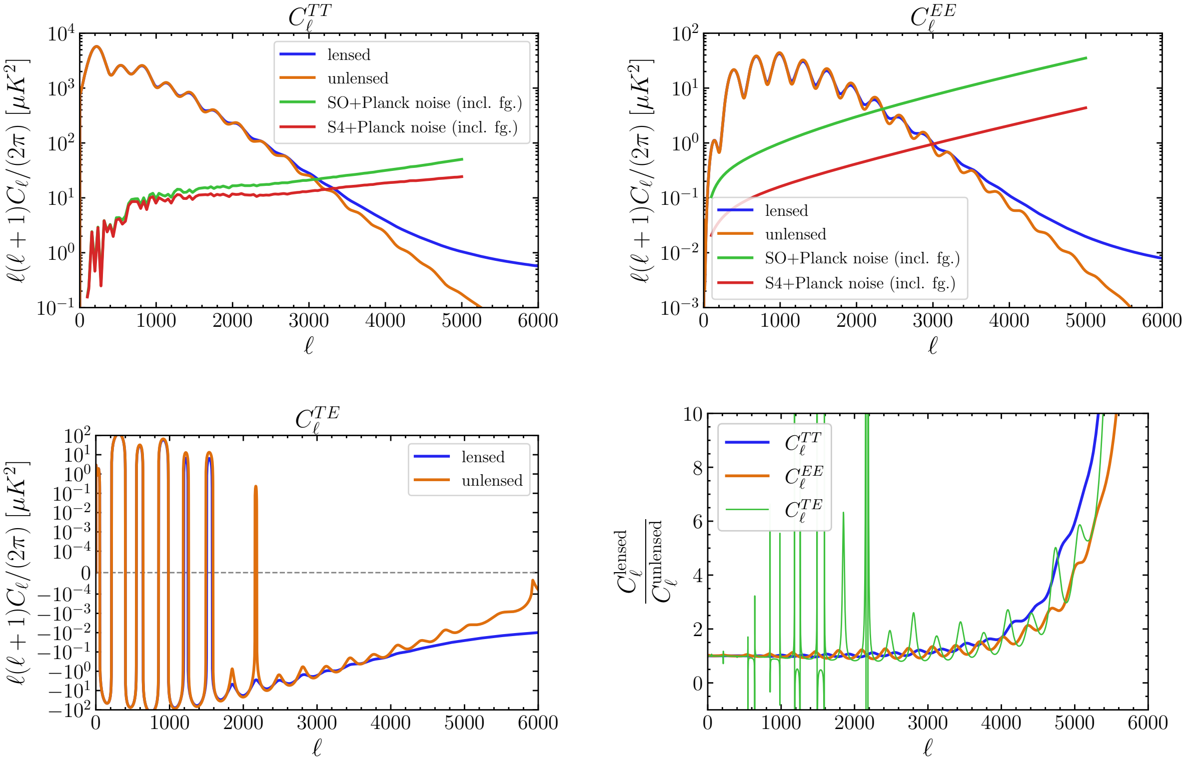

Figure 10.1: The lensed (blue) and unlensed (orange) CMB TT (*top left*), EE (*top right*), and TE (*bottom left*) power spectra and their ratios (*bottom right*). We see in the lensed spectra an increase of power on small scales, also clearly illustrated in the bottom right plot. We also see the smoothing effect of lensing, in the lowering of peak heights and the raising of trough heights. The post-component-separation noise power spectra (including residual foregrounds) expected from SO [16] and CMB-S4 [80], both including *Planck* data as well, are also indicated on the C_ℓ^{TT} and C_ℓ^{EE} plots (see Sec. 10.3 for details). It is clear that for precision cosmology with these experiments we will need to have an accurate calculation of the *lensed* CMB power.

The lensed power spectra, C_ℓ^{lensed}, are functions of the unlensed power spectra C_ℓ^{unlensed}, and the lensing potential power spectrum, $C_L^{\phi\phi}$. It is also common to consider, instead of $C_L^{\phi\phi}$, the lensing convergence power spectrum $C_L^{\kappa\kappa}$, which is related to $C_L^{\phi\phi}$ in harmonic space by

$$C_L^{\kappa\kappa} = \frac{(L(L+1))^2}{4} C_L^{\phi\phi}. \tag{10.1}$$

$C_L^{\kappa\kappa}$ is given in the Limber [49] and Born approximations by

$$C_L^{\kappa\kappa} = \int_0^{\chi_S} d\chi \left(\frac{W^\kappa_{\text{CMB}}(\chi)}{\chi} \right)^2 P_m \left(k = \frac{L+1/2}{\chi}, z \right), \tag{10.2}$$

where $P_m(k, z)$ is the matter power spectrum and $W^\kappa_{\text{CMB}}(\chi)$ is the CMB lensing efficiency kernel

$$W^\kappa_{\text{CMB}}(\chi) = \frac{3}{2}\Omega_m \left(\frac{H_0}{c} \right)^2 \frac{\chi}{a(\chi)} \frac{\chi_{\text{S}} - \chi}{\chi_{\text{S}}} \tag{10.3}$$

with χ_{S} the comoving distance to the surface of last scattering.

The lensing potential affects the observed temperature anisotropies. In particular, when we look in a direction $\hat{\boldsymbol{n}}$, we do not observe the temperature emitted at $\hat{\boldsymbol{n}}$ but the temperature that has been lensed into that direction, which was in fact sourced in the direction $\hat{\boldsymbol{n}} + \vec{\boldsymbol{\alpha}}$, where the total deflection angle induced by lensing $\vec{\boldsymbol{\alpha}}$ is given by the gradient (in the plane of the sky) of the lensing potential ϕ. Section 4 of Ref. [90] provides a thorough review of the calculation of the C_ℓ^{lensed} from C_ℓ^{unlensed} and $C_\ell^{\phi\phi}$, and we refer the interested reader to Section 4.2 of that paper for details of the exact calculation. Note, however, that to first order in $C_\ell^{\phi\phi}$ ($\sim$ to second order in $\vec{\boldsymbol{\alpha}}$) the lensed temperature power spectrum can be expressed as a convolution between the unlensed temperature power spectrum and the lensing potential power spectrum

$$\begin{aligned} C_\ell^{TT\,\text{lensed}} &\approx \left(1 - \ell^2 R^\phi\right) C_\ell^{TT\,\text{unlensed}} \\ &+ \int \frac{d^2\vec{\ell'}}{(2\pi)^2} C^{\phi\phi}_{|\vec{\ell}-\vec{\ell'}|} C_{\ell'}^{TT\,\text{unlensed}} \end{aligned} \tag{10.4}$$

where R^ϕ is given by

$$R^\phi \equiv \frac{1}{4\pi} \int \frac{d\ell}{\ell} \ell^4 C_\ell^{\phi\phi}. \tag{10.5}$$

In the small-scale limit, while the expansion in small $C_\ell^{\phi\phi}$ is not accurate, the fact that the unlensed power is so small and can be described by a single gradient term also allows for an approximation:

$$C_\ell^{TT\,\text{lensed}} \approx \ell^2 C_\ell^{\phi\phi} R^\Theta \tag{10.6}$$

where

$$R^{\Theta} = \frac{1}{4\pi} \int \frac{d\ell}{\ell} \ell^4 C_\ell^{TT\,\mathrm{unlensed}} \,. \tag{10.7}$$

For details of the above approximations we refer the reader to Section 4.1 of [90] and references therein; the calculation of the exact lensed TT spectrum by means of the correlation function, which is the method used in CAMB and CLASS, is also discussed in Section 4.2 of that reference. Similarly, the lensing of the EE spectrum is discussed in Section 5.3 of [90]. There are a number of important aspects to consider in the accurate calculation of $C_L^{\kappa\kappa}$ (and thus the accurate calculation of the lensed C_ℓ^{TT}, C_ℓ^{TE}, and C_ℓ^{EE}). Upcoming CMB surveys, including SO and CMB-S4, will be sufficiently sensitive that seemingly small effects need to be taken into account (our modeling of the noise for these surveys is discussed in the next section). Inaccuracies in the modeling of $P_m(k, z)$ due to gravitational non-linearities and baryonic feedback effects will become sufficiently important as to affect not only the interpretation of the reconstructed lensing power spectrum [274], but also the lensed primary CMB power spectra themselves. We will quantify this statement in the following sections.

The linear matter power spectrum is computed with cosmological perturbation theory, with non-linearities incorporated through, e.g., a halo-model-based fitting function such as Halofit [282, 283] or HMCode [284, 285]. HMCode further includes free parameters intended to capture the effects of complex baryonic phenomena on the matter power spectrum, including gas cooling and AGN and supernova feedback. These baryonic effects significantly alter the clustering of matter on $\lesssim 10\,\mathrm{Mpc}$ scales. We do not currently have a first-principles calculation of such effects, and as such they are sources of systematic error in the modeling of non-linear power spectra. To gain some understanding of the effects of baryonic interactions on matter clustering, we can perform cosmological hydrodynamics simulations (e.g., [270, 271, 272]); indeed, hydrodynamical simulations are used to construct the parametric HMCode model. However, one should keep in mind that the true non-linear power spectrum in our universe could (and likely does) differ at some level from these models (see, e.g., [286, 287]). As we will show, accounting for this uncertainty will be important in upcoming CMB experiments focused on the small-scale *primary* CMB power spectra.

10.3 Inference of cosmological parameters: statistical and systematic errors

10.3.1 The Fisher matrix formalism

The Fisher matrix formalism is widely used to calculate the uncertainties expected from statistical error alone on the analysis of a given parameter, assuming a (theoretical) calculation of the covariance of the data expected, including noise contributions. We summarize this approach briefly here.

We take as a data vector the (lensed) CMB power spectra: We calculate the theoretical C_ℓ with CAMB. The covariances between the different C_ℓ's are given by

$$\mathbb{C}\left(\hat{C}_\ell^{\alpha\beta}, \hat{C}_\ell^{\gamma\delta}\right) = \frac{1}{(2\ell+1) f_{\rm sky}} \left[\left(C_\ell^{\alpha\gamma} + N_\ell^{\alpha\gamma}\right) \left(C_\ell^{\beta\delta} + N_\ell^{\beta\delta}\right) + \left(C_\ell^{\alpha\delta} + N_\ell^{\alpha\delta}\right) \left(C_\ell^{\beta\gamma} + N_\ell^{\beta\gamma}\right) \right], \tag{10.8}$$

where N_ℓ^{XY} is the noise on the measurement of C_ℓ^{XY}, including contributions from the instrument, atmosphere, and residual foregrounds after component separation. We assume the noise on the polarization and intensity measurements to be uncorrelated, i.e., $N_\ell^{TE} = 0$. Finally, in Equation (10.8) $f_{\rm sky}$ is the sky fraction covered by the survey; we take $f_{\rm sky} = 0.4$ for SO and $f_{\rm sky} = 0.45$ for CMB-S4.

We include post-component-separation noise power spectra N_ℓ^{TT} and N_ℓ^{EE}, as computed for either SO (using the "Goal" noise levels)[1] [16] or CMB-S4[2] [80], both in combination with *Planck* data. The noise power spectra include contributions from instrumental and atmospheric noise, as well as residual foregrounds after multi-frequency internal linear combination (ILC) foreground cleaning has been applied in the harmonic domain (e.g., [81, 82]). The foregrounds include models for Galactic dust and synchrotron in both temperature and polarization, as well as Galactic free-free, Galactic spinning dust, extragalactic radio and infrared point sources, the thermal and kinematic Sunyaev-Zel'dovich effects, and the cosmic infrared background in temperature, with realistic correlations amongst the constituent Galactic and extragalactic components (full details can be found in [16, 80]). While the modeling of these components is not perfectly known, this uncertainty will only affect the post-component-separation noise power spectra in Figure 10.1 at the ∼ 10% level; the biases computed in this Chapter will thus be expected to differ slightly in practice compared

---

[1] `https://simonsobservatory.org/assets/supplements/20180822_SO_Noise_Public.tgz`

[2] `https://cmb-s4.uchicago.edu/wiki/index.php/Survey_Performance_Expectations`

to our forecasts, but not dramatically so. However, we note that in a fully realistic analysis of multi-frequency power spectrum data, the contributions from various foregrounds would be parameterized and explicitly marginalized over in the likelihood (e.g., [86, 288]). If the foregrounds are sufficiently orthogonal to the primary CMB (as is the case with non-blackbody foregrounds probed in multiple frequency channels) and the model has sufficient flexibility, then the foregrounds will not bias cosmological parameter estimation, and their effect is primarily to contribute to the noise power captured in our post-ILC noise curves[3]. Non-Gaussian contributions of the foregrounds to the post-ILC noise covariance matrix, as well as the question of whether currently used foreground models are sufficiently flexible so as to not bias cosmological parameters are outside the scope of this work. Similarly, in this Chapter, we do not include contributions from non-Gaussian covariance due to lensing and super-sample variance [275, 48, 289], which would especially be of importance in a mitigation strategy involving joint analysis with the CMB lensing four-point function (see Sec. 10.4.2).

The Fisher matrix for the parameter vector Π^i can be calculated from the covariance $\mathbb{C}_\ell$ and derivatives of the data vector C_ℓ with respect to Π^i:[4]

$$F_{ij} = \sum_\ell \frac{\partial C_\ell^T}{\partial \Pi^i} \mathbb{C}_\ell^{-1} \frac{\partial C_\ell}{\partial \Pi^j}. \tag{10.9}$$

Within this formalism, the forecast statistical error on the parameter i, marginalized over the other parameters in Π, is

$$\sigma(\Pi^i) = \sqrt{(F^{-1})_{ii}}. \tag{10.10}$$

Note that Equation (10.10) represents a *lower bound* on the true error bars, with the true error bar approaching $\sqrt{(F^{-1})_{ii}}$ in the case of Gaussian covariances.

The standard Fisher formalism above can be extended to consider errors that are not statistical, but instead are caused by a systematic miscalculation of the theoretical signal, e.g., an incorrect theory model. If we perform data analysis with incorrect theoretical power spectra — let us call this $C_\ell^{\rm fiducial}$ — the dependence of $C_\ell^{\rm fiducial}$ on the parameters Π^i will be different to those of the true theory ($C_\ell^{\rm true}$), and we will get a biased inference of Π^i. The size of the bias is given by the bias vector (see, e.g., [290, 291])

$$B(\Pi^i) = F_{ij}^{-1} \sum_\ell \frac{\partial C_\ell^{{\rm fiducial},T}}{\partial \Pi^j} \mathbb{C}_\ell^{-1} \Delta C_\ell, \tag{10.11}$$

---

[3] This statement was explicitly verified for SO forecasts by comparing the post-ILC effective noise curve approach to a full, parametric likelihood calculation in Sec. 4.1.2 of Ref. [16].

[4] Here we have assumed that the covariance matrix $\mathbb{C}$ does not depend on the parameters, i.e., it is computed at a fixed cosmology.

where

$$\Delta C_\ell \equiv C_\ell^{\rm true} - C_\ell^{\rm fiducial}. \tag{10.12}$$

Equation (10.11) thus allows us to compute *systematic* errors in the Fisher formalism, arising due to differences between the correct and assumed theoretical power spectra.

10.3.2 Constraints from upcoming surveys

We can use the Fisher formalism to predict the statistical error bars on cosmological parameters for upcoming experiments, e.g., SO and CMB-S4. In particular, we show in Figure 10.2 the predicted CMB-S4 constraints on the six parameters of the ΛCDM model, and on an extension of this model where the effective number of relativistic species $N_{\rm eff}$ is allowed to vary. We sum over all multipoles from $\ell_{\rm min} = 100$ to $\ell_{\rm max}$, the quantity labeled on the x-axis. We also include a Gaussian prior on the parameter τ of 0.0543 ± 0.007, which is constrained to this level by the large-scale *Planck* EE data [41][5]. From the figure, it is clear that CMB-S4 can constrain all parameters in the base ΛCDM model to sub-percent precision (except τ), and $N_{\rm eff}$ to near-percent precision, solely using the primary CMB power spectra. As expected, the constraints begin to saturate once $\ell_{\rm max}$ is greater than the multipole at which CMB-S4 is cosmic-variance-limited (roughly $\ell \approx 3500$ in TT and $\ell \approx 3000$ in EE, as shown in Figure 10.1). For experiments with even lower noise levels than CMB-S4, these constraints would continue to improve with increasing $\ell_{\rm max}$ (e.g., [292, 293]). While we only show the $\ell_{\rm max}$-dependence of the CMB-S4 statistical forecast here for brevity, we note that SO will yield very precise constraints as well (prior to the start of the CMB-S4 survey), e.g., with a forecast error bar on $N_{\rm eff}$ of roughly 2% [16]; the values of the constraints that we calculate are listed in Tables 10.4 and 10.5. Thus, it is well-motivated to consider both experiments in our analysis.

10.4 Physical systematics: mismodeling of baryons

10.4.1 Quantifying the bias from baryons

The lensed CMB power spectra are sensitive to non-linearities in the CMB lensing potential. On small scales, poorly understood "baryonic" processes, caused by the behavior of complex visible ("baryonic") matter (such as AGN feedback and gas cooling) can cause a

---

[5] The SO and CMB-S4 large aperture telescopes are not expected to measure the largest-scale modes on the sky due to atmospheric $1/f$ noise [16, 80], which necessitates the use of our prior on τ here.

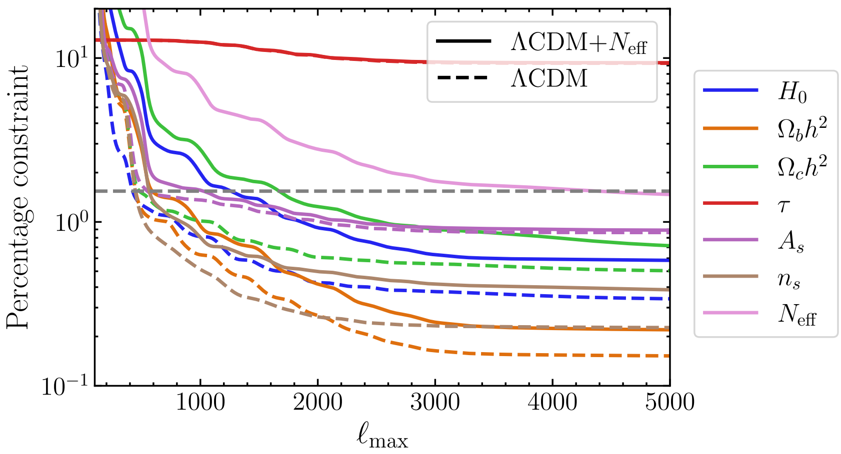

Figure 10.2: The forecast CMB-S4 constraints on the parameters of the ΛCDM model (dashed) and of ΛCDM+$N_{\rm eff}$ (solid), plotted against the maximum multipole included in the analysis. The constraints are shown as the fractional statistical uncertainty on each parameter, in units of percent.

non-negligible suppression in the matter power spectrum $P_m(k)$, and therefore the lensing power spectrum $C_L^{\kappa\kappa}$; this lends uncertainties to the modeling that propagate to the lensed CMB power spectra.

As we do not have first-principles calculations of these effects, much of our current understanding comes from performing large numerical simulations, and comparing runs with and without baryonic effects included, to measure the power spectrum suppression. In this section we explore the bias induced by *not* incorporating these effects into the analysis of the lensed CMB.

In Figure 10.3, we show the suppression in $C_L^{\kappa\kappa}$ induced by baryonic feedback effects in various hydrodynamical simulations [274, 4].[6] The figure also shows how the baryonic suppression in the CMB lensing power spectrum propagates to suppression in the lensed primary CMB power spectra. We show results for the OWLS-AGN simulation [187, 189], the fiducial BAHAMAS simulation as well as its "low-AGN" and "high-AGN" variants [189, 270, 294], the Horizon-AGN simulation [295, 296, 272], and the TNG100 and TNG300 runs from the Illustris-TNG simulation suite [297, 271, 298, 299, 300, 301]. All of the simulations yield qualitatively similar predictions for the power suppression due to baryonic

---

[6] The CMB lensing power spectrum suppression calculations are available at `https://github.com/sjforeman/cmblensing_baryons`.

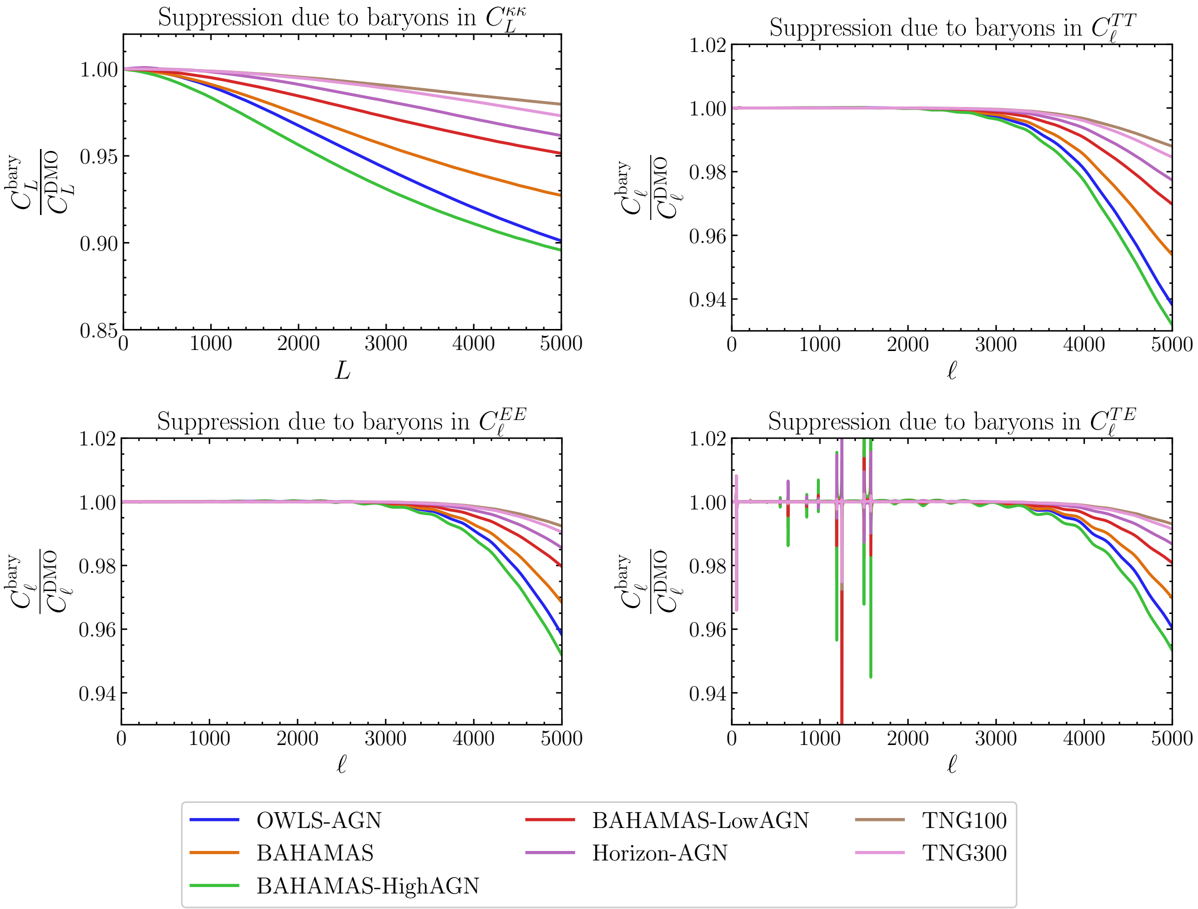

Figure 10.3: Suppression in power due to baryonic feedback effects in various different hydrodynamical simulations. The top left panel shows the suppression in the CMB lensing power spectrum relative to a (non-linear) dark-matter-only calculation. The other panels show the resulting impact on the lensed primary CMB power spectra ($TT/TE/EE$), as labeled.

feedback on the range of scales of interest here; however, the exact shape and amplitude of the suppression varies depending on the exact implementation (e.g., comparing the three BAHAMAS runs, one can see that the stronger the feedback prescription, the larger the predicted suppression, as gas is blown further out of halos into the intergalactic medium). We consider all seven of these baryonic models in the following, although our tabulated numerical results (e.g., Table 10.1) will generally focus on the OWLS-AGN run from the

OWLS simulation suite [187, 189].

The power *suppression* can be computed from each simulation by comparing the power spectrum from a "dark-matter-only" (DMO) run with the full baryonic physics ("AGN") run. The measured power spectrum ratio,

$$\hat{R}(k,z) \equiv \frac{\hat{P}^{\rm AGN}(k,z)}{\hat{P}^{\rm DMO}(k,z)}, \tag{10.13}$$

can be constrained from the simulations much better than either of the power spectra $\hat{P}^{\rm DMO,AGN}(k,z)$ directly, as much of the sample variance in the measurements of the separate power spectra cancel in their ratio. We can then incorporate baryons into the nonlinear matter power spectrum by modifying a theoretically calculated $P^{\rm DMO}(k,z)$ according to

$$P^{\rm bary}(k,z) = \hat{R}(k,z)P^{\rm DMO}(k,z). \tag{10.14}$$

While $\hat{R}(k,z)$ has some dependence on the cosmology [189] we do not consider this effect here; this is sufficient for our forecasts, particularly as derivatives with respect to power spectra computed with $\hat{R}(k,z)$ are never computed.

By using $P^{\rm bary}(k,z)$ in Equation (9.1), we compute the CMB lensing power spectrum incorporating baryonic feedback, $C_L^{\kappa\kappa {\rm bary}}$. We then use the CAMB to obtain the $C_\ell^{TT,TE,EE{\rm bary}}$ from $C_L^{\kappa\kappa{\rm bary}}$[7]. We then define our ΔC_ℓ to be used in Equation (10.11),

$$\Delta C_\ell \equiv C_\ell^{\rm bary} - C_\ell^{\rm DMO}, \tag{10.15}$$

where $C_\ell{}^{\rm DMO}$ is the fiducial $C_\ell^{TT,TE,EE}$ computed with $C_L^{\kappa\kappa{\rm DMO}}$. Note that the Fisher matrix (Equation (10.9)) in this section is always computed by taking derivatives of $C_\ell^{\rm DMO}$, as this is the fiducial model that would be used in data analysis in this scenario (and indeed, this is the fiducial model used in standard CMB analyses to date)[8].

Figure 10.4 presents a key result of this Chapter. In this plot, we show the fractional biases (in units of σ) on the parameters in the ΛCDM and ΛCDM+$N_{\rm eff}$ models induced by neglecting the baryonic suppression in $C_L^{\kappa\kappa}$, using the method described above. We use the OWLS-AGN baryonic model here, and show results for the CMB-S4 post-ILC noise power spectra presented in Figure 10.1. The biases are presented as a function of $\ell_{\rm max}$, the maximum multipole considered in the analysis of the TT, TE, and EE power spectra

---

[7] We have explicitly checked that the output of this function when using $C_L^{\kappa\kappa{\rm DMO}}$ agrees with the usual CAMB output for the lensed CMB power spectra, i.e., the DM-only model here matches that in fiducial CAMB calculations.

[8] Note that the default HMCode setting in CAMB, as of writing, is a DM-only model.

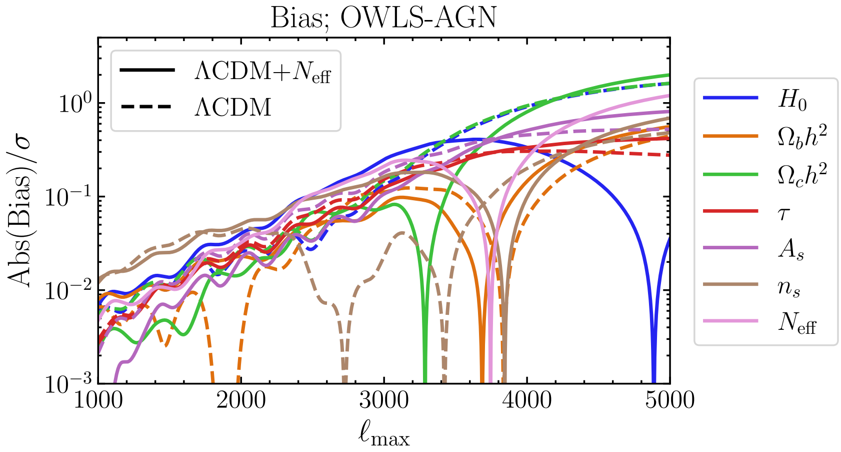

Figure 10.4: Baryonic-feedback-induced fractional biases (in absolute value) on the inferences of parameters in the ΛCDM and ΛCDM+$N_{\rm eff}$ models, as a fraction of the forecast 1σ constraints (which are shown in Figure 10.2), plotted against the maximum multipole included in the analysis, $\ell_{\rm max}$. Results are shown specifically for CMB-S4 here (see Table 10.1 for numerical results, including for SO). The baryonic model used here is from the OWLS-AGN simulation.

($\ell_{\rm max}$ is taken to be the same for all three spectra here). At high $\ell_{\rm max}$ the biases become increasingly significant, with some parameter biases exceeding their forecast statistical error bar. For example, with $\ell_{\rm max} = 5000$, the bias on H_0 reaches 1.6σ in ΛCDM, while the bias on $N_{\rm eff}$ reaches 1.2σ in ΛCDM+$N_{\rm eff}$. The exact numerical values are given in Table 10.1 for $\ell_{\rm max} = 5000$, along with analogous results computed for SO. These results clearly illustrate that these biases are potentially significant for upcoming high-precision, high-resolution CMB experiments.

10.4.2 Strategies to mitigate the baryonic biases

Removing small-scale TT information

If unaccounted for, baryonic feedback effects will bias cosmological parameter inference from the primary CMB; these systematic effects will require mitigation. A simple approach is to impose a lower $\ell_{\rm max}$ cut than 5000 on the data used for the analysis; it is clear from Figure 10.2 that there is not much constraining power at $\ell \gtrsim 3000$, while in Figure 10.4 we see that the biases increase significantly on these scales. Indeed, if one removes *only* the

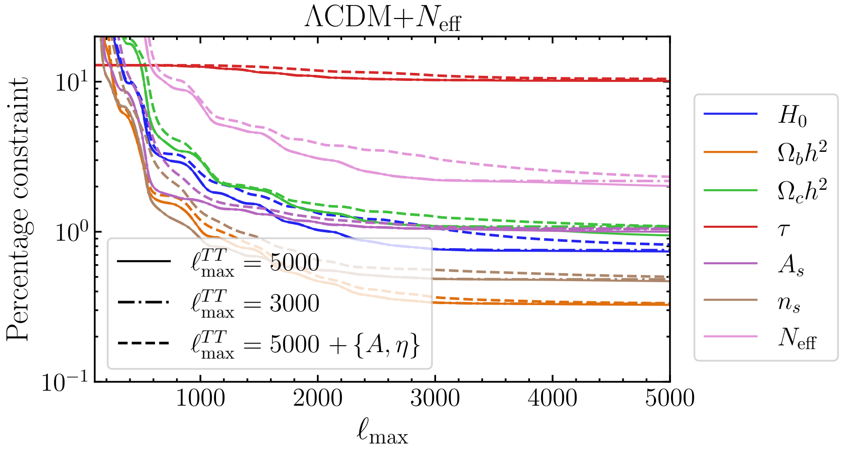

Figure 10.5: The impact of the various mitigation methods — a strict $\ell_{\text{max}} = 3000$ cut on TT and marginalization over baryonic feedback parameters (A, η) — on the constraints in the ΛCDM+N_{eff} model. The errors are only marginally increased in both cases, with the biggest increase seen in $\Omega_c h^2$; similar conclusions hold for the ΛCDM model analysis. Note that the horizontal axis here has the same meaning as in Figure 10.4, but that ℓ_{max}^{TT} is not increased above 3000 in the case shown in the dash-dotted curves.

TT information at $\ell > 3000$, while keeping the TE and EE spectra in the analysis, the bias is significantly reduced, as we now show.

The forecast constraints with TT data discarded at $\ell > 3000$ are shown in Figure 10.5 in the dash-dotted curves for the ΛCDM+N_{eff} model (the results for the ΛCDM model are similar). For comparison, the previous case where TT data are included up to $\ell = 5000$ is shown in the solid curves. While it is clear that the marginalized parameter error bars increase somewhat, the overall penalty is generally mild ($\lesssim 5\%$, except for $\Omega_c h^2$, which is impacted somewhat more than this). Numerical results for this increase in error bars are collected in Tables 10.4 (ΛCDM) and 10.5 (ΛCDM+N_{eff}).

The parameter biases in this case (when no TT information is considered above $\ell = 3000$) are shown in Figure 10.6 for all eight baryonic physics models. It is clear from the flattening of the bias curves at $\ell \gtrsim 3000$, above which TT data are excluded, that most of the bias is incurred from C_ℓ^{TT} in this small-scale regime. Thus, the baryonic biases can be controlled with a strict ℓ_{max} cut on TT. Numerical results for this approach, analogous to those in Table 10.1, are collected in Table 10.2 (for the OWLS-AGN simulation).

There are two primary reasons why the baryonic biases are dominated by the TT power spectrum: (1) SO and CMB-S4 will measure more signal-dominated modes in temperature

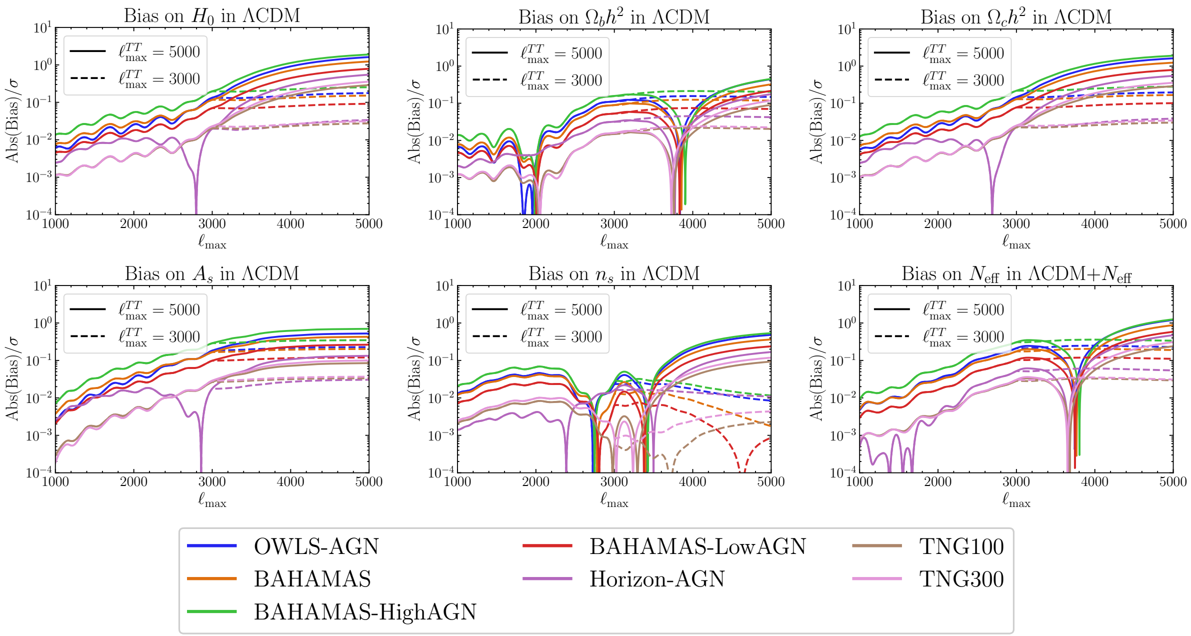

Figure 10.6: The $\ell_{\rm max}$ dependence of the biases for each parameter in the ΛCDM model, and also for $N_{\rm eff}$ in the ΛCDM+$N_{\rm eff}$ model, for the different simulations shown in Figure 10.3. The solid curves show the unmitigated biases (as in Figure 10.4 for OWLS-AGN), while the dashed curves show the results after mitigating the biases by imposing an $\ell^{TT}_{\rm max} = 3000$ cut. All results here are computed for CMB-S4.

	SO ($\ell^{TT}_{\rm max} = 3000$)		CMB-S4 ($\ell^{TT}_{\rm max} = 3000$)	
	ΛCDM	ΛCDM+$N_{\rm eff}$	ΛCDM	ΛCDM+$N_{\rm eff}$
H_0	0.098	0.25	0.18	0.23
$\Omega_b h^2$	0.13	0.085	0.15	0.065
$\Omega_c h^2$	0.12	0.12	0.20	0.05
τ	0.15	0.11	0.19	0.15
A_s	0.18	0.076	0.23	0.15
n_s	0.016	0.19	0.0084	0.18
$N_{\rm eff}$		0.24		0.23

Table 10.2: Fractional biases from the OWLS-AGN model (in units of the forecast 1σ statistical error bar) on each of the parameters in the various setups, when an $\ell^{TT}_{\rm max} = 3000$ cutoff is imposed (to be compared with Table 10.1.)

than in polarization (see the noise curves in Figure 10.1); (2) at a given multipole in the damping tail, the fractional contribution of lensing to the total power is larger in TT than in TE or EE, due to the larger gradient in the unlensed temperature field. Thus, since the high-ℓ TT data are more sensitive to lensing (at fixed ℓ), and a greater number of such modes are measured in temperature than in polarization, the baryonic feedback biases that enter via CMB lensing will be dominated by their effects on TT. Explicitly discarding the TT data on small scales is thus a simple and relatively robust approach to mitigate these biases.

In fact, this approach is consistent with the methodology often used in forecasts to account for the presence of extragalactic foregrounds at $\ell > 3000$ in TT, i.e., the data in this region are frequently assumed to be unusable for primary CMB science. This approach was used for the SO forecasting analysis, which set $\ell_{\rm max}^{TT} = 3000$, $\ell_{\rm max}^{TE} = 5000$, and $\ell_{\rm max}^{EE} = 5000$ (see Sec. 4 of Ref. [16]). However, for the CMB-S4 forecasting analysis, it was assumed that $\ell_{\rm max} = 5000$ for all of the spectra, including TT (see Sec. A.2.4 of Ref. [80]). In addition, the Atacama Cosmology Telescope (ACT) DR4 CMB likelihood considers $TT/TE/EE$ data to $\ell_{\rm max} = 4325$ for all of the spectra (see Table 18 of Ref. [87]). Our results provide motivation to explicitly discard the TT data at $\ell > 3000$ when performing primary CMB data analysis.

Marginalizing over a model for baryons

An alternative way to avoid biases from mismodeling baryons is to incorporate them into the model for $C_L^{\kappa\kappa}$, as was done in Chapter 9.6 when we considered the inference of M_ν from $C_L^{\kappa\kappa}$. The two extra parameters, A and η_0 can be included in our Fisher matrix and we can marginalize over them in order to mitigate the impact of baryons in a parametric manner.

Figure 10.5 (dashed curves) shows the effect of this marginalization on the ΛCDM+$N_{\rm eff}$ parameter constraints for CMB-S4. In contrast to the approach of discarding high-ℓ TT data, this method increases the error bars somewhat more noticeably. However, the penalties are still relatively mild, generally $\lesssim 10\%$. Numerical results illustrating the increase in error bars are collected in Tables 10.4 (ΛCDM) and 10.5 (ΛCDM+$N_{\rm eff}$). We note that these penalties could be decreased by performing a joint analysis of the primary CMB power spectra with $C_L^{\kappa\kappa}$ inferred from the CMB four-point function; the latter observable would constrain (A, η_0), thus yielding a smaller penalty when marginalizing over these parameters in the analysis. However, a careful treatment of the joint covariance [48, 275] would be required, which we defer to a dedicated analysis of this method.

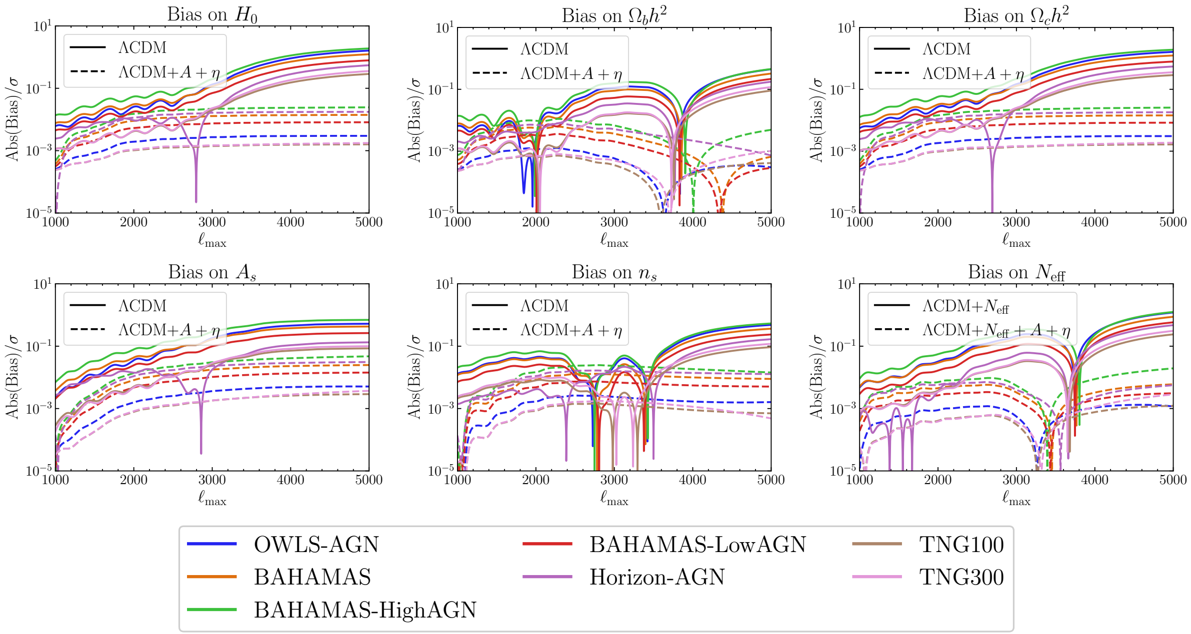
Bias on H_0

Bias on $\Omega_b h^2$

Bias on $\Omega_c h^2$

Bias on A_s

Bias on n_s

Bias on $N_{\rm eff}$

Figure 10.7: The $\ell_{\rm max}$ dependence of the biases for each parameter in the ΛCDM model, computed for the different hydrodynamical simulations shown in Figure 10.3. The solid curves show the unmitigated biases (as in Figure 10.4 for OWLS-AGN), while the dashed curves show the results after mitigating the biases by marginalizing over baryonic feedback parameters (A, η). We also include (bottom right) the biases on $N_{\rm eff}$ in the ΛCDM+$N_{\rm eff}$ model. All results here are computed for CMB-S4.

In Figure 10.7, we show the effect of this marginalization on the baryonic-feedback biases for CMB-S4 for the ΛCDM parameters and also for $N_{\rm eff}$ for the full set of baryonic models; the biases generally decrease by factors of > 100, illustrating that the marginalization is extremely effective. Numerical results for this approach (for OWLS-AGN), analogous to those in Table 10.1, are given in Table 10.3.

Overall, we conclude that this method is very promising, although one may worry that if there is a significant mismatch between the assumed parameterization and the actual baryonic effects in our universe, its effectiveness could be curtailed (note that Figure 10.7 provides evidence against this concern). A range of hydrodynamical simulations should be used to ensure its robustness in upcoming high-precision CMB analyses.

	SO		CMB-S4	
	ΛCDM	ΛCDM+$N_{\rm eff}$	ΛCDM	ΛCDM+$N_{\rm eff}$
H_0	0.0028	0.0022	0.0030	0.0026
$\Omega_b h^2$	0.00048	0.00098	0.00030	0.00060
$\Omega_c h^2$	0.0028	0.00091	0.0031	0.0012
τ	0.0026	0.0025	0.0038	0.0036
A_s	0.0035	0.0031	0.0051	0.0046
n_s	0.0014	0.0015	0.0016	0.0018
$N_{\rm eff}$		0.00091		0.0011

Table 10.3: Fractional biases from the OWLS-AGN model (in units of the forecast 1σ statistical error bar) on each of the parameters in the various setups, when the baryonic parameters A, η_0 are marginalized over (to be compared with Table 10.1).

Delensing

Delensing is the process of "undoing" the effects of gravitational lensing on the CMB. It requires knowledge of the actual CMB lensing potential on our sky, as derived from a reconstructed lensing map — or proxies for it, such as the measured CIB field or galaxy surveys (e.g., [45, 46, 47]). In the ideal case, the "delensed" CMB maps will recover the *unlensed* CMB temperature and polarization fields. This procedure is very important for enabling tight constraints on the tensor-to-scalar ratio in upcoming B-mode surveys [80]. For T and E-mode maps, delensing can provide slightly improved constraints on some of the parameters [48], but we note here that it is to be expected that it will provide *unbiased* constraints on the parameters as well, as sensitivity to low-z baryonic feedback effects will be reduced (or, ideally, removed).

Note that as we want to delens the high-ℓ power spectra here, a good proxy of the high-L CMB lensing potential will be required. In particular, Equation (10.4) indicates that to delens the CMB spectra up to $\ell \approx 5000$, we will need to have knowledge of $C_L^{\phi\phi}$ also out to $L \approx 5000$. This is a much smaller-scale regime than has been focused on in most previous delensing work, e.g., for primordial B-mode delensing. The reconstructed CMB lensing potential maps from SO or CMB-S4 are unlikely to have high fidelity at $L \approx 5000$ (e.g., see Figure 6 of Ref. [16]), although improved small-scale estimators could help to some extent [302]. Fortunately, external delensing tracers could be reasonably effective in this domain. In particular, dense galaxy samples from LSST and other photometric surveys may present a feasible option — see, e.g., Appendix B of Ref. [47]. However, a dedicated study would be needed to forecast the effectiveness of small-scale delensing.

One advantage of the delensing approach is that (at least in an ideal case), a model of the baryon-affected non-linear lensing power would no longer be needed for the interpretation; if one delensed the maps perfectly, then clearly there would be no need for a model of the nonlinear lensing power to interpret the primary CMB data at all. In a more pessimistic case in which the delensing efficiency is much less than 100%, it may simply introduce more complexity to consider the delensing operation for mitigating baryonic biases, and one may prefer to simply use a forward model of the nonlinear lensing power as we considered in the previous two subsections. We leave to future work the calculation of the baryonic feedback biases from delensed CMB power spectra.

	1σ error [%]: SO			1σ error [%]: CMB-S4		
	$\ell^{TT}_{\rm max} = 5000$	$\ell^{TT}_{\rm max} = 3000$	$\ell^{TT}_{\rm max} = 5000 + A + \eta$	$\ell^{TT}_{\rm max} = 5000$	$\ell^{TT}_{\rm max} = 3000$	$\ell^{TT}_{\rm max} = 5000 + A + \eta$
H_0	0.40	0.43	0.44	0.34	0.37	0.38
$\Omega_b h^2$	0.22	0.23	0.23	0.15	0.15	0.16
$\Omega_c h^2$	0.58	0.63	0.64	0.50	0.55	0.56
τ	10	10	10	9.3	9.3	9.5
A_s	0.95	0.97	1.0	0.86	0.87	0.90
n_s	0.26	0.27	0.27	0.23	0.23	0.23

Table 10.4: Forecast constraints (as percentages of the fiducial parameter values) for the ΛCDM parameters, for the various mitigation methods for SO and CMB-S4.

	1σ error [%]: SO			1σ error [%]: CMB-S4		
	$\ell^{TT}_{\rm max} = 5000$	$\ell^{TT}_{\rm max} = 3000$	$\ell^{TT}_{\rm max} = 5000 + A + \eta$	$\ell^{TT}_{\rm max} = 5000$	$\ell^{TT}_{\rm max} = 3000$	$\ell^{TT}_{\rm max} = 5000 + A + \eta$
H_0	0.74	0.75	0.82	0.58	0.60	0.63
$\Omega_b h^2$	0.33	0.33	0.33	0.22	0.23	0.23
$\Omega_c h^2$	0.95	1.1	1.1	0.72	0.87	0.87
τ	10	10	10	9.3	9.4	9.5
A_s	1.0	1.0	1.1	0.89	0.91	0.92
n_s	0.47	0.48	0.50	0.39	0.40	0.41
$N_{\rm eff}$	2.0	2.2	2.3	1.5	1.7	1.7

Table 10.5: Forecast constraints (as percentages of the fiducial parameter values) for the ΛCDM+$N_{\rm eff}$ model parameters, for the various mitigation methods for SO and CMB-S4.

10.5 Discussion and conclusions

In this Chapter, we have shown that inadequate modeling of baryonic feedback can lead to significant biases on cosmological parameters inferred from the primary CMB power spectra. The biases enter through the gravitational lensing contribution in the damping tail of the CMB power spectra, which in turn is dependent on the matter power spectrum and hence susceptible to mismodeling of non-linear and baryonic feedback effects. As can be seen from Table 10.1, for the number of light relativistic species $N_{\rm eff}$, the biases are as large as 0.38σ (1.2σ) for SO (CMB-S4). For the Hubble constant H_0 in a fit to the ΛCDM model, they are as large as 0.96σ (1.62σ) for SO (CMB-S4). These biases are estimated by assuming that the OWLS-AGN baryonic feedback model is the true model that describes the matter power spectrum in our universe, while the parameter inference is performed assuming no baryonic feedback prescription. The OWLS-AGN model is a reasonable prescription to consider in this context, given the large spread of predictions from various subgrid prescriptions and AGN feedback strengths in modern hydrodynamical simulations (see, e.g., [273, 189]).

We have suggested multiple mitigation methods to avoid these uncertain late-universe effects in the primary CMB. Our first recommendation is to explicitly discard all data at $\ell > 3000$ in the TT spectra; we find that this choice reduces the biases on parameters considered here to be no more than 30% of the statistical error bar (for both SO and CMB-S4). Alternatively, or in addition, we show that one can marginalize over a two-parameter model describing the effects of baryonic feedback. We find that this procedure reduces the biases on cosmological parameters by factors of $\mathcal{O}(100 - 1000)$. For both of these mitigation strategies, the size of the statistical uncertainties on cosmological parameters increases, albeit not dramatically (generally $\lesssim 10\%$, with a maximum increase of 21% on $\Omega_c h^2$; the $N_{\rm eff}$ error bar increases by 13% for CMB-S4). For the baryonic-parameter-marginalization approach, the increase could be mitigated by performing a joint analysis with $C_L^{\kappa\kappa}$. It is conceivable that delensing will be useful as a data-driven solution — that is, a solution without marginalization over a baryonic feedback model — to avoid these biases. However, this will require significant delensing of the small-scale maps ($\ell >$ 3000); we leave to future work a quantitative study of the effectiveness of delensing with efficiencies expected for SO and CMB-S4 in combination with *Planck* CIB and galaxy surveys. Finally, we note that in the coming decade, cross-correlations between CMB experiments like SO and CMB-S4 and galaxy surveys like DESI and LSST will allow for percent-level measurements of the distribution of ionized electrons across a wide range of redshifts through the kinematic Sunyaev-Zel'dovich (kSZ) effect (e.g., [303, 304, 131, 305, 306, 307, 286, 287, 308, 309, 310]). In tandem, percent-level measurements of the ionized gas pressure across a wide range of halo masses and redshifts will be enabled by cross-correlations of these galaxy surveys with thermal Sunyaev-Zel'dovich (tSZ) maps (e.g., [128, 311, 312, 313, 314, 315, 316, 317, 318, 319]), enabling joint constraints on all thermodynamic quantities describing the ionized gas in and around galaxies [320]. A wide variety of other probes will also be crucial in this endeavor, including X-ray measurements, fast radio burst dispersion measures, absorption line measurements, intensity-mapping measurements, and more. These measurements will significantly reduce uncertainties on baryonic feedback models, thus motivating joint analyses of CMB power spectra and the kSZ and tSZ effects, as well as folding in external information from the full complement of baryonic probes.

Given the non-negligible size of the baryonic-feedback biases for upcoming experiments, it is possible that ongoing experiments like ACT and the South Pole Telescope (SPT) that probe the CMB damping tail could also be mildly impacted by these effects. While recent SPT analyses have either used $\ell_{\text{max}} = 3000$ [321] or excluded TT data altogether [322, 258], the recent ACT DR4 analysis [13, 87] used TT data out to $\ell = 4325$. However, we expect any biases in analyses to date to be well below the 0.2σ level given that (a) the uncertainties on H_0 are more than five times larger than the forecast for SO (with a bias from baryonic feedback of $\Delta H_0 = 0.96\sigma$, c.f. Table 10.1) and (b) the absolute bias should also be lower than found here since the instrument noise level is larger in comparison with the gravitational lensing contribution to the power spectra. We also emphasize that these biases are irrelevant for *Planck* CMB power spectra, which do not probe multipoles $\ell \gtrsim 3000$ where the baryonic effects become important. These considerations do, however, highlight that mitigation strategies should be adopted for upcoming analyses from Advanced ACT [12] and SPT-3G [323, 324, 325].

Our work has only considered the ΛCDM parameters and the N_{eff} parameter, but similar considerations may apply to other parameters that affect the damping tail of the CMB. Inference of the sum of the neutrino masses may be of concern, but we note that the dominant constraint on this parameter comes from a more direct reconstruction of the gravitational lensing signal through the four-point function of the CMB, where the contribution from small scales in the matter power spectrum is easier to control (see [4] for a detailed study). Inference of blackbody secondary anisotropy parameters like the amplitude of the kSZ power spectrum (both late-time as well as from the reionization epoch) could also be affected, as these parameters can be degenerate with the primary cosmological parameters (which can be biased, as we have shown). For the same reason, free parameters in the blackbody components in the foreground model (e.g., the kSZ power spectrum amplitude) could also mitigate the baryonic feedback biases considered in this Chapter to some extent, by absorbing their effects (at the cost of a biased inference of the kSZ amplitude). We leave investigation of these issues to future work.

Several decades of cosmological inference from the primary CMB have benefited from the simplicity of the linear physics responsible for the observed temperature and polarization anisotropies. This will change in the coming decade with the next generation of CMB surveys. While these surveys extract new cosmological and astrophysical information from late-time effects, the primary CMB signal also becomes increasingly sensitive to uncertain astrophysical phenomena. A careful consideration of mitigation strategies, including delensing and/or joint analyses with the kSZ and tSZ effects, will therefore be of great importance in the coming decade of CMB surveys.

Chapter 11

Conclusions and future directions

This thesis (in particular Part II) consists of a compilation of various projects completed during my PhD. They are connected in that they all relate to upcoming CMB surveys and the new data products we will have. In many cases, a "future direction" is obvious: apply the methods developed here to the data products when they become available.

In Chapter 7 we discussed how CIB models can be improved through cross-correlation with CMB lensing data. One other aspect of how this cross-correlation is interesting is the possibility of using it to constrain primordial non-Gaussianity, by using large-scale maps to detect the scale dependent bias of the dusty galaxies sourcing the CIB [326]. A *large-scale* scale-dependent bias is a very promising way to detect primordial non-Gaussianity, an effect that has implications for discriminating between different inflationary theories. The signal of interest is strongest on very large scales and for objects with high bias; the star-forming CIB galaxies are ideal candidates for the second condition but it is difficult to make large-scale CIB maps due to the contamination of galactic dust potentially biasing the measured signal. However, this is a systematic that is not so important in the cross-correlation between the CIB and CMB lensing, and so it is possible that we could access larger scales.

In Chapter 8, we developed an estimator to reconstruct the large-scale remote dipole field through cross-correlation between the kSZ and the CIB. Work is ongoing to create a pipeline to apply this estimator on realistic datasets, including real-world effects such as a masked sky, instrumental noise, and foregrounds. We plan to apply this to existing datasets from *Planck* and ACT, and eventually (when they become available) from the Simons Observatory, with the hope of detecting the remote dipole field in this manner. The formalism that we developed is also applicable for reconstruction with any two-dimensional tracer (not only the CIB) such as galaxy surveys with little redshift resolution, and could also be applied to such datasets to make a detection of the remote dipole field.

In Chapters 9 and 10 we discussed mitigation techniques to mitigate the baryonic bias on CMB lensing and primary CMB measurements and inference. For some work that directly follows on for this, it will be of interest to quantify how much of the baryonic bias can be removed from the lensed 2-point CMB power spectra through delensing. In particular, delensing has not been demonstrated on the small scales necessary to remove the baryonic information from the CMB, but with a high-density galaxy survey this could be possible. This would be analagous to the mitigation strategy in Chapter 9.5 where we "subtracted" the low-z contribution to the cosmic shear kernel with external tracers.

On a wider note, it will be important to consider the joint analysis of the lensed CMB and the CMB lensing fields, to understand whether the neutrino mass marginalization might incorporate all the bias from the baryons, removing the bias from the other parameters. Also, a drawback of the approaches currently taken is that they assume fiducial CIB and SZ foregrounds, although minimized through the ILC procedure; however allowing for the significant modelling uncertainty by incorporating parameters for the physical CIB and SZ models and marginalizing over them would be appropriate (currently all CIB and SZ foregrounds are treated with precomputed templates). As well as this, the SZ has the potential to map the baryons to such a degree that we will perhaps not need to mitigate bias; a combined study of these surveys would be interesting to understand to what level we will be able to reduce baryonic uncertainty in the small-scale CMB.

References

[1] F. McCarthy, D. Kubizňák and R. B. Mann, *Dilatonic imprints on exact gravitational wave signatures*, *Phys Rev D* **97** (May, 2018) 104025, [1803.01862].

[2] F. McCarthy and M. S. Madhavacheril, *Improving models of the cosmic infrared background using CMB lensing mass maps*, *Phys. Rev. D* **103** (2021) 103515, [2010.16405].

[3] F. McCarthy and M. C. Johnson, *Remote dipole field reconstruction with dusty galaxies*, *Phys Rev D* **102** (August, 2020) 043520, [1907.06678].

[4] F. McCarthy, S. Foreman and A. van Engelen, *Avoiding baryonic feedback effects on neutrino mass measurements from cmb lensing*, *Phys. Rev. D* **103** (May, 2021) 103538.

[5] F. McCarthy, J. C. Hill and M. S. Madhavacheril, *Baryonic feedback biases on fundamental physics from lensed CMB power spectra*, *arXiv e-prints* (Mar., 2021) arXiv:2103.05582, [2103.05582].

[6] B. L. Webster and P. Murdin, *Cygnus X-1-a Spectroscopic Binary with a Heavy Companion ?*, Nature **235** (Jan., 1972) 37–38.

[7] Virgo, LIGO Scientific collaboration, B. P. Abbott et al., *Observation of Gravitational Waves from a Binary Black Hole Merger*, *Phys. Rev. Lett.* **116** (2016) 061102, [1602.03837].

[8] Event Horizon Telescope Collaboration, K. Akiyama, A. Alberdi, W. Alef, K. Asada, R. Azulay et al., *First M87 Event Horizon Telescope Results. I. The Shadow of the Supermassive Black Hole*, *APJL* **875** (Apr., 2019) L1, [1906.11238].

[9] A. A. Penzias and R. W. Wilson, *A Measurement of Excess Antenna Temperature at 4080 Mc/s.*, *Astrophys J* **142** (July, 1965) 419–421.

[10] G. F. Smoot, C. L. Bennett, A. Kogut, E. L. Wright, J. Aymon, N. W. Boggess et al., *Structure in the COBE differential microwave radiometer first-year maps*, *apjl* **396** (Sept., 1992) L1–L5.

[11] Planck Collaboration, N. Aghanim, Y. Akrami, F. Arroja, M. Ashdown, J. Aumont et al., *Planck 2018 results. I. Overview and the cosmological legacy of Planck*, A&A **641** (Sept., 2020) A1, [`1807.06205`].

[12] S. W. Henderson, R. Allison, J. Austermann, T. Baildon, N. Battaglia, J. A. Beall et al., *Advanced ACTPol Cryogenic Detector Arrays and Readout*, *Journal of Low Temperature Physics* **184** (August, 2016) 772–779, [`1510.02809`].

[13] S. Aiola, E. Calabrese, L. Maurin, S. Naess, B. L. Schmitt, M. H. Abitbol et al., *The Atacama Cosmology Telescope: DR4 maps and cosmological parameters*, *JCAP* **2020** (December, 2020) 047, [`2007.07288`].

[14] J. E. Carlstrom, P. A. R. Ade, K. A. Aird, B. A. Benson, L. E. Bleem, S. Busetti et al., *The 10 Meter South Pole Telescope*, PASP **123** (May, 2011) 568, [`0907.4445`].

[15] SPT-3G collaboration, B. Benson et al., *SPT-3G: A Next-Generation Cosmic Microwave Background Polarization Experiment on the South Pole Telescope*, *Proc. SPIE Int. Soc. Opt. Eng.* **9153** (2014) 91531P, [`1407.2973`].

[16] SIMONS OBSERVATORY collaboration, J. Aguirre et al., *The Simons Observatory: Science goals and forecasts*, *JCAP* **1902** (2019) 056, [`1808.07445`].

[17] CMB-S4 collaboration, K. N. Abazajian et al., *CMB-S4 Science Book, First Edition*, `1610.02743`.

[18] A. Lewis, A. Challinor and A. Lasenby, *Efficient Computation of Cosmic Microwave Background Anisotropies in Closed Friedmann-Robertson-Walker Models*, *Astrophys J* **538** (August, 2000) 473–476, [`astro-ph/9911177`].

[19] VIRGO, LIGO SCIENTIFIC collaboration, B. Abbott et al., *GW170817: Observation of Gravitational Waves from a Binary Neutron Star Inspiral*, *Phys. Rev. Lett.* **119** (2017) 161101, [`1710.05832`].

[20] L. Blanchet, *Gravitational Radiation from Post-Newtonian Sources and Inspiralling Compact Binaries*, *Living Rev. Rel.* **17** (2014) 2, [`1310.1528`].

[21] F. Pretorius, *Evolution of binary black hole spacetimes*, *Phys. Rev. Lett.* **95** (2005) 121101, [`gr-qc/0507014`].

[22] M. Campanelli, C. O. Lousto, P. Marronetti and Y. Zlochower, *Accurate evolutions of orbiting black-hole binaries without excision*, *Phys. Rev. Lett.* **96** (2006) 111101, [`gr-qc/0511048`].

[23] J. G. Baker, J. Centrella, D.-I. Choi, M. Koppitz and J. van Meter, *Gravitational wave extraction from an inspiraling configuration of merging black holes*, *Phys. Rev. Lett.* **96** (2006) 111102, [`gr-qc/0511103`].

[24] L. Lehner and F. Pretorius, *Numerical Relativity and Astrophysics*, *Ann. Rev. Astron. Astrophys.* **52** (2014) 661–694, [`1405.4840`].

[25] E. W. Hirschmann, L. Lehner, S. L. Liebling and C. Palenzuela, *Black Hole Dynamics in Einstein-Maxwell-Dilaton Theory*, `1706.09875`.

[26] F.-L. Julié, *On the motion of hairy black holes in Einstein-Maxwell-dilaton theories*, *JCAP* **1801** (2018) 026, [`1711.10769`].

[27] P. Jai-akson, A. Chatrabhuti, O. Evnin and L. Lehner, *Black hole merger estimates in Einstein-Maxwell and Einstein-Maxwell-dilaton gravity*, Phys. Rev. D **96** (Aug., 2017) 044031, [`1706.06519`].

[28] R. C. Ferrell and D. M. Eardley, *Slow-motion scattering and coalescence of maximally charged black holes*, *Phys. Rev. Lett.* **59** (Oct, 1987) 1617–1620.

[29] R. C. Ferrell and D. M. Eardley, *Slowly moving maximally charged black holes*. 1989.

[30] J. Camps, S. Hadar and N. S. Manton, *Exact Gravitational Wave Signatures from Colliding Extreme Black Holes*, *Phys. Rev.* **D96** (2017) 061501, [`1704.08520`].

[31] S. D. Majumdar, *A class of exact solutions of einstein's field equations*, *Phys. Rev.* **72** (Sep, 1947) 390–398.

[32] A. Papapetrou, *A static solution of the equations of the gravitational field for an arbitary charge-distribution*, *Proceedings of the Royal Irish Academy. Section A: Mathematical and Physical Sciences* **51** (1945) 191–204.

[33] K. S. Thorne, *Multipole expansions of gravitational radiation*, *Rev. Mod. Phys.* **52** (Apr, 1980) 299–339.

[34] G. Gibbons and K. ichi Maeda, *Black holes and membranes in higher-dimensional theories with dilaton fields*, *Nuclear Physics B* **298** (1988) 741 – 775.

[35] D. Garfinkle, G. T. Horowitz and A. Strominger, *Charged black holes in string theory*, *Phys. Rev. D* **43** (May, 1991) 3140–3143.

[36] K. Shiraishi, *Multicentered solution for maximally charged dilaton black holes in arbitrary dimensions*, *J. Math. Phys.* **34** (1993) 1480–1486, [`1402.5484`].

[37] K. Shiraishi, *Moduli space metric for maximally charged dilaton black holes*, *Nucl. Phys.* **B402** (1993) 399–410, [`1407.5377`].

[38] S. Dodelson, *Modern Cosmology*. Academic Press, Amsterdam, 2003.

[39] V. Mukhanov, *Physical Foundations of Cosmology*. Cambridge University Press, Oxford, 2005.

[40] S. Weinberg, *Cosmology*. 2008.

[41] Planck Collaboration, N. Aghanim, Y. Akrami, M. Ashdown, J. Aumont, C. Baccigalupi et al., *Planck 2018 results. VI. Cosmological parameters*, *AAP* **641** (September, 2020) A6, [`1807.06209`].

[42] Planck collaboration, N. Aghanim et al., *Planck 2018 results. VI. Cosmological parameters*, *Astron. Astrophys.* **641** (2020) A6, [`1807.06209`].

[43] Y. B. Zeldovich and R. A. Sunyaev, *The Interaction of Matter and Radiation in a Hot-Model Universe*, Ap&SS **4** (July, 1969) 301–316.

[44] T. Okamoto and W. Hu, *CMB lensing reconstruction on the full sky*, *Phys. Rev.* **D67** (2003) 083002, [`astro-ph/0301031`].

[45] K. M. Smith, D. Hanson, M. LoVerde, C. M. Hirata and O. Zahn, *Delensing CMB polarization with external datasets*, *JCAP* **2012** (June, 2012) 014, [`1010.0048`].

[46] B. D. Sherwin and M. Schmittfull, *Delensing the CMB with the Cosmic Infrared Background*, *Phys. Rev.* **D92** (2015) 043005, [`1502.05356`].

[47] B. Yu, R. Z. Knight, B. D. Sherwin, S. Ferraro, L. Knox and M. Schmittfull, *Towards Neutrino Mass from Cosmology without Optical Depth Information*, `1809.02120`.

[48] D. Green, J. Meyers and A. van Engelen, *CMB delensing beyond the B modes*, *JCAP* **2017** (December, 2017) 005, [`1609.08143`].

[49] D. N. Limber, *The Analysis of Counts of the Extragalactic Nebulae in Terms of a Fluctuating Density Field.*, ApJ **117** (Jan, 1953) 134.

[50] R. A. Sunyaev and I. B. Zeldovich, *The velocity of clusters of galaxies relative to the microwave background - The possibility of its measurement*, MNRAS **190** (Feb., 1980) 413–420.

[51] E. T. Vishniac, *Reionization and Small-Scale Fluctuations in the Microwave Background*, ApJ **322** (Nov., 1987) 597.

[52] W. Hu, *Reionization Revisited: Secondary Cosmic Microwave Background Anisotropies and Polarization*, ApJ **529** (Jan., 2000) 12–25, [`astro-ph/9907103`].

[53] A. Mead, C. Heymans, L. Lombriser, J. Peacock, O. Steele and H. Winther, *Accurate halo-model matter power spectra with dark energy, massive neutrinos and modified gravitational forces*, MNRAS **459** (2016) 1468–1488, [`1602.02154`].

[54] LSST Science Collaboration et al., *LSST Science Book, Version 2.0*, *arXiv e-prints* (Dec, 2009) arXiv:0912.0201, [`0912.0201`].

[55] A. Cooray and R. K. Sheth, *Halo models of large scale structure*, *Phys. Rept.* **372** (2002) 1–129, [`astro-ph/0206508`].

[56] W. H. Press and P. Schechter, *Formation of Galaxies and Clusters of Galaxies by Self-Similar Gravitational Condensation*, ApJ. **187** (Feb., 1974) 425–438.

[57] R. K. Sheth and G. Tormen, *Large-scale bias and the peak background split*, MNRAS **308** (Sept., 1999) 119–126, [`astro-ph/9901122`].

[58] J. L. Tinker, B. E. Robertson, A. V. Kravtsov, A. Klypin, M. S. Warren, G. Yepes et al., *The Large-scale Bias of Dark Matter Halos: Numerical Calibration and Model Tests*, ApJ **724** (Dec, 2010) 878–886, [`1001.3162`].

[59] J. Tinker, A. V. Kravtsov, A. Klypin, K. Abazajian, M. Warren, G. Yepes et al., *Toward a Halo Mass Function for Precision Cosmology: The Limits of Universality*, ApJ **688** (Dec., 2008) 709–728, [`0803.2706`].

[60] J. F. Navarro, C. S. Frenk and S. D. M. White, *The Structure of Cold Dark Matter Halos*, ApJ **462** (May, 1996) 563, [`astro-ph/9508025`].

[61] A. R. Duffy, J. Schaye, S. T. Kay and C. Dalla Vecchia, *Dark matter halo concentrations in the Wilkinson Microwave Anisotropy Probe year 5 cosmology*, MNRAS **390** (Oct., 2008) L64–L68, [0804.2486].

[62] P. S. Behroozi, C. Conroy and R. H. Wechsler, *A Comprehensive Analysis of Uncertainties Affecting the Stellar Mass-Halo Mass Relation for 0 < z < 4*, ApJ **717** (Jul, 2010) 379–403, [1001.0015].

[63] A. A. Berlind and D. H. Weinberg, *The Halo Occupation Distribution: Toward an Empirical Determination of the Relation between Galaxies and Mass*, ApJ **575** (Aug., 2002) 587–616, [astro-ph/0109001].

[64] A. Leauthaud, J. Tinker, P. S. Behroozi, M. T. Busha and R. H. Wechsler, *A Theoretical Framework for Combining Techniques that Probe the Link Between Galaxies and Dark Matter*, ApJ **738** (Sept., 2011) 45, [1103.2077].

[65] J. L. Tinker and A. R. Wetzel, *What does Clustering Tell us About the Buildup of the Red Sequence?*, ApJ **719** (Aug, 2010) 88–103, [0909.1325].

[66] C. Chang, M. Jarvis, B. Jain, S. M. Kahn, D. Kirkby, A. Connolly et al., *The Effective Number Density of Galaxies for Weak Lensing Measurements in the LSST Project*, MNRAS **434** (2013) 2121, [1305.0793].

[67] C. Shang, Z. Haiman, L. Knox and S. P. Oh, *Improved models for cosmic infrared background anisotropies: new constraints on the infrared galaxy population*, MNRAS **421** (Apr., 2012) 2832–2845, [1109.1522].

[68] L. Knox, A. Cooray, D. Eisenstein and Z. Haiman, *Probing Early Structure Formation with Far-Infrared Background Correlations*, ApJ **550** (Mar., 2001) 7–20, [astro-ph/0009151].

[69] Planck Collaboration, P. A. R. Ade, N. Aghanim, C. Armitage-Caplan, M. Arnaud, M. Ashdown et al., *Planck 2013 results. XXX. Cosmic infrared background measurements and implications for star formation*, *Astron. Astrophys.* **571** (Nov., 2014) A30, [1309.0382].

[70] M. P. Viero, L. Wang, M. Zemcov, G. Addison, A. Amblard, V. Arumugam et al., *HerMES: Cosmic Infrared Background Anisotropies and the Clustering of Dusty Star-forming Galaxies*, ApJ **772** (Jul, 2013) 77, [1208.5049].

[71] A. W. Blain, V. E. Barnard and S. C. Chapman, *Submillimetre and far-infrared spectral energy distributions of galaxies: the luminosity-temperature relation and consequences for photometric redshifts*, MNRAS **338** (Jan., 2003) 733–744, [`astro-ph/0209450`].

[72] N. R. Hall, R. Keisler, L. Knox, C. L. Reichardt, P. A. R. Ade, K. A. Aird et al., *Angular Power Spectra of the Millimeter-wavelength Background Light from Dusty Star-forming Galaxies with the South Pole Telescope*, ApJ **718** (Aug, 2010) 632–646, [`0912.4315`].

[73] J. Kennicutt, Robert C., *Star Formation in Galaxies Along the Hubble Sequence*, *araa* **36** (Jan., 1998) 189–232, [`astro-ph/9807187`].

[74] H.-Y. Wu and O. Doré, *A minimal empirical model for the cosmic far-infrared background anisotropies*, MNRAS **466** (2017) 4651–4658, [`1611.04517`].

[75] D. Lenz, O. Doré and G. Lagache, *Large-scale Maps of the Cosmic Infrared Background from Planck*, ApJ **883** (September, 2019) 75, [`1905.00426`].

[76] N. Battaglia, *The Tau of Galaxy Clusters*, *JCAP* **1608** (2016) 058, [`1607.02442`].

[77] E. Komatsu and U. Seljak, *The Sunyaev-Zel'dovich angular power spectrum as a probe of cosmological parameters*, MNRAS **336** (Nov., 2002) 1256–1270, [`astro-ph/0205468`].

[78] J. C. Hill and E. Pajer, *Cosmology from the thermal Sunyaev-Zel'dovich power spectrum: Primordial non-Gaussianity and massive neutrinos*, *Phys Rev. D* **88** (Sept., 2013) 063526, [`1303.4726`].

[79] N. Battaglia, J. R. Bond, C. Pfrommer and J. L. Sievers, *On the Cluster Physics of Sunyaev-Zel'dovich and X-Ray Surveys. II. Deconstructing the Thermal SZ Power Spectrum*, ApJ **758** (Oct., 2012) 75, [`1109.3711`].

[80] K. Abazajian, G. Addison, P. Adshead, Z. Ahmed, S. W. Allen, D. Alonso et al., *CMB-S4 Science Case, Reference Design, and Project Plan*, *arXiv e-prints* (July, 2019) arXiv:1907.04473, [`1907.04473`].

[81] M. Tegmark, A. de Oliveira-Costa and A. J. Hamilton, *High resolution foreground cleaned CMB map from WMAP*, *Phys Rev D* **68** (Dec., 2003) 123523, [`astro-ph/0302496`].

[82] H. K. Eriksen, A. J. Banday, K. M. Górski and P. B. Lilje, *On Foreground Removal from the Wilkinson Microwave Anisotropy Probe Data by an Internal Linear Combination Method: Limitations and Implications*, *Astrophys J* **612** (Sept., 2004) 633–646, [`astro-ph/0403098`].

[83] G. E. Addison, J. Dunkley, A. Hajian, M. Viero, J. R. Bond, S. Das et al., *Power-law Template for Infrared Point-source Clustering*, ApJ **752** (June, 2012) 120, [`1108.4614`].

[84] M.-A. Miville-Deschênes and G. Lagache, *IRIS: A New Generation of IRAS Maps*, *apjs* **157** (Apr, 2005) 302–323, [`astro-ph/0412216`].

[85] Planck Collaboration, P. A. R. Ade, N. Aghanim, M. Arnaud, M. Ashdown, J. Aumont et al., *Planck early results. XVIII. The power spectrum of cosmic infrared background anisotropies*, *Astron. Astrophys.* **536** (Dec., 2011) A18, [`1101.2028`].

[86] J. Dunkley, E. Calabrese, J. Sievers, G. E. Addison, N. Battaglia, E. S. Battistelli et al., *The Atacama Cosmology Telescope: likelihood for small-scale CMB data*, *JCAP* **2013** (July, 2013) 025, [`1301.0776`].

[87] S. K. Choi, M. Hasselfield, S.-P. P. Ho, B. Koopman, M. Lungu, M. H. Abitbol et al., *The Atacama Cosmology Telescope: A Measurement of the Cosmic Microwave Background Power Spectra at 98 and 150 GHz*, *arXiv e-prints* (July, 2020) arXiv:2007.07289, [`2007.07289`].

[88] A. Maniyar, M. Béthermin and G. Lagache, *Star formation history from the cosmic infrared background anisotropies*, *Astron. Astrophys.* **614** (2018) A39, [`1801.10146`].

[89] A. Maniyar, M. Béthermin and G. Lagache, *A simple halo model formalism for the cosmic infrared background and its correlation with the thermal Sunyaev Zel'dovich effect*, *arXiv e-prints* (June, 2020) arXiv:2006.16329, [`2006.16329`].

[90] A. Lewis and A. Challinor, *Weak gravitational lensing of the CMB*, *Phys. Rept.* **429** (2006) 1–65, [`astro-ph/0601594`].

[91] Planck collaboration, P. A. R. Ade et al., *Planck 2013 results. XVIII. The gravitational lensing-infrared background correlation*, *Astron. Astrophys.* **571** (2014) A18, [`1303.5078`].

[92] ACT collaboration, A. van Engelen et al., *The Atacama Cosmology Telescope: Lensing of CMB Temperature and Polarization Derived from Cosmic Infrared Background Cross-Correlation*, ApJ. **808** (2015) 7, [1412.0626].

[93] O. Darwish, M. S. Madhavacheril, B. Sherwin, S. Aiola, N. Battaglia, J. A. Beall et al., *The Atacama Cosmology Telescope: A CMB lensing mass map over 2100 square degrees of sky and its cross-correlation with BOSS-CMASS galaxies*, *arXiv e-prints* (April, 2020) arXiv:2004.01139, [2004.01139].

[94] B. Yu, J. C. Hill and B. D. Sherwin, *Multitracer CMB delensing maps from Planck and WISE data*, Phys. Rev. D **96** (December, 2017) 123511, [1705.02332].

[95] P. Larsen, A. Challinor, B. D. Sherwin and D. Mak, *Demonstration of Cosmic Microwave Background Delensing Using the Cosmic Infrared Background*, Phys. Rev. Lett. **117** (October, 2016) 151102, [1607.05733].

[96] The CMB-S4 Collaboration, :, K. Abazajian, G. E. Addison, P. Adshead, Z. Ahmed et al., *CMB-S4: Forecasting Constraints on Primordial Gravitational Waves*, *arXiv e-prints* (August, 2020) arXiv:2008.12619, [2008.12619].

[97] G. J. Stacey, M. Aravena, K. Basu, N. Battaglia, B. Beringue, F. Bertoldi et al., *CCAT-Prime: science with an ultra-widefield submillimeter observatory on Cerro Chajnantor*, in *Ground-based and Airborne Telescopes VII* (H. K. Marshall and J. Spyromilio, eds.), vol. 10700 of *Society of Photo-Optical Instrumentation Engineers (SPIE) Conference Series*, p. 107001M, July, 2018, 1807.04354, DOI.

[98] S. K. Choi, J. Austermann, K. Basu, N. Battaglia, F. Bertoldi, D. T. Chung et al., *Sensitivity of the Prime-Cam Instrument on the CCAT-Prime Telescope*, *Journal of Low Temperature Physics* **199** (March, 2020) 1089–1097, [1908.10451].

[99] C. L. Reichardt, S. Patil, P. A. R. Ade, A. J. Anderson, J. E. Austermann, J. S. Avva et al., *An Improved Measurement of the Secondary Cosmic Microwave Background Anisotropies from the SPT-SZ + SPTpol Surveys*, *arXiv e-prints* (February, 2020) arXiv:2002.06197, [2002.06197].

[100] Planck Collaboration, N. Aghanim, Y. Akrami, M. Ashdown, J. Aumont, C. Baccigalupi et al., *Planck 2018 results. VIII. Gravitational lensing*, *AAP* **641** (September, 2020) A8, [1807.06210].

[101] W. L. K. Wu, L. M. Mocanu, P. A. R. Ade, A. J. Anderson, J. E. Austermann, J. S. Avva et al., *A Measurement of the Cosmic Microwave Background Lensing*

Potential and Power Spectrum from 500 deg^2 of SPTpol Temperature and Polarization Data, ApJ **884** (October, 2019) 70, [1905.05777].

[102] Y. Cao, Y. Gong, C. Feng, A. Cooray, G. Cheng and X. Chen, *Cross-correlation of Far-infrared Background Anisotropies and CMB Lensing from Herschel and Planck Satellites*, ApJ **901** (September, 2020) 34, [1912.12840].

[103] U. Seljak, *Extracting primordial non-gaussianity without cosmic variance*, *Phys. Rev. Lett.* **102** (2009) 021302, [0807.1770].

[104] P. Serra, G. Lagache, O. Doré, A. Pullen and M. White, *Cross-correlation of cosmic far-infrared background anisotropies with large scale structures*, *Astron. Astrophys.* **570** (2014) A98, [1404.1933].

[105] Planck collaboration, P. A. R. Ade et al., *Planck 2013 results. XVI. Cosmological parameters*, *Astron. Astrophys.* **571** (2014) A16, [1303.5076].

[106] H.-Y. Wu and O. Doré, *Optimizing future experiments of cosmic far-infrared background: a principal component approach*, MNRAS **467** (June, 2017) 4150–4160, [1612.02474].

[107] M. Béthermin, E. Daddi, G. Magdis, C. Lagos, M. Sargent, M. Albrecht et al., *Evolution of the dust emission of massive galaxies up to $z = 4$ and constraints on their dominant mode of star formation*, *AAP* **573** (January, 2015) A113, [1409.5796].

[108] M. Tucci, L. Toffolatti, G. de Zotti and E. Martínez-González, *High-frequency predictions for number counts and spectral properties of extragalactic radio sources. New evidence of a break at mm wavelengths in spectra of bright blazar sources*, *AAP* **533** (Sept., 2011) A57, [1103.5707].

[109] B. Ménard, R. Scranton, S. Schmidt, C. Morrison, D. Jeong, T. Budavari et al., *Clustering-based redshift estimation: method and application to data*, *arXiv e-prints* (March, 2013) arXiv:1303.4722, [1303.4722].

[110] Planck Collaboration, *Planck 2013 results. IX. HFI spectral response*, *Astron. Astrophys.* **571** (Nov, 2014) A9, [1303.5070].

[111] Planck Collaboration, Ade, P. A. R., Aghanim, N., Armitage-Caplan, C., Arnaud, M., Ashdown, M. et al., *Planck 2013 results. vi. high frequency instrument data processing*, *A&A* **571** (2014) A6.

[112] M. S. Madhavacheril, N. Battaglia and H. Miyatake, *Fundamental physics from future weak-lensing calibrated Sunyaev-Zel'dovich galaxy cluster counts*, Phys. Rev. D **96** (November, 2017) 103525, [1708.07502].

[113] P. Madau and M. Dickinson, *Cosmic Star-Formation History*, *ARAA* **52** (August, 2014) 415–486, [1403.0007].

[114] O. Cucciati, L. Tresse, O. Ilbert, O. Le Févre, B. Garilli, V. Le Brun et al., *The star formation rate density and dust attenuation evolution over 12 Gyr with the VVDS surveys*, *AAP* **539** (March, 2012) A31, [1109.1005].

[115] B. Magnelli, P. Popesso, S. Berta, F. Pozzi, D. Elbaz, D. Lutz et al., *The deepest Herschel-PACS far-infrared survey: number counts and infrared luminosity functions from combined PEP/GOODS-H observations*, *AAP* **553** (May, 2013) A132, [1303.4436].

[116] C. Gruppioni, F. Pozzi, G. Rodighiero, I. Delvecchio, S. Berta, L. Pozzetti et al., *The Herschel PEP/HerMES luminosity function - I. Probing the evolution of PACS selected Galaxies to z=4*, MNRAS **432** (June, 2013) 23–52, [1302.5209].

[117] M. Béthermin, L. Wang, O. Doré, G. Lagache, M. Sargent, E. Daddi et al., *The redshift evolution of the distribution of star formation among dark matter halos as seen in the infrared*, *AAP* **557** (September, 2013) A66, [1304.3936].

[118] R. Reischke, V. Desjacques and S. Zaroubi, *The information content of Cosmic Infrared Background anisotropies*, MNRAS **491** (2020) 1079–1092, [1909.03761].

[119] S. J. Osborne, D. Hanson and O. Doré, *Extragalactic foreground contamination in temperature-based CMB lens reconstruction*, *JCAP* **2014** (March, 2014) 024, [1310.7547].

[120] The LSST Dark Energy Science Collaboration, R. Mandelbaum, T. Eifler, R. Hložek, T. Collett, E. Gawiser et al., *The LSST Dark Energy Science Collaboration (DESC) Science Requirements Document*, *arXiv e-prints* (September, 2018) arXiv:1809.01669, [1809.01669].

[121] A. Maniyar, G. Lagache, M. Béthermin and S. Ilić, *Constraining cosmology with the cosmic microwave and infrared backgrounds correlation*, *AAP* **621** (January, 2019) A32, [1809.04551].

[122] C. L. Bennett, A. J. Banday, K. M. Gorski, G. Hinshaw, P. Jackson, P. Keegstra et al., *Four-Year COBE DMR Cosmic Microwave Background Observations: Maps and Basic Results*, ApJ **464** (Jun, 1996) L1, [`astro-ph/9601067`].

[123] Planck collaboration, Y. Akrami et al., *Planck 2018 results. I. Overview and the cosmological legacy of Planck*, `1807.06205`.

[124] S. C. Parshley et al., *CCAT-prime: a novel telescope for sub-millimeter astronomy*, in *Ground-based and Airborne Telescopes VII*, vol. 10700 of *Society of Photo-Optical Instrumentation Engineers (SPIE) Conference Series*, p. 107005X, Jul, 2018, `1807.06675`, DOI.

[125] NASA PICO collaboration, S. Hanany et al., *PICO: Probe of Inflation and Cosmic Origins*, `1902.10541`.

[126] N. Sehgal et al., *Science from an Ultra-Deep, High-Resolution Millimeter-Wave Survey*, `1903.03263`.

[127] N. Hand et al., *Evidence of Galaxy Cluster Motions with the Kinematic Sunyaev-Zel'dovich Effect*, Phys. Rev. Lett. **109** (Jul, 2012) 041101, [`1203.4219`].

[128] Planck collaboration, P. A. R. Ade et al., *Planck Intermediate Results. XI: The gas content of dark matter halos: the Sunyaev-Zeldovich-stellar mass relation for locally brightest galaxies*, *Astron. Astrophys.* **557** (2013) A52, [`1212.4131`].

[129] ACTPol collaboration, E. Schaan et al., *Evidence for the kinematic Sunyaev-Zel?dovich effect with the Atacama Cosmology Telescope and velocity reconstruction from the Baryon Oscillation Spectroscopic Survey*, *Phys. Rev.* **D93** (2016) 082002, [`1510.06442`].

[130] DES, SPT collaboration, B. Soergel et al., *Detection of the kinematic Sunyaev?Zel'dovich effect with DES Year 1 and SPT*, MNRAS **461** (2016) 3172–3193, [`1603.03904`].

[131] J. C. Hill, S. Ferraro, N. Battaglia, J. Liu and D. N. Spergel, *Kinematic Sunyaev-Zel?dovich Effect with Projected Fields: A Novel Probe of the Baryon Distribution with Planck, WMAP, and WISE Data*, *Phys. Rev. Lett.* **117** (2016) 051301, [`1603.01608`].

[132] F. De Bernardis et al., *Detection of the pairwise kinematic Sunyaev-Zel'dovich effect with BOSS DR11 and the Atacama Cosmology Telescope*, *JCAP* **1703** (2017) 008, [`1607.02139`].

[133] E. M. George et al., *A measurement of secondary cosmic microwave background anisotropies from the 2500-square-degree SPT-SZ survey*, ApJ. **799** (2015) 177, [`1408.3161`].

[134] P.-J. Zhang and U.-L. Pen, *Deprojecting Sunyaev-Zeldovich statistics*, ApJ. **549** (2001) 18, [`astro-ph/0007462`].

[135] S. Ho, S. Dedeo and D. Spergel, *Finding the Missing Baryons Using CMB as a Backlight*, *arXiv e-prints* (Mar, 2009) arXiv:0903.2845, [`0903.2845`].

[136] J. Shao, P. Zhang, W. Lin, Y. Jing and J. Pan, *Kinetic Sunyaev-Zel'dovich tomography with spectroscopic redshift surveys*, MNRAS **413** (May, 2011) 628–642, [`1004.1301`].

[137] D. Munshi, I. T. Iliev, K. L. Dixon and P. Coles, *Extracting the late-time kinetic Sunyaev?Zel'dovich effect*, MNRAS **463** (2016) 2425–2442, [`1511.03449`].

[138] P. Zhang and M. C. Johnson, *Testing eternal inflation with the kinetic Sunyaev Zel'dovich effect*, *JCAP* **1506** (2015) 046, [`1501.00511`].

[139] A. Terrana, M.-J. Harris and M. C. Johnson, *Analyzing the cosmic variance limit of remote dipole measurements of the cosmic microwave background using the large-scale kinetic Sunyaev Zel'dovich effect*, *JCAP* **1702** (2017) 040, [`1610.06919`].

[140] A.-S. Deutsch, E. Dimastrogiovanni, M. C. Johnson, M. Münchmeyer and A. Terrana, *Reconstruction of the remote dipole and quadrupole fields from the kinetic Sunyaev Zel?dovich and polarized Sunyaev Zel?dovich effects*, *Phys. Rev.* **D98** (2018) 123501, [`1707.08129`].

[141] J. I. Cayuso, M. C. Johnson and J. B. Mertens, *Simulated reconstruction of the remote dipole field using the kinetic Sunyaev Zel?dovich effect*, *Phys. Rev.* **D98** (2018) 063502, [`1806.01290`].

[142] K. M. Smith, M. S. Madhavacheril, M. Münchmeyer, S. Ferraro, U. Giri and M. C. Johnson, *KSZ tomography and the bispectrum*, `1810.13423`.

[143] M. Münchmeyer, M. S. Madhavacheril, S. Ferraro, M. C. Johnson and K. M. Smith, *Constraining local non-Gaussianities with kinetic Sunyaev-Zel'dovich tomography*, *Phys. Rev.* **D100** (2019) 083508, [`1810.13424`].

[144] J. I. Cayuso and M. C. Johnson, *Towards testing CMB anomalies using the kinetic and polarized Sunyaev Zel'dovich effects*, `1904.10981`.

[145] D. Contreras, M. C. Johnson and J. B. Mertens, *Towards detection of relativistic effects in galaxy number counts using kSZ Tomography*, `1904.10033`.

[146] Z. Pan and M. C. Johnson, *Forecasted constraints on modified gravity from Sunyaev Zel'dovich tomography*, `1906.04208`.

[147] M. P. Viero, P. A. R. Ade, J. J. Bock, E. L. Chapin, M. J. Devlin, M. Griffin et al., *BLAST: Correlations in the Cosmic Far-Infrared Background at 250, 350, and 500 μm Reveal Clustering of Star-forming Galaxies*, ApJ **707** (Dec, 2009) 1766–1778, [`0904.1200`].

[148] J. Dunkley et al., *The Atacama Cosmology Telescope: likelihood for small-scale CMB data*, *JCAP* **1307** (2013) 025, [`1301.0776`].

[149] M. Tucci, V. Desjacques and M. Kunz, *Cosmic Infrared Background anisotropies as a window into primordial non-Gaussianity*, MNRAS **463** (2016) 2046–2063, [`1606.02323`].

[150] G. P. Holder et al., *A Cosmic Microwave Background Lensing Mass Map and Its Correlation with the Cosmic Infrared Background*, ApJ. **771** (2013) L16, [`1303.5048`].

[151] A. Manzotti, K. T. Story, W. L. K. Wu, J. E. Austermann, J. A. Beall, A. N. Bender et al., *CMB Polarization B-mode Delensing with SPTpol and Herschel*, ApJ **846** (Sept., 2017) 45, [`1701.04396`].

[152] M. S. Madhavacheril, N. Battaglia, K. M. Smith and J. L. Sievers, *Cosmology with kSZ: breaking the optical depth degeneracy with Fast Radio Bursts*, `1901.02418`.

[153] T. Namikawa, D. Hanson and R. Takahashi, *Bias-hardened CMB lensing*, MNRAS **431** (May, 2013) 609–620, [`1209.0091`].

[154] A. Lewis, A. Challinor and A. Lasenby, *Efficient computation of CMB anisotropies in closed FRW models*, *apj* **538** (2000) 473–476, [`astro-ph/9911177`].

[155] Planck collaboration, N. Aghanim et al., *Planck 2018 results. III. High Frequency Instrument data processing and frequency maps*, `1807.06207`.

[156] P. McDonald and U. Seljak, *How to measure redshift-space distortions without sample variance*, *JCAP* **0910** (2009) 007, [`0810.0323`].

[157] G. Stein, M. A. Alvarez, J. R. Bond, A. van Engelen and N. Battaglia, *The Websky Extragalactic CMB Simulations*, 2001.08787.

[158] Super-Kamiokande Collaboration collaboration, Y. Fukuda, T. Hayakawa, E. Ichihara, K. Inoue, K. Ishihara, H. Ishino et al., *Evidence for oscillation of atmospheric neutrinos*, *Phys. Rev. Lett.* **81** (Aug, 1998) 1562–1567.

[159] SNO Collaboration collaboration, Q. R. Ahmad, R. C. Allen, T. C. Andersen, J. D.Anglin, J. C. Barton, E. W. Beier et al., *Direct evidence for neutrino flavor transformation from neutral-current interactions in the sudbury neutrino observatory*, *Phys. Rev. Lett.* **89** (Jun, 2002) 011301.

[160] Particle Data Group collaboration, C. Patrignani et al., *Review of Particle Physics*, *Chin. Phys. C* **40** (2016) 100001.

[161] J. Lesgourgues and S. Pastor, *Massive neutrinos and cosmology*, *Phys. Rept.* **429** (2006) 307–379, [astro-ph/0603494].

[162] J. Lesgourgues and S. Pastor, *Neutrino mass from Cosmology*, *Adv. High Energy Phys.* **2012** (2012) 608515, [1212.6154].

[163] R. Allison, P. Caucal, E. Calabrese, J. Dunkley and T. Louis, *Towards a cosmological neutrino mass detection*, *Phys. Rev. D* **92** (2015) 123535, [1509.07471].

[164] M. J. White, *Baryons and weak lensing power spectra*, *Astropart. Phys.* **22** (2004) 211–217, [astro-ph/0405593].

[165] H. Zhan and L. Knox, *Effect of hot baryons on the weak-lensing shear power spectrum*, ApJ. **616** (2004) L75–L78, [astro-ph/0409198].

[166] Y. P. Jing, P. Zhang, W. P. Lin, L. Gao and V. Springel, *The influence of baryons on the clustering of matter and weak lensing surveys*, ApJ. **640** (2006) L119–L122, [astro-ph/0512426].

[167] D. H. Rudd, A. R. Zentner and A. V. Kravtsov, *Effects of Baryons and Dissipation on the Matter Power Spectrum*, ApJ. **672** (2008) 19–32, [astro-ph/0703741].

[168] E. Semboloni, H. Hoekstra, J. Schaye, M. P. van Daalen and I. J. McCarthy, *Quantifying the effect of baryon physics on weak lensing tomography*, MNRAS **417** (2011) 2020, [1105.1075].

[169] A. Natarajan, A. R. Zentner, N. Battaglia and H. Trac, *Systematic errors in the measurement of neutrino masses due to baryonic feedback processes: Prospects for stage IV lensing surveys*, *Phys. Rev. D* **90** (2014) 063516, [`1405.6205`].

[170] D. Copeland, A. Taylor and A. Hall, *Towards determining the neutrino mass hierarchy: weak lensing and galaxy clustering forecasts with baryons and intrinsic alignments*, MNRAS **493** (2020) 1640–1661, [`1905.08754`].

[171] A. Schneider, A. Refregier, S. Grandis, D. Eckert, N. Stoira, T. Kacprzak et al., *Baryonic effects for weak lensing. Part II. Combination with X-ray data and extended cosmologies*, *JCAP* **04** (2020) 020, [`1911.08494`].

[172] E. Chung, S. Foreman and A. van Engelen, *Baryonic effects on CMB lensing and neutrino mass constraints*, *Phys. Rev. D* **101** (2020) 063534, [`1910.09565`].

[173] J. Harnois-Déraps, L. van Waerbeke, M. Viola and C. Heymans, *Baryons, Neutrinos, Feedback and Weak Gravitational Lensing*, MNRAS **450** (2015) 1212–1223, [`1407.4301`].

[174] S. Foreman, M. R. Becker and R. H. Wechsler, *Cosmic Shear as a Probe of Galaxy Formation Physics*, MNRAS **463** (2016) 3326–3338, [`1605.09056`].

[175] DES collaboration, H.-J. Huang et al., *Dark Energy Survey Year 1 Results: Constraining Baryonic Physics in the Universe*, `2007.15026`.

[176] M. Yoon and M. J. Jee, *Baryonic feedback measurement from KV450 cosmic shear analysis*, `2007.16166`.

[177] G. Pratten and A. Lewis, *Impact of post-Born lensing on the CMB*, *JCAP* **1608** (2016) 047, [`1605.05662`].

[178] G. Fabbian, M. Calabrese and C. Carbone, *CMB weak-lensing beyond the Born approximation: a numerical approach*, *JCAP* **1802** (2018) 050, [`1702.03317`].

[179] A. R. Duffy, J. Schaye, S. T. Kay, C. Dalla Vecchia, R. A. Battye and C. Booth, *Impact of baryon physics on dark matter structures: a detailed simulation study of halo density profiles*, MNRAS **405** (2010) 2161, [`1001.3447`].

[180] DESI collaboration, A. Aghamousa et al., *The DESI Experiment Part I: Science,Targeting, and Survey Design*, `1611.00036`.

[181] J. Peloton, M. Schmittfull, A. Lewis, J. Carron and O. Zahn, *Full covariance of CMB and lensing reconstruction power spectra*, *Phys. Rev. D* **95** (2017) 043508, [`1611.01446`].

[182] D. Green, J. Meyers and A. van Engelen, *CMB Delensing Beyond the B Modes*, *JCAP* **12** (2017) 005, [`1609.08143`].

[183] A. Cooray, *Integrated sachs-Wolfe effect: Large scale structure correlation*, *Phys. Rev. D* **65** (2002) 103510, [`astro-ph/0112408`].

[184] A. Lewis, A. Challinor and D. Hanson, *The shape of the CMB lensing bispectrum*, *JCAP* **03** (2011) 018, [`1101.2234`].

[185] L. Pagano, J. M. Delouis, S. Mottet, J. L. Puget and L. Vibert, *Reionization optical depth determination from Planck HFI data with ten percent accuracy*, `1908.09856`.

[186] Z. Li, V. Gluscevic, K. K. Boddy and M. S. Madhavacheril, *Disentangling Dark Physics with Cosmic Microwave Background Experiments*, *Phys. Rev.* **D98** (2018) 123524, [`1806.10165`].

[187] M. P. van Daalen, J. Schaye, C. M. Booth and C. D. Vecchia, *The effects of galaxy formation on the matter power spectrum: A challenge for precision cosmology*, MNRAS **415** (2011) 3649–3665, [`1104.1174`].

[188] M. P. van Daalen, J. Schaye, C. Booth and C. D. Vecchia, *The effects of galaxy formation on the matter power spectrum: A challenge for precision cosmology*, MNRAS **415** (2011) 3649–3665, [`1104.1174`].

[189] M. P. van Daalen, I. G. McCarthy and J. Schaye, *Exploring the effects of galaxy formation on matter clustering through a library of simulation power spectra*, MNRAS **491** (2020) 2424–2446, [`1906.00968`].

[190] I. G. McCarthy, J. Schaye, S. Bird and A. M. Le Brun, *The BAHAMAS project: Calibrated hydrodynamical simulations for large-scale structure cosmology*, MNRAS **465** (2017) 2936–2965, [`1603.02702`].

[191] I. G. Mccarthy, S. Bird, J. Schaye, J. Harnois-Deraps, A. S. Font and L. Van Waerbeke, *The BAHAMAS project: the CMB–large-scale structure tension and the roles of massive neutrinos and galaxy formation*, MNRAS **476** (2018) 2999–3030, [`1712.02411`].

[192] Y. Dubois et al., *Dancing in the dark: galactic properties trace spin swings along the cosmic web*, MNRAS **444** (2014) 1453–1468, [1402.1165].

[193] Y. Dubois et al., *The HORIZON-AGN simulation: morphological diversity of galaxies promoted by AGN feedback*, MNRAS **463** (2016) 3948–3964, [1606.03086].

[194] N. E. Chisari, M. L. Richardson, J. Devriendt, Y. Dubois, A. Schneider, M. Brun, Amandine Le et al., *The impact of baryons on the matter power spectrum from the Horizon-AGN cosmological hydrodynamical simulation*, MNRAS **480** (2018) 3962–3977, [1801.08559].

[195] A. Pillepich et al., *First results from the IllustrisTNG simulations: the stellar mass content of groups and clusters of galaxies*, MNRAS **475** (2018) 648–675, [1707.03406].

[196] V. Springel et al., *First results from the IllustrisTNG simulations: matter and galaxy clustering*, MNRAS **475** (2018) 676–698, [1707.03397].

[197] D. Nelson et al., *First results from the IllustrisTNG simulations: the galaxy colour bimodality*, MNRAS **475** (2018) 624–647, [1707.03395].

[198] J. P. Naiman et al., *First results from the IllustrisTNG simulations: A tale of two elements – chemical evolution of magnesium and europium*, MNRAS **480** (2018) 1206, [1707.03401].

[199] F. Marinacci et al., *First results from the IllustrisTNG simulations: radio haloes and magnetic fields*, MNRAS **480** (2018) 5113–5139, [1707.03396].

[200] D. Nelson et al., *The IllustrisTNG Simulations: Public Data Release*, 1812.05609.

[201] S. Foreman, W. Coulton, F. Villaescusa-Navarro and A. Barreira, *Baryonic effects on the matter bispectrum*, MNRAS **498** (2020) 2887–2911, [1910.03597].

[202] A. Mead, J. Peacock, C. Heymans, S. Joudaki and A. Heavens, *An accurate halo model for fitting non-linear cosmological power spectra and baryonic feedback models*, MNRAS **454** (2015) 1958–1975, [1505.07833].

[203] B. O. Mummery, I. G. McCarthy, S. Bird and J. Schaye, *The separate and combined effects of baryon physics and neutrino free-streaming on large-scale structure*, MNRAS **471** (2017) 227–242, [1702.02064].

[204] K. Abazajian et al., *CMB-S4 Science Case, Reference Design, and Project Plan*, 1907.04473.

[205] A. van Engelen, S. Bhattacharya, N. Sehgal, G. Holder, O. Zahn and D. Nagai, *CMB Lensing Power Spectrum Biases from Galaxies and Clusters using High-angular Resolution Temperature Maps*, ApJ. **786** (2014) 13, [1310.7023].

[206] S. J. Osborne, D. Hanson and O. Doré, *Extragalactic Foreground Contamination in Temperature-based CMB Lens Reconstruction*, *JCAP* **03** (2014) 024, [1310.7547].

[207] S. Das, J. Errard and D. Spergel, *Can CMB Lensing Help Cosmic Shear Surveys?*, 1311.2338.

[208] E. Schaan, E. Krause, T. Eifler, O. Doré, H. Miyatake, J. Rhodes et al., *Looking through the same lens: Shear calibration for LSST, Euclid, and WFIRST with stage 4 CMB lensing*, *Phys. Rev.* **D95** (2017) 123512, [1607.01761].

[209] E. Schaan, S. Ferraro and U. Seljak, *Photo-z outlier self-calibration in weak lensing surveys*, 2007.12795.

[210] N. Jeffrey, F. Lanusse, O. Lahav and J.-L. Starck, *Deep learning dark matter map reconstructions from DES SV weak lensing data*, MNRAS **492** (2020) 5023–5029, [1908.00543].

[211] DES collaboration, B. Mawdsley et al., *Dark Energy Survey Year 1 Results: Wide Field Mass Maps via Forward Fitting in Harmonic Space*, MNRAS **493** (2020) 5662–5679, [1905.12682].

[212] EUCLID collaboration, S. Pires et al., *Euclid: Reconstruction of Weak Lensing mass maps for non-Gaussianity studies*, *Astron. Astrophys.* **638** (2020) A141, [1910.03106].

[213] M. A. Price, J. D. McEwen, L. Pratley and T. D. Kitching, *Spherical Bayesian mass-mapping with uncertainties: full sky observations on the celestial sphere*, 2004.07855.

[214] N. Kaiser and G. Squires, *Mapping the dark matter with weak gravitational lensing*, ApJ. **404** (1993) 441–450.

[215] B. Yu, J. Hill and B. D. Sherwin, *Multitracer CMB delensing maps from Planck and WISE data*, *Phys. Rev. D* **96** (2017) 123511, [1705.02332].

[216] C. M. Hirata and U. c. v. Seljak, *Intrinsic alignment-lensing interference as a contaminant of cosmic shear*, *Phys. Rev. D* **70** (Sep, 2004) 063526.

[217] S. Bridle and L. King, *Dark energy constraints from cosmic shear power spectra: impact of intrinsic alignments on photometric redshift requirements*, *New Journal of Physics* **9** (Dec., 2007) 444, [`0705.0166`].

[218] M. Brown, A. Taylor, N. Hambly and S. Dye, *Measurement of intrinsic alignments in galaxy ellipticities*, MNRAS **333** (2002) 501, [`astro-ph/0009499`].

[219] DES collaboration, S. Samuroff et al., *Dark Energy Survey Year 1 Results: Constraints on Intrinsic Alignments and their Colour Dependence from Galaxy Clustering and Weak Lensing*, MNRAS **489** (2019) 5453–5482, [`1811.06989`].

[220] H. Johnston et al., *KiDS+GAMA: Intrinsic alignment model constraints for current and future weak lensing cosmology*, *Astron. Astrophys.* **624** (2019) A30, [`1811.09598`].

[221] J. Yao, H. Shan, P. Zhang, J.-P. Kneib and E. Jullo, *Unveiling the Intrinsic Alignment of Galaxies with Self-Calibration and DECaLS DR3 data*, `2002.09826`.

[222] LSST Dark Energy Science collaboration, R. Mandelbaum et al., *Wide-field Multi-object Spectroscopy to Enhance Dark Energy Science from LSST*, `1903.09323`.

[223] Z. Vlah, N. E. Chisari and F. Schmidt, *An EFT description of galaxy intrinsic alignments*, *JCAP* **01** (2020) 025, [`1910.08085`].

[224] M. C. Fortuna, H. Hoekstra, B. Joachimi, H. Johnston, N. E. Chisari, C. Georgiou et al., *The halo model as a versatile tool to predict intrinsic alignments*, `2003.02700`.

[225] M. Lewandowski, A. Perko and L. Senatore, *Analytic Prediction of Baryonic Effects from the EFT of Large Scale Structures*, *JCAP* **1505** (2015) 019, [`1412.5049`].

[226] S.-F. Chen, E. Castorina and M. White, *Biased Tracers of Two Fluids in the Lagrangian Picture*, *JCAP* **1906** (2019) 006, [`1903.00437`].

[227] D. P. Bragança, M. Lewandowski, D. Sekera, L. Senatore and R. Sgier, *Baryonic effects in the Effective Field Theory of Large-Scale Structure and an analytic recipe for lensing in CMB-S4*, `2010.02929`.

[228] E. Semboloni, H. Hoekstra and J. Schaye, *Effect of baryonic feedback on two- and three-point shear statistics: prospects for detection and improved modelling*, MNRAS **434** (2013) 148, [1210.7303].

[229] A. Mead, T. Tröster, C. Heymans, L. Van Waerbeke and I. McCarthy, *A hydrodynamical halo model for weak-lensing cross correlations*, *Astron. Astrophys.* **641** (2020) A130, [2005.00009].

[230] A. Mead, S. Brieden, T. Tröster and C. Heymans, *HMcode-2020: Improved modelling of non-linear cosmological power spectra with baryonic feedback*, 2009.01858.

[231] S. N. Debackere, J. Schaye and H. Hoekstra, *The impact of the observed baryon distribution in haloes on the total matter power spectrum*, MNRAS **492** (2020) 2285–2307, [1908.05765].

[232] T. Eifler, E. Krause, S. Dodelson, A. Zentner, A. Hearin and N. Gnedin, *Accounting for baryonic effects in cosmic shear tomography: Determining a minimal set of nuisance parameters using PCA*, MNRAS **454** (2015) 2451–2471, [1405.7423].

[233] I. Mohammed and N. Y. Gnedin, *Baryonic Effects in Cosmic Shear Tomography: PCA Parameterization and the Importance of Extreme Baryonic Models*, ApJ. **863** (2018) 173, [1707.02332].

[234] H.-J. Huang, T. Eifler, R. Mandelbaum and S. Dodelson, *Modelling baryonic physics in future weak lensing surveys*, MNRAS **488** (2019) 1652–1678, [1809.01146].

[235] A. Schneider and R. Teyssier, *A new method to quantify the effects of baryons on the matter power spectrum*, *JCAP* **12** (2015) 049, [1510.06034].

[236] A. Schneider, R. Teyssier, J. Stadel, N. E. Chisari, A. M. C. Le Brun, A. Amara et al., *Quantifying baryon effects on the matter power spectrum and the weak lensing shear correlation*, *JCAP* **03** (2019) 020, [1810.08629].

[237] G. Aricò, R. E. Angulo, C. Hernández-Monteagudo, S. Contreras, M. Zennaro, M. Pellejero-Ibañez et al., *Modelling the large scale structure of the Universe as a function of cosmology and baryonic physics*, MNRAS **495** (2020) 4800, [1911.08471].

[238] G. Aricò, R. E. Angulo, C. Hernández-Monteagudo, S. Contreras and M. Zennaro, *Simultaneous modelling of matter power spectrum and bispectrum in the presence of baryons*, 2009.14225.

[239] A. Schneider, N. Stoira, A. Refregier, A. J. Weiss, M. Knabenhans, J. Stadel et al., *Baryonic effects for weak lensing. Part I. Power spectrum and covariance matrix*, *JCAP* **04** (2020) 019, [1910.11357].

[240] T. Tröster, C. Ferguson, J. Harnois-Déraps and I. G. McCarthy, *Painting with baryons: augmenting N-body simulations with gas using deep generative models*, MNRAS **487** (2019) L24–L29, [1903.12173].

[241] F. Villaescusa-Navarro et al., *The CAMELS project: Cosmology and Astrophysics with MachinE Learning Simulations*, 2010.00619.

[242] G. Parimbelli, M. Viel and E. Sefusatti, *On the degeneracy between baryon feedback and massive neutrinos as probed by matter clustering and weak lensing*, *JCAP* **01** (2019) 010, [1809.06634].

[243] A. H. Gonzalez, S. Sivanandam, A. I. Zabludoff and D. Zaritsky, *Galaxy Cluster Baryon Fractions Revisited*, ApJ. **778** (2013) 14, [1309.3565].

[244] S. Grandis, J. J. Mohr, J. P. Dietrich, S. Bocquet, A. Saro, M. Klein et al., *Impact of weak lensing mass calibration on eROSITA galaxy cluster cosmological studies – a forecast*, MNRAS **488** (2019) 2041–2067, [1810.10553].

[245] V. Vikram, A. Lidz and B. Jain, *A measurement of the galaxy-group thermal Sunyaev–Zel'dovich effect cross-correlation function*, MNRAS **467** (2017) 2315–2330, [1608.04160].

[246] H. Tanimura, S. Zaroubi and N. Aghanim, *Direct detection of the kinetic Sunyaev-Zel'dovich effect in galaxy clusters*, 2007.02952.

[247] S. Lim, H. Mo, H. Wang and X. Yang, *Detection of missing baryons in galaxy groups with kinetic Sunyaev-Zel'dovich effect*, ApJ. **889** (2020) 48, [1912.10152].

[248] N. Battaglia, S. Ferraro, E. Schaan and D. Spergel, *Future constraints on halo thermodynamics from combined Sunyaev-Zel'dovich measurements*, *JCAP* **11** (2017) 040, [1705.05881].

[249] H. Tanimura, G. Hinshaw, I. G. McCarthy, L. Van Waerbeke, N. Aghanim, Y.-Z. Ma et al., *Probing hot gas around luminous red galaxies through the Sunyaev–Zel'dovich effect*, MNRAS **491** (2020) 2318–2329, [1903.06654].

[250] S. Amodeo et al., *The Atacama Cosmology Telescope: Modelling the Gas Thermodynamics in BOSS CMASS galaxies from Kinematic and Thermal Sunyaev-Zel'dovich Measurements*, `2009.05558`.

[251] Y.-Z. Ma, Y. Gong, T. Troster and L. Van Waerbeke, *Probing the cluster pressure profile with thermal Sunyaev-Zeldovich effect and weak lensing cross-correlation*, `2010.15064`.

[252] S. Pandey, E. Baxter and J. Hill, *Constraining the properties of gaseous halos via cross-correlations of upcoming galaxy surveys and thermal Sunyaev-Zel'dovich maps*, *Phys. Rev. D* **101** (2020) 043525, [`1909.00405`].

[253] N. Battaglia et al., *Probing Feedback in Galaxy Formation with Millimeter-wave Observations*, `1903.04647`.

[254] A. Hojjati, I. G. McCarthy, J. Harnois-Deraps, Y.-Z. Ma, L. Van Waerbeke, G. Hinshaw et al., *Dissecting the thermal Sunyaev-Zeldovich-gravitational lensing cross-correlation with hydrodynamical simulations*, *JCAP* **10** (2015) 047, [`1412.6051`].

[255] A. Hojjati et al., *Cross-correlating Planck tSZ with RCSLenS weak lensing: Implications for cosmology and AGN feedback*, MNRAS **471** (2017) 1565–1580, [`1608.07581`].

[256] J. Hill and D. N. Spergel, *Detection of thermal SZ-CMB lensing cross-correlation in Planck nominal mission data*, *JCAP* **02** (2014) 030, [`1312.4525`].

[257] C. L. Bennett, D. Larson, J. L. Weiland, N. Jarosik, G. Hinshaw, N. Odegard et al., *Nine-year Wilkinson Microwave Anisotropy Probe (WMAP) Observations: Final Maps and Results*, *apjs* **208** (Oct., 2013) 20, [`1212.5225`].

[258] D. Dutcher, L. Balkenhol, P. A. R. Ade, Z. Ahmed, E. Anderes, A. J. Anderson et al., *Measurements of the E-Mode Polarization and Temperature-E-Mode Correlation of the CMB from SPT-3G 2018 Data*, *arXiv e-prints* (January, 2021) arXiv:2101.01684, [`2101.01684`].

[259] G. Jungman, M. Kamionkowski, A. Kosowsky and D. N. Spergel, *Weighing the Universe with the Cosmic Microwave Background*, *Phys Rev Lett* **76** (February, 1996) 1007–1010, [`astro-ph/9507080`].

[260] G. Jungman, M. Kamionkowski, A. Kosowsky and D. N. Spergel, *Cosmological-parameter determination with microwave background maps*, *Phys Rev D* **54** (July, 1996) 1332–1344, [`astro-ph/9512139`].

[261] J. R. Bond, G. Efstathiou and M. Tegmark, *Forecasting cosmic parameter errors from microwave background anisotropy experiments*, MNRAS **291** (November, 1997) L33–L41, [`astro-ph/9702100`].

[262] M. Zaldarriaga, D. N. Spergel and U. Seljak, *Microwave Background Constraints on Cosmological Parameters*, *Astrophys J* **488** (October, 1997) 1–13, [`astro-ph/9702157`].

[263] A. Blanchard and J. Schneider, *Gravitational lensing effect on the fluctuations of the cosmic background radiation*, *AAP* **184** (October, 1987) 1–6.

[264] U. Seljak, *Gravitational Lensing Effect on Cosmic Microwave Background Anisotropies: A Power Spectrum Approach*, *Astrophys J* **463** (May, 1996) 1, [`astro-ph/9505109`].

[265] M. Zaldarriaga and U. Seljak, *Gravitational lensing effect on cosmic microwave background polarization*, *Phys Rev D* **58** (July, 1998) 023003, [`astro-ph/9803150`].

[266] Y. P. Jing, P. Zhang, W. P. Lin, L. Gao and V. Springel, *The Influence of Baryons on the Clustering of Matter and Weak-Lensing Surveys*, *APJL* **640** (April, 2006) L119–L122, [`astro-ph/0512426`].

[267] D. H. Rudd, A. R. Zentner and A. V. Kravtsov, *Effects of Baryons and Dissipation on the Matter Power Spectrum*, *Astrophys J* **672** (January, 2008) 19–32, [`astro-ph/0703741`].

[268] E. Semboloni, H. Hoekstra, J. Schaye, M. P. van Daalen and I. G. McCarthy, *Quantifying the effect of baryon physics on weak lensing tomography*, MNRAS **417** (November, 2011) 2020–2035, [`1105.1075`].

[269] A. Natarajan, A. R. Zentner, N. Battaglia and H. Trac, *Systematic errors in the measurement of neutrino masses due to baryonic feedback processes: Prospects for stage IV lensing surveys*, *Phys Rev D* **90** (September, 2014) 063516, [`1405.6205`].

[270] I. G. McCarthy, J. Schaye, S. Bird and A. M. C. Le Brun, *The BAHAMAS project: calibrated hydrodynamical simulations for large-scale structure cosmology*, MNRAS **465** (March, 2017) 2936–2965, [`1603.02702`].

[271] V. Springel, R. Pakmor, A. Pillepich, R. Weinberger, D. Nelson, L. Hernquist et al., *First results from the IllustrisTNG simulations: matter and galaxy clustering*, MNRAS **475** (March, 2018) 676–698, [`1707.03397`].

[272] N. E. Chisari, M. L. A. Richardson, J. Devriendt, Y. Dubois, A. Schneider, A. M. C. Le Brun et al., *The impact of baryons on the matter power spectrum from the Horizon-AGN cosmological hydrodynamical simulation*, MNRAS **480** (November, 2018) 3962–3977, [`1801.08559`].

[273] A. Schneider, R. Teyssier, J. Stadel, N. E. Chisari, A. M. C. Le Brun, A. Amara et al., *Quantifying baryon effects on the matter power spectrum and the weak lensing shear correlation*, *JCAP* **2019** (March, 2019) 020, [`1810.08629`].

[274] E. Chung, S. Foreman and A. van Engelen, *Baryonic effects on CMB lensing and neutrino mass constraints*, *Phys Rev D* **101** (March, 2020) 063534, [`1910.09565`].

[275] J. Peloton, M. Schmittfull, A. Lewis, J. Carron and O. Zahn, *Full covariance of CMB and lensing reconstruction power spectra*, *Phys Rev D* **95** (February, 2017) 043508, [`1611.01446`].

[276] N. Sehgal, M. S. Madhavacheril, B. Sherwin and A. van Engelen, *Internal delensing of cosmic microwave background acoustic peaks*, *Phys Rev D* **95** (May, 2017) 103512, [`1612.03898`].

[277] J. Carron, A. Lewis and A. Challinor, *Internal delensing of Planck CMB temperature and polarization*, *JCAP* **2017** (May, 2017) 035, [`1701.01712`].

[278] J. Carron and A. Lewis, *Maximum a posteriori CMB lensing reconstruction*, *Phys Rev D* **96** (September, 2017) 063510, [`1704.08230`].

[279] M. Millea, E. Anderes and B. D. Wandelt, *Bayesian delensing of CMB temperature and polarization*, *Phys Rev D* **100** (July, 2019) 023509, [`1708.06753`].

[280] D. Green, J. Meyers and A. van Engelen, *CMB delensing beyond the B modes*, *JCAP* **2017** (December, 2017) 005, [`1609.08143`].

[281] G. Simard, D. Hanson and G. Holder, *Prospects for Delensing the Cosmic Microwave Background for Studying Inflation*, *Astrophys J* **807** (July, 2015) 166, [`1410.0691`].

[282] R. Takahashi, M. Sato, T. Nishimichi, A. Taruya and M. Oguri, *Revising the Halofit Model for the Nonlinear Matter Power Spectrum*, *Astrophys J* **761** (December, 2012) 152, [1208.2701].

[283] R. E. Smith, J. A. Peacock, A. Jenkins, S. D. M. White, C. S. Frenk, F. R. Pearce et al., *Stable clustering, the halo model and non-linear cosmological power spectra*, MNRAS **341** (June, 2003) 1311–1332, [astro-ph/0207664].

[284] A. J. Mead, J. A. Peacock, C. Heymans, S. Joudaki and A. F. Heavens, *An accurate halo model for fitting non-linear cosmological power spectra and baryonic feedback models*, MNRAS **454** (December, 2015) 1958–1975, [1505.07833].

[285] A. J. Mead, S. Brieden, T. Tröster and C. Heymans, *HMCODE-2020: improved modelling of non-linear cosmological power spectra with baryonic feedback*, MNRAS **502** (March, 2021) 1401–1422, [2009.01858].

[286] E. Schaan, S. Ferraro, S. Amodeo, N. Battaglia, S. Aiola, J. E. Austermann et al., *The Atacama Cosmology Telescope: Combined kinematic and thermal Sunyaev-Zel'dovich measurements from BOSS CMASS and LOWZ halos*, *arXiv e-prints* (September, 2020) arXiv:2009.05557, [2009.05557].

[287] S. Amodeo, N. Battaglia, E. Schaan, S. Ferraro, E. Moser, S. Aiola et al., *The Atacama Cosmology Telescope: Modeling the Gas Thermodynamics in BOSS CMASS galaxies from Kinematic and Thermal Sunyaev-Zel'dovich Measurements*, *arXiv e-prints* (September, 2020) arXiv:2009.05558, [2009.05558].

[288] Planck Collaboration, N. Aghanim, Y. Akrami, M. Ashdown, J. Aumont, C. Baccigalupi et al., *Planck 2018 results. V. CMB power spectra and likelihoods*, *AAP* **641** (Sept., 2020) A5, [1907.12875].

[289] P. Motloch and W. Hu, *Lensing covariance on cut sky and SPT -Planck lensing tensions*, *Phys Rev D* **99** (Jan., 2019) 023506, [1810.09347].

[290] D. Huterer and M. Takada, *Calibrating the nonlinear matter power spectrum: Requirements for future weak lensing surveys*, *Astroparticle Physics* **23** (May, 2005) 369–376, [astro-ph/0412142].

[291] A. Amara and A. Réfrégier, *Systematic bias in cosmic shear: extending the Fisher matrix*, MNRAS **391** (Nov., 2008) 228–236, [0710.5171].

[292] N. Sehgal, S. Aiola, Y. Akrami, K. Basu, M. Boylan-Kolchin, S. Bryan et al., *CMB-HD: An Ultra-Deep, High-Resolution Millimeter-Wave Survey Over Half the Sky*, in *Bulletin of the American Astronomical Society*, vol. 51, p. 6, Sept., 2019, `1906.10134`.

[293] S. Hanany, M. Alvarez, E. Artis, P. Ashton, J. Aumont, R. Aurlien et al., *PICO: Probe of Inflation and Cosmic Origins*, *arXiv e-prints* (Feb., 2019) arXiv:1902.10541, [`1902.10541`].

[294] I. G. McCarthy, S. Bird, J. Schaye, J. Harnois-Deraps, A. S. Font and L. van Waerbeke, *The BAHAMAS project: the CMB-large-scale structure tension and the roles of massive neutrinos and galaxy formation*, MNRAS **476** (May, 2018) 2999–3030, [`1712.02411`].

[295] Y. Dubois, C. Pichon, C. Welker, D. Le Borgne, J. Devriendt, C. Laigle et al., *Dancing in the dark: galactic properties trace spin swings along the cosmic web*, MNRAS **444** (Oct., 2014) 1453–1468, [`1402.1165`].

[296] Y. Dubois, S. Peirani, C. Pichon, J. Devriendt, R. Gavazzi, C. Welker et al., *The HORIZON-AGN simulation: morphological diversity of galaxies promoted by AGN feedback*, MNRAS **463** (Dec., 2016) 3948–3964, [`1606.03086`].

[297] A. Pillepich, D. Nelson, L. Hernquist, V. Springel, R. Pakmor, P. Torrey et al., *First results from the IllustrisTNG simulations: the stellar mass content of groups and clusters of galaxies*, MNRAS **475** (Mar., 2018) 648–675, [`1707.03406`].

[298] D. Nelson, A. Pillepich, V. Springel, R. Weinberger, L. Hernquist, R. Pakmor et al., *First results from the IllustrisTNG simulations: the galaxy colour bimodality*, MNRAS **475** (Mar., 2018) 624–647, [`1707.03395`].

[299] J. P. Naiman, A. Pillepich, V. Springel, E. Ramirez-Ruiz, P. Torrey, M. Vogelsberger et al., *First results from the IllustrisTNG simulations: a tale of two elements - chemical evolution of magnesium and europium*, MNRAS **477** (June, 2018) 1206–1224, [`1707.03401`].

[300] F. Marinacci, M. Vogelsberger, R. Pakmor, P. Torrey, V. Springel, L. Hernquist et al., *First results from the IllustrisTNG simulations: radio haloes and magnetic fields*, MNRAS **480** (Nov., 2018) 5113–5139, [`1707.03396`].

[301] D. Nelson, V. Springel, A. Pillepich, V. Rodriguez-Gomez, P. Torrey, S. Genel et al., *The IllustrisTNG simulations: public data release*, *Computational Astrophysics and Cosmology* **6** (May, 2019) 2, [1812.05609].

[302] B. Hadzhiyska, B. D. Sherwin, M. Madhavacheril and S. Ferraro, *Improving small-scale CMB lensing reconstruction*, *Phys Rev D* **100** (July, 2019) 023547, [1905.04217].

[303] Planck Collaboration, P. A. R. Ade, N. Aghanim, M. Arnaud, M. Ashdown, E. Aubourg et al., *Planck intermediate results. XXXVII. Evidence of unbound gas from the kinetic Sunyaev-Zeldovich effect*, *AAP* **586** (February, 2016) A140, [1504.03339].

[304] E. Schaan, S. Ferraro, M. Vargas-Magaña, K. M. Smith, S. Ho, S. Aiola et al., *Evidence for the kinematic Sunyaev-Zel'dovich effect with the Atacama Cosmology Telescope and velocity reconstruction from the Baryon Oscillation Spectroscopic Survey*, *Phys Rev D* **93** (April, 2016) 082002, [1510.06442].

[305] B. Soergel, S. Flender, K. T. Story, L. Bleem, T. Giannantonio, G. Efstathiou et al., *Detection of the kinematic Sunyaev-Zel'dovich effect with DES Year 1 and SPT*, MNRAS **461** (September, 2016) 3172–3193, [1603.03904].

[306] S. Ferraro, J. C. Hill, N. Battaglia, J. Liu and D. N. Spergel, *Kinematic Sunyaev-Zel'dovich effect with projected fields. II. Prospects, challenges, and comparison with simulations*, *Phys Rev D* **94** (Dec., 2016) 123526, [1605.02722].

[307] F. De Bernardis, S. Aiola, E. M. Vavagiakis, N. Battaglia, M. D. Niemack, J. Beall et al., *Detection of the pairwise kinematic Sunyaev-Zel'dovich effect with BOSS DR11 and the Atacama Cosmology Telescope*, *JCAP* **2017** (March, 2017) 008, [1607.02139].

[308] E. M. Vavagiakis, P. A. Gallardo, V. Calafut, S. Amodeo, S. Aiola, J. E. Austermann et al., *The Atacama Cosmology Telescope: Probing the Baryon Content of SDSS DR15 Galaxies with the Thermal and Kinematic Sunyaev-Zel'dovich Effects*, *arXiv e-prints* (January, 2021) arXiv:2101.08373, [2101.08373].

[309] V. Calafut, P. A. Gallardo, E. M. Vavagiakis, S. Amodeo, S. Aiola, J. E. Austermann et al., *The Atacama Cosmology Telescope: Detection of the Pairwise Kinematic Sunyaev-Zel'dovich Effect with SDSS DR15 Galaxies*, *arXiv e-prints* (January, 2021) arXiv:2101.08374, [2101.08374].

[310] A. Kusiak, B. Bolliet, S. Ferraro, J. C. Hill and A. Krolewski, *Constraining the Baryon Abundance with the Kinematic Sunyaev-Zel'dovich Effect: Projected-Field Detection Using Planck, WMAP, and unWISE*, *arXiv e-prints* (Feb., 2021) arXiv:2102.01068, [2102.01068].

[311] J. P. Greco, J. C. Hill, D. N. Spergel and N. Battaglia, *The Stacked Thermal Sunyaev-Zel'dovich Signal of Locally Brightest Galaxies in Planck Full Mission Data: Evidence for Galaxy Feedback?*, *Astrophys J* **808** (Aug., 2015) 151, [1409.6747].

[312] A. Spacek, E. Scannapieco, S. Cohen, B. Joshi and P. Mauskopf, *Constraining AGN Feedback in Massive Ellipticals with South Pole Telescope Measurements of the Thermal Sunyaev-Zel'dovich Effect*, *Astrophys J* **819** (Mar., 2016) 128, [1601.01330].

[313] V. Vikram, A. Lidz and B. Jain, *A Measurement of the Galaxy Group-Thermal Sunyaev-Zel'dovich Effect Cross-Correlation Function*, MNRAS **467** (May, 2017) 2315–2330, [1608.04160].

[314] J. C. Hill, E. J. Baxter, A. Lidz, J. P. Greco and B. Jain, *Two-halo term in stacked thermal Sunyaev-Zel'dovich measurements: Implications for self-similarity*, *Phys Rev D* **97** (Apr., 2018) 083501, [1706.03753].

[315] A. Spacek, M. L. A. Richardson, E. Scannapieco, J. Devriendt, Y. Dubois, S. Peirani et al., *Using Real and Simulated Measurements of the Thermal Sunyaev-Zel'dovich Effect to Constrain Models of AGN Feedback*, *Astrophys J* **865** (Oct., 2018) 109, [1711.05304].

[316] S. Pandey, E. J. Baxter, Z. Xu, J. Orlowski-Scherer, N. Zhu, A. Lidz et al., *Constraints on the redshift evolution of astrophysical feedback with Sunyaev-Zel'dovich effect cross-correlations*, *Phys Rev D* **100** (Sept., 2019) 063519, [1904.13347].

[317] H. Tanimura, G. Hinshaw, I. G. McCarthy, L. Van Waerbeke, N. Aghanim, Y.-Z. Ma et al., *Probing hot gas around luminous red galaxies through the Sunyaev-Zel'dovich effect*, MNRAS **491** (Jan., 2020) 2318–2329, [1903.06654].

[318] S. Pandey, E. J. Baxter and J. C. Hill, *Constraining the properties of gaseous halos via cross-correlations of upcoming galaxy surveys and thermal Sunyaev-Zel'dovich maps*, *Phys Rev D* **101** (Feb., 2020) 043525, [1909.00405].

[319] N. Koukoufilippas, D. Alonso, M. Bilicki and J. A. Peacock, *Tomographic measurement of the intergalactic gas pressure through galaxy-tSZ cross-correlations*, MNRAS **491** (Feb., 2020) 5464–5480, [`1909.09102`].

[320] N. Battaglia, S. Ferraro, E. Schaan and D. N. Spergel, *Future constraints on halo thermodynamics from combined Sunyaev-Zel'dovich measurements*, *JCAP* **2017** (Nov., 2017) 040, [`1705.05881`].

[321] R. Keisler, C. L. Reichardt, K. A. Aird, B. A. Benson, L. E. Bleem, J. E. Carlstrom et al., *A Measurement of the Damping Tail of the Cosmic Microwave Background Power Spectrum with the South Pole Telescope*, *Astrophys J* **743** (December, 2011) 28, [`1105.3182`].

[322] J. W. Henning, J. T. Sayre, C. L. Reichardt, P. A. R. Ade, A. J. Anderson, J. E. Austermann et al., *Measurements of the Temperature and E-mode Polarization of the CMB from 500 Square Degrees of SPTpol Data*, *Astrophys J* **852** (January, 2018) 97, [`1707.09353`].

[323] B. A. Benson, P. A. R. Ade, Z. Ahmed, S. W. Allen, K. Arnold, J. E. Austermann et al., *SPT-3G: a next-generation cosmic microwave background polarization experiment on the South Pole telescope*, in *Millimeter, Submillimeter, and Far-Infrared Detectors and Instrumentation for Astronomy VII*, vol. 9153 of *Proceedings of SPIE*, p. 91531P, July, 2014, `1407.2973`, DOI.

[324] W. Everett, P. A. R. Ade, Z. Ahmed, A. J. Anderson, J. E. Austermann, J. S. Avva et al., *Design and Bolometer Characterization of the SPT-3G First-Year Focal Plane*, *Journal of Low Temperature Physics* **193** (Dec, 2018) 1085–1093, [`1902.09640`].

[325] A. J. Anderson, P. A. R. Ade, Z. Ahmed, J. E. Austermann, J. S. Avva, P. S. Barry et al., *SPT-3G: A Multichroic Receiver for the South Pole Telescope*, *Journal of Low Temperature Physics* **193** (December, 2018) 1057–1065.

[326] M. Tucci, V. Desjacques and M. Kunz, *Cosmic infrared background anisotropies as a window into primordial non-Gaussianity*, MNRAS **463** (Dec., 2016) 2046–2063, [`1606.02323`].

[327] G. L. Bryan and M. L. Norman, *Statistical Properties of X-Ray Clusters: Analytic and Numerical Comparisons*, ApJ **495** (Mar., 1998) 80–99, [`astro-ph/9710107`].

APPENDICES

Appendix A

Projection of three-dimensional power spectra to two dimensions

A.1 3-dimensional to 2-dimensional power

Many cosmological observables are three dimensional quantities that are projected and integrated along our line of sight. In this Appendix we describe how to calculate the two-dimensional angular power spectrum C_ℓ^{AB} of two such quantities A and B by taking the CMB lensing angular power spectrum as an example.

Consider the CMB lensing potential ϕ:

$$\phi(\hat{\boldsymbol{n}}) = \int d\chi W^{\Phi}(\chi)\Phi(\chi\hat{\boldsymbol{n}}, \chi). \tag{A.1}$$

Its angular power spectrum is defined as $C_\ell^{\phi\phi}$ by

$$\langle \phi_{\ell m}\phi^*_{\ell' m'} \rangle \equiv C_\ell^{\phi\phi}\delta_{\ell\ell'}\delta_{mm'}. \tag{A.2}$$

Using the spherical harmonic decompositions (1.4), this can be explicitly evaluated:

$$\begin{aligned}\langle \phi_{\ell m}\phi^*_{\ell' m'} \rangle &= \int d^2\hat{\boldsymbol{n}} d^2\hat{\boldsymbol{n}}' Y^*_{\ell m}(\hat{\boldsymbol{n}}) Y_{\ell' m'}(\hat{\boldsymbol{n}}') \left\langle \phi(\hat{\boldsymbol{n}})\phi^*(\hat{\boldsymbol{n}}')\right\rangle \\ &= \int d^2\hat{\boldsymbol{n}} d^2\hat{\boldsymbol{n}}' Y^*_{\ell m}(\hat{\boldsymbol{n}}) Y_{\ell' m'}(\hat{\boldsymbol{n}}') \int d\chi d\chi' W^{\Phi}(\chi) W^{\Phi *}(\chi') \left\langle \Phi(\chi\hat{\boldsymbol{n}}, \chi)\Phi^*(\chi'\hat{\boldsymbol{n}}', \chi')\right\rangle .\end{aligned} \tag{A.3}$$

Using the three-dimensional Fourier space conventions (1.2), and dropping the conjugation on $W^{\Phi}(\chi)$ as it is real, this becomes

$$\begin{aligned}\langle \phi_{\ell m}\phi^{*}_{\ell' m'}\rangle = \int d^2\hat{\boldsymbol{n}} d^2\hat{\boldsymbol{n}}' Y^{*}_{\ell m}(\hat{\boldsymbol{n}}) Y_{\ell' m'}(\hat{\boldsymbol{n}}') \int d\chi d\chi' W^{\Phi}(\chi) W^{\Phi}(\chi') \\ \int \frac{d^3\vec{\boldsymbol{k}}}{(2\pi)^3}\frac{d^3\vec{\boldsymbol{k}}'}{(2\pi)^3} e^{i\vec{\boldsymbol{k}}\cdot\vec{\chi}} e^{-i\vec{\boldsymbol{k}}'\cdot\vec{\chi}'} \left\langle \Phi(\vec{\boldsymbol{k}})\Phi^{*}(\vec{\boldsymbol{k}}')\right\rangle,\end{aligned} \tag{A.4}$$

where $(\chi\hat{\boldsymbol{n}}, \chi) = \vec{\chi}$. Using the definition of the power spectrum,

$$\left\langle \Phi(\vec{\boldsymbol{k}})\Phi^{*}(\vec{\boldsymbol{k}}')\right\rangle = (2\pi)^3 P(k)\delta^3(\vec{\boldsymbol{k}} - \vec{\boldsymbol{k}}'), \tag{A.5}$$

and performing the integration over $\vec{\boldsymbol{k}}'$ we get

$$\langle \phi_{\ell m}\phi^{*}_{\ell' m'}\rangle = \int d^2\hat{\boldsymbol{n}} d^2\hat{\boldsymbol{n}}' Y_{\ell m}(\hat{\boldsymbol{n}}) Y^{*}_{\ell' m'}(\hat{\boldsymbol{n}}') \int d\chi d\chi' W^{\Phi}(\chi) W^{\Phi}(\chi') \int \frac{d^3\vec{\boldsymbol{k}}}{(2\pi)^3} e^{i\vec{\boldsymbol{k}}\cdot(\vec{\chi}-\vec{\chi}')} P_{\Phi}(k). \tag{A.6}$$

From here we use the projection formula

$$e^{i\vec{\boldsymbol{k}}\cdot\vec{\boldsymbol{x}}} = 4\pi \sum_{\ell m} i^{\ell} j_{\ell}(kx) Y^{*}_{\ell m}(\hat{\boldsymbol{k}}) Y_{\ell m}(\hat{\boldsymbol{x}}), \tag{A.7}$$

where $j_\ell(x)$ are the spherical Bessel functions of degree ℓ, such that

$$\begin{aligned}\langle \phi_{\ell m}\phi^{*}_{\ell' m'}\rangle = \frac{2}{\pi} \int d^2\hat{\boldsymbol{n}} d^2\hat{\boldsymbol{n}}' Y_{\ell m}(\hat{\boldsymbol{n}}) Y^{*}_{\ell' m'}(\hat{\boldsymbol{n}}') \int d\chi d\chi' W^{\Phi}(\chi) W^{\Phi}(\chi') \int d^3\vec{\boldsymbol{k}} P_{\Phi}(k) \\ \sum_{\ell_1 m_1 \ell_2 m_2} i^{\ell_1-\ell_2} j_{\ell_1}(k\chi) j_{\ell_2}(k\chi') Y^{*}_{\ell_1 m_1}(\hat{\boldsymbol{k}}) Y_{\ell_2 m_2}(\hat{\boldsymbol{k}}) Y_{\ell_1 m_1}(\hat{\mathbf{n}}) Y^{*}_{\ell_2 m_2}(\hat{\mathbf{n}}').\end{aligned} \tag{A.8}$$

Performing the integration over $\hat{\boldsymbol{n}}$ and $\hat{\boldsymbol{n}}'$ gives

$$\begin{aligned}\langle \phi_{\ell m}\phi^{*}_{\ell' m'}\rangle = \frac{2}{\pi} \int d\chi d\chi' W^{\Phi}(\chi) W^{\Phi}(\chi') \int d^3\vec{\boldsymbol{k}} P_{\Phi}(k) \\ \sum_{\ell_1 m_\ell l_2 m_2} i^{\ell_1-\ell_2} j_{\ell_1}(k\chi) j_{\ell_2}(k\chi') Y^{*}_{\ell_1 m_1}(\hat{\boldsymbol{k}}) Y_{\ell_2 m_2}(\hat{\boldsymbol{k}}) \delta_{\ell\ell_1}\delta_{mm_1}\delta_{\ell'\ell_2}\delta_{m'm_2}\end{aligned} \tag{A.9}$$

and performing the sum gives

$$\langle \phi_{\ell m}\phi^{*}_{\ell' m'}\rangle = \frac{2}{\pi} \int d\chi d\chi' W^{\Phi}(\chi) W^{\Phi}(\chi') \int d^3\vec{\boldsymbol{k}} P_{\Phi}(k) i^{\ell-\ell'} j_{\ell}(k\chi) j_{\ell'}(k\chi') Y^{*}_{\ell m}(\hat{\boldsymbol{k}}) Y_{\ell' m'}(\hat{\boldsymbol{k}}). \tag{A.10}$$

Writing the $\vec{\boldsymbol{k}}$ integration as an integration over modulus and angle gives

$$\langle \phi_{\ell m} \phi^*_{\ell' m'} \rangle = \frac{2}{\pi} \int d\chi d\chi' W^\Phi(\chi) W^\Phi(\chi') \int k^2 dk \int d^2\hat{\boldsymbol{k}} \\ P_\Phi(k) i^{\ell-\ell'} j_\ell(k\chi) j_{\ell'}(k\chi') Y^*_{\ell m}(\hat{\boldsymbol{k}}) Y_{\ell' m'}(\hat{\boldsymbol{k}}), \tag{A.11}$$

and performing the integration over the angle gives

$$\langle \phi_{\ell m} \phi^*_{\ell' m'} \rangle = \frac{2}{\pi} \int d\chi d\chi' W^\Phi(\chi) W^\Phi(\chi') \int k^2 dk P_\Phi(k) i^{\ell-\ell'} j_\ell(k\chi) j_{\ell'}(k\chi') \delta_{\ell\ell'} \delta_{mm'}; \tag{A.12}$$

comparison with (A.2) tells us that

$$C_\ell^{\phi\phi} = \frac{2}{\pi} \int d\chi d\chi' W^\Phi(\chi) W^\Phi(\chi') \int k^2 dk P_\Phi(k) j_\ell(k\chi) j_\ell(k\chi'). \tag{A.13}$$

A.2 Limber Approximation

In general, Equation (A.1) is difficult to integrate numerically: there are three separate integrals (over χ, χ', and k), and the highly oscillatory behaviour of the $j_\ell(x)$ (particularly at high ℓ) requires that a high number of k sample points are taken in the numerical integration. Fortunately there exists a widely-used simplifying assumption, the *Limber approximation* [49], which is valid in the small-scale (high-l) limit; using

$$j_\ell(x) \to \sqrt{\frac{\pi}{2(\ell+1/2)}} \delta(\ell + 1/2 - x) \tag{A.14}$$

we get

$$\begin{aligned} C_\ell^{\phi\phi} &= \int d\chi d\chi' W^\Phi(\chi) W^\Phi(\chi') \int k^2 dk P_\Phi(k) \frac{1}{(\ell+1/2)} \delta(\ell + 1/2 - k\chi) \delta(\ell + 1/2 - k\chi') \\ &= \int d\chi \int k dk W^\Phi(\chi) W^\Phi\left(\frac{\ell+1/2}{k}\right) P_\Phi(k) \frac{1}{(\ell+1/2)} \delta(\ell + 1/2 - k\chi) \\ &= \int d\chi \frac{W^\Phi(\chi)^2}{\chi^2} P_\Phi\left(k = \frac{\ell+1/2}{\chi}\right) \end{aligned} \tag{A.15}$$

The final expression (A.15) can be generalized to a z-dependent power spectrum $P(k, z)$

$$C_\ell^{\phi\phi} = \int d\chi \frac{W^\Phi(\chi)^2}{\chi^2} P_\Phi \left(k = \frac{\ell + 1/2}{\chi}, z\right); \tag{A.16}$$

this is an extremely convenient and easily integrated expression, given $P(k, z)$. More generally we can Limber approximate the angular power spectra between any projected observables defined by

$$A^{2d}(\hat{\boldsymbol{n}}) = \int d\chi W^A(\chi) A^{3d}(\chi \hat{\boldsymbol{n}}, \chi) \tag{A.17}$$

by projecting the known three-dimensional power spectrum of the 3-dimensional observables according to

$$C_\ell^{AB} = \int d\chi \frac{W^A(\chi) W^B(\chi)}{\chi^2} P_{AB} \left(k = \frac{\ell + 1/2}{\chi}, z\right) \tag{A.18}$$

where P_{AB} is the three-dimensional cross power-spectrum between the 3-dimensional observables A and B.

Appendix B

Parametric expressions within the halo model

When we calculate quantities within the halo model, we use the halo mass function and bias of Tinker [58]; in this Appendix we present their parametric forms. Prior to doing this, we will discuss some subtleties in the definition of halo mass.

B.1 Definitions of halo mass

The halo model is "split" whereby the continuous density field is replaced by the discrete halos and regions of empty space. However, this is artificial: the true Universe is described by a continuous density field. It is clear that the most overdense regions should be replaced by halos when going from the continuous to the discrete picture; but when doing so, how do we define the boundary of the halo? In general the mass within a radius R is given by

$$M(R) = \int_0^R dr 4\pi r^2 \rho(r) \tag{B.1}$$

where $\rho(r)$ is the *halo density profile.* Thus different prescriptions of halo-boundary (specifications of R) correspond to a different halo masses M (defined as the mass contained within the chosen halo boundary).

Given a halo density profile $\rho(r)$ some common ways of defining the halo boundary / mass are:

- The mass within a sphere of radius $R_{\Delta m}$ that has mean density equal to some constant factor Δ times the mean matter density; in this case the $M-R$ relation is

$$M_{\Delta m} \equiv \int_0^{R_{\Delta m}} dr 4\pi r^2 \rho(r) = \frac{4\pi}{3} R_{\Delta m}^3 \rho_m(z). \tag{B.2}$$

- The mass within a sphere of radius $R_{\Delta c}$ that has mean density equal to some constant factor Δ times the critical density; in this case the $M-R$ relation is

$$M_{\Delta c} \equiv \int_0^{R_{\Delta c}} dr 4\pi r^2 \rho(r) = \frac{4\pi}{3} R_{\Delta c}^3 \rho_c(z). \tag{B.3}$$

- The mass within the sphere of radius R_{vir} at which the halo is virialized:

$$M_{\text{vir}} = \int_0^{R_{\text{vir}}} dr 4\pi r^2 \rho(r) = \frac{4\pi}{3} R_{\text{vir}}^3 \rho_{\text{vir}}(z). \tag{B.4}$$

  $\rho_{\text{vir}}(z)$, the mean density within the virial radius, is defined as being $\Delta_{\text{vir}}\rho_c(z)$, such that

$$M_{\text{vir}} = \frac{4\pi}{3} R_{\text{vir}}^3 \Delta_{\text{vir}} \rho_c(z) \tag{B.5}$$

  where Δ_{vir} is a z-dependent function given in Equation (6) of [327]:

$$\Delta_{\text{vir}} = 18\pi^2 + 82x - 32x^2 \tag{B.6}$$

  where $x = \Omega(z) - 1$ with $\Omega(z) = \frac{\Omega_m(1+z)^3}{\Omega_m(1+z)^3+(1-\Omega_m)}$.

Note that while each $M-R$ relation is given *independently* of the halo-density profile $\rho(r)$, to convert between two different mass definitions—eg to find the $M_{\Delta c}$ of a halo given the $M_{\Delta m}$—knowledge of $\rho(r)$ is needed and Equation (B.1) must be integrated.

B.2 Explicit expressions for the halo mass function, bias, and concentration

B.2.1 Halo mass function and bias

We use the halo mass function of [58], with the M_{200m} definition of halo mass.

The halo multiplicity function is given by

$$f(\nu) = \nu\alpha\left(1 + (\beta\nu)^{-2\phi}\right)\nu^{2\eta}e^{-\left(\frac{\gamma\nu^2}{2}\right)} \tag{B.7}$$

with

$$\beta = 0.589\,(1+z)^{0.20}\,; \tag{B.8}$$
$$\phi = -\,0.729\,(1+z)^{-0.08}\,; \tag{B.9}$$
$$\eta = -\,0.243\,(1+z)^{0.27}\,; \tag{B.10}$$
$$\gamma = 0.864\,(1+z)^{-0.01}\,. \tag{B.11}$$

While these parameters are redshift-dependent, [58] cautions that these are not valid to arbitrarily high z and recommends to use the $z = 3.5$ values for $z \geq 3.5$. Finally, the parameter α is not specified; in fact it is found by imposing the consistency relation

$$\int b(\nu)f(\nu)d\ln\nu = 1 \tag{B.12}$$

at all redshifts[1], where $b(\nu)$ is the halo bias, discussed below. For $\Delta = 200$, α is equal to 0.368 at $z = 0$ but decreases by up to 30% as $z \to 3.5$.

The halo mass function $\frac{dN}{dM}$ can be calculated from $f(\nu)$ according to

$$\frac{dN}{dM} \equiv \frac{\bar{\rho}_m}{M}f(\nu)\frac{d\ln\nu}{dM}. \tag{B.13}$$

B.2.2 Halo bias

We use the halo bias of Tinker [58], which is defined consistently with the halo mass function above. [58] finds that

$$b(\nu) = 1 - A\frac{\nu^a}{\nu^a + \delta_c^a} + B\nu^b + C\nu^c. \tag{B.14}$$

where $\delta_c \sim 1.686$ is again the critical density required for collapse. Defining

$$y \equiv \log_{10}\Delta \tag{B.15}$$

---

[1] It has been a point of contention whether this should be imposed at all redshifts or just at $z = 0$; while it does not make physical sense to only impose this at $z = 0$, an inclarity of [58] on the matter led this to be (erroneously) imposed only at $z = 0$ in many cases in the literature. Thanks to Boris Bolliet, Colin Hill, Matt Johnson, and Mat Madhavacheril for discussions on this issue.

where Δ is the factor used in the definition of the halo mass (we use $\Delta = 200$) the values of the parameters are

$$A = 1.0 + 0.24 y e^{-(4/y)^4} \tag{B.16}$$

$$a = 0.44y - 0.88 \tag{B.17}$$

$$B = 0.183 \tag{B.18}$$

$$b = 1.5 \tag{B.19}$$

$$C = 0.0109 + 0.107y + 0.19e^{-(4/y)^4} \tag{B.20}$$

$$c = 2.4. \tag{B.21}$$

B.2.3 Concentration

To calculate the halo mass profile, as well as to convert between different definitions of halo mass, one needs the concentration relation. We use the concentration relations of [61] which gives parametrized expressions for the concentration for different mass definitions, and will be different depending on the mass definition being used. In general c has a parametric form

$$c_X = A_X \left(\frac{M}{M_{\text{pivot}}} \right)^{B_X} (1+z)^{C_X}, \tag{B.22}$$

where in all cases $M_{\text{pivot}} = 2{\times}10^{12} h^{-1} M_\odot$. Values of $\{A_X, B_X, C_X\}$ for $X = \{200m, 200c, \text{vir}\}$ are given in Table B.1.

Parameter	M_{200m}	M_{200c}	M_{vir}
A	10.14	5.71	7.85
B	-0.081	-0.084	-0.081
C	-1.01	-0.47	-0.71

Table B.1: Values of the parameters for the parametric halo concentration relation (B.22) from [61].

Appendix C

Conversion between μK and Jy

We have presented the CIB power spectra throughout in Jy, a unit of surface intensity commonly used for CIB measurements and in radio astronomy. However, we quote the CMB lensing power spectra in $\mu\mathrm{K}_{\mathrm{CMB}}$; additionally, some of the instrumental noise levels we quote are in μK. Thus, as it is convenient to have a formula to convert between these units Jy and $\mu\mathrm{K}_{\mathrm{CMB}}$, we present one in this Appendix.

ν[Ghz]	U [Jy $^{-}$K$^{-1}_{\mathrm{CMB}}$]
217	483.69
353	287.45
545	58.04
857	2.27

Table C.1: Conversion factors between Jy and $\mu\mathrm{K}_{\mathrm{CMB}}$, from [110].

The surface brightness of a black body is given by the Planck formula

$$B_\nu(T) = \frac{2h\nu^3}{c^2}\frac{1}{e^{\frac{h\nu}{kT}} - 1}. \tag{C.1}$$

To convert from brightness to temperature we use

$$dB_\nu(T) = \frac{2h^2\nu^4 e^{\frac{h\nu}{kT}}}{c^2 kT^2\left(e^{\frac{h\nu}{kT}} - 1\right)^2} dT. \tag{C.2}$$

Defining

$$x \equiv \frac{h\nu}{kT_{\mathrm{CMB}}} = \frac{\nu[\mathrm{GHz}]}{56.233\mathrm{GHz}} \tag{C.3}$$

and using the definition of a Jansky $\mathrm{Jy} = 10^{-26}\frac{\mathrm{W}}{\mathrm{m^2Hz}}$ we can write

$$dB_\nu[\mathrm{MJy}] = 968\frac{e^x\left(\frac{\nu[\mathrm{GHz}]}{100}\right)^4}{\left(e^x-1\right)^2}{}^{-}\mathrm{K}. \tag{C.4}$$

While this formula is useful, in general a more accurate conversion between the units is dependent on the specifications (spectral response, etc) of the instrument used and so for *Planck* frequencies we use the units quoted in [110]; see Table C.1.

Appendix D

Comparison of simulations and parametric model for baryonic effects

In Section 9.6, we investigated whether including a model for baryonic effects in the prediction for the matter power spectrum can reduce the bias on M_ν after marginalization over the model's parameters. For this to be a valid method, we must be reasonably confident that the model can capture a realistic range of baryonic effects. In this appendix, we check this for the hydrodynamical simulations we use, assuming that this set of simulations itself spans a realistic range of effects. More detailed comparisons between these simulations and observations will likely be required to fully justify this assumption, but this is beyond the scope of this thesis.

We compare model predictions from Ref. [53] with the power spectrum ratios $\hat{R}(k,z)$ measured from simulations, using the following statistic:

$$\Delta(A,\eta_0) \equiv \sum_{i,j} \left(\hat{R}(k_i,z_j) - \frac{P_m(k_i,z_j;A,\eta_0)}{P_{\rm DMO}(k_i,z_j)} \right)^2 , \tag{D.1}$$

where $P_{\rm DMO}$ is evaluated with the fiducial values of A and η_0 from Sec. 9.6. We sum over k and z points at which simulation measurements are available over $0 \leq z \leq 2$ and $1 \leq k \leq 10$, chosen to correspond roughly to the ranges in which baryonic effects significantly affect $C_L^{\kappa\kappa}$ for $L \lesssim 3000$ [172]. Eq. (D.1) is equivalent to a χ^2 statistic that weights all points equally, motivated by other work that has found sample-variance uncertainties on $\hat{R}$ to be roughly scale-independent [194, 189, 201]. Our goal is only to examine the "best-fit" predictions of the model for each simulation, rather than fully quantify the goodness of fit (which we cannot do without better knowledge of the uncertainties on $\hat{R}$), so we simply use

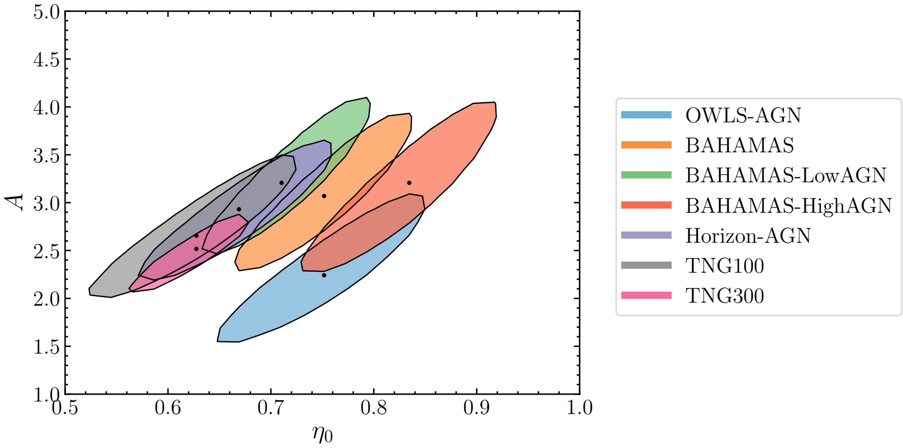

Figure D.1: Contour plots in the A, η_0 plane. We show contours of $\Delta(A, \eta_0)$, where $\Delta(A, \eta_0)$ is defined in Eq. (D.1). The points that minimize $\Delta(A, \eta_0)$ are shown, and the contours are filled in for values of $\Delta(A, \eta_0)$ which $\Delta(A, \eta_0) < \Delta_{\rm min} + 5 \times 10^{-5}$, corresponding to the separate $\Delta_{\rm min}$ for each simulation.

unit weights in Eq. (D.1). We evaluate P_m and $P_{\rm DMO}$ at our fiducial cosmology, because our goal is to check how well the model from Ref. [53] can reproduce our range of $\hat{R}$ curves with cosmology held fixed.

In Fig. D.1, we show contour plots of $\Delta(A, \eta_0)$ for each simulation. These plots clearly imply a degeneracy between A and η_0 for each simulation, roughly consistent with the degeneracy directions seen in the fits in Ref. [202] (see their Fig. 6). Fig. D.2 shows the "best-fitting" predictions for $\hat{R}(k, z)$ from minimizing $\Delta(A, \eta_0)$ with respect to the two parameters, at a few representative redshifts. We find that for all simulations, the model can describe the power spectrum suppression to better than $\sim 5\%$ over the scales of interest, with better fits at lower z. While other models have been shown to match a subset of these simulations at higher precision (e.g. [230]), the $\sim 5\%$ precision we find for the model from Ref. [53] is sufficient to use it our proof-of-concept forecast in Sec. 9.6. To see this, note that 5% systematic errors in P_m over the scales we fit for translate into ~2% errors in $C_L^{\kappa\kappa}$ (see Fig. D.3), and Fig. 9.1 shows that the simulation-derived $C_L^{\kappa\kappa}$ curves are still distinguishable from the effect of massive neutrinos even with this level of errors.

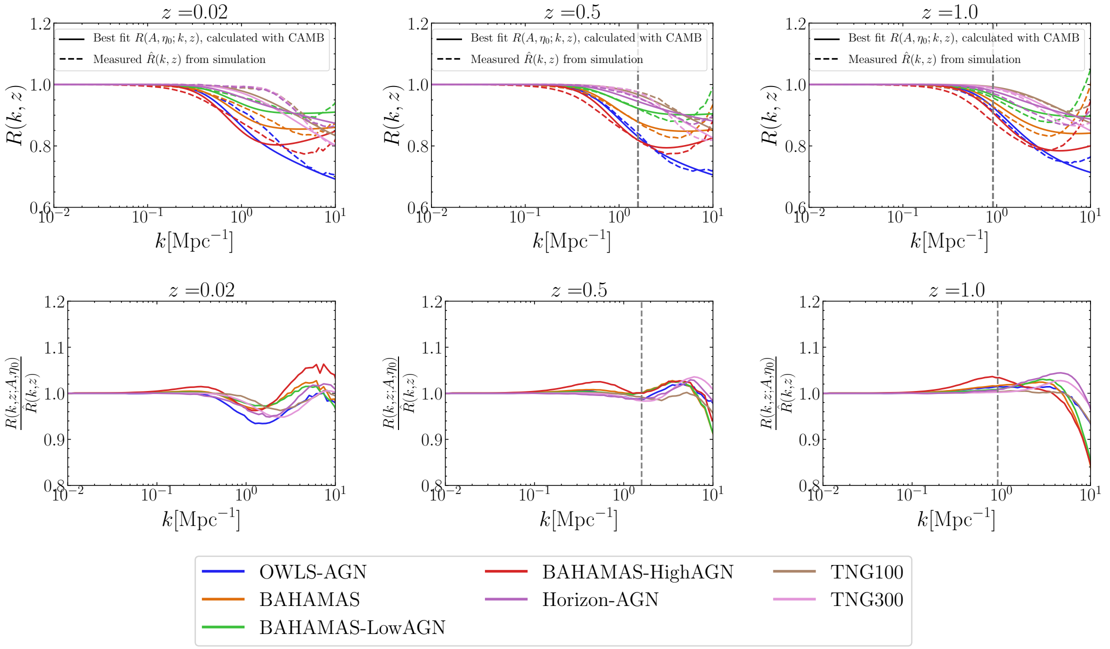

Figure D.2: *Top:* The response functions $\hat{R}(k,z)$ measured from the simulations (solid lines) and the $R(A,\eta_0;k,z)$ (from the baryonic model) that minimize $\Delta(A,\eta_0)$, at various redshifts. Bottom: Ratios of "best-fit" and measured R functions. A dashed vertical line is shown at the k that is equivalent to $3100/\chi(z)$ at each redshift, i.e. the maximum k used to calculate $C_L^{\kappa\kappa}$ in the Limber approximation at each z.

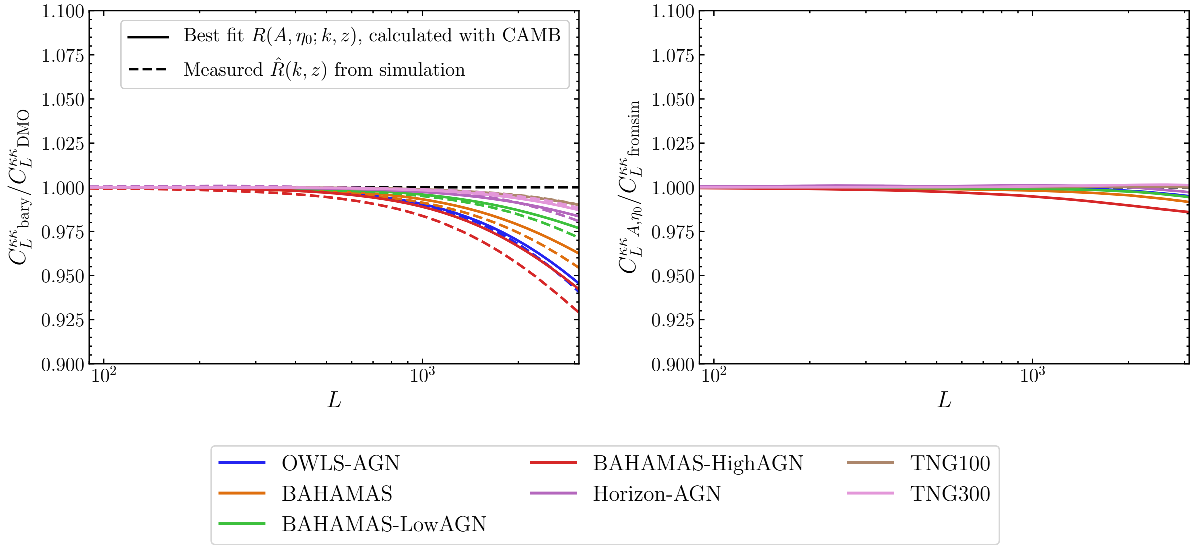

Figure D.3: *Left:* The ratio of the baryonic lensing power spectra to the DMO power spectra, computed with the $P(k, z; A, \eta_0)$ at the "best fit" values found for each simulation (in dashed lines). Also shown (in solid lines) is the ratio of the power spectra with the response function $\hat{R}(k, z)$ measured directly from the simulations. *Right:* The ratio of the lensing power spectra computed at the "best-fit" A,η_0 and that computed with $\hat{R}(k, z)$ from the simulations. We find that the model is capable of reproducing the simulation measurements at better than 2% accuracy for $L < 3100$.